Exploration of *s*-process elemental abundances in globular cluster stars using medium- and high-resolution spectra

A thesis submitted in partial fulfilment of the requirements for
the Degree of Doctor of Philosophy in Astronomy
at the University of Canterbury

by C. Clare Worley

Department of Physics and Astronomy
University of Canterbury
December 18, 2009

Abstract

This thesis has used medium- and high-resolution spectral data to derive elemental abundances, in particular light and heavy *s*-process elemental abundances, for groups of giant stars in the globular clusters 47 Tuc, NGC 6388 and NGC 362. These analyses were undertaken using both curve-of-growth and spectrum synthesis techniques. The techniques were calibrated with respect to the metal-poor giant star Arcturus in order to reduce systematic errors in the analysis process.

A feasibility study was undertaken that compared synthetic spectra at different resolutions throughout the colour-magnitude diagram (CMD) of a metal-rich ([Fe/H] ~ -0.5 dex) globular cluster. This study identified where on the CMD light and heavy *s*-process elemental abundances could be derived at medium resolution ($R \sim 10,000$). Abundance analyses could be undertaken on the giant branches down to just below the horizontal branch and then again on the main sequence below $T_{eff} \sim 4500$ K. At all other places on the CMD high-resolution spectra ($R \sim 30,000$) are required to derive these abundances.

Performance verification data at $R \sim 5,000$ was obtained using the Robert Stobie Spectrograph (RSS) on the Southern African Large Telescope (SALT) and showed that there were no large scale *s*-process elemental abundance variations in 47 Tuc giant branch stars. The level of precision in this preliminary data was [X/Fe] ~ 0.5 dex. A resolution of $R \sim 10,000$ should be achievable with SALT RSS in the future which will improve this limit. The AAOmega survey of 47 Tuc stars at $R \sim 6,500$ was more promising in certain aspects of elemental abundance determination. The observed wavelengths included the key features of CN and CH molecular bands, and light ($Z \leq 30$) and heavy ($38 \leq Z \leq 63$) element spectral lines. CN indices were measured and calibrated to previous results. The well-known CN bimodality was observed in the 47 Tuc stars, as well as a radial gradient in CN strength. A preliminary subset of ten of the survey stars have undergone an abundance analysis for which the abundances of Fe, Si, and Ca were found to be homogeneous within this cluster. The Na abundances had a large range in values that were observed to correlate with CN strength. The *s*-process elemental abundance results were inconclusive. The Zr abundances showed little to no enhancement in the sample and the Ba abundances varied considerably due to strong lines of Ba II being extremely sensitive to microturbulence.

Various high-resolution studies were carried out using spectra of giant stars in 47 Tuc, NGC 6388 and NGC 362 observed on the Australian National Observatory (ANO) 2.3 m échelle spectrograph and the Ultra-Violet Échelle Spectrograph (UVES) on the Very Large Telescope (VLT). The high-resolution analysis of 47 Tuc giant star Lee 2525 found an enhanced Zr abundance in this star which resolved a discrepancy between two previous 47 Tuc elemental abundance studies (Brown & Wallerstein 1992; Wylie et al. (2006)). The stars in the VLT dataset that were analysed here included five giant branch stars in 47 Tuc, two in NGC 6388 and thirteen in NGC 362. The low temperatures and gravities of these stars caused departures from local thermodynamic equilibrium in low excitation potential neutral species, particularly Fe and Zr, that needed to be taken into account before reliable stellar parameters and elemental abundances could be determined for these stars. Veiling effects due to circumstellar dust were postulated to have produced artificially low metallicities for the infra-red excess stars in this sample, particularly for the 47 Tuc stars.

The element abundance analyses of 47 Tuc, NGC 6388 and NGC 362 stars found the derived metallicities to be homogeneous for each cluster ($\langle$[Fe/H]$\rangle_{47Tuc} = -0.88 \pm 0.09$ dex; $\langle$[Fe/H]$\rangle_{NGC6388} = -0.60 \pm 0.06$ dex; $\langle$[Fe/H]$\rangle_{NGC362} = -1.21 \pm 0.08$ dex). The 47 Tuc sample included Lee 2525 and the five VLT stars. The derived metallicities were in reasonable agreement with previously reported values. The light (*ls*) and heavy (*hs*) *s*-process element abundances were enhanced and homogeneous in the stars of each cluster. The abundances determined for 47 Tuc and NGC 6388 were in good agreement, reflecting the similarity in metallicity of the stars in these two clusters ($\langle[ls/\mathrm{Fe}]\rangle_{47Tuc} = +0.53 \pm 0.02$ dex; $\langle[hs/\mathrm{Fe}]\rangle_{47Tuc} = +0.40 \pm 0.06$ dex; $\langle[ls/\mathrm{Fe}]\rangle_{NGC6388} = +0.58 \pm 0.13$ dex; $\langle[hs/\mathrm{Fe}]\rangle_{NGC6388} = +0.39 \pm 0.07$ dex). The more metal-poor cluster NGC 362 was less enhanced in ls elemental abundances and slightly more enhanced in hs elemental abundances ($\langle[ls/\mathrm{Fe}]\rangle_{NGC362} = +0.32 \pm 0.10$ dex, $\langle[hs/\mathrm{Fe}]\rangle_{NGC362} = +0.46 \pm 0.09$ dex).

The clear enhancement in the *s*-process elemental abundances and homogeneity in the results for each globular cluster is evidence that these stars have been enhanced extrinsically in *s*-process elements. Pollution events in the history of each cluster has resulted in the abundance distribution in both the light elements and the heavy elements that has been observed in the stars analysed in this thesis. The enhancements in Na, *ls* and *hs* elemental abundances favours intermediate mass AGB stars as the source of the pollution.

Let all my themes within - of ancient light,
Of origins and change and human worth -
let all their melodies still intertwine
Evolve and merge with ever growing unity . . .

Beatrice Tinsley 1981

Contents

List of Figures

List of Tables

Acknowledgments

....

The completion of this thesis has been the result of a great deal of support and encouragement from many people.

First and foremost, I would like to thank my supervisor, Professor Peter Cottrell, for his guidance and enthusiasm in my undertaking this thesis. His patience and support has been invaluable and I have greatly enjoyed working with him. Thank you also to my associate-supervisor, Professor Ken Freeman, for readily offering his insights and opinions whenever I needed them.

I was supported financially through this process by a number of sources: The University of Canterbury Doctoral Scholarship, the Carlisle Trust Scholarship, the Dennis William Moore Scholarship, the New Zealand Federation of Graduate Women Fellowship and the Edmond and Isabel Kidson Scholarship. Further funding for travel to conferences and for collaborative work was provided by the University of Canterbury Physics and Astronomy Department, the Royal Society of New Zealand and the Canterbury Royal Society.

My friends have been incredibly supportive throughout my PhD experience. Thank you particularly to Helen and Charlotte who have always been so enthusiastic and interested in my work. Thank you to my colleagues, Mita, Nikolai, Pauline, Robyn and Liz, for the many fruitful discussions, much appreciated help, and delightful camaraderie over the years.

Last, but not least, thank you to my family, especially to my sister Victoria who fed and sheltered me through it all. Thank you to my Dad, Bill, my Mum, Carole, and also to Chris M., Adrian and Siobhan, and my twin brother Chris, who have listened, sympathised and cheered me on.

Chapter 1

Introduction

1.1 Chemical Nucleosynthesis in the Universe

The analysis of chemical abundances within stars and galaxies provides a unique insight into the evolution of the Universe. Nucleosynthesis describes the processes involved in combining atomic nuclei in order to create other atomic nuclei. Stars provide the ideal environment for the different reactions needed for nucleosynthesis to occur. The two key ingredients required for nucleosynthesis are energy and time. The evolution of stars through the different stages of nuclear burning provide both these ingredients, and so stars are slowly but surely converting the Universe from its original pristine state of hydrogen and helium atoms into a metal-rich mecca.

Until the 1950's the origin of the elements was a matter of debate (Burbidge et al., 1957). Two competing theories existed where the key point of contention was the environment in which temperatures, or rather energies, were high enough for all the elements to be created. The first theory argued that the required temperature could only have been achieved during the creation of the Universe. It implied that the abundance of each element had been set in the first moments of our Universe and that no more nucleosynthesis of the elements was possible. The second theory argued that stellar interiors reached temperatures that were high enough to cause the nucleosynthesis of elements heavier than helium. This theory implied that the chemical composition of the Universe now differs from that at its birth.

In 1957 the paper referred to as B^2FH was published, so-called because of its authors, Burbidge, Burbidge, Fowler and Hoyle (Burbidge et al., 1957). It settled the nucleosynthesis argument by outlining how the evolution of the stars was the primary source for the creation of most of the elements on the periodic table. B^2FH outlined eight nucleosynthesis processes, and their likely environments, that accounted for most of the elements. The elements not accounted for at the time, such as the beryllium group, have since had their nucleosynthesis processes identified. Review papers in 1975 and 1997 have updated B^2FH accordingly (Trimble 1975; Wallerstein et al. 1997). More recent reviews include Gratton et al. (2004) and

Sneden et al. (2008). The recent book by Christian Iliades entitled 'Nuclear Physics of Stars' provides a very comprehensive summary of the creation of the elements in stellar interiors, including a detailed discussion of nuclear physics and nucleosynthesis in the different stages of stellar evolution (Iliadis, 2007).

1.1.1 The Elements

In astrophysics the elements on the periodic table are generally thought of in two groups based on atomic number, Z: the 'light' elements ($Z \leq 30$); and the 'heavy' elements ($38 \leq Z \leq 63$). Figure 1.1 displays the abundances of the elements in the giant star, Arcturus, against Z, as deduced from the derived stellar model for Arcturus in Peterson et al. (1993).

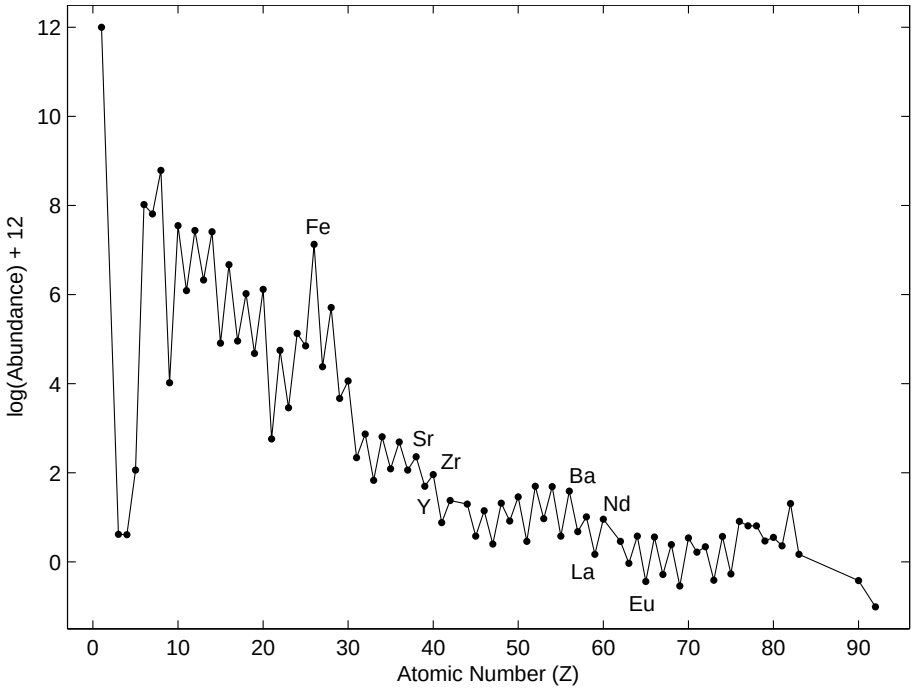

Figure 1.1: Chemical abundances for Arcturus deduced from determination of the stellar model in Peterson et al. (1993). The 'light' elements have $Z \leq 30$, while the 'heavy' elements have $38 \leq Z \leq 63$. The location of the Fe-peak can be seen at Fe (Z=26); the heavy elements Sr (Z=38), Y (Z=39) and Zr (Z=40) indicate the so-called light *s*-process peak; and Ba (Z=56), La (Z=57) and Nd (Z=60) indicate the heavy *s*-process peak. The *r*-process element Eu (Z=63) is also labelled. Arcturus has similar stellar parameters to the stars analysed in this thesis and is used throughout the thesis for comparison and calibration.

Iron (Fe) represents a change in regime as to how the elements can be created. The light elements heavier than boron (B) and lighter than Fe are typically formed in charged-particle reactions during nuclear burning in stars. The innate charge of these particles is sufficiently low that Coulomb repulsion can be overcome and the nuclei can capture charge particles such as protons and alpha particles (helium nuclei stripped of their electrons). Hence the light elements are often referred to as 'proton-capture' elements. The heavy

elements have sufficiently high charges that extreme energies are required for interacting protons to overcome the Coulomb repulsion. The temperatures within stars are not high enough for heavy elements to be formed via proton-capture. Instead the neutrally charged particle, the aptly named neutron, is the key to heavy element formation as there is no Couloumb repulsion to overcome in interactions between neutrons and heavy elements (Iliadis 2007; Sneden et al. 2008).

The separation in the light and heavy elements is also representative of the binding energy associated with the nucleus of each element. The binding energy is how much energy is required to break a nucleus into its constituent nucleons, or alternatively how much energy is required to combine nucleons in order to create a nucleus. Energy is released when the light nucleons are combined to create a light element nucleus. This is called nuclear fusion. Nuclear fusion is the mechanism for the nuclear burning of the light elements in stellar cores. On the other hand energy must be added in order to combine heavy nucleons to create a heavy element nucleus. In stellar environments the available energy is not high enough for the nuclear fusion of heavy elements. Instead, the main nucleosynthesis process for the creation of heavy elements within stellar interiors is neutron capture as described above.

Two other key element groupings are the 'α' elements and the 'Fe-peak' elements. The former are light elements which have an even atomic number and their major form is some multiple of the ^{4}He nucleus. Key α elements used in abundance analysis are carbon (C), oxygen (O), magnesium (Mg), silicon (Si), and calcium (Ca), although titanium (Ti) is often included (Sneden et al., 2008). The Fe-peak refers to the elements about Fe which are observed to peak in abundance compared to the general trend of decreasing abundance with increasing atomic mass as can be seen in Figure 1.1. Within this general trend is the odd-even effect where even atomic elements are more abundant then the neighbouring odd atomic elements. Fe-peak elements have the highest binding energy of all the elements and so are tightly bound and very stable. As such the sequential nuclear fusion of the light elements within stellar cores ultimately results in building up the abundances of the Fe-peak elements in the Universe (Iliadis, 2007).

1.1.2 Stellar evolution and the light elements

The main ingredient of stars, and indeed the Universe, is hydrogen (Burbidge et al., 1957). In the interior of stars hydrogen can undergo nuclear fusion by one of two processes: the 'pp chain' and the 'CNO cycle' (Rolfs & Rodney, 1988).

The pp chain occurs when the temperature of the stellar core reaches approximately 1×10^7 K (Rolfs & Rodney, 1988). There are three distinct reaction sequences referred to as pp chains. The essential process converts four protons into one helium nucleus while also releasing energy in the form of a gamma ray (γ) and a neutrino (υ). The following sequence

of reactions describes the pp1 chain (Iliadis, 2007):

$$\begin{aligned} p + p &\rightarrow {}^{2}\mathrm{H} + e^{+} + v \\ {}^{2}\mathrm{H} + p &\rightarrow {}^{3}\mathrm{He} + \gamma \\ {}^{3}\mathrm{He} + {}^{3}\mathrm{He} &\rightarrow {}^{4}\mathrm{He} + 2p \end{aligned}$$

For stars whose composition is essentially just hydrogen and helium this is the dominant hydrogen burning process. This describes the first generation of stars which, as they evolved, then created the heavier elements in a series of nuclear burning stages. In stellar death the heavy elements were then distributed throughout the interstellar medium and it was from this enriched material that the subsequent generations of stars were formed. The presence of carbon, nitrogen, oxygen and fluorine in these stars meant the alternate hydrogen burning process, the CNO cycle, could be initiated. However the temperature required to ignite the CNO cycle is greater than that required for the pp chain. The temperature of a star's interior is determined by its mass, so for stars with mass similar to or less than the mass of our Sun the pp chain is the dominant process. Higher mass stars have internal temperatures greater than $\sim 2 \times 10^{7}$ K and the CNO cycle dominates (Rolfs & Rodney, 1988). The exact temperature where the CNO cycle dominates also depends on the metallicity of the star as a high mass but low metallicity star would have insufficient amounts of heavy elements for the CNO cycle to occur (Iliadis, 2007).

There are four sets of reactions which are referred to as the CNO cycles. These use the isotopes of C, N, O and F to turn hydrogen into helium (Iliadis, 2007). The outcome is the same as for the *p*-*p* chain in which four protons are converted into a single helium atom. The most basic CNO cycle occurs in the following series of reactions:

$$\begin{aligned} {}^{12}\mathrm{C} + p &\rightarrow {}^{13}\mathrm{N} + \gamma \\ {}^{13}\mathrm{N} + e^{+} &\rightarrow {}^{13}\mathrm{C} + v \\ {}^{13}\mathrm{C} + p &\rightarrow {}^{14}\mathrm{N} + \gamma \\ {}^{14}\mathrm{N} + p &\rightarrow {}^{15}\mathrm{O} + \gamma \\ {}^{15}\mathrm{O} + e^{+} &\rightarrow {}^{15}\mathrm{N} + v \\ {}^{15}\mathrm{N} + p &\rightarrow {}^{12}\mathrm{C} + {}^{4}\mathrm{He} \end{aligned}$$

While the relative abundances of the seed nuclei vary during the CNO cycle the total abundance of the seed nuclei does not change. This is an important chemical signature which can be used to distinguish between the types of nuclear processing a star has undergone.

The 'main sequence' (MS) defines the initial stage of a star's life during which time it burns hydrogen in its core either by the pp chain or the CNO cycle as describe above.

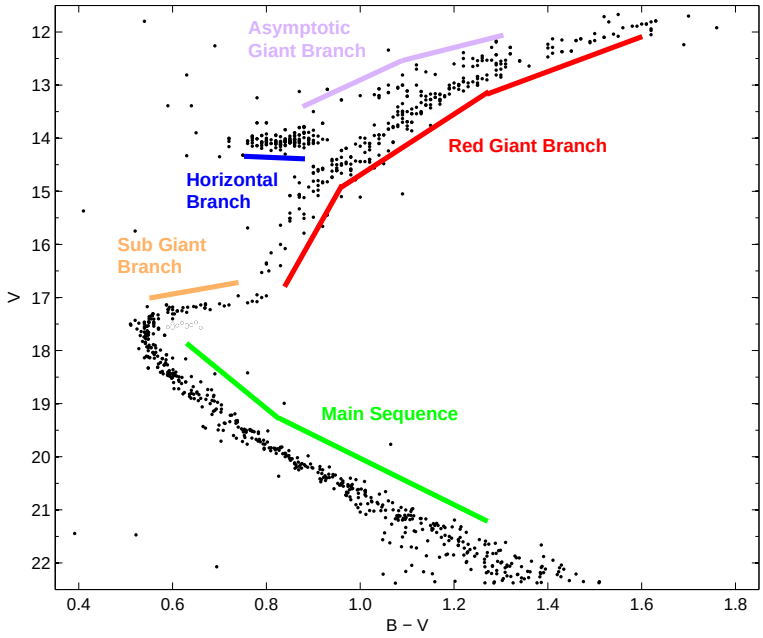

Figure 1.2: Colour-magnitude diagram (CMD) of 47 Tuc showing the different stages of stellar evolution. This is a composite image from Cannon et al. (1998) and Hesser et al. (1987).

Figure 1.2 shows a colour magnitude diagram (CMD) of stars in the globular cluster 47 Tucanæ (47 Tuc) for which the different branches of stellar evolution are indicated. During a star's time on the MS the hydrogen burning core is gradually replaced by an inactive helium core. This is the longest stage in a star's life and can take from 10^6 years for a massive star ($\sim 25M_\odot$)[1], to 10^{10} years for a low mass star ($\sim 1M_\odot$) (Wallerstein et al., 1997). These hydrogen core-burning stars, or dwarfs, are theorised to have no mechanism that mixes up products of the hydrogen burning to the surface of the star (Cannon et al., 1998). Therefore the spectrum of a main sequence star represents the chemical composition of the gas from which the star was formed.

Once helium is all that remains in the stellar core, the core shrinks and its temperature rises, but the star's outer radius increases and the surface temperature cools (Rolfs & Rodney, 1988). The star has turned off the MS and migrated onto the red giant branch (RGB, see Figure 1.2). Hydrogen burning still continues in a shell around the core but the steep temperature gradient from the high temperature in the core to the low temperature at the surface causes convection in the atmosphere of the star outside the core (Iliadis, 2007). It is this process, called the 'first dredge-up', that mixes the products of hydrogen burning throughout the star's envelope. Hence the spectrum of a giant star differs from when it was a dwarf star due to the pollution of its atmosphere by the elements mixed up from the hydrogen burning regions. The comparison of the spectrum of a dwarf star with that of a

[1] $M_\odot$ = 1 solar mass = 1.99×10^{30} kg

giant star of similar initial mass, formed from the same gas cloud, can be used to determine the type and quantity of elements that have been created in nuclear burning during the evolutionary process.

An important outcome of the CNO cycle is that, for the key isotopes of ^{12}C, ^{13}C, ^{14}N and ^{16}O, the abundance of N is increased but both C and O abundances are decreased. The processing of these elements during the CNO cycle can also impact on the abundances of other elements due to leakage via the ^{19}F isotope (Lattanzio 2007; private communication). Depending on temperature and metallicity the NeNa and MgAl cycles can occur. These cycles operate by proton capture, where Ne and Mg are the respective catalysts, resulting in depletion of Ne (and Mg), and enhancements in Na (and Al). If the conditions in the star activate these cycles the net result is that, for key isotopes, Na and Al are enhanced but Ne and Mg are depleted (Iliadis, 2007).

As the star ascends the RGB the hydrogen burning products (C, N, O, Na, Mg, Al) are mixed to the surface of the star modifying the chemical composition of the outer envelope. In the ascent of the RGB the stellar core contracts and the outer envelope expands. Eventually the core starts to burn helium. This occurs gently for stars of initial mass $M \geq 2\ M_{\odot}$ such that as the core temperature increases the helium burning gradually switches on and the star moves on to the horizontal branch (HB) (Herwig, 2005). For stars of initial mass $M < 2\ M_{\odot}$ the inactive helium core is degenerate during the RGB ascent and the increasing temperature eventually results in the ignition of the helium in the core. However, as the gas is degenerate, the increased energy output from the nuclear reactions does not result in an expansion of the core, which would lower the temperature and so lower the energy generation rate. Instead the temperature continues to increase which in turn increases the energy generation rate. Eventually so much energy is released that the electron degeneracy is lifted in a core helium flash. Hence the stellar radius contracts and the luminosity decreases such that the star appears on the HB (Herwig, 2005).

Once on the HB the stellar structure is a core that is burning helium in carbon and oxygen, surrounded by a hydrogen burning shell. The ashes of the hydrogen burning are deposited directly on top of the helium core. Both hydrogen burning products and the products of helium burning are now being enriched in the star. The main process for converting helium into carbon is the triple-alpha process, the alpha referring to a helium nucleus (Herwig, 2005). This occurs via the following reactions:

$$^{4}\mathrm{He} + {}^{4}\mathrm{He} \rightarrow {}^{8}\mathrm{Be}$$
$$^{8}\mathrm{Be} + {}^{4}\mathrm{He} \rightarrow {}^{12}\mathrm{C} + \gamma$$

The carbon produced via the triple-alpha reaction is then processed into oxygen when com-

bined with another alpha particle as follows:

$$^{12}\mathrm{C} + {}^{4}\mathrm{He} \rightarrow {}^{16}\mathrm{O} + \gamma$$

Not all the carbon is converted as this process occurs at a slower rate than the triple-alpha process (Iliadis, 2007). The He-core burning eventually ceases leaving a CO stellar core. The core contracts again, as there is no radiation pressure, until the CO becomes degenerate. Helium ignites in a shell around the CO core and the star begins its ascent of the asymptotic giant branch (AGB). At the start of the AGB the structure of the star is an inactive CO core, a He burning shell, a He-rich inter-shell region, a H-burning shell and a H-rich convective envelope as shown in Figure 1.3 (Herwig, 2005).

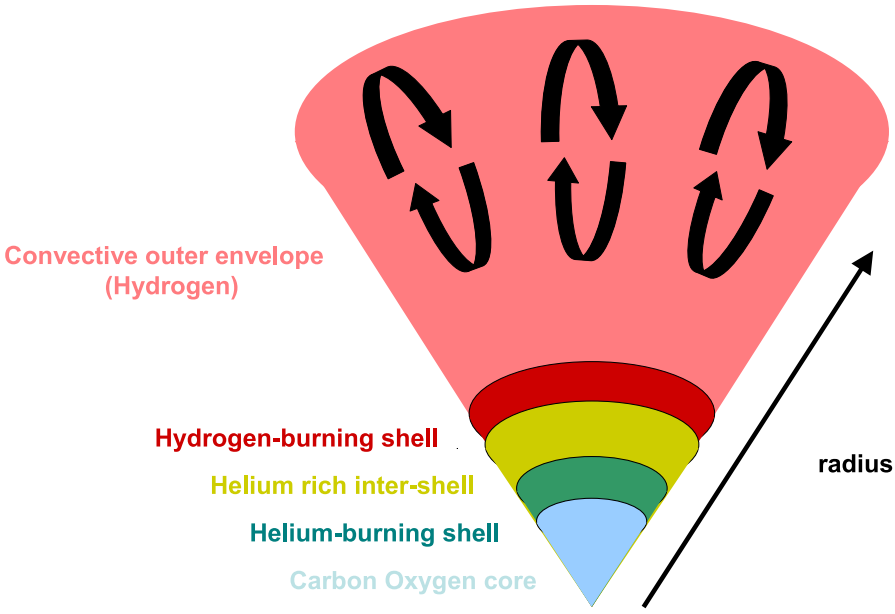

Figure 1.3: Schematic of the interior of an AGB star showing the H-burning shell, the He rich inter-shell region, the He-burning shell and the CO core.

The high energy output from the He-burning shell causes the star to expand. This also pushes the H-burning shell out to greater radii although the H-burning shell is still the dominant energy source for the star. For stars of mass $M \gtrsim 4\ M_{\odot}$ the H-burning shell is pushed out so far that it is extinguished. The convective, H-rich envelope then extends into the region rich in H-burning products and mixes them up into the envelope. This is the second dredge-up. The H-burning shell is re-ignited due to the dredge up pushing the H-burning shell region inwards and the net result is that the two nuclear burning shells are positioned closer together and the envelope has been once again enriched in H-burning products. There is no second dredge up for stars of mass $M \lesssim 4M_{\odot}$ and while the H-burning

shell is not extinguished the He-burning shell does progress outwards to be located closer to the H-burning shell (Iliadis, 2007).

This close proximity of the two nuclear burning shells leads to another stage in a star's evolution called the thermally pulsing AGB (TP-AGB). It is during this stage that the conditions are met for the production of heavy elements.

1.1.3 Heavy elements: the *s*- and *r*-processes

As discussed above the elements heavier than Fe have very low charged particle probabilities and so the main synthesis process available to create these elements is neutron capture. In this process a free neutron is captured by the seed nucleus creating a heavier element. The build-up of additional neutrons makes the nucleus unstable. Eventually it must decay to produce stable nuclei and energy (Sneden & Cowan, 2003). The majority of the heavy elements can be produced by neutron capture processes.

There are two types of neutron capture: the slow (s) -process and the rapid (r) -process. The main difference between the two processes is the rate at which neutrons are captured compared to rate of beta-decay for the seed nuclei. For the s-process the mean lifetime for neutron capture, or the time between potential neutron captures, is typically $\tau_{n\gamma} \gtrsim 10$ y (Iliadis, 2007). Stars in the later stages of evolution are the environment most likely to produce elements via the s-process. The nuclear reactions involving the light elements n these interiors produce the required low densities of free neutrons ($N_n \approx 10^8$ cm^{-3}) that can then be captured by seed nuclei (Iliadis, 2007). Due to the long time frame between neutron captures the nucleus has time to re-stabilise by beta-decay before another neutron is captured and so the gradual build up of s-process elements lies along a path of stable isotopes, as can be seen in Figure 1.4.

For the r-process, the mean lifetime for neutron capture is on the order of $\tau_{n\gamma} \lesssim 10^{-4}$ s (Iliadis, 2007). Supernovæ can provide an environment for such high densities of free neutrons. The explosive reactions involved in a supernova create many free neutrons ($N_n \approx 10^{21}$ cm^{-3}) which bombard the nuclei (Iliadis, 2007). Typically the nuclei do not have time to stabilise before another neutron is captured resulting in very unstable isotopes. Eventually the instability cause the nuclei to decay into stable isotopes as indicated by black lines in Figure 1.4. While some isotopes are made purely by the s-process, due to being shielded from the r-process by another stable isotope, others are made purely by the r-process as the preceding isotopes will decay before enough neutrons can be captured via the s-process. As can be seen in Figure 1.4 the majority of the heavy element isotopes have contributions from both s- and r processes and determining the level of contribution from each source provides evidence with which to distinguish between differing star forming scenarios (Travaglio et al., 2004).

The contributions from these different sources can be disentangled by determining the contributions of each neutron-capture process to the abundances of each heavy element and

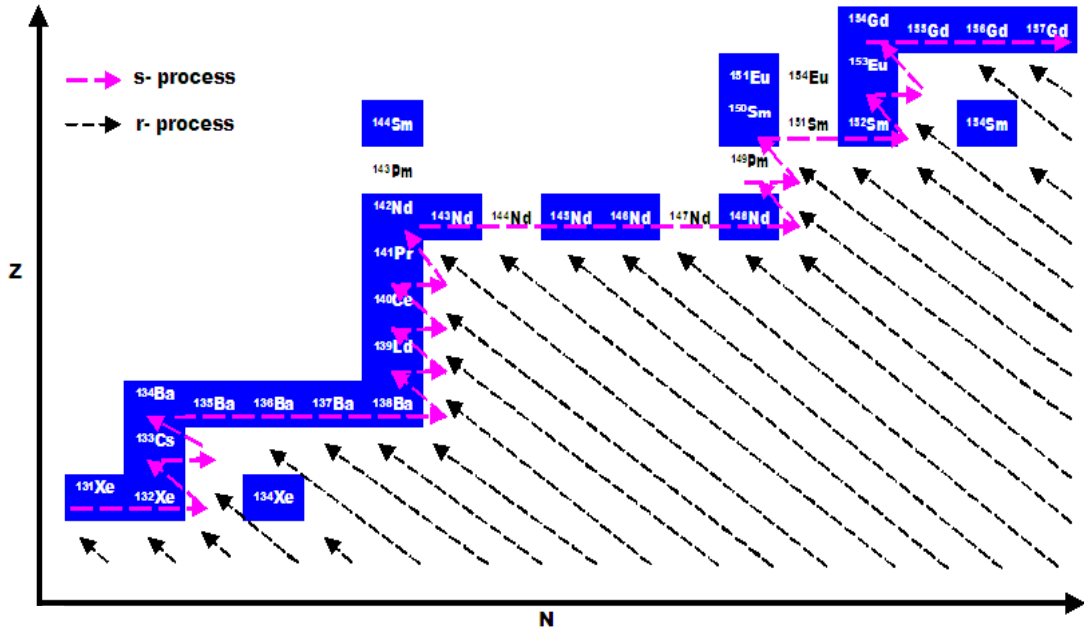

Figure 1.4: The Table of Nuclides about Nd showing the *s*-process and *r*-process paths to each element. The *s*-process contributes to the heavy elements in a path along stable isotopes (pink lines). The *r*-process contributes by decay from very unstable isotopes (black lines).

then comparing the heavy elements whose abundances are mainly due to the *s*-process (for example Sr and Y) to those that are mainly to due the *r*-process (for example Eu) (Gratton & Sneden, 1994). This is a very complicated interplay and an element whose abundance is mainly due to the *r*-process in one star, may be mainly *s*-process in another star. It is important to understand exactly the origins of these elements in order to trace the history of star formation in stellar systems.

In Figure 1.1 there are two abundance peaks corresponding to the light *s*-process peak, indicated by the elements Sr, Y and Zr, and the heavy *s*-process peak indicated by the elements Ba, La and Nd. The elements in these peaks are very stable and have small reaction cross-sections, which means they are less likely to capture neutrons than the other *s*-process elements. Consequently the *s*-process builds up these elements from the elements with larger neutron capture cross-sections. The light *s*-process elements, referred to as '*ls*' elements, are built up first. For the *s*-process to progress to the heavy *s*-process elements, referred to as '*hs*' elements, the neutron flux must be sufficiently high, or there must be a small reservoir of seed nuclei. This forces the *ls* elements to capture neutrons and continue the build up of the *s*-process elements. The same effect occurs for the *hs* elements resulting in the second *s*-process peak. A third *s*-process peak is also created at Pb (Z=82) and Bi

(Z=83) where the *s*-process path ends (Sneden et al., 2008).

The elements included in the definition of *ls* and *hs* differ between studies due to which elements are measured. For the purposes of this research the following definitions apply:

$$\begin{aligned} ls &\equiv \text{Sr, Y, Zr} \\ hs &\equiv \text{Ba, Nd, La} \end{aligned}$$

Abundances for elements in stars are typically quantified using logarithmic ratio notation. Two fundamental ratios used in this work are [Fe/H] and [X/Fe] which are defined as follows;

$$[\text{X/H}] = log_{10}(N_{\text{X}}/N_{\text{H}})_{\star} - log_{10}(N_{\text{X}}/N_{\text{H}})_{\odot} \quad (1.1)$$

$$[\text{Fe/H}] = log_{10}(N_{\text{Fe}}/N_{\text{H}})_{\star} - log_{10}(N_{\text{Fe}}/N_{\text{H}})_{\odot} \quad (1.2)$$

$$[\text{X/Fe}] = [\text{X/H}]_{\star} - [\text{Fe/H}]_{\star} \quad (1.3)$$

where 'X' refers to the particular element under consideration, N_{X} is the number density of X and N_{H} is the number density of H, as shown in the specific case for Fe. Typically [Fe/H] is used to represent the metallicity of the star, which is a measure of the abundance of the metals (all the elements except hydrogen and helium) in the star compared with hydrogen. The notation as above quantifies this as being a measure of the ratio of the number of Fe atoms to H atoms in the star relative to the ratio of the number of Fe atoms to H atoms in the Sun. As these are quantities are on a log scale the relevant units are referred to as 'dex'. Stars with [Fe/H] less than 0.0 dex are metal-poor stars and stars with [Fe/H] greater than 0.0 dex are metal-rich stars, with [Fe/H] $\sim$ 0.0 dex being of solar metallicity.

The quantity [X/Fe] provides the abundance of the element, X, with respect to Fe in the star. In some analyses this can be more useful than the [X/H] notation as it provides an internal comparison of the star's abundances rather than making a comparison to the Sun. This ratio can also be used to represent a group of elements, such as *ls* or *hs*, by taking the mean of their component abundances.

The three key logarithmic ratios for *s*-process element abundances that are used in this thesis are defined as follows:

$$[ls/\text{Fe}] = \langle\, [\text{Sr/Fe}],\ [\text{Y/Fe}],\ [\text{Zr/Fe}] \,\rangle \quad (1.4)$$

$$[hs/\text{Fe}] = \langle\, [\text{Ba/Fe}],\ [\text{La/Fe}],\ [\text{Nd/Fe}] \,\rangle \quad (1.5)$$

$$[hs/ls] = [hs/\text{Fe}] - [ls/\text{Fe}] \quad (1.6)$$

The [*ls*/Fe] and [*hs*/Fe] ratios represent the abundance of the light *s*-process peak and the heavy *s*-process peak respectively with respect to the Fe abundance of the star. They are typically used as a measure of the enrichment that has occurred for these two peaks (Busso et al., 2001). The [*hs*/*ls*] ratio measures the relative difference in abundance between the *ls*

and *hs* peaks. This indicates the efficiency of the *s*-process. For low efficiencies the *s*-process does not build up elements past the *ls* peak, whereas for high efficiencies the *s*-process paths continues past the *ls* peak to build up the *hs* peak (Busso et al., 2001). The efficiency of the *s*-process can also be referred to as the efficiency of the neutron flux causing the *s*-processing and so [*hs*/*ls*] is sensitive to the neutron flux. More neutrons corresponds to a greater build up of the heavier *s*-process elements. Also important is the number of seed nuclei available. Fewer seed nuclei, such as Fe, causes more neutrons to be captured by a single seed, so for metal-poor stars the *ls* peak is drained in favour of the *hs* peak resulting in a high [*hs*/*ls*]. For a detailed exploration of the trends between [*ls*/Fe], [*hs*/Fe], [*hs*/*ls*] and [Fe/H] see Busso et al. (2001).

There are two key sites of *s*-process production in late-type stars: AGB stars ($0.8\ M_\odot < M_\star < 8\ M_\odot$) and massive He-core burning stars ($13\ M_\odot < M_\star$).

1.1.4 AGB stars and the *s*-process

As a star ascends the AGB the H-burning and the He-burning shells move closer together and the significantly greater temperature of the He-burning shell causes an extreme temperature gradient (Iliadis, 2007). Helium produced by the H-burning shell builds up in the inter-shell region until it reaches a density beyond which the He-burning shell cannot maintain equilibrium. The star ignites the built-up helium in a helium flash that sends a wave of energy through the inter-shell region to the H-burning shell. This is a thermal pulse (Herwig, 2005). Initially the pulse does not affect the H-burning shell, but successive pulses that are of increasing energy eventually move the H-burning shell outwards in radius and extinguish it. At this point the convective envelope can reach through the area of the H-burning shell down into the inter-shell region and material from this region can mixed back through the envelope. This is called the third dredge-up (TDU) (Herwig, 2005). Initially the convection may not reach far enough into the intershell for TDU to occur and it can take several pulses before material is mixed from the intershell into the convective envelope. As the energy from the flash is dispersed the star resettles into equilibrium, the H-burning shell re-ignites, although it has moved further outward, and the inter-shell region is re-established. However, key developments are that inter-shell material has been mixed up into the envelope, and protons from the H-burning region have been injected into the inter-shell region. It is these protons that begin the series of reactions needed to produce *s*-process elements (Herwig, 2005). The protons interact with carbon and nitrogen in the following reaction:

$$\begin{aligned} {}^{12}\mathrm{C} + p &\rightarrow {}^{13}\mathrm{N} + \gamma \\ {}^{13}\mathrm{N} + \beta^+ &\rightarrow {}^{13}\mathrm{C} + v \\ {}^{13}\mathrm{C} + p &\rightarrow {}^{14}\mathrm{N} + \gamma \end{aligned}$$

These reactions result in a region enriched in ^{13}C, called the ^{13}C pocket, and another region enriched in ^{14}N, the ^{14}N pocket, in the inter-shell region. The high density of He in the inter-shell region interacts with the high density of ^{13}C in the pocket resulting in the following reaction:

$$^{13}\mathrm{C} + \alpha \rightarrow {}^{16}\mathrm{O} + n$$

The neutron that is freed in this reaction is soon captured by a seed nucleus, typically either Fe or *s*-process nuclei, to create an *s*-process isotope. This occurs between successive thermal pulses, so that with every thermal pulse more protons are mixed into the inter-shell region and more *s*-processing can occur. Also *s*-processed material is mixed up into the envelope when the H-burning shell is extinguished. The ^{13}C reaction is the main source of neutrons for the creation of *s*-process elements in AGB stars Iliadis (2007). However, a secondary source, due to the enriched N, does occur during the thermal pulse. As the energy from the thermal pulse moves through the inter-shell region, and if the temperature is sufficiently high, the following reactions can occur:

$$\begin{aligned} ^{14}\mathrm{N} + \alpha &\rightarrow {}^{18}\mathrm{F} + \gamma \\ ^{18}\mathrm{F} + \beta^{+} &\rightarrow {}^{18}\mathrm{O} + v \\ ^{18}\mathrm{O} + \alpha &\rightarrow {}^{22}\mathrm{Ne} + \gamma \end{aligned}$$

The Ne isotope then reacts with helium to produce neutrons as follows:

$$^{22}\mathrm{Ne} + \alpha \rightarrow {}^{25}\mathrm{Mg} + n$$

This process is not as significant as the ^{13}C reaction for producing the free neutrons. However both produce 'main' *s*-process elements which are defined as those with atomic mass number A$\gtrsim$ 90. The *ls* peak elements border this limit and so their abundances can be attributed to either the 'main' *s*-process from AGB stars or the 'weak' *s*-process (Iliadis, 2007). There is a third component to the *s*-process called the 'strong' component which produces the heaviest of the *s*-process elements (e.g. Pb). It is postulated to occur in low mass, low metallicity AGB stars (Travaglio et al., 2004).

The TDU does not occur for every star that ascends the AGB. Only AGB stars with an initial mass between 0.8 $M_{\odot}$ and 8 $M_{\odot}$ undergo sufficient thermal pulses for TDU to occur often enough for the observed enhancements in *s*-process elemental abundances (Busso et al. 2001, Iliadis 2007). Stars lower in mass may only experience a few thermal pulses before the

hydrogen burning shell is permanently extinguished. Stars higher in mass expand too far during He-shell burning, due to the high temperatures in the core, so that the H-burning shell is permanently extinguished at an early phase (Iliadis, 2007). In the mass range of AGBs that can produce *s*-process elements the observed signature is that of the 'main' component.

1.1.5 Massive stars and the *s*-process

The most likely site for the production of the 'weak' *s*-process is core He-burning in massive stars. The ^{14}N isotope, which is a residue of the CNO cycle during the H-burning phase of the star, reacts with He as outlined in the previous set of reactions, resulting in ^{25}Mg and a free neutron. As above, the free neutron is then captured by a seed nucleus to form *s*-process elements. Very high temperatures ($>$ 300 million K) are required for this reaction to occur and so the more massive the star the more able it is to initiate weak *s*-processing. Typically the stars must be of mass $M \geq 13\ M_{\odot}$. There is only one neutron burst in these stars that allows the creation of *s*-process elements, hence elements beyond the light *s*-process peak are not produced (Arlandini et al. 1999; Iliadis 2007).

Massive stars may also produce weak *s*-process elements during shell C-burning when the temperatures are again sufficiently high for the ^{22}Ne reaction to produce high neutron densities. It has also been theorised that *s*-processing in massive stars may produce isotopes of light elements such as S, Cl, Ar and K (Iliadis, 2007). In this case the massive stars are producing an *s*-process signature that may be distinguishable from the *s*-process signature of TP-AGB stars.

Both the *ls* elements and the products of H burning (C, N, O, Na, Mg, Al) are mixed through the atmosphere of these stars due to convection. Slow stellar winds are the mechanism by which the material, and so the *ls* elements, from the atmosphere of these stars are injected into the interstellar medium (Prantzos & Charbonnel, 2006). Further development of this theory has focused on massive rotating stars. The rotation of the stars creates more efficient mixing up of the H-burning products. However, the stars still eject their material slowly in stellar winds (Decressin et al., 2007a). The stars are too hot to have the required it s-process efficiency to produce the *hs* elements. In this manner massive (rotating) stars pollute the surrounding material with H-burning products but only some *ls* elements.

In summary, TP-AGB stars, of mass 0.8 $M_{\odot} \geq M_{\star} \geq 8\ M_{\odot}$, produce the 'main' component of the *s*-process elements which includes both the *ls* and the *hs* peaks. Massive rotating stars produce the 'weak' component of the *s*-process elements which includes the *ls* peak and lighter *s*-process elements as well as potentially some light element isotopes. The 'strong' component is the classification for the heaviest of the *s*-process elements and these are thought to be produced in low mass (0.8 $M_{\odot} \geq M_{\star} \geq 3\ M_{\odot}$), low metallicity ([Fe/H] $\lesssim -1.5$ dex) TP-AGB stars (Gallino et al., 1998). These are distinct chemical signatures which allow the sources of chemical pollution to be determined.

1.1.6 Supernova and the r-process

Heavy element production also occurs in supernova via the r-process, where high neutron fluxes allow the rapid build up of seed nuclei to create the heaviest elements. When the rate of neutron capture exceeds the decay time the nuclei build up into more and more unstable isotopes until these isotopes finally decay to become stable isotopes along the paths indicated in black in Figure 1.4 (Sneden et al., 2008).

Type II supernovæ are theorised to be the most likely sites for r-process production. The exact circumstances that result in a Type II supernova are still unclear but the progenitors are thought to be massive stars of $M > 8\ M_{\odot}$. The explosive death of these massive stars results in the creation of O, Na, Al and the α elements (Edvardsson et al., 1993). The high neutron flux that occurs in a Type II supernova also produces the r-process elements (Sneden et al., 2008). The temperature of the explosion is important as too high a temperature will result in photo-ionisation of the r-process elements, destroying them before they can pollute the interstellar medium (Iliadis, 2007).

The progenitors of Type Ia supernovæ are postulated to be a carbon-oxygen white dwarf with either a giant or main sequence companion, or another white dwarf (Iliadis, 2007). The white dwarf accretes material from the companion until it reaches critical mass and the carbon-oxygen core ignites catastrophically. The C and O react with α particles to produce Fe-peak elements. There is no excessive production of neutrons in this process and hence no r-process elements are formed. The chemical signature of Type Ia supernovæ is predominantly Fe-peak elements with some α elements (Edvardsson et al., 1993).

Type Ia supernova occur on a much longer timescale ($\geq 10^9$ y) than Type II supernova ($\leq 10^7$ y) and their contributions can be traced in the chemical evolution of the galaxy by the enrichment of the interstellar medium first with α and r-process elements from Type II supernova then with Fe-peak elements from Type Ia supernova. This process is still ongoing in the galactic disk (Edvardsson et al., 1993) but the origins of the chemical composition of halo stars and globular clusters can be traced using the chemical signatures of explosive stellar death combined with the chemical signatures of pollution by AGBs and massive stars.

1.2 Globular Clusters as stellar laboratories

The Milky Way globular clusters are very old objects and can be studied as remnants of the early Galaxy and Universe. The galactic orbit of each of these clusters, and their orbits considered together as a system of clusters, provide information regarding galaxy formation and structure. In addition, based on the assumption that all the stars in a globular cluster (GC) were formed from the same gas cloud, they provide a unique view of stellar evolution and nucleosynthesis. Variations in chemical abundances between the stars can be investigated as evidence of the different types of nuclear processing that occur as the stars evolve, or as evidence of inhomogeneities in the initial gas cloud.

1.2.1 Formation and evolution of GCs

If all stars in a GC are of the same initial chemical composition and as they contain stars at many different stages of evolution, then the only chemical abundance variations between the cluster stars would be due to internal nucleosynthesis. However, accumulating evidence indicates that this cannot be the sole explanation for the abundance anomalies that have been observed in globular cluster stars (Lattanzio & Tout, 2006).

The basic formation process for GCs is that a vast gas cloud condensed forming stars of high then low mass. The high mass stars evolved quickly, eventually resulting in supernova that blew away the remaining gas in the cluster preventing the formation of any more stars. As the GC aged the higher mass stars died in sequence until what remained are the low mass stars that are currently observed in the Milky Way clusters.

In this basic scenario the initial chemical composition of the stars is the same. However there are well documented variations in cluster star elemental abundances which cannot be explained solely by internal nucleosynthesis. The technological advances in telescope and instrument design since the abundance anomalies in GCs were first observed have resulted in detailed studies of the light and heavy elemental abundances in GC stars. Extensive literature is available on abundance variations in GC stars and the recent review paper, Gratton et al. (2004), outlines in detail the observed abundance anomalies in GCs and the pollution and primordial scenarios that may account for them. Other recent papers discussing the sources of abundance anomalies are Cannon et al. (1998), Sneden et al. (2008) and Lattanzio & Tout (2006).

Chemical abundance studies have indicated the presence of light elemental abundance anomalies between the stars at all stages of stellar evolution. These higher resolution and higher signal-to-noise (SNR) studies of larger samples of stars within clusters have enabled a more detailed investigation of the exact nature of the abundance anomalies. A significant advance has been the greater number of abundances derived for the elements heavier than iron. In particular the light and heavy *s*-process elements provide signatures of key stages in stellar evolution.

Initially spectroscopic observations of GC stars were restricted to the luminous giant stars, as the less evolved dwarf stars were too faint to be observed for abundance analysis. Hence the abundances that were determined for the evolved stars were a combination of the initial chemical composition of the stars and the chemical signatures of the nuclear processes occurring within the stars. As telescope technology has advanced observations have been made down onto the main sequence and the spectra of these stars should only show the chemical composition of the gas from which they formed. Abundance anomalies in main sequence GC stars can only be caused by some external pollution mechanism, not internal self-enrichment.

1.2.2 Light elemental abundance anomalies in GCs

There are several key light elemental abundance anomalies that have been observed in globular cluster stars, the main ones relating to variations in C, N, O, Na, Mg and Al.

Initially low resolution spectra and indices on CN and CH molecular bands determined an anti-correlation between CH and CN in globular cluster stars. Further study showed that while some clusters showed evidence of both CN-weak and CN-strong stars at all stages of evolution (e.g. 47 Tuc, Cannon et al. 1998), others had only one or the other at different stages, although typically both were present on the RGB (Gratton et al. 2004 and references therein). CN-weak stars are defined generally as having solar C and N abundances, while for CN-strong star N is enhanced by up to +1 dex and C is depleted by ~ -0.4 dex (Cannon et al., 2003).

Variations in O, Na, Al and Mg have also been observed and appear related to the variations in C and N (Cottrell & Da Costa, 1981). H-burning via the CNO cycle affects the abundances of all of these elements, either directly in the cycle itself, or indirectly through leakage into the NeNa and MgAl cycles as discussed previously. The variations that have been observed are consistent with CNO cycle processing, where Na, Al and Mg are correlated to CN-strength, while O is anti-correlated. However, the metallicity of the cluster seems to be correlated with the variations observed. The correlation of Na, Al and Mg with CN-strength is seen in metal-poor clusters, Na and Al with CN-strength in less metal-poor clusters and only Na with CN-strength in metal-rich clusters (Gratton et al., 2004).

These variations in light elements can be attributed to either the CNO cycle due to H-burning or p-captures during Hot Bottom Burning in intermediate mass AGB stars. Sufficiently high temperatures exist at the bottom of the envelope (top of the H-burning shell) in these stars that allow these p-capture events to occur (Cottrell & Da Costa, 1981).

1.2.3 Heavy elements abundances in GCs

The heavy elements are thought to be homogeneous between GC stars in a given cluster because they are most likely sourced from the chemical composition of the gas from which the stars formed. Iron has consistently been show to be homogeneous within a cluster. Other Fe-peak elements show this homogeneity as well as some of the heavier *alpha* elements.

The AGB stars in GCs that are currently observed are theorised to be too low in mass for TDU to occur and so *s*-process abundances in GC stars represent either the initial chemical composition of the cluster or some pollution signature (Busso et al., 2001). The majority of work on heavy elements has determined a homogeneous distribution of these elements for most GCs (Gratton et al. 2004, Sneden et al. 2008). 47 Tuc seems to be an exception with some evidence of a star-to-star scatter in *s*-process element abundances in giant stars (Brown & Wallerstein 1992, Wylie et al. 2006).

Correlations between light and heavy elements are being investigated in order to distinguish between potential sources of the observed abundance anomalies. Yong et al. (2008) found small amplitude variations in *s*-process elements (Y, Zr, Ba and Nd) as well as in light elements (Si, Ca, Sc, Ti, Ni and Cu) that correlate with N in NGC 6752. However, both intermediate mass AGBs and massive stars can potentially produce these correlations.

1.2.4 Scenarios for abundance anomalies

Different scenarios have been postulated to explain the abundance distributions observed in GC stars. They range from primordial scenarios, where the initial gas cloud was inhomogeneous in chemical abundances; self-enrichment scenarios involving multiple generations of stars where previous generations enriched the material from which the next formed; pollution scenarios where material from massive stars enriched the atmospheres of other stars via stellar winds; to mixing scenarios where internal nucleosynthesis processes altered the abundances within the stars (Cannon et al., 1998).

No single one of these scenarios has proved satisfactory for explaining all of the observed abundance anomalies, although self-enrichment seems to be currently favoured Cannon et al. (1998). The key is to determine which objects could produce the abundances anomalies in the time frame available.

AGB stars and massive stars are the potential candidates for the observed abundance anomalies. They both produce the elements in which abundance anomalies have been observed. Enhanced He abundances can also be expected from these objects. Helium is difficult to measure directly from stellar spectra, but some key features of GCs are indicative of helium enhancements, such as a well-developed blue horizontal branch (Villanova et al., 2009) and multiple main sequences which are believed to be due to enhanced helium (Karakas et al., 2006).

Intermediate mass AGB stars are candidates for the enhancements because they can produced the observed Na and O enhancements through Hot Bottom Burning (Cottrell & Da Costa, 1981). However, they are not able to produce the He enhancements that are thought to be necessary (Karakas et al., 2006). Super-AGB stars ($6.5\mathrm{M}_{\odot} \leq M \leq 8\mathrm{M}_{\odot}$) have been proposed as possible sources as they can produce the enhancements in He as well as the light element enhancements (Pumo et al., 2008).

Massive stars are also potential sources of the helium enrichment and the light element enhancements. Stellar winds gently eject material from the massive star's atmosphere, enriched in H-burning products, into the interstellar medium. Stars formed in this material would be enriched in helium, as well as H-burning products (Prantzos & Charbonnel, 2006). It is thought that massive rotating stars might be more efficient at mixing up the H-burning material and perhaps are better pollution candidates then the non-rotating massive stars (Decressin et al., 2007b). Recent work argues that massive rotating low metallicity stars

could also be significant producers of the 'weak' *s*-process component, in particular the light *s*-process elements Sr, Y and Zr. The heavy *s*-process elements would not be so enhanced resulting in enriched Sr abundances compared to Ba abundances that have been observed in halo stars (Pignatari et al., 2008).

A key constraint on pollution sources for GCs is the observed homogeneity of Fe and the heavy elements between GC stars. Supernovæ are potential pollution candidates as they produce elements in which abundance patterns have been observed. Type II supernova produce α and *r*-process elements while Type Ia produce some α elements but mainly Fe-peak elements. Key issues for these polluters are the time frames of pollution by supernovæ occurring before or during cluster formation, the expulsion of the gas from the cluster by supernovæ which would effectively end further star formation within the cluster, and scatter in the Fe abundances as expected from Type Ia supernovæ. However it is becoming clear that a single pollution source cannot account for all the abundance anomalies within a GC and therefore more detailed scenarios are being considered in which supernova play a part (Marcolini et al., 2009).

Whichever mechanism is responsible, its signature in the GC stars is then modified by the mixing up of H-burning products in the various dredge-up events as the polluted stars evolve. It is the goal of this research to disentangle the different signatures and determine the origin of the elemental abundances in GCs.

1.3 The GCs analysed in this thesis

Data sets for three GCs are analysed in this research. The primary cluster under consideration is 47 Tuc. The analysis of giant stars in this cluster was undertaken in order to continue work that began with the *s*-process elemental abundance analysis of giant branch stars by Wylie et al. (2006). One of the 47 Tuc data sets analysed here was accompanied by data sets for five other clusters. Two of those, NGC 362 and NGC 6388, had stellar samples that could also be potentially analysed for *s*-process elemental abundances and so provide a comparison between GCs of different metallicity. A summary of previous abundance analysis work carried out for each of these clusters is given in the following sections.

1.3.1 47 Tuc chemical abundances: previous work

47 Tuc is the fifth brightest observable galactic GC (Harris, 1996) and is only visible in the southern sky. It has proven to be plentiful source of study with regards to the structure and evolution of stars and stellar systems as it is a bright cluster for which a large sample of stars can be resolved. A large collection of work has been carried out on abundance variations between 47 Tuc stars. The main results for light and heavy element abundances are summarised in Table 1.1.

Table 1.1: Elemental abundance results for 47 Tuc stars from Brown & Wallerstein (1992) (BW92), James et al. (2004) and Carretta et al. (2004) (J04/C04), Alves-Brito et al. (2005) (AB05), Wylie et al. (2006) (W06) and Koch & McWilliam (2008) (K08). The number of stars (N) for each study are listed along with the mean abundances and uncertainties. SG = subgiant, TO = turn off.

Paper	BW92		J04/C04				AB05		W06		K08	
			SG		TO							
N	4		9		3		5		7		9	
⟨[Fe/H]⟩	-0.80	0.09	-0.69	0.06	-0.68	0.01	-0.68	0.07	-0.62	0.06	-0.76	0.04
⟨[O/Fe]⟩	-		0.23	0.12	0.48	0.09	0.35	0.10	-		0.45	0.40
⟨[Na/Fe]⟩	0.11	0.06	0.23	0.09	-0.09	0.28	0.03	0.11	0.67	0.23	0.21	0.07
⟨[Al/Fe]⟩	0.67	0.05	0.23	0.07	-0.07	0.14	0.13	0.08	-		0.45	0.07
⟨[Sr/Fe]⟩	-		0.36	0.16	0.28	0.14	-		-	-		
⟨[Y/Fe]⟩	0.51	0.28	-0.11	0.10	0.06	0.01	-		0.66	0.20		
⟨[Zr/Fe]⟩	-0.43	0.10					-0.17	0.12	0.64	0.15	-	
⟨[Ba/Fe]⟩	-		0.35	0.12	0.22	0.12	0.31	0.07	-		-	
⟨[La/Fe]⟩	0.17	0.09	-		-		0.05	0.10	0.31	0.10	-	
⟨[Nd/Fe]⟩	-		-		-		-	-	0.42	0.12	-	
⟨[Eu/Fe]⟩	0.31	0.10	0.17		0.11		0.33	0.04	0.14	0.12	-	

Overall [Fe/H] for 47 Tuc stars

47 Tuc is considered to be a metal-rich GC, although the stars in the cluster are metal-poor compared to the Sun. The most recent metallicity determination of 47 Tuc was found to be [Fe/H]= -0.76 ± 0.04 dex (Koch & McWilliam, 2008). This is more metal poor than other recent values (see Table 1.1), although the associated uncertainties provide reasonable agreement between the studies. It was concluded in each study that [Fe/H] is homogeneous between the stars in 47 Tuc.

Light elemental abundances in 47 Tuc stars

Variations in the light elements in 47 Tuc have been well documented. The CN and CH indices have, for the last thirty years, provided a useful means to analyse large samples of stars at reasonably low resolutions for their C and N abundances. The key result has been that there exists a CN bimodality in 47 Tuc stars that can be detected on the giant branches and the main sequence (Norris & Freeman 1979, Cannon et al. 1998, Cannon et al. 2003, Briley et al. 2004). It has also been shown that more CN-strong stars are present in the central regions of the cluster, than in the outer regions (Norris & Freeman 1979, Paltoglou 1990)

There is also a correlation of Na to CN strength (Cottrell & Da Costa, 1981). This correlation was confirmed in the analysis of four giant stars carried out in Brown & Wallerstein (1992), who also noted a correlation of Al with Na. More recent work found no observational evidence of a correlation of either Mg or Al with CN or Na in twelve 47 Tuc stars (Carretta et al., 2004). This correlation is not expected for a metal-rich cluster (Gratton et al., 2004). However, an anti-correlation between Na and O was observed (Carretta et al., 2004). This anti-correlation was also seen in five giant stars in 47 Tuc (Alves-Brito et al., 2005). As these anomalies have been observed in giants and dwarfs it is hypothesised that they are most likely due to primordial scenarios rather than solely due to internal mixing in GC stars.

Heavy elemental abundances in 47 Tuc stars

Recent stellar studies have investigated the abundances of elements heavier than iron and have shown an enhancement in *s*-process elemental abundances in 47 Tuc. The AGB stars in 47 Tuc have masses less than 1 $M_{\odot}$ (Gilliland et al., 1998) and therefore the enhancements are unlikely to be explained by the stars undergoing TDU (Busso et al., 2001). Four of the studies in Table 1.1 derived heavy elemental abundances for stars in 47 Tuc.

Two of the studies found a possible star-to-star scatter in the *s*-process elemental abundances which indicated a possible inhomogeneity between 47 Tuc stars (Brown & Wallerstein 1992; Wylie et al. 2006). The remaining two found that the *s*-process elemental abundances were homogeneous between the stars (James et al. 2004; Alves-Brito et al. 2005).

Table 1.1 shows the variation in results between the studies for the heavy elemental abundances. No two studies seem to agree completely on the abundance pattern observed in the stars. The *ls* elemental abundances are scattered between depleted and enriched values. Of the *hs* elements, Ba shows an overall enhancement between the three studies and La ranged from solar to enhanced values. Eu shows reasonable agreement across the studies which supports its origin as a predominantly *r*-process element and a signature of the enrichment of the gas cloud by Type II supernovæ. It was noted in Alves-Brito et al. (2005) that this was compatible with the enhancement in alpha elements that was also observed.

While the results are consistent within each study, the variation between studies are contradictory to the expected homogeneous distribution of heavy elements in GC stars. However, all studies agree that the observed enhancements are most likely due to some primordial or pollution event in the cluster's history.

As the samples contained stars from different stages of evolution, and as there is no internal mechanism equivalent to TDU that would produce the *s*-process enhancements in RGB or MS stars, internal nucleosynthesis of *s*-process elements in the observed stars is effectively ruled out as the source of the *s*-process enhancements. The most likely explanation for the enhancements is that the gas cloud from which the stars formed was itself *s*-process enhanced. Alternatively, the stellar atmospheres were polluted by stellar winds that were rich in *s*-processed material (Cannon et al., 1998).

1.3.2 NGC 6388 and NGC 362: previous work

NGC 6388 is a metal-rich cluster considered to be more metal-rich than 47 Tuc. Metallicity values for this cluster range from [Fe/H]= -0.44 ± 0.03 dex (Carretta et al., 2007), to [Fe/H]= -0.60 dex (Harris, 1996). Wallerstein et al. (2007) found two values of metallicity. The first was derived photometrically to be [Fe/H]= -0.58 ± 0.09 dex and was in good agreement with previous values. The second was derived spectroscopically to be [Fe/H]= -0.79 ± 0.08 dex. The difference in these values was attributed to a possible metallicity spread in the cluster.

In a study of seven giant stars in NGC 6388, Carretta et al. (2007) found Na to be anti-correlated with O, and Al anti-correlated with Mg, while Na and Al were correlated. The α elements were found to be enhanced as were the n-capture elements, although it was concluded that the latter were homogeneous within the cluster.

Wallerstein et al. (2007) analysed eight cool giants and also found a Na-O anti-correlation, and Na correlated with Al. The n-capture elements were slightly enhanced but homogeneous throughout the cluster, though Rb was noted to have a higher excess.

NGC 362 is a metal-poor cluster with reported metallicities of [Fe/H]= -1.2 dex (Gratton, 1987b), [Fe/H]= -1.05 ± 0.10 dex (Caldwell & Dickens, 1988) and -1.16 dex (Harris, 1996). A more recent value gives a metallicity of [Fe/H]= -1.33 ± 0.01 dex (Shetrone & Keane, 2000).

Kayser et al. (2008) found evidence of a CN-weak, CN-strong bimodality, much like that observed in 47 Tuc, including evidence that it extended down to the main sequence. This agrees with previous work carried out in the 1980's showing the same bimodality for this cluster (Smith, 1984). Also in the 1980s, NGC 362 was included in a series of papers that derived abundances for GC stars (Gratton 1987a,b) where NGC 362 was shown to be enhanced in α elements and in O. These enhancements were also observed in Caldwell & Dickens (1988). Similarly in Pilachowski et al. (1983), the Na-O anti-correlation was seen for the three stars analysed in NGC 362 (see their Table 7D). Abundances were also derived for La, showing an overall enhancement. Barium, however, was depleted in the single star for which it could be measured.

Shetrone & Keane (2000) analysed twelve red HB stars in NGC 362 and compared them with thirteen blue HB stars in NGC 288. Both clusters were found to show an Na-O anti-correlation, and an Al-O anti-correlation (Na-Al correlation) was also shown for NGC 362. There was no detectable correlation between Al and Mg for NGC 362. This effect should only be observable when the O depletions and Al enhancements are extreme. Eu and Ba abundances were determined for both clusters. The Eu abundance was comparable between both clusters. The Ba abundances was commented to be susceptible to error due to the strong lines upon which the abundance was based and so not conclusive.

1.4 High- and medium-resolution surveys of GCs

This thesis was undertaken to specifically investigate the magnitude and distribution of *s*-process elemental abundances in 47 Tuc. The *s*-process elements are created in very specific stellar environments, as outlined in the previous sections. The abundances of these elements within GC stars provides evidence either that these stellar environments currently exist in GCs, or that these environments have influenced the evolution of GCs at some point in the past. The exact signature of *s*-process elemental abundances in GC stars can be used to distinguish between the possible scenarios that lead to the observed abundance patterns. In particular, to distinguish between the scenarios of enhancement due to internal nucleosynthesis within the observed stars, pollution by a previous generation of intermediate mass AGB stars, and pollution by a previous generation of massive rotating stars.

A range of data at medium- and high-resolution was obtained in order to pursue this chemical abundance analysis. The analysis was extended to two other clusters, NGC 6388 and NGC 362, which provided a comparison of *s*-process elemental abundances for GCs of different metallicity. The data was analysed where possible for the *r*-process element, Eu, as well as for light elemental abundances and the strength of CN molecular bands. The link between heavy and light elements provides further evidence for distinguishing between GC formation and pollution scenarios.

The number of stars that have been observed for their chemical abundances in GC stars is growing and a more detailed picture is being constructed. However, systematic differences between studies blur the picture somewhat. Large scale surveys, in which a large number of stars are analysed consistently, will clarify the abundance spread in GC stars. Ideally high resolution spectra are needed for abundance analysis, but the new generation of multi-object medium-resolution instruments are capable of providing some of the necessary detail, particularly for the light elements. The thesis will test the feasibility of using medium-resolution instruments to conduct surveys of it s-process elemental abundances in GC stars. The techniques to undertake the analysis of the medium- and high-resolution spectra obtained for this thesis are described in Chapter 2 and the instruments that have been used to pursue this line of research are summarised below.

1.4.1 SALT and RSS

The Southern African Large Telescope (SALT) is a 10m class telescope with instrumentation at the forefront of astronomical technology (Buckley et al., 2006). Two key instruments for SALT are the high resolution spectrograph (HRS), which has completed the design stage (Cottrell et al., 2005) and construction has now commenced at the University of Durham in the United Kingdom, and the low- to medium-resolution Robert Stobie Spectrograph (RSS), currently operating at SALT (Nordsieck et al., 2001). RSS obtains spectra using slit masks and so the number of stars that can be observed is only limited by the number of slits that can be made in the mask. During the performance verification phase of RSS in July 2006 Canterbury PhD student Mita Brierley observed eleven 47 Tuc giant stars for the author. These data were taken in order to test the feasibility of using RSS to measure *s*-process elements in GC stars. The analysis of these data are discussed in Chapter 3.

1.4.2 AAT and ANU 2.3 m

Located at Siding Spring in New South Wales, Australia, the Anglo-Australian Telescope (AAT) is a 3.9 m class telescope that has capabilities for multiple-object surveys using the medium-resolution spectrograph AAOmega (Sharp et al., 2006). AAOmega is a fibre-fed spectrograph attached to the telescope via 2dF, which is the robotic fibre positioner. The multi-object capabilities on the AAT have already been used successfully for light elemental abundance surveys of globular clusters, including 47 Tuc (Cannon et al., 2003). Service time observations of giant stars in 47 Tuc were obtained using AAOmega in October of 2008. The analysis of these data is carried out in Chapter 4

Also located at Siding Spring is the Australian National University (ANU) 2.3 m Advanced Technology Telescope. The high-resolution échelle spectrograph covers the visible wavelengths from 3200 Å to 9000 Å. The ANU 2.3 m telescope was used to obtain high-

resolution observations of the 47 Tuc giant star, Lee 2525. The analysis of this object is carried out in Chapter 5.

1.4.3 VLT and UVES

An archive search was carried out looking for appropriate data sets of high-resolution spectra of GC stars. The spectra of giant stars in six globular clusters taken using the Ultra Violet *É*chelle Spectrograph (UVES) on the Very Large Telescope (VLT) had been observed for study into mass loss undertaken by McDonald & van Loon (2007). The data relating to three of the GCs provided an opportunity to investigate *s*-process elemental abundances using high resolution data of sizeable samples of giant stars in GCs. The reduced spectra were obtained courtesy of the principal investigators for the programme.

UVES is a high-resolution optical *é*chelle spectrograph that operates a blue and red arm. The data used here was obtained on the red arm only, covering wavelengths from 6000 Å to 9000 Å at a maximum resolution of 110,000. The analysis of these data was carried out in Chapters 6 and 7.

A summary of the results from this thesis is given in Chapter 8. The table of stellar parameters for the AAOmega 47 Tuc medium resolution survey is given in Appendix A. The wavelength region from 4100 Å to 4350 Å for each of the stars in the 47 Tuc survey are displayed in Appendix B with the star's name, Norris & Freeman (1979) and Paltoglou & Freeman (1984) CN excess (δC), T_{eff} and *log g*. The equivalent width measurements for the high resolution spectra are given in Appendix C. Three posters based on the work carried out in this thesis and presented at key meetings are also included in Appendices D to F

Chapter 2

Medium- & high-resolution studies: Methods and techniques

The range of spectra analysed in this thesis made it very important to establish methods and techniques that would produce consistent results. The cool giant stars that were being analysed also introduced unique uncertainties which needed to be understood in order to derive reliable elemental abundances.

2.1 The derivation of stellar abundances

The chemical composition of a star is determined by the analysis of absorption lines in the stellar spectrum. Every line corresponds to the absorption of energy by an atom and there is a direct relationship between the strength of a line and how much of the corresponding element is present in the star's atmosphere. However, there are other factors that affect the observed strength of a line. These include the temperature, pressure and opacity in the star's atmosphere. The resulting strength of a stellar absorption line is given by the ratio of the line to the continuous opacity.

2.1.1 Neutral & ionised lines

The atoms of a particular element do not all exist in the same ionisation state. In a stellar spectrum there can be neutral and ionised lines associated with an element. With care, both can be used to derive abundances. In stars with surface temperatures less than 6000 K, the majority of an element population will exist in either a neutral or ionised state which, under local thermodynamic equilibrium (LTE), is governed by Saha's equation. Boltzmann's equation governs to what degree a given species is distributed over its excited states. The temperature and pressure sensitivities of neutral and ionised lines vary depending on which state dominates the population as a whole.

In terms of temperature sensitivity the following four scenarios can be considered:

1. neutral line in neutral dominated population;
2. neutral line in ionised dominated population;
3. ionised line in neutral dominated population;
4. ionised line in ionised dominated population.

Temperature dependency relationships for the ratio of line to continuous opacity for each of these scenarios are derived in chapter 13 of Gray (2005).

Scenarios 1 and 3 apply to cooler stars of $T_{eff} \leq 4700$ K. As the temperature increases greater quantities of the element become excited and hence both the neutral and ionised lines become stronger. However, with increasing temperature the majority of a given element becomes ionised, decreasing the strength of the neutral lines, and so the population becomes dominated by the ionised species. For the now ionised-dominated population (scenarios 2 and 4) as the temperature increases the strength of the neutral line decreases (scenario 2) and the strength of the ionised line increases (scenario 4). However, the strength of the ionised line does not continue to increase indefinitely. The increase in free electrons due to ionisation means the line to continuous opacity ratio decreases which weakens the observed strength of the ionised line. Overall neutral and ionised lines will decrease in strength with temperature after reaching some maximum strength due to increased excitation (Gray, 2005). Temperature variations affect line strength to a greater degree than pressure variations, but pressure effects are still significant depending on the species of the line and the dominant ionisation state.

In summary, for a weak metal line in a particular ionisation state: if the element population is in the next higher ionisation state then the line strength does not change with pressure; if the population is in the same ionisation state the line strength decreases with increased pressure; and if the population is in the next lower ionisation state the line strength decreases greatly with increased pressure (Gray, 2005).

2.1.2 Curve-of-growth analysis

A curve-of-growth analysis allows the simultaneous determination of the effective temperature (T_{eff}), surface gravity ($log\ g$), metallicity ([Fe/H]) and microturbulence (ξ) of a star (chapter 16, Gray 2005). The equivalent widths of atomic lines are measured from the normalised spectrum of a star and then used in the curve-of-growth analysis to determine the stellar parameters for the star. Typically Fe I and Fe II lines are used due to the high number of lines that be observed in most spectra. The curve of growth, derived from the equivalent widths and selected stellar atmosphere model, is compared to a theoretical curve of growth in order to determine an abundance $log(A)$ for each spectral line.

Equation 2.1 equates the measured equivalent widths, in the form of the reduced equiv-

alent width $log(\frac{W}{\lambda})$, with the abundance of the species, $log(A)$ for a specific model:

$$log(\frac{W}{\lambda}) = log(C) + log(A) + log(g_n f\lambda) - \theta_{ex}\chi - log(\kappa_\nu) \quad (2.1)$$

The abundance, A, is defined as $A = \frac{N_X}{N_H}$ when N_X is the number of atoms of the element in the star, and N_H is the number of hydrogen atoms in the star. The following terms are specific for a particular line: g_n is the statistical weight of the nth excited level of the atom; f is the oscillator strength; λ is the wavelength; and χ is the excitation potential. The remaining terms are specific for the stellar atmosphere model: $\theta_{ex} = \frac{5040}{T_{eff}}$, where T_{eff} is the effective temperature of the star; and κ_ν is the opacity co-efficient. Equation 2.1 is derived from the Saha and Boltzmann equations as shown in chapter 16 of Gray (2005).

Certain conditions must be met in order to find the most appropriate stellar model atmosphere. The abundances derived from the spectral lines and stellar model should show no trend with excitation potential (χ) in order to determine the effective temperature (T_{eff}) of the star. To determine the microturbulence of the star there should be no trend of abundance with reduced equivalent width ($log(\frac{W}{\lambda})$). The gravity ($log\ g$) of the star is determined by finding an equilibrium between the mean abundance derived for the neutral species and the mean abundance derived for the ionised species. Finally, if there is no trend of abundance with wavelength then the equivalent width were measured relative to the same continuum level. These four conditions must be met simultaneously in order to determine a best fit stellar atmosphere model for the star.

Determining a stellar model atmosphere from observational data is a computationally intensive exercise and programmes have been developed to perform this task. This research uses the spectrum synthesis programme MOOG (Sneden, 1973). This programme has several functions of which the two key functions used here are *abfind* and *synth*. The *abfind* function carries out the curve-of-growth analysis described above using a list of measured equivalent widths and a stellar atmosphere model to derive abundances. The *synth* function compares an observed spectrum with a synthesised spectrum that has been calculated using an atomic and molecular line list with a stellar atmosphere model. The programme assumes LTE calculations and a plane parallel geometry for the stellar model.

2.1.3 Departures from LTE in stellar atmospheres

The curve-of-growth analysis relies on the assumption of LTE. However, for stars of low gravity and low surface temperature the LTE assumption breaks down. The LTE derivation of stellar atmospheric parameters for these stars can result in values that do not accurately represent the structure of the star, if the departures from LTE are not taken into account.

Departures from LTE can be observed when comparing the abundances derived for each line of a particular species. Fe I is the prime example as it is the species most often used to

derive stellar parameters due to the quantity of Fe lines observed in a stellar spectrum. The abundances derived from high excitation potential lines may be different to those derived from low excitation potential lines. This is because the low excitation potential lines form at shallower levels in the stellar atmosphere where, for low gravity, low temperature stars, LTE breaks down.

The discrepancy between derived abundances from high excitation potential compared with low excitation potential lines has been well documented. In a spectroscopic analysis of two giants, Pollux and Arcturus, Ruland et al. (1980) made a detailed investigation of departures from LTE in these stars. The primary effect that was noted was an underabundance of the element being analysed, assuming an LTE analysis, when derived from low excitation potential lines. This was attributed to over ionisation of the element for low excitation levels as these lines are formed in higher atmospheric layers and so are susceptible to departures from LTE. High excitation potential lines form much deeper in the stellar atmosphere where LTE can be assumed. This departure from LTE for low excitation potential lines skews the overall LTE abundance to a lower value than if the departures were taken into account. Ruland et al. (1980) recommends using element lines whose excitation potential (χ) is greater than the element's ionisation potential minus 4.4eV. A more recent review of departures from LTE and the effect on stellar abundances was carried out in Asplund (2005). It was commented that LTE analysis of late-type stars using Fe I lines at all χ will overestimate T_{eff} by $\sim$200K in low [Fe/H] stars. Coaxing a best fit between the high and low excitation potential lines therefore results in a stellar atmosphere model that overestimates the actual effective temperature of the star.

The recommended course of action is to use 3D atmospheric models that better represent the stellar atmosphere and the departures from LTE. This is an advancing field of research and such an analysis of these stars would be useful in future work. For the purposes of the current study the alternative course of action is to discard the low excitation potential lines and derive stellar parameters based solely on the high excitation Fe I lines.

2.1.4 Veiling effects on stellar spectra

Dust can surround a star either because it is residual material from which the star has formed, or the material is being, or has been, ejected from the star. Evolved stars experience mass loss at certain stages in their evolution. As AGB stars experience thermal pulsing they lose mass to the surrounding medium. The added layer of dust about the star has an effect on the star's light as it passes through the dust in a phenomenon known as 'veiling'.

This effect is typically observed in T Tauri stars, where optically thick dust surrounds the star, scattering the light that is emitted. For T Tauri stars a circumstellar disk was favoured over a circumstellar envelope to better explain the observed amount of veiling (Myers et al., 1987). Basri & Batalha (1990) found a correlation between near infrared excess and veiling

with regard to accretion disks around T Tauri stars. The main effect of veiling is that photospheric absorption features appear weaker, or diluted. A similar effect occurs for R Coronae Borealis stars in the initial phases of their spectacular declines (Cottrell et al. 1990, Skuljan & Cottrell 2002).

Veiling can be explained by the circumstellar dust introducing a layer of 'grey' atmosphere about the star. The main assumption for a 'grey' atmosphere is that the absorption coefficient is independent of wavelength, hence each wavelength undergoes the same lessening of intensity as it passes through the material (Gray, 2005). This affects the continuum of the spectrum such that when normalisation occurs the individual lines are scaled to smaller depths than if the veiling effect was not there. This effect is simulated in Figure 2.1 where a

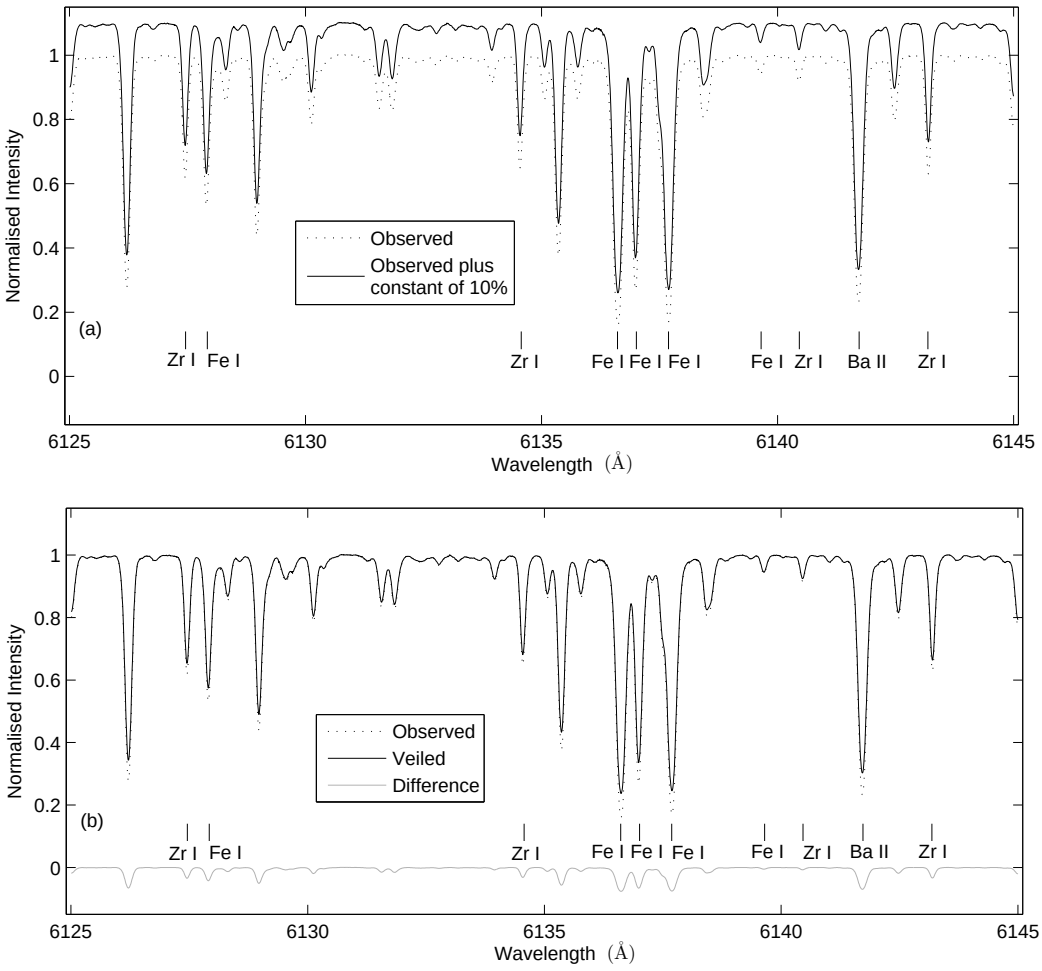

Figure 2.1: The effects of veiling on a stellar spectrum. (a) Observed normalised spectrum (dashed line) and observed spectrum shifted vertically to simulate the addition of a layer of grey atmosphere (solid line). (b) Vertically shifted spectrum re-scaled to 1 to simulate observed spectrum after veiling (solid line), compared with original observed spectrum (dashed line). The difference between the two is shown in grey. The strongest lines (Fe and Ba) are most affected compared to the weaker Zr lines.

normalised observed spectrum is shifted vertically to represent the addition of an extra layer of grey atmosphere.

The veiled spectrum, when re-normalised to 1, results in the strong lines being significantly weaker than in the original spectrum, i.e. the spectrum that would have been observed if it had not passed through the dust cloud. The weak lines are less affected as shown by the relative heights of the difference between the original and veiled spectra. The measured equivalent widths of the veiled spectrum are therefore smaller in value. When analysed this corresponds to lower metallicities, particularly for the strong lines.

2.1.5 Differential analysis to a standard star

A differential analysis of the observed stars to a standard star of similar atmospheric structure and metallicity reduces systematic errors introduced by the equivalent width measurement process and the LTE analysis. Many studies carry out a differential analysis first to the Sun then to a standard star. This is useful for determining the *log gf* values for each line under consideration against two independent stars. The *log gf* is specific for each spectral line, combining its statistical weight (g_n) and oscillator strength (f). It is a term in the curve-of-growth equation (Equation 2.1) for which a change in the *log gf* value changes the derived abundance for the line by the same amount. Recent work on accurately measuring laboratory *log gf* values has negated the need to determine *log gf* values by comparison to the Sun for many species (Den Hartog et al. 2003, Lawler et al. 2001a, Biemont et al. 1981, Hannaford et al. 1982). Online databases, such as VALD Kupka et al. (2000) and NIST ASD [1], provide easy access to the most recent published *log gf* values.

Calibrating the analysis process to a star of similar stellar structure to the stars being analysed (programme stars) is useful for reducing systematic errors in the derivation of the element abundances. Typically, standard stars are available as high-resolution atlases and there are generally a series of published results that provide a framework in which to ensure a consistent analysis. Quoting abundances for the programme stars differentially to the standard star can reduce internal inconsistencies in the analysis.

The typical choice of standard star for comparison with stars of moderately low metallicity is the giant star Arcturus. Recent stellar parameters determined for Arcturus are T_{eff} = 4290 K, $log\ g$ = 1.60, ξ = 1.67 kms^{-1}, [Fe/H]= −0.5 dex (Fulbright et al., 2006). Koch & McWilliam (2008) used Arcturus in a differential analysis with 47 Tuc giant stars in order to minimise uncertainties in their analysis. Other standard stars may be a more appropriate choice depending on the sample of stars. In a study of cool AGB stars Smith & Lambert (1990) carried out a differential analysis with respect to the cool giant α Tau, in order to reduce systematic errors. The analysis also discarded low excitation potential Fe I lines in order to minimise the effects of departures from LTE on the derived stellar parameters. This

[1] National Institute of Stands and Technology Atomic Spectra Database (http://www.physics.nist.gov/PhysRefData/ASD)

type of differential analysis minimises systematic errors in the analysis process due to the similarity in atmospheric structure between the standard and programme stars.

The data analysed in this study comprised of both medium- and high-resolution spectra. Both equivalent width curve-of-growth analyses and spectrum synthesis techniques were used in the analysis of the high-resolution spectra. Spectrum synthesis and spectral indices were used in the analysis of the medium-resolution spectra. The broadening of the lines at this resolution meant spectral features were not sufficiently distinct such that equivalent widths could be measured. The high resolution atlas of the standard giant star Arcturus was used to calibrate the techniques for both spectral resolutions (Hinkle & Wallace, 2005).

As discussed above, deriving the abundances of a stellar sample relative to a standard star of similar metallicity will reduce errors in the analysis process (Koch & McWilliam, 2008). Arcturus was selected as an appropriate choice with which to calibrate the analysis techniques as it has a metallicity of [Fe/H]~ -0.50dex (Fulbright et al., 2006) which is comparable to the metallicity of 47 Tuc ([Fe/H] = -0.76 dex, Harris 1996), the primary globular cluster studied in this thesis. A consequence of this is that stellar atmosphere parameters and abundances were derived for Arcturus in the course of this work. The process used to measure equivalent widths and the determination of a stellar atmosphere model for Arcturus are summarised in Section 2.2. An outline of the spectrum synthesis process that was used to derive elemental abundances and the equivalent width and spectrum synthesis abundance results for Arcturus are given in Section 2.2.4. Further techniques specific to each of the medium- and high-resolution data sets are summarised in Sections 2.3 and 2.4.

2.2 Derivation of stellar parameters: Arcturus

The normalisation of spectra is necessary in order to place the continuum so that the Fe line equivalent widths are all measured consistently. A general normalisation was carried out for each set of stars to remove profile characteristics of the instrument that carried out the observations. This is described in greater detail in the relevant sections. A further normalisation locally about each Fe line was necessary to account for any residual curvature in the observed spectrum. The Arcturus high-resolution atlas is provided as a normalised spectrum and, as the atlas is at such high resolution (R$\sim$60,000) (Hinkle & Wallace, 2005), the continuum is sufficiently well-placed such that further local normalisation made no significant changes. The steps involved in normalising and measuring the Fe lines are described in the following sections. The equivalent width results for Arcturus are then compared to other studies.

2.2.1 Fe lines and continuum regions

There are several elements that can be used in the curve-of-growth analysis to determine stellar parameters. The element most often used is Fe which has many neutral and ionised

lines that are visible in most stellar spectra. Other elements, such as Ti, have large numbers of measurable spectral features that can also be used in a stand-alone analysis or as confirmation of the stellar parameters derived from Fe. Only Fe was used in this study, although some confirmation was carried out using Ti lines.

The Fe lines used in this analysis were compiled from several sources, mainly from previous studies to which this analysis was making a comparison (Brown & Wallerstein 1992, Fulbright et al. 2006, Wylie et al. 2006). The wavelengths, excitation potentials and oscillator strengths of these lines were taken from VALD in order to use the latest published values in the curve-of-growth analysis (Kupka et al., 2000) and are listed in Table 2.1.

Local normalisation about each Fe line in the stellar spectra was necessary to ensure the correct location of the continuum. Fulbright et al. (2006) defined continuum regions that were clear of molecular bands about each of the Fe lines that were considered in that paper.

Figure 2.2 shows the region of the Arcturus spectrum from 6120 Å to 6190 Å. There are seven Fe lines in this region that were used in this analysis of Arcturus. The line at 6149 Å is an Fe II line. Initially the Fulbright et al. (2006) continuum regions were used in the local normalisation. However, the 47 Tuc giant stars that were analysed in this study had strong molecular bands that contaminated some of these regions. The stars that were analysed in Fulbright et al. (2006) were generally hotter ($T_{eff} > 4100$ K) than the stars considered here and hence this was not as significant an issue in that paper.

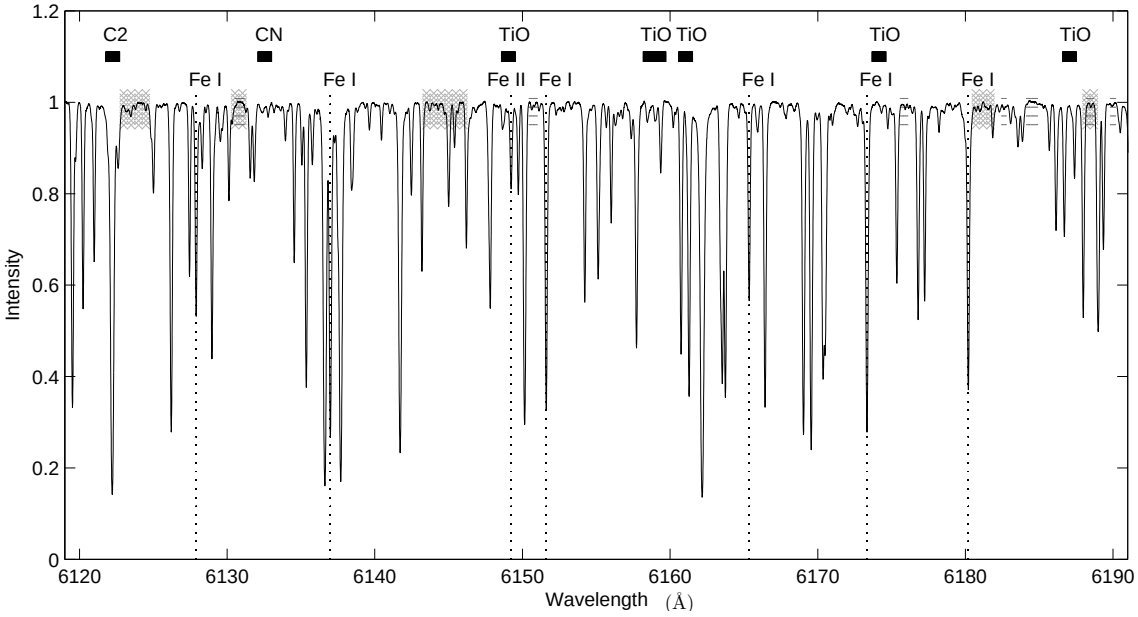

Figure 2.2: Arcturus spectrum from 6120 Å to 6190 Å. The Fe lines in the region are indicated by vertical dotted lines. The Fulbright et al. (2006) continuum regions are indicated as blocks of short horizontal lines. The regions used in this study are indicated as shaded sections. The location of C_2, CN and TiO bands are also indicated.

Table 2.1: Fe line list (26.0 = Fe I, 26.1 = Fe II) used to determine the stellar parameters for Arcturus and the high-resolution globular cluster stellar spectra. The values are taken from the latest published values available on VALD (Kupka et al., 2000). The lines used, where possible, for each key object/GC are indicated in columns 5 to 9.

λ (Å)	Species	χ (eV)	*log gf*	Arcturus	Lee 2525	47 Tuc	NGC 362	NGC 6388
6127.90	26.0	4.143	-1.399	✓	✓	✓	✓	✓
6136.99	26.0	2.198	-2.950	✓				
6151.62	26.0	2.176	-3.299	✓	✓			
6165.36	26.0	4.143	-1.474	✓	✓		✓	✓
6173.33	26.0	2.223	-2.880	✓	✓			
6180.20	26.0	2.727	-2.586	✓	✓	✓	✓	✓
6229.23	26.0	2.845	-2.805	✓			✓	✓
6232.64	26.0	3.654	-1.223	✓		✓	✓	✓
6246.32	26.0	3.602	-0.733	✓	✓	✓	✓	✓
6270.22	26.0	2.858	-2.464	✓		✓	✓	✓
6271.28	26.0	3.332	-2.703	✓		✓	✓	✓
6301.50	26.0	3.654	-0.718	✓	✓	✓	✓	✓
6311.50	26.0	2.831	-3.141	✓	✓	✓	✓	✓
6322.69	26.0	2.588	-2.426	✓				
6336.82	26.0	3.686	-0.856	✓		✓	✓	✓
6344.15	26.0	2.433	-2.923	✓				
6380.74	26.0	4.186	-1.376	✓	✓	✓	✓	✓
6408.02	26.0	3.686	-1.018	✓	✓	✓	✓	✓
6481.87	26.0	2.279	-2.984	✓	✓			
6518.37	26.0	2.831	-2.460	✓	✓	✓	✓	✓
6574.23	26.0	0.990	-5.023	✓	✓			
6575.02	26.0	2.588	-2.710	✓				
6581.21	26.0	1.485	-4.679	✓	✓			
6609.11	26.0	2.559	-2.692	✓	✓			
6699.15	26.0	4.593	-2.101	✓				
6750.15	26.0	2.424	-2.621	✓	✓			
6810.26	26.0	4.607	-0.986	✓	✓	✓	✓	✓
6837.02	26.0	4.593	-1.687	✓	✓		✓	✓
6855.16	26.0	4.558	-0.742	✓	✓	✓	✓	✓
4923.93	26.1	2.891	-1.504	✓				
5234.63	26.1	3.221	-2.279	✓				
5425.26	26.1	3.199	-3.390	✓				
5991.36	26.1	3.153	-3.647	✓				
6084.11	26.1	3.199	-3.881	✓	✓			
6149.24	26.1	3.889	-2.841	✓			✓	✓
6247.56	26.1	3.892	-2.435	✓	✓			
6369.46	26.1	2.891	-4.231	✓			✓	✓
6432.68	26.1	2.891	-3.687	✓		✓	✓	✓
6456.39	26.1	3.903	-2.185	✓	✓	✓	✓	✓
6516.08	26.1	2.891	-3.432	✓		✓	✓	✓

For the purposes of this study each of the Fe lines and respective continuum regions were compared between Arcturus and one of the stars in the 47 Tuc sample (*tc*04) in order to find continuum regions that were clear of molecular bands and échelle order breaks in the 47 Tuc spectra. Both the Fulbright et al. (2006) continuum regions and the continuum regions used in this study are shown in Figure 2.2. Also indicated are the locations of various bands of C_2, CN and TiO.

The continuum regions selected for each Fe line used in the analysis of Arcturus are listed in Table 2.2. In two instances the continuum region reads as zero. This was due to the Fe line being located too close to an échelle order break in the spectrum of *tc*04 such that no continuum region was available. In these cases a single continuum region was used to normalise the spectrum about the Fe line. The normalisation was made by finding the mean intensity and wavelength of each of the Fe lines' two continuum regions. The mean was calculated iteratively, discarding points that lay outside 2σ of the mean and then recalculating until less than 5% of the remaining points lay outside the 2σ limit. A linear relation between the two mean points was then divided out from the spectrum resulting in the required normalisation. If only one continuum region was available, the mean intensity of that region was divided out of the spectrum to effect the normalisation.

2.2.2 Measurement of equivalent widths

A programme was written in MATLAB[2] which carried out the local normalisation, fitting of a gaussian profile, and calculation of the equivalent width for each specified Fe line in the spectrum of the star under analysis. A gaussian profile was assumed with the expectation of later discarding lines that were too strong and therefore not well approximated by this assumption. The programme allowed visual inspection of each line before and after the equivalent widths were measured. This allowed for visual confirmation that the correct line was being measured by comparison to the Arcturus spectrum. A wavelength shift was necessary due to the doppler shift of the observed globular cluster stellar spectrum. A global wavelength shift was first applied for the star, then a local shift in order for each line to match the Arcturus wavelength. This procedure was obviously not necessary for the Arcturus spectrum. The Fe line was then normalised locally and the depth of the line was measured. The local wavelength shifts and line depths were recorded for the next stage in the programme which was to measure the Fe line equivalent widths for the star. The full width at half maximum was measured based on the line depth and the local normalisation. The equivalent width was then calculated using the following equation;

$$Equivalent\ width = \frac{LW}{2C}\sqrt{\frac{\pi}{ln(\frac{L}{H})}} \quad , \tag{2.2}$$

[2]MATrix LABoratory, a numerical computing environment (http://www.mathworks.com).

Table 2.2: List of continuum regions used about each Fe line for local normalisation in Arcturus. For explanation of the '0.00' see text.

Fe		Continuum Region 1		Continuum Region 2	
λ (Å)	Species	min λ	max λ	min λ	max λ
4923.930	26.1	4922.50	4922.70	4926.30	4926.60
5234.630	26.1	5228.60	5229.70	5235.60	5236.10
5425.260	26.1	5424.80	5425.10	5426.90	5427.20
5991.361	26.1	5987.50	5988.20	5992.10	5992.60
6084.110	26.1	6082.90	6083.30	6085.50	6086.00
6127.904	26.0	6123.00	6124.50	6130.54	6131.20
6136.994	26.0	6130.54	6131.20	6143.50	6146.00
6149.240	26.1	6143.50	6146.00	6180.70	6181.70
6151.617	26.0	6143.50	6146.00	6180.70	6181.70
6165.360	26.0	6143.50	6146.00	6180.70	6181.70
6173.334	26.0	6143.50	6146.00	6180.70	6181.70
6180.203	26.0	6143.50	6146.00	6180.70	6181.70
6229.230	26.0	6197.85	6198.90	6235.00	6235.80
6232.640	26.0	6197.85	6198.90	6235.00	6235.80
6246.322	26.0	6240.75	6241.35	6247.60	6248.05
6247.560	26.0	6240.75	6241.35	6250.80	6251.15
6270.220	26.0	6263.20	6263.60	6271.85	6272.30
6271.282	26.0	6263.20	6263.60	6271.85	6272.30
6301.501	26.0	6291.35	6291.80	6308.30	6308.90
6311.500	26.0	6308.30	6308.90	6313.20	6314.20
6322.685	26.0	6316.60	6317.30	6325.40	6326.60
6336.823	26.0	6329.10	6329.45	6337.10	6338.00
6344.150	26.0	6337.10	6338.00	6348.50	6351.20
6353.840	26.0	6348.50	6351.20	6354.00	6354.40
6369.460	26.1	6365.10	6365.90	6377.00	6378.00
6380.742	26.0	0.00	0.00	6382.05	6382.50
6408.020	26.0	6406.00	6406.90	6411.90	6412.70
6432.680	26.1	6427.10	6428.30	6433.90	6434.40
6456.391	26.1	6454.40	6454.80	6457.70	6458.25
6481.870	26.0	6467.50	6468.10	6492.50	6493.25
6516.080	26.1	6513.70	6514.40	6517.20	6518.10
6518.366	26.0	6517.20	6518.10	6524.00	6525.70
6574.230	26.0	6571.38	6572.20	6576.60	6577.60
6575.020	26.0	6571.38	6572.20	6576.60	6577.60
6581.210	26.0	6576.90	6577.50	6586.50	6587.10
6609.110	26.0	6603.30	6604.30	6612.00	6613.30
6648.080	26.0	6641.40	6643.20	6648.80	6649.20
6699.153	26.0	6689.50	6690.10	6699.65	6700.10
6739.520	26.0	6737.35	6737.75	6744.45	6745.10
6750.152	26.0	6744.45	6745.10	6756.70	6757.30
6810.260	26.0	6808.40	6809.20	0.00	0.00
6837.020	26.0	6834.75	6835.05	6843.80	6844.30
6855.161	26.0	6853.15	6853.90	6857.35	6857.85

where L is the depth of the line, W is the width of the line at the depth H, and C is the height of the continuum, which is 1. This equation is derived from the integral of the gaussian function and, as a gaussian profile is a reasonable approximation for the shape of most spectral lines, the equivalent width corresponds to the area under or, in the case of absorption lines, above the curve. It is equivalent to the area of the line if it were a rectangle extending from zero to the continuum.

The best fit gaussian profile based on this equation was then overlaid on the spectrum for visual confirmation that the programme had accurately measured the equivalent width for the line.

Initially equivalent widths for a much larger Fe line list than the one in Table 2.1 were measured in Arcturus in order to test the code. Lines with equivalent widths greater than 180 mÅ were rejected as they were more likely to be saturated and also less accurate due to the assumption of a gaussian profile fit. The equivalent widths for Arcturus and the high resolution stars in this study are included in Appendix C. This process was also used to measure the equivalent widths of the light elements (O, Na, Mg, Al, Si, Ca, Sc, Ti, V, Co, Ni, Zn) in order to determine their abundances. This is discussed further in Section 2.7

2.2.3 Arcturus equivalent width comparison

The measured Fe equivalent widths for Arcturus were compared with two previous studies (Griffin & Griffin c.1980, private communication; Fulbright et al. 2006). The comparison between this study and the Griffin & Griffin (c.1980) equivalent widths for the Fe lines is shown in Figure 2.3 and the other light elements in Figure 2.4.

There is reasonable agreement with the Griffin & Griffin (c.1980) values for the Fe line equivalent widths indicated by the diagonal line. The mean difference in equivalent widths between this study and Griffin & Griffin (c.1980) was found to be $\langle \Delta EW_{FeI} \rangle = 4.2 \pm 3.3$ mÅ and $\langle \Delta EW_{FeII} \rangle = 5.9 \pm 9.9$ mÅ for the Fe I and Fe II lines respectively. The large scatter in the Fe II values is due to the Fe II lines that were measured being weak spectral features and so differences in continuum placement between the studies will correspond to relatively large differences in equivalent width values than for strong spectral features. The comparison of the non-Fe equivalent widths found a mean difference of $\langle \Delta EW_{nonFe} \rangle = 6.1 \pm 8.3$ mÅ between the studies. There is a reasonably large scatter between the measurements of these light elements.

The comparison with the more recent study of Fulbright et al. (2006) is shown in Figure 2.5 for the Fe lines and Figure 2.6 for the light elements. There is much better agreement between the studies for the Fe lines, although there are less lines in common. The mean difference in equivalent widths between this study and Fulbright et al. (2006) was found to be $\langle \Delta EW_{FeI} \rangle = 3.7 \pm 0.9$ mÅ and $\langle \Delta EW_{FeII} \rangle = 2.3 \pm 1.7$ mÅ for the Fe I and Fe II lines respectively. There is a slight systematic offset indicating this study measured the equiva-

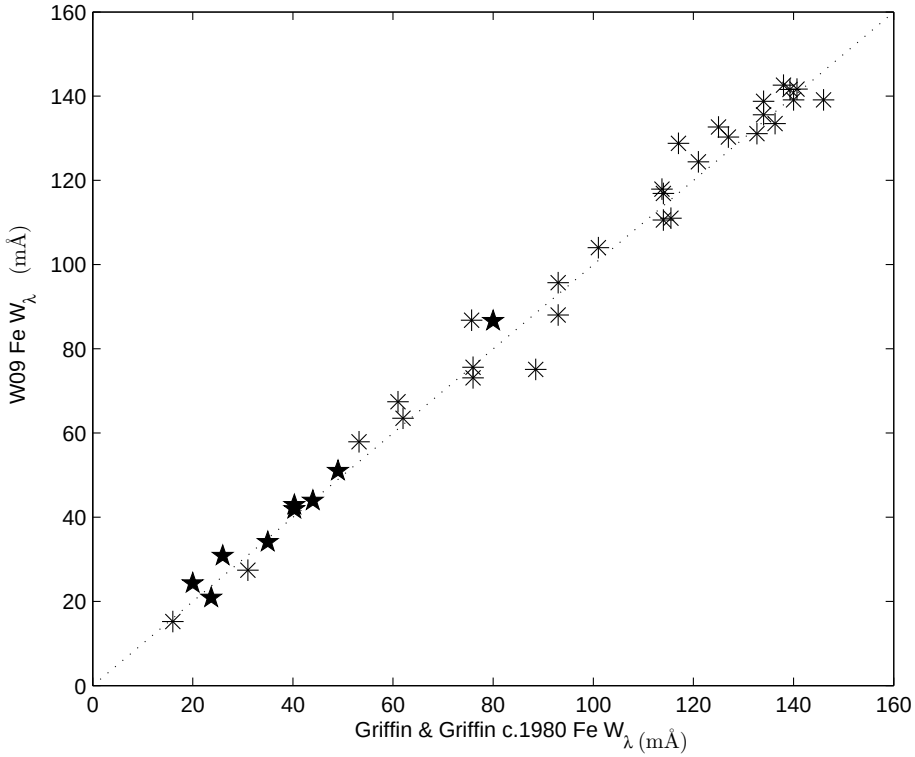

Figure 2.3: Comparison of the Fe equivalent widths measured in this research compared with those measured in Griffin & Griffin (c.1980). ($*$ - Fe I; ★ - Fe II)

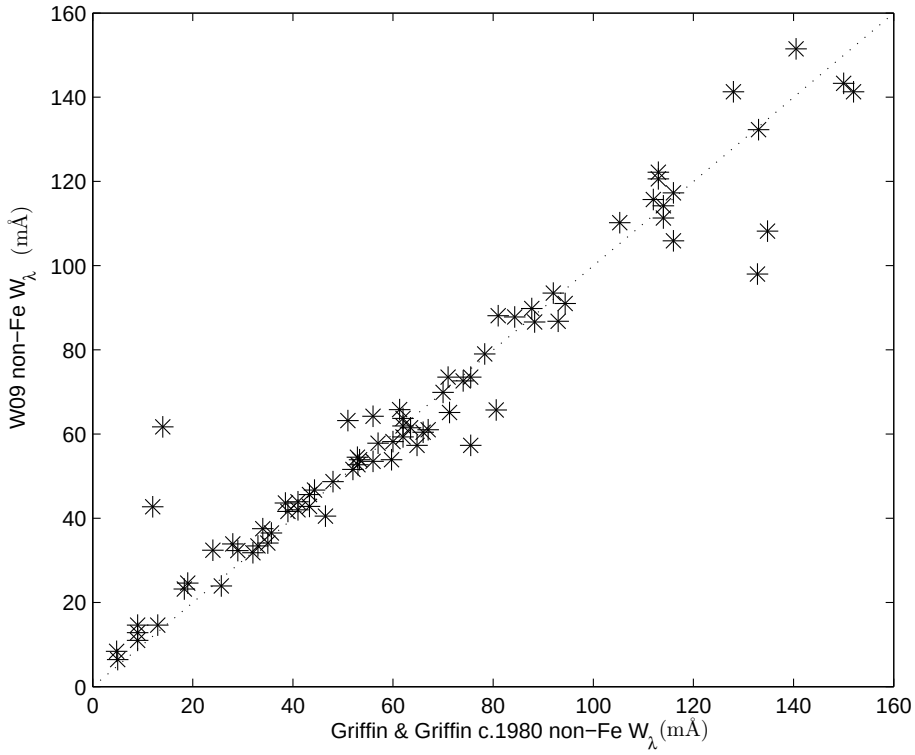

Figure 2.4: Comparison of the non-Fe equivalent widths measured in this research compared with those measured in Griffin & Griffin (c.1980).

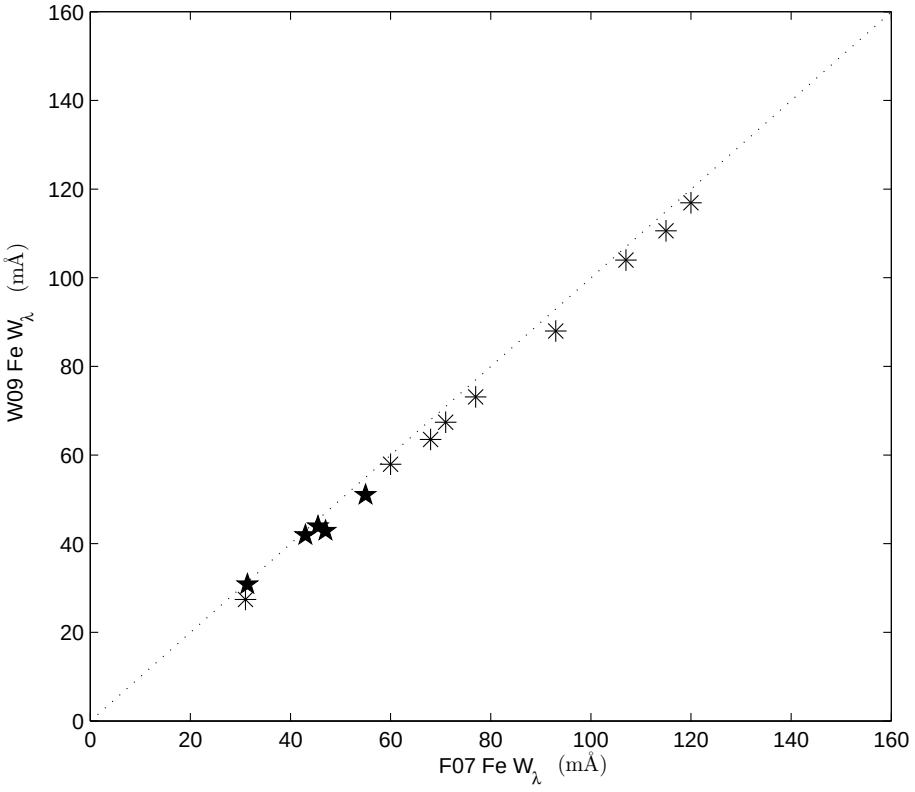

Figure 2.5: Comparison of the Fe equivalent widths measured in this research compared with those measured in Fulbright et al. (2006). ($*$ - Fe I; $\star$ - Fe II)

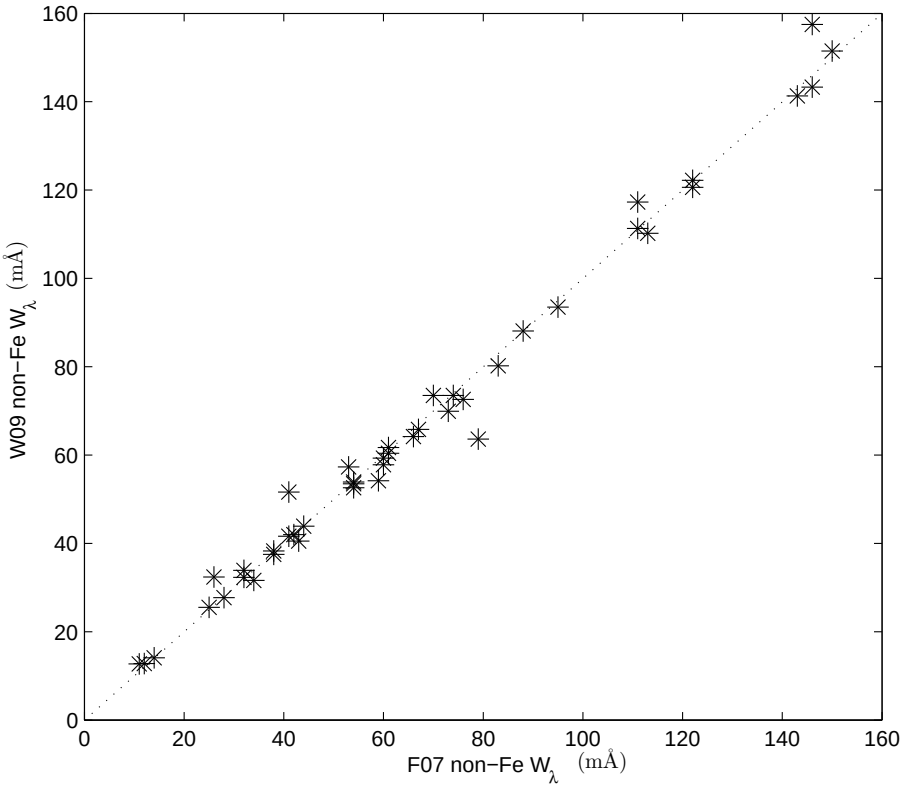

Figure 2.6: Comparison of the non-Fe equivalent widths measured in this research compared with those measured in Fulbright et al. (2006).

lent widths to be slightly smaller than in Fulbright et al. (2006). This may be due to the difference in continuum regions used for the local normalisation. This offset is also apparent in the light element equivalent widths in Figure 2.6, although the larger quantity of lines masks this effect. The comparison of the non-Fe equivalent widths found a mean difference of $\langle \Delta EW_{nonFe} \rangle = 2.4 \pm 3.2$ mÅ between the studies showing a slightly larger scatter. The two outliers in the light element sample may be due to a discrepancy in line selection.

Overall there is good agreement between this study and the previous equivalent widths measured in Griffin & Griffin (c.1980) and, in particular, Fulbright et al. (2006) indicating the equivalent width programme written for this research can be reliably used on unknown stars.

The equivalent widths were then used to determine the stellar atmosphere model that best met the conditions on the derived abundances as outlined in Section 2.1.2. The MOOG function *abfind* constructs theoretical curves of growth for the species under consideration using the details of the species' lines and the stellar atmosphere model.

Figures 2.7 to 2.10 show the relationship between key parameters that are derived during the curve-of-growth analysis. These figures were created during the analysis of Arcturus using the equivalent widths for the Fe lines and four separate stellar models. The three relationships shown in each figure are displayed during the *abfind* analysis.

Figure 2.7(a) compares the [Fe/H] value derived for each of the Fe I ($*$) and Fe II ($\circ$) lines with the excitation potential (χ) for each line. There is no trend of [Fe/H] with χ for this model. This indicates that the temperature of the stellar atmosphere model is a good fit for Arcturus. Figure 2.7(b) compares [Fe/H] with the reduced equivalent width ($log_{10}(W/\lambda)$) for each line. Again there is no trend indicating the microturbulence (ξ) is a good fit for this model. Figure 2.7(c) compares [Fe/H] with wavelength (λ) and again there is no trend indicating that the lines have all been measured consistently with regards to the placement of the continuum in the Arcturus spectrum. The mean abundances derived from the Fe I and Fe II lines are shown in Figure 2.7(a) and are in good agreement within the uncertainties, which indicates that the gravity of the model is correct for Arcturus. The stellar atmosphere model used to derive the abundances in Figure 2.7 is the best fit stellar model that was determined for Arcturus in this thesis.

Figures 2.8 to 2.10 show the same relationships but with stellar parameter variations in T_{eff}, $log\ g$ and ξ. The stellar atmosphere model used to derive the Fe abundances in Figure 2.8 differed from the best fit model in T_{eff} of +100 K. The stellar parameters were otherwise the same. Both Figures 2.8(b) and (c) still show no trend of [Fe/H] with either $log_{10}(W/\lambda)$ or λ. While it can be argued that there is no trend of [Fe/H] with χ either, there is a greater spread in [Fe I/H] and [Fe II/H], and less agreement between the two mean abundances. This indicates that the temperature and gravity for this model are not as good a fit as in Figure 2.7.

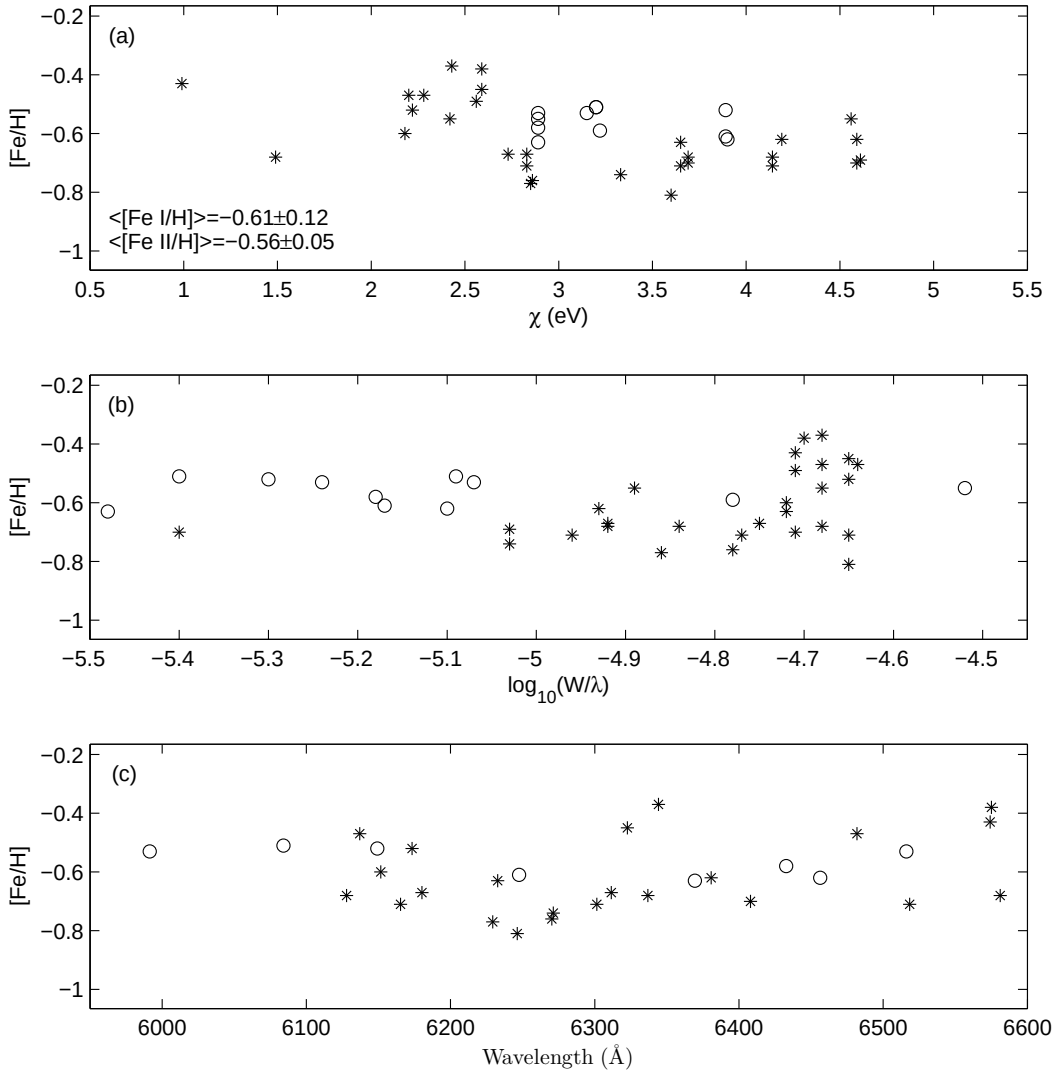

Figure 2.7: Key relations derived during the curve-of-growth analysis used in the derivation of Arcturus stellar parameters using Fe I ($*$) and Fe II ($\circ$) lines. The stellar model used here is the best fit model determined for Arcturus with $T_{eff} = 4300$ K, $log\ g = 1.6$, $\xi = 1.5$ kms^{-1} and [Fe/H] $= -0.6$ dex. The mean abundances derived from the Fe I and Fe II lines are shown. (a) [Fe/H] versus excitation potential (χ). (b) [Fe/H] versus reduced equivalent width ($log_{10}(W/\lambda)$). (c) [Fe/H] versus wavelength λ.

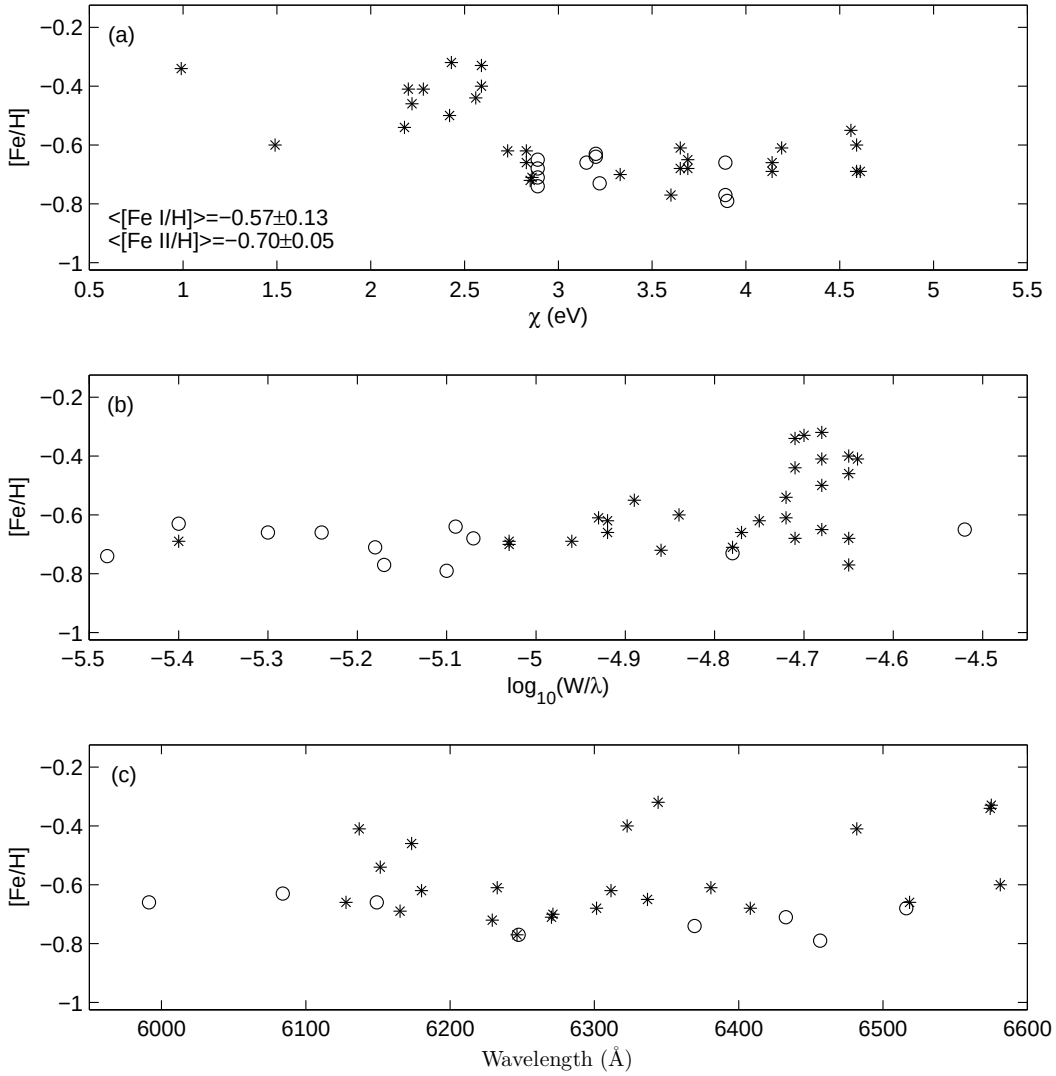

Figure 2.8: As for Figure 2.7 but the stellar model is varied by $\Delta T_{eff} = +100$ K such that its parameters are $T_{eff} = 4400$ K, $log\ g = 1.6$, $\xi = 1.5$ kms^{-1} and [Fe/H] $= -0.6$ dex.

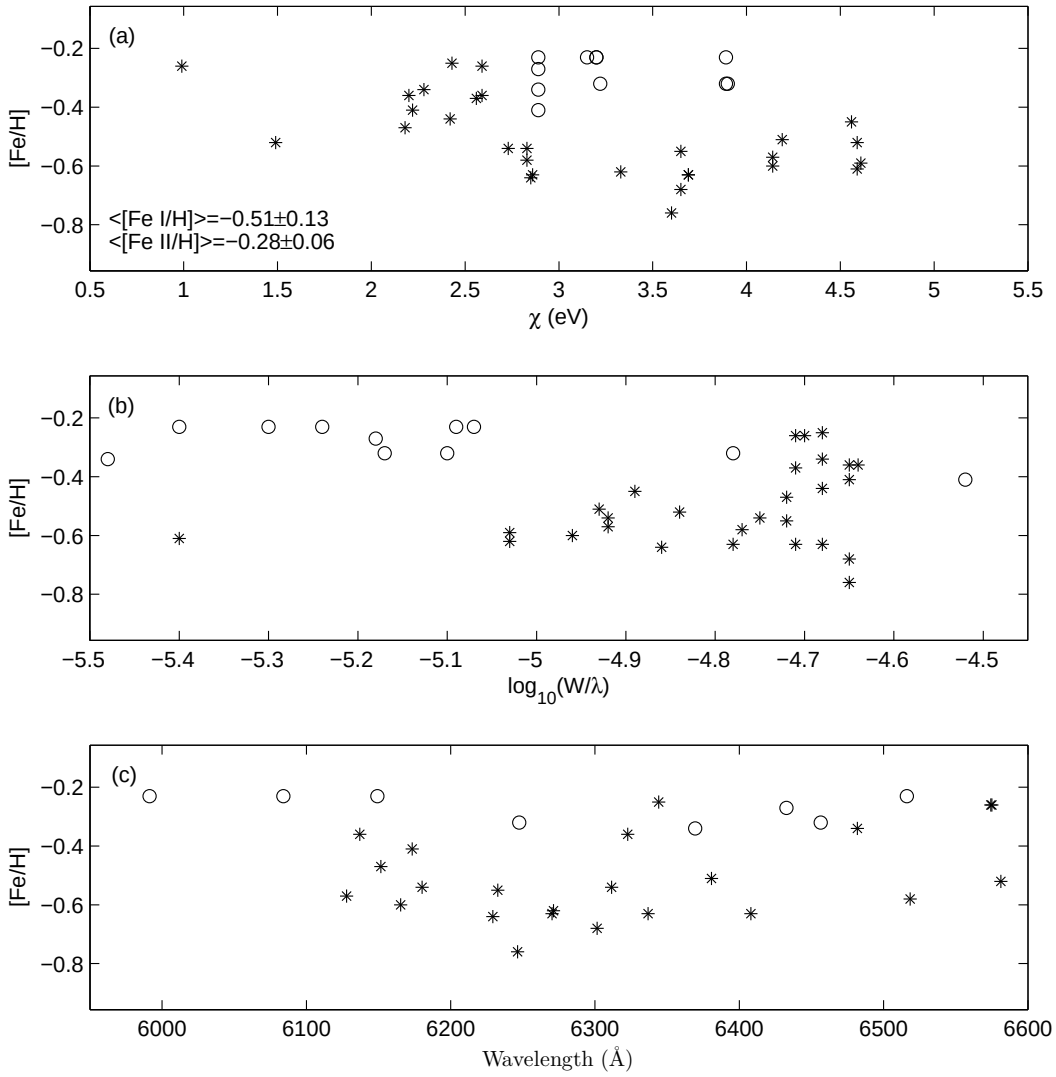

Figure 2.9: As for Figure 2.7 but the stellar model is varied by $\Delta log\ g\ = +0.5$ such that its parameters are $T_{eff} = 4300$ K, $log\ g = 2.1$, $\xi = 1.5$ kms^{-1} and [Fe/H] $= -0.6$ dex.

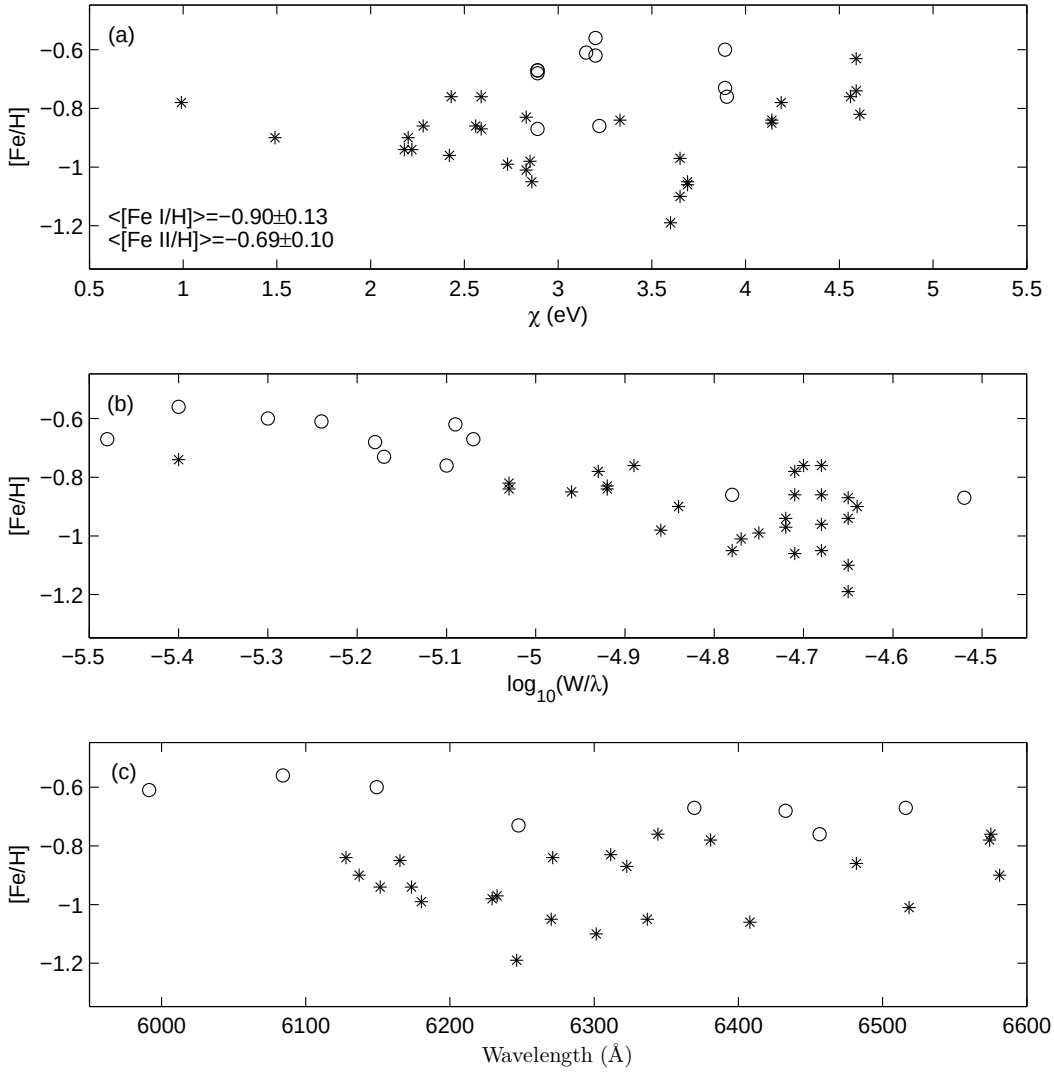

Figure 2.10: As for Figure 2.7 but the stellar model is varied by $\Delta\xi = +0.5$ kms^{-1} such that its parameters are $T_{eff} = 4300$ K, $log\ g = 1.6$, $\xi = 2.0$ kms^{-1} and [Fe/H] $= -0.6$ dex.

In Figure 2.9 the stellar atmosphere model differed in *log g* by +0.5 from the best fit model. The mean abundances derived from the Fe I and Fe II lines do not agree at this gravity. No obvious trends occur for the other parameters but the [Fe II/H] values are clearly much higher than the [Fe I/H] values.

In Figure 2.10 the model differed in ξ by +0.5 kms^{-1} from the best fit model. The trend of [Fe/H] with $log_{10}(W/\lambda)$ is obvious in Figure 2.10(b). The extension of the trend between the two Fe species makes it clear that this microturbulence value is a poor choice for Arcturus. It has forced the [Fe II/H] abundances to higher values than were derived for the best fit model and created a larger spread in [Fe/H] values for both species.

The investigation of these trends for different stellar parameters is the type of analysis that takes place while working with *abfind* in MOOG. The discussions associated with each of Figures 2.7 to 2.10 led to the refinement of the appropriate choice of stellar atmosphere parameters for each of the high-resolution stars analysed in this thesis.

The stellar parameters derived for Arcturus using this method are $T_{eff} = 4300 \pm 50$ K, *log* $g = 1.6 \pm 0.2$, $\xi = 1.5 \pm 0.25$ kms^{-1} and [Fe/H] $= -0.59 \pm 0.12$. The stellar parameters derived in Fulbright et al. (2006) were found to be $T_{eff} = 4290$ K, *log* $g = 1.5$, $\xi = 1.67$ kms^{-1} and [Fe/H] $= -0.50 \pm 0.07$ dex. These are in reasonable agreement, although this study found Arcturus to be more metal-poor. This may be attributable to the smaller equivalent widths that were determined in the thesis compared with Fulbright et al. (2006) (see Section 2.2.3).

2.2.4 Derivation of chemical abundances

The determination of the light (Z $\leq$ 30) and heavy (38 $\leq$ Z $\leq$ 63) elemental abundances proceeded by two methods. For the light elements, using sufficiently clean lines, equivalent widths were measured as outlined above. These were then used with the best fit stellar atmosphere model and *abfind* in MOOG to derive the respective elemental abundances. The list of light element lines for which abundances were measured is given in Table 2.3.

The spectral features of the heavy elements were generally either weak lines or intermediate strength lines in reasonably crowded spectral regions. Their abundances were derived by comparing synthesised and observed spectra using the *synth* function in MOOG. The heavy element lines that were used in the spectrum synthesis are listed in Table 2.4. The references associated with the VALD linelists used in this study are given in Table 2.5.

The *log gf* values for the key heavy element lines were taken where possible from the latest published laboratory values (Lawler et al. 2001a, Lawler et al. 2001b, Biemont et al. 1981, Den Hartog et al. 2003, Hannaford et al. 1982, Kupka et al. 2000) and, in the case where no laboratory value was available, the list was supplemented from other key studies (Wylie et al., 2006).

Using the stellar atmosphere model that was determined for Arcturus, the list of atomic

lines about each key line was calibrated to fit the Arcturus spectrum. This was done by adjusting the *gf* values of the neighbouring lines to provide a good fit to the Arcturus spectrum using *synth*. In three instances, (Y I at 6435.022Å, La II at 5797.965Å and Nd II at 5165.130Å) the laboratory *gf* value for the line was a very poor fit to the spectral feature in Arcturus. It provided abundances that were significantly different to the abundances derived for other lines of the same species that did use laboratory *gf* values. In these three cases *gf* values derived using reverse solar analysis in Wylie et al. (2006) were used as they provided better agreement with the other abundances derived for the species. The reason for these discrepancies may be due to the stellar model deduced for Arcturus.

The line lists also included molecular lines for C_2, CN, TiO, and MgH in order to better represent the conditions in the stellar atmosphere and so provide a better fit to the spectrum. The Kurucz molecular line lists were used (Kurucz, 1993) and, as these are semi-empirical, there were some discrepancies that needed to be addressed.

Table 2.3: Line list of the light ($Z \leq 30$) elements used to derive light elemental abundances via equivalent widths and the curve-of-growth techniques. The values are taken from the latest published values available on VALD (Kupka et al., 2000). The lines used in Arcturus and Lee 2525 are noted in columns 5 and 6.

λ (Å)	Atom	Species	χ (eV)	*log gf*	Arcturus	Lee 2525	Reference [a] [b]
5577.340	O	8.0	1.967	-8.204	✓		VALD
6300.304	O	8.0	0.000	-9.819	✓	✓	VALD
6363.776	O	8.0	0.020	-10.303	✓		VALD
6154.226	Na	11.0	2.102	-1.560	✓	✓	VALD
6160.747	Na	11.0	2.104	-1.260	✓	✓	VALD
5711.088	Mg	12.0	4.346	-1.833	✓		VALD
6318.717	Mg	12.0	5.108	-1.730	✓	✓	VALD
6319.237	Mg	12.0	5.108	-1.950	✓	✓	VALD
6799.001	Mg	12.0	5.753	-1.560	✓		VALD
6841.084	Mg	12.0	5.753	-1.610	✓		VALD
6894.918	Mg	12.0	5.753	-1.640	✓	✓	VALD
6965.409	Mg	12.0	5.753	-1.510	✓		VALD
7387.689	Mg	12.0	5.753	-1.020	✓		VALD
7875.434	Mg	12.0	5.932	-2.130	✓		VALD
5557.063	Al	13.0	3.143	-2.110	✓		VALD
6696.023	Al	13.0	3.143	-1.347	✓	✓	VALD
6698.673	Al	13.0	3.143	-1.647	✓	✓	VALD
7835.309	Al	13.0	4.022	-0.649	✓		VALD
5517.533	Si	14.0	5.082	-2.611	✓		VALD
5690.425	Si	14.0	4.930	-1.769	✓	✓	VALD
6142.483	Si	14.0	5.619	-1.295	✓	✓	VALD
6145.018	Si	14.0	5.616	-1.310	✓	✓	VALD
6155.134	Si	14.0	5.619	-0.754	✓	✓	VALD
6237.319	Si	14.0	5.614	-0.975	✓	✓	VALD
6243.815	Si	14.0	5.616	-1.242	✓		VALD
6244.466	Si	14.0	5.616	-1.093	✓	✓	VALD

continued on next page

continued from previous page

λ (Å)	Atom	Species	χ (eV)	*log gf*	Arcturus	Lee 2525	Reference [a] [b]
6414.980	Si	14.0	5.871	-1.035	✓	✓	VALD
6635.687	Si	14.0	5.863	-1.664	✓	✓	VALD
5512.980	Ca	20.0	2.933	-0.464	✓	✓	VALD
5590.114	Ca	20.0	2.521	-0.571	✓	✓	VALD
5867.562	Ca	20.0	2.933	-1.570	✓		VALD
6156.023	Ca	20.0	2.521	-2.497	✓	✓	VALD
6161.297	Ca	20.0	2.523	-1.266	✓	✓	VALD
6162.173	Ca	20.0	1.899	-0.090	✓	✓	VALD
6166.439	Ca	20.0	2.521	-1.142	✓	✓	VALD
6169.042	Ca	20.0	2.523	-0.797	✓		VALD
6169.563	Ca	20.0	2.526	-0.478	✓		VALD
6455.598	Ca	20.0	2.523	-1.340	✓		VALD
6464.673	Ca	20.0	2.526	-4.274	✓	✓	VALD
6471.662	Ca	20.0	2.526	-0.686	✓	✓	VALD
6493.781	Ca	20.0	2.521	-0.109	✓	✓	VALD
6499.650	Ca	20.0	2.523	-0.818	✓	✓	VALD
6508.850	Ca	20.0	2.526	-2.162	✓	✓	VALD
6572.779	Ca	20.0	0.000	-4.240	✓	✓	VALD
6245.637	Sc	21.1	1.507	-1.030	✓	✓	VALD
6604.601	Sc	21.1	1.357	-1.309	✓	✓	VALD
4758.118	Ti	22.0	2.249	0.425	✓	✓	VALD
4820.410	Ti	22.0	1.502	-0.441	✓	✓	VALD
4840.874	Ti	22.0	0.900	-0.509	✓	✓	VALD
4915.229	Ti	22.0	1.887	-1.019	✓	✓	VALD
4926.148	Ti	22.0	0.818	-2.170	✓	✓	VALD
5453.643	Ti	22.0	1.443	-1.610	✓		VALD
5648.565	Ti	22.0	2.495	-0.260	✓	✓	VALD
5739.469	Ti	22.0	2.249	-0.600	✓	✓	VALD
5766.359	Ti	22.0	3.294	0.389	✓		VALD
5913.728	Ti	22.0	0.021	-4.198	✓		VALD
5918.535	Ti	22.0	1.067	-1.460	✓		VALD
5944.660	Ti	22.0	0.000	-4.059	✓		VALD
6092.792	Ti	22.0	1.887	-1.379	✓		VALD
6126.216	Ti	22.0	1.067	-1.425	✓	✓	VALD
6146.206	Ti	22.0	1.873	-1.151	✓	✓	VALD
6186.140	Ti	22.0	2.175	-1.365	✓	✓	VALD
6273.388	Ti	22.0	0.021	-4.248	✓	✓	VALD
6303.756	Ti	22.0	1.443	-1.566	✓	✓	VALD
6312.236	Ti	22.0	1.460	-1.552	✓	✓	VALD
6336.099	Ti	22.0	1.443	-1.743	✓	✓	VALD
6497.684	Ti	22.0	1.443	-2.085	✓	✓	VALD
6508.120	Ti	22.0	1.430	-2.146	✓	✓	VALD
6554.223	Ti	22.0	1.443	-1.218	✓	✓	VALD
6556.062	Ti	22.0	1.460	-1.074	✓	✓	VALD
6599.105	Ti	22.0	0.900	-2.085	✓	✓	VALD
6716.666	Ti	22.0	2.487	-1.409	✓	✓	VALD
6743.122	Ti	22.0	0.900	-1.630	✓		VALD
7138.072	Ti	22.0	1.430	-2.375	✓		VALD
7271.506	Ti	22.0	1.443	-2.294	✓		VALD

continued on next page

continued from previous page

λ (Å)	Atom	Species	χ (eV)	*log gf*	Arcturus	Lee 2525	Reference [a] [b]
7352.119	Ti	22.0	2.487	-0.967	✓		VALD
7391.513	Ti	22.0	1.502	-1.210	✓		VALD
4865.611	Ti	22.1	1.116	-2.590	✓	✓	NIST ASD
5492.862	Ti	22.1	1.582	-2.450	✓		VALD
6491.561	Ti	22.1	2.061	-1.793	✓	✓	VALD
6559.588	Ti	22.1	2.048	-2.019	✓	✓	VALD
6606.949	Ti	22.1	2.061	-2.790	✓		VALD
7214.716	Ti	22.1	2.590	-1.740	✓		VALD
6216.354	V	23.0	0.275	-1.290	✓	✓	VALD
6251.827	V	23.0	0.287	-1.340	✓	✓	VALD
6504.164	V	23.0	1.183	-1.230	✓	✓	VALD
6454.990	Co	27.0	3.632	-0.250	✓	✓	VALD
6632.433	Co	27.0	2.280	-2.000	✓	✓	VALD
6175.360	Ni	28.0	4.089	-0.559	✓	✓	VALD
6186.709	Ni	28.0	4.105	-0.960	✓	✓	VALD
6204.600	Ni	28.0	4.088	-1.100	✓	✓	VALD
6223.981	Ni	28.0	4.105	-0.910	✓	✓	VALD
6635.118	Ni	28.0	4.419	-0.820	✓	✓	VALD
4722.153	Zn	30.0	4.030	-0.338	✓	✓	VALD
4810.528	Zn	30.0	4.078	-0.137	✓	✓	VALD

[a] VALD (Kupka et al., 2000)
[b] NIST ASD (Sugar & Corliss, 1985)

Table 2.4: Line list of the heavy ($38 \leq Z \leq 63$) elements that were used to derive heavy element abundances via spectrum synthesis. The lines used in the key object/GC are noted in columns 5 to 9. The reference for each line is listed in column 10.

λ (Å)	Atom	Species	χ (eV)	*log gf*	Arcturus	Lee 2525	47 Tuc	NGC 362	NGC 6388	Reference [a]
7070.070	Sr	38.0	1.847	-0.030	✓			✓	✓	VALD
5527.561	Y	39.0	1.397	0.400	✓	✓				Hannaford et al. (1982)
6222.579	Y	39.0	0.000	-1.700	✓	✓		✓	✓	Hannaford et al. (1982)
6435.022	Y	39.0	0.070	-1.020	✓	✓	✓	✓	✓	Wylie et al. (2006)
4883.685	Y	39.1	1.084	0.070	✓	✓				Hannaford et al. (1982)
5119.111	Y	39.1	0.990	-1.360	✓					Hannaford et al. (1982)
5123.211	Y	39.1	0.992	-0.830	✓					Hannaford et al. (1982)
5544.610	Y	39.1	1.740	-1.090	✓					Hannaford et al. (1982)
7264.164	Y	39.1	1.840	-1.500	✓		✓	✓	✓	Hannaford et al. (1982)
4805.890	Zr	40.0	0.690	-0.420	✓					Biemont et al. (1981)
4809.477	Zr	40.0	1.580	0.160	✓					Biemont et al. (1981)
6127.460	Zr	40.0	0.150	-1.060	✓		✓	✓	✓	Biemont et al. (1981)
6134.570	Zr	40.0	0.000	-1.280	✓	✓	✓	✓	✓	Biemont et al. (1981)
6140.460	Zr	40.0	0.520	-1.410	✓	✓	✓	✓	✓	Biemont et al. (1981)
6143.183	Zr	40.0	0.070	-1.100	✓	✓	✓	✓	✓	Biemont et al. (1981)
6445.720	Zr	40.0	1.000	-0.830	✓	✓	✓	✓		Biemont et al. (1981)
7819.350	Zr	40.0	1.820	-0.380	✓				✓	Biemont et al. (1981)
5112.280	Zr	40.1	1.660	-0.590	✓					Biemont et al. (1981)
5350.089	Zr	40.1	1.827	-0.940	✓	✓				Wylie et al. (2006)
6141.728	Ba	56.1	0.704	-0.076	✓	✓	✓	✓	✓	VALD
6496.897	Ba	56.1	0.604	-0.377	✓	✓	✓	✓	✓	VALD
5114.559	La	57.1	0.235	-1.030	✓	✓				VALD
5769.060	La	57.1	1.250	-0.690	✓					Lawler et al. (2001a)
5797.565	La	57.1	0.244	-1.510	✓	✓				Wylie et al. (2006)
5805.770	La	57.1	0.126	-1.610	✓	✓				Wylie et al. (2006)

continued on next page

continued from previous page

λ (Å)	Atom	Species	χ (eV)	*log gf*	Arcturus	Lee 2525	47 Tuc	NGC 362	NGC 6388	Reference [a]
6390.483	La	57.1	0.320	-1.410	✓	✓	✓	✓	✓	Lawler et al. (2001a)
5165.130	Nd	60.1	0.680	-0.060	✓					Wylie et al. (2006)
5804.000	Nd	60.1	0.744	-0.530	✓					Den Hartog et al. (2003)
5811.572	Nd	60.1	0.859	-0.860	✓	✓				Den Hartog et al. (2003)
6428.645	Nd	60.1	0.205	-1.831	✓	✓	✓	✓	✓	VALD
6637.190	Nd	60.1	1.451	-0.840	✓			✓	✓	Den Hartog et al. (2003)
6637.960	Nd	60.1	1.772	-0.320	✓			✓	✓	Den Hartog et al. (2003)
6437.698	Eu	63.1	1.320	-0.320	✓	✓		✓	✓	Lawler et al. (2001b)
6645.127	Eu	63.1	1.380	0.120	✓	✓	✓	✓	✓	Lawler et al. (2001b)

[a] VALD (Kupka et al., 2000)

Table 2.5: References associated with VALD line lists in Tables 2.3 and 2.4

VALD Line List	Reference
Vald:NLTE lines:O	Kurucz CDROM 18 (1993)
Vald:NLTE lines:Na	Kurucz CDROM 18 (1993)
Vald:NLTE lines:Mg	Kurucz CDROM 18 (1993)
Vald:NLTE lines:Al	Kurucz CDROM 18 (1993)
VALD:Si 1 Kurucz 2007	http://cfaku5.cfa.harvard.edu /ATOMS/1400
VALD:NLTE lines:Ca	Kurucz CDROM 18 (1993)
VALD 2: VanderWaals new corCr	Barklem, P. S.; Piskunov, N.; O'Mara, B. J. 2000, A&AS 142, 467
GFIRON obs. energy level: Sc	Kupka, F., et al., 2000, Baltic Astronomy, 9, 590 Barklem, P. S.; Piskunov, N.; O'Mara, B. J. 2000, A&AS 142, 467
VALD 2: Sc	Lawler & Dakin (1989); Kurucz CDROM 20-22 (1994)
GFIRON obs. energy level: Ti	Kurucz CDROM 20-22 (1994)
VALD: VanderWaals new corC	Kurucz CDROM 20-22 (1994)
GFIRON obs. energy level: V	Kurucz CDROM 20-22 (1994)
GFIRON obs. energy level: Co	Kurucz CDROM 20-22 (1994)
GFIRON obs. energy level: Ni	Kurucz CDROM 20-22 (1994)
Bell heavy: Cu to Zn	Kurucz CDROM 18 (1993)
Bell heavy: Ga to Ba	Kurucz CDROM 18 (1993)
Bell heavy: La to Lu & g Lande	Kurucz CDROM 18 (1993)
GFIRON	Kurucz CDROM 20-22 (1994)
VALD2:Fe	O'Brian T.R., et al., 1991, JOSA B8, 1185 Bard A., Kock A., Kock M., 1991, A&A 248, 315 Bard A., Kock M., 1994, A&A 282, 1014 Johansson S., et al., 1994b, ApJ 429, 419 Shoenfeld W.G., et al., 1995, A&A, 301, 593-601 Bergeson S.D., Mullman K.L., Lawler J.E. 1994, ApJ 435, L157-L159 Bergeson S.D., et al., 1996, ApJ 464, 1044-1049 Mullman K.L., Sakai M., Lawler J.E., 1997, A&AS 122, 157 Johansson S., et al., 1995, ApJ 446, 361-370 Biemont E., Johansson S., Palmeri P., 1997, Phys. Scripta 55, 559-564 Rosberg M., Johansson S., 1992, Phys. Scripta 45, 590-597 Whaling W., 1983, Tech. Rep. 84 A, Calif. Inst. of Techn., Pasadena (USA) Pauls U., Grevesse N., Huber M.C.E., 1990, A&A 231, 536 Kroll S., Kock M., 1987, A&AS 67, 225 Heise C., Kock M., 1990, A&A 230, 244 Hannaford P., Lowe R.M., Grevesse N., Noels A., 1992, A&A 259, 301-306 Blackwell D.E., Shallis M.J., Simmons G.J., 1980, A&A 81, 340-343 Bridges J.M., 1973, in Int. Conf. on Phenom. in Ionezed Gases, 11th, ed. I. Stoll, Czech. Acad. Sci., Inst. Phys., Prague, p. 418 Baschek B., Garz T., Holweger H., Richter J., 1970, A&A 4, 229 Kupka, F., et al., 2000, Baltic Astronomy, 9, 590 Garcia G. & Campos J., 1988, JQSRT 39, 477 Den Hartog E.A., Lawler J.E., Sneden C. & Cowan J.J., 2003, ApJS, 148, 543 Smith G. & Raggett D.St.J., 1981, J. Phys. B. At. Mol. Phys., 14, 4015 Raassen A.J.J. & Uylings P.H.M., 1998, A A, 340, 300 Biemont E., Palmeri P. & Quinet P., 1999, Astrophys. Space Sci. 269-270, 635 Quinet P. & Biemont E., 2004, At. Data Nucl. Data Tables 87, 207-230 Nave, G., et al., 1994, Astron. Astrophys. Suppl., 94, 221

Figure 2.11 shows the Arcturus spectrum in the region from 6138 Å to 6145 Å. In order to simulate changes in CN the C abundance was altered in MOOG and then the CN *log gf* values were changed in the line list and that line list was then synthesised in MOOG to ensure the adjustment was still a good fit. Similarly, changes in Mg were used to simulate the changes in MgH. The *log gf* values were then altered and synthesised to confirm the adjustment using *synth*.

Figure 2.11(a) compares the observed spectrum with synthesised spectrum generated using a line list that included only atomic lines and CN lines from the semi-empirical Kurucz list. Spectra are synthesised corresponding to no CN being present; the best fitting adjustment to the CN *log gf* values; and the unadjusted Kurucz CN *log gf* values . Clearly the unadjusted Kurucz CN line list is a poor fit to the observed spectrum as the lines in the synthesised spectrum are too strong.

Similarly, Figure 2.11(b) compares a synthesised spectrum generated using only atomic lines and MgH lines with the observed spectrum. Again synthesised spectra are shown with no MgH, best fitting adjusted MgH *log gf* values and unadjusted Kurucz MgH *log gf* values. The unadjusted Kurucz MgH line list is also a poor fit for the MgH features and also with regard to the lack of features in the rest of the continuum. Comparing (a) and (b) shows that the strong MgH features are not present in (a), and the CN features are not present in (b). These are definitely molecular features and cannot be attributed to simple atomic lines.

Figure 2.11(c) is a combination of the line lists used in (a) and (b) in order to see where the molecular features overlap such as at 6140 Å and 6143 Å. The individual adjustments to the CN and MgH molecular *log gf* values were compared in the combined line list to ensure a best fitting to the spectrum in general. The best fit is shown by the blue line in (c) where the CN molecular *log gf* values were adjusted by -0.35 dex, and the MgH molecular *log gf* values were adjusted by -0.55 dex. The remaining discrepancies are due to the atomic line list. The lines not being investigated for their abundances were then fitted to the spectrum, based on the adjustments to the CN and MgH lines, by individual adjustment of their *log gf* values resulting in the final best fit shown in blue in Figure 2.11(d).

This process was carried out for each wavelength region that was used in the spectrum synthesis and the analysis included varying TiO and C_2 to investigate the effect of those molecules on the fit to the observed spectrum. The line lists for which the molecular and atomic *log gf* values had been adjusted were then used in the chemical abundance analysis.

2.2.5 Stellar atmosphere models

The spectrum synthesis programme MOOG was used in this research to derive the stellar parameters and chemical abundances. MOOG accepts several types of stellar atmosphere models, including the Kurucz stellar models (Kurucz, 1979) and the MARCS stellar models (Gustafsson et al., 2008), both of which were used in this research.

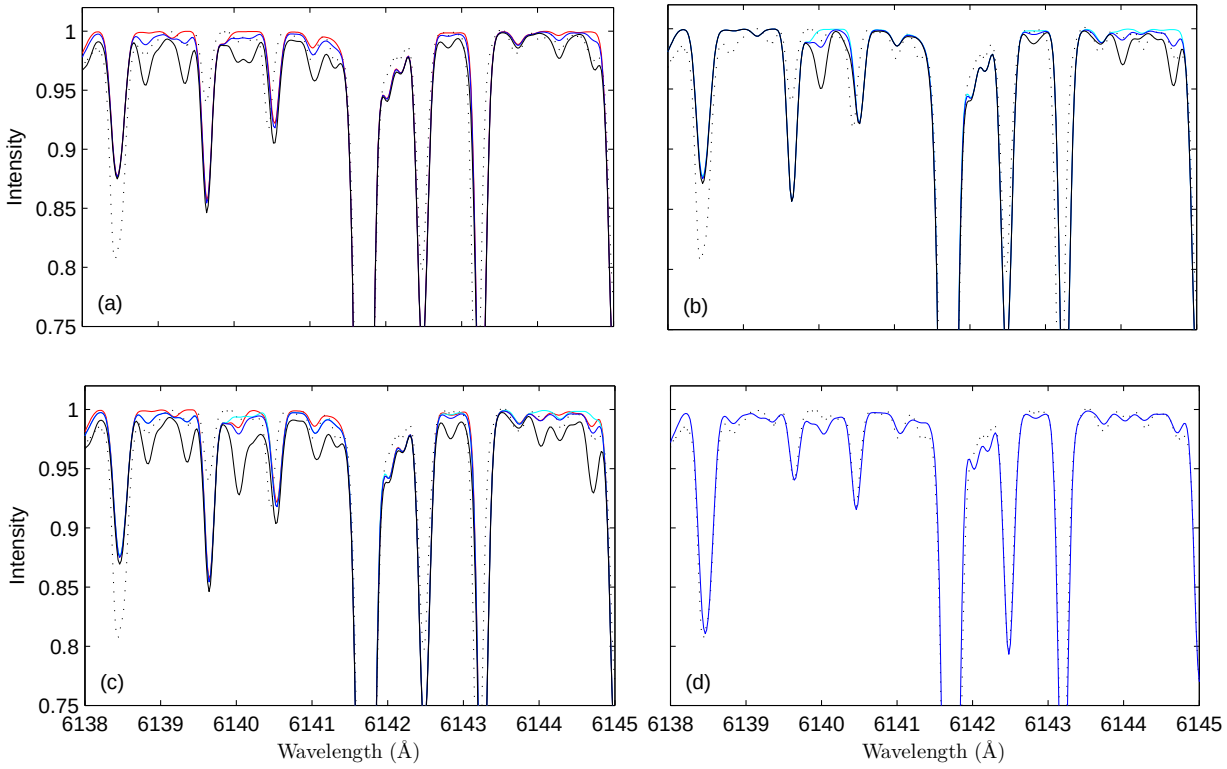

Figure 2.11: Comparison of the Arcturus observed spectrum with synthesised spectra showing changes in CN and MgH in the wavelength region 6138 Å to 6145 Å. (a) Synthesised spectrum generated from a line list with atomic lines and CN features only. Black dotted line = observed Arcturus spectrum; Red line = simulation of no CN with Δ[C/Fe]= −8.0 dex; Blue line = best fit to CN features (Δ[C/Fe]= −0.35 dex); Black line = unadjusted Kurucz CN *log gf* values (Δ[C/Fe]= 0.00 dex). (b) Synthesised spectrum generated from a line list with atomic lines and MgH features only. Cyan line = simulation of no MgH with Δ[Mg/Fe]= −8.0 dex; Blue line = best fit to MgH features (Δ[Mg/Fe]= −0.55 dex); Black line = unadjusted Kurucz MgH *log gf* values (Δ[Mg/Fe]= 0.00 dex). (c) Line list includes atomic lines with both CN and MgH features. Synthesised spectra as for (a) and (b). The blue line is the best fit with Δ[C/Fe]= −0.35 dex and Δ[Mg/Fe]= −0.55 dex. The atomic lines have not been adjusted to fit the spectrum. (d) Line list includes atomic lines with both CN and MgH features. The *log gf* values of the atomic lines not being analysed for abundances have been adjusted individually where necessary to fit the spectrum. The final best fit is shown in blue.

The programme Atlas9 can either extrapolate from a single Kurucz model to generate a model at the required stellar parameters or converge a model at those stellar parameters (Kurucz 1979; Castelli & Kurucz 2003; Sbordone et al. 2006). However, the majority of the high resolution spectra considered for analysis in this study comprised very cool, metal-poor giants which did not all fall within the Kurucz grid ($T_{eff} \geq 3500$ K).

The MARCS stellar models are available in a grid with effective temperatures from 2500 K to 8000 K. Tools are available that will interpolate between eight models which are separated in temperature, gravity and metallicity (Masseron 2006; Gustafsson et al. 2008). Issues with non-linearities in the stellar parameters when varied between the gridpoint models were noted, although the interpolation code was extensively tested over a range of stellar temperatures (Masseron, 2006). The MARCS models are available in two types of atmospheric geometry, plane parallel and spherical, although the cool models needed for the cool AGB stars in this research are only available in spherical geometry. Plane-parallel geometry assumes the flux is being emitted from the star in just one dimension through a series of planes defined by the temperature and gravity. Spherical geometry assumes a 3-dimensional flux where the spherical shells define the atmospheric structure. While all stars have a spherical structure the plane-parallel geometry is typically a reasonable representation of smaller hotter stars. Spherical geometry better represents the extended atmosphere of very cool giant stars.

MOOG derives abundances based on LTE calculations and it assumes the model has a plane-parallel geometry for the structure of the stellar atmosphere. Spherical geometry models can be used in MOOG, although some differences are observed. The stellar parameters for Arcturus were derived using a MARCS spherical geometry model and a Kurucz/Atlas9 plane-parallel model to investigate these differences. Table 2.6 compares the Arcturus stellar parameters derived here using plane-parallel and spherical geometry with the values obtained in Fulbright et al. (2007).

An abundance analysis of the light elements in Arcturus was carried out in Fulbright et al. (2007) and the values derived here are compared with that study also in Table 2.6. In the current study there is very little change between the light element abundances derived using the spherical model compared with the plane-parallel model. Except for Si, which showed a difference of 0.03 dex, the variations are of the order of 0.01 dex. Comparing the spherical model to the Fulbright et al. (2007) values there is reasonable agreement to within ± 0.1 dex between the two sets of abundances. Given the close agreement between the derived abundances of the spherical and plane-parallel models, and the good agreement with Fulbright et al. (2007), the spherical model was selected as the stellar atmosphere model for Arcturus in this analysis. As the MARCS models provided the range in temperatures to cover the entire stellar sample they were selected to be used for the majority of this analysis.

The final light and heavy elemental abundances for Arcturus that were derived during calibration of the above analysis process are listed in Table 2.7, along with the related

Table 2.6: Comparison of the derived light elemental abundances for Arcturus from Fulbright et al. (2007) and this study. In this study two stellar models were considered in order to compare the results from MOOG of spherical and plane parallel geometry. N indicates the number of lines of a particular element used in these analyses.

	Fulbright et al. (2007)			This study				
Geometry	Plane-parallel			Spherical		Plane-parallel		
T_{eff}	4290 K			4300 K		4270 K		
log g	1.55			1.6		1.7		
[Fe/H]	-0.50 dex			-0.60 dex		-0.60 dex		
ξ	1.67kms^{-1}			1.50kms^{-1}		1.50kms^{-1}		
	[X/Fe]	σ	N	[X/Fe]	σ	[X/Fe]	σ	N
O	0.48	-	1	0.57	0.02	0.56	0.03	2
Na	0.09	-	1	0.15	0.04	0.14	0.04	2
Mg	0.39	0.06	5	0.34	0.15	0.32	0.15	8
Al	0.38	0.03	3	0.25	0.07	0.24	0.07	4
Si	0.35	0.05	15	0.24	0.14	0.21	0.14	10
Ca	0.21	0.01	2	0.19	0.06	0.19	0.06	12
Ti	0.26	0.04	24	0.34	0.15	0.34	0.11	29
				[X/H]	σ	[X/H]	σ	N
Fe	-0.50[a]	0.07	-	-0.59	0.12	-0.62	0.11	40

[a] Fulbright et al. (2006)

Table 2.7: Derived elemental abundances for Arcturus with uncertainties in [Fe/H] and [X/Fe] associated with changes in T_{eff}, *log g* and ξ.

Species X	N	[X/H]	σ	Δ[X/H] ΔT_{eff} +100K	$\Delta log\ g$ +0.5	$\Delta\xi$ +0.5kms^{-1}
Fe I	29	-0.61	0.12	0.06	0.13	-0.29
Fe II	11	-0.56	0.05	-0.20	0.21	-0.13
X	N	[X/Fe]	σ	Δ[X/Fe]		
O I	2	0.57	0.02	-0.01	0.20	-0.02
Na I	2	0.15	0.04	0.09	0.01	-0.10
Mg I	8	0.34	0.15	0.01	0.03	-0.04
Al I	4	0.25	0.07	0.07	0.01	-0.07
Si I	10	0.24	0.14	-0.06	0.13	-0.06
Ca I	12	0.19	0.06	0.12	-0.03	-0.26
Ti I	24	0.35	0.12	-0.02	0.22	-0.18
Ti II	5	0.33	0.10	0.17	0.04	-0.15
Y I	3	0.07	0.24	0.21	0.03	-0.07
Y II	5	0.12	0.11	0.02	0.22	-0.04
Zr I	7	0.01	0.07	0.13	0.07	0.00
Zr II	3	0.12	0.10	-0.01	0.24	-0.01
Ba II	2	-0.19	0.08	0.27	0.26	-0.16
La II	6	0.04	0.08	0.04	0.19	-0.02
Nd II	4	0.10	0.07	0.03	0.17	-0.09
Eu II	2	0.36	0.04	-0.02	0.23	-0.01

uncertainties due to changes in T_{eff}, *log g* and ξ.

The uncertainties associated with changes in T_{eff}, *log g* and ξ are more significant than the differences in abundance between the spherical and plane-parallel models. Hence the determination of the stellar parameters can be considered to have a greater impact on the errors introduced in the analysis process than the geometry upon which the model is based. Based on this analysis we were satisfied that we could reliably use the MARCS stellar atmosphere models with MOOG.

The parameter uncertainties can account for the differences in the light elemental abundances between this study and Fulbright et al. (2007), although the difference between the Al I abundances are out the range of these uncertainties. This may be due to the third Al I line, which was measured in Fulbright et al. (2007) but not in this study, having a larger equivalent width than the other two lines, which were measured in this study. If an equivalent width for this line was measured that was similar to the line in Fulbright et al. (2007) then the inclusion of this line would result in the larger overall abundance of Al I as

specified in Fulbright et al. (2007). The line was outside the range of wavelengths that were investigated in this thesis and so not included in the calibration to Arcturus.

The Ba abundance derived from Ba II lines had the most significant associated uncertainties. The two lines from which this abundance was derived are both strong lines with underlying Fe lines contributing to the strength of the feature. As such, the Ba abundance is sensitive to changes in T_{eff}, *log g* and ξ and must be treated with caution. In a general consideration of all the elements analysed here, the neutral species are most sensitive to changes in T_{eff}, while the ionised species are most sensitive to changes in *log g* as expected.

2.3 Medium-resolution analysis

Two sets of medium resolution spectra were analysed in this thesis. The first set was part of a feasibility study into using medium resolution instruments to survey *s*-process elemental abundances in GC stars (see Chapter 3). These spectra were observed using RSS on SALT and the raw data was reduced and normalised using the reduction software IRAF[3]. As this was a preliminary study the techniques used were less robust than those outlined above. The Kurucz model closest to the accepted Arcturus stellar parameters was selected with which to calibrate the line lists for spectrum synthesis. This model had the parameters of T_{eff} = 4250 K, *log g* = 1.5, ξ = 2.0 kms^{-1} and [Fe/H]= −0.50 dex. A ξ of 2.0 kms^{-1} was used here as a default value because this analysis pre-dated the robust determination of stellar parameters outlined in the previous sections. In line with the method outlined above, the line lists were adjusted until a good fit to the Arcturus spectrum was found.

As equivalent widths could not be measured for individual lines at this low resolution (R$\sim$ 5,000)the photometric stellar parameters for each star were determined from the V magnitude and $(B-V)$ colour index using the equations derived in Alonso et al. (1999). The Kurucz stellar model closest to the photometric parameters was then selected for each star. The models, along with the modified line lists, were used to derive the chemical abundances for these stars using *synth* in MOOG.

In the analysis of the second medium-resolution data set, obtained using AAOmega on the AAT, the line lists and Arcturus model had been superceded by the more detailed calibration outlined in Section 2.2. The stellar parameters for these stars were estimated from the available photometry. Ultimately the V magnitude and $(V-K)$ colour for each star provided the best estimate for the stellar parameters. The comparison between parameters derived from the $(B-V)$, $(V-K)$ and $(J-K)$ colours is included in Chapter 4. The normalisation of the spectra was carried out using the hottest star in the sample to remove the shape of the instrumental profile. The spectra were analysed for their abundances by spectrum synthesis (see Section 2.2.4) and and the measurement of CN indices. Further

[3]Image Reduction and Analysis Facility (http://iraf.noao.edu)

discussion on this is included in Chapter 4. Key light elements were also analysed for their abundances using spectrum synthesis. The lines and molecular bands investigated in this data set are listed in Table 2.8.

Table 2.8: Spectral features that were used to derive elemental abundances and molecular indices in the AAOmega medium-resolution 47 Tuc giant star survey.

λ Å	Element	Species	χ (eV)	*log g*	Reference
4305 to 4325	CH	106	-	-	Kurucz (1993)
4142 to 4216	CN	607	-	-	Kurucz (1993)
6154.226	Na	11.0	2.102	-1.560	VALD
6160.747	Na	11.0	2.104	-1.260	VALD
6131.573	Si	14.0	5.616	-1.556	VALD
6131.852	Si	14.0	5.616	-1.615	VALD
6145.018	Si	14.0	5.616	-1.310	VALD
6155.134	Si	14.0	5.619	-0.754	VALD
6156.023	Ca	20.0	2.521	-2.497	VALD
6166.439	Ca	20.0	2.521	-1.142	VALD
6169.563	Ca	20.0	2.526	-0.478	VALD
6147.834	Fe	26.0	4.076	-1.671	VALD
6157.728	Fe	26.0	4.076	-1.260	VALD
6143.183	Zr	40.0	0.070	-1.100	Biemont et al. (1981)
6141.728	Ba	56.1	0.704	-0.076	VALD
5805.770	La	57.1	0.126	-1.610	Wylie et al. (2006)
5811.572	Nd	60.1	0.859	-0.860	Den Hartog et al. (2003)

[a] VALD (Kupka et al., 2000)

2.4 High-resolution analysis

The high-resolution data consisted of a single giant star in 47 Tuc observed on the ANO 2.3 m telescope at Siding Spring Observatory, and eighteen cool giant stars over three GCs observed using UVES on the VLT.

The single star was reduced from the raw data using IRAF. The normalised spectrum was then analysed for its stellar parameters and chemical abundances as described in Section 2.2.

The large high-resolution sample was provided in a reduced form from the VLT reduction pipeline such that only re-merging of the individual échelle orders and normalisation of the spectra was required. It was necessary to remove the shape of the instrumental profile from each of the échelle orders. The hottest star in the sample, which was observed in the

globular cluster M15, was analysed in IRAF to determine the shape of the continuum in each order. This was then divided out of each of the stellar spectra in a general normalisation. The analysis process derived using Arcturus was then carried out on each of the spectra to determine their stellar parameters and chemical abundances.

In the derivation of the Fe I and Fe II abundances for the cool giants in 47 Tuc an issue arose when using the low gravity ($log\ g < 0.4$ dex) interpolated stellar models. Table 2.9 lists a series of results for two of the stars that illustrate this problem. The derived Fe I and Fe II abundances for the first star (*tc*03) show an extreme change between a *log g* of 0.4 and 0.3. This change in *log g* results in a sharp increase of ~ 0.4 dex for [Fe I/H] and ~ 0.6 dex for [Fe II/H]. In comparison, the change from $log\ g = 0.3$ to 0.2 (and $log\ g = 0.5$ to 0.4) results in a change in abundance of only ~ 0.04 dex for both [Fe I/H] and [Fe II/H].

For the second star (*tc*09) a similar jump in abundance values is observed at $log\ g \sim 0.4$ dex. Two separate values of microturbulence were investigated for this star and both resulted in the same jump in derived abundance which implies that the effect is not a microturbulence issue.

The photometric and resulting derived stellar parameters for the majority of the stars in the sample favoured very low gravities. However this issue with the low gravity interpolation models made it difficult to hone in on the best fit stellar model for these stars as the derived abundances would change so significantly at the key value of $log\ g \sim 0.4$ dex.

The observed effect may be due to forcing MOOG to use spherical geometry models.

Table 2.9: Examples of the discrepancy in derived abundances with changes to lower interpolated gravities. For *tc*03 the break occurs from a *log g* of 0.4 to 0.3 for abundances derived from both Fe I and Fe II lines. The effect also shows up for *tc*09 which compares the effect at two values of ξ, 2.0 kms^{-1} and 1.5 kms^{-1}.

Star	T_{eff} (K)	*log g*	[Fe/H]	ξ	[Fe I/H]	[Fe II/H]	[Fe I/H] - [Fe II/H]
tc03	4000	0.20	-0.85	1.5	-0.66	-0.38	-0.28
	4000	0.30	-0.85	1.5	-0.63	-0.33	-0.30
	4000	0.40	-0.85	1.5	-1.00	-0.92	-0.08
	4000	0.50	-0.85	1.5	-0.97	-0.87	-0.10
tc09	4200	0.15	-0.70	2.0	-0.91	-0.54	-0.37
	4200	0.30	-0.70	2.0	-0.87	-0.46	-0.41
	4200	0.50	-0.70	2.0	-1.15	-1.04	-0.11
	4200	0.70	-0.70	2.0	-1.09	-0.93	-0.16
	4200	0.15	-0.70	1.5	-0.61	-0.41	-0.20
	4200	0.30	-0.70	1.5	-0.56	-0.34	-0.22
	4200	0.50	-0.70	1.5	-0.86	-0.92	0.06
	4200	0.70	-0.70	1.5	-0.80	-0.82	0.02

The MARCS spherical geometry models were successfully used with MOOG to derive stellar parameters for Arcturus that agreed with previously determined stellar parameters. However the gravity of Arcturus is significantly higher than the gravity at which this issue has been observed and so spherical geometry complications in MOOG are not necessarily ruled out.

Alternatively the effect may be due to the interpolation of such low gravity models and so the resulting T-τ relationship within the stellar atmosphere model maybe poorly approximated. To order to make a comparison, a similar low gravity model was interpolated from the Bell et al. (1976) models using an interpolation programme written specifically for those models (Citation for Peter's Modint). In an analysis of the same data no such discrepancy was observed using the interpolated Bell et al. (1976) models and the derived Fe I and Fe II abundances increased smoothly with increased gravity.

The abrupt changes in derived Fe I and Fe II abundances between the low gravity interpolated models was an unexpected issue for which the cause could not be exactly determined for the purposes of this thesis. For the interpolated models with gravities higher than *log* $g \sim 0.4$ dex, and for the models taken directly from the MARCS website, this issue did not arise. As the stellar parameters for the majority of the 47 Tuc stars returned gravity values above this limit, interpolated models were used for their analysis. The cool giants in NGC 362 and NGC 6388 were analysed using models from the MARCS website only in order to avoid this issue. Due to time constraints a more detailed examination of this effect could not be pursued for this thesis.

The assessment of the entire sample of cool giants carried out in this thesis resulted in only the hottest of the stars being analysed due to the strong molecular bands that were present in the spectra of the coolest stars. The resulting smaller sample could have been adequately represented by Kurucz/Atlas9 models. However, future work to analyse the remaining coolest stars, whose stellar parameters lie outside the Kurucz parameter grid, advocates pursuing this research using the MARCS models.

Chapter 3

Medium-resolution *s*-process element survey of 47 Tuc: Feasibility study & SALT RSS

This chapter considers the feasibility of using RSS on SALT and AAOmega on the AAT for the medium-resolution survey of *s*-process elemental abundances in 47 Tuc stars. These instruments have comparable maximum resolving powers, RSS at $R \sim 10\,000$ and AAOmega at $R \sim 8\,000$. Comparison will be made with the high-resolution capabilities of SALT HRS, which has a nominal maximum resolving power of $R \sim 60\,000$. The following analysis addresses the question of whether or not variations in *s*-process elemental abundance enhancements of at least +0.5 dex (seen in some high-resolution studies (Brown & Wallerstein 1992; Wylie et al. 2006)) will be visible in spectra obtained at the medium resolving power of these instruments. The line strength visibility for a range of key *r*- and *s*-process elements will be explored in the effective temperature (T_{eff}) - surface gravity (*log g*) space represented by the colour magnitude diagram (CMD) of 47 Tuc for both high- and medium-resolving powers.

3.1 The HR Diagram: 'T_{eff} - *log g*' space

The traditional form of the Hertzspung Russell (HR) diagram is luminosity (L) versus effective temperature (T_{eff}). This is equivalent to the directly observed quantities of apparent magnitude V and colour index $(B-V)$ which are used as the axes in a CMD. Another useful version is to replace luminosity with surface gravity, *log g*, where the gravity is derived from luminosity via the ideal gas law and the principles of hydrostatic equilibrium. Thus a decrease in luminosity corresponds to an increase in surface gravity.

It is particularly useful to interpret the HR diagram as having axes of *log g* and T_{eff}), as these are two of the stellar parameters used to generate synthesised spectra from stellar

atmosphere models. These values can be calculated from V and $(B-V)$ values using the calibration equations from Alonso et al. (1999) and the following equation for *log g*;

$$log(g_\star) \;=\; log(g_\odot) \;+\; log(\frac{M_\star}{M_\odot}) \;+\; 4\times log(\frac{T_{eff}(\star)}{T_{eff}(\odot)}) \;-\; 0.4\times(M_{bol}(\odot) \;-\; M_{bol}(\star)) \qquad (3.1)$$

where $log(g_\star)$ and $log(g_\odot)$ are the surface gravities of the star($\star$) and Sun ($\odot$) respectively, $M_\star$ and $M_\odot$ are the masses, $T_{eff}(\star)$ and $T_{eff}(\odot)$ are the effective temperatures, and $M_{bol}(\star)$ and $M_{bol}(\odot)$ are the bolometric magnitudes.

The different branches in the HR diagram can be traced out by specific combinations of T_{eff} and *log g*. Synthesised spectra can be generated using stellar atmosphere models with these different combinations of parameters and so, with the previously discussed conditions on neutral and ionised lines in mind (see Section 2.1.1), variations in line strength for weak metal lines can be explored in the $T_{eff} - log\ g$ space for any sample of stars.

3.2 Line strengths in the 47 Tuc '$T_{eff} - log\ g$' space

Figure 3.1 is the CMD of 47 Tuc (Hartwick & Hesser 1974; Lee 1977; Cannon et al. 1998). The stars range in T_{eff} from $\sim$ 4000 K to $\sim$ 6000 K, and in *log g* from $\sim$ 1.0 to $\sim$ 4.5.

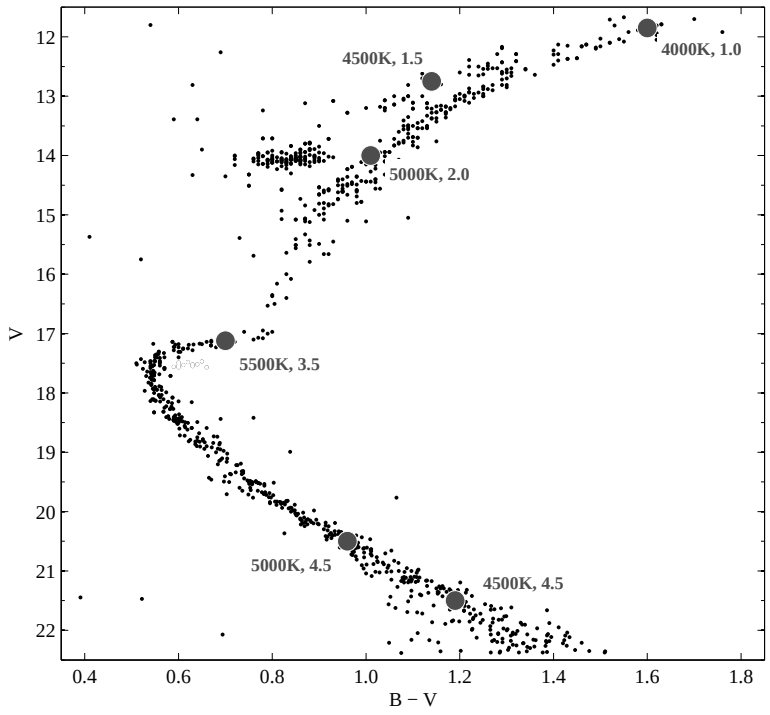

Figure 3.1: Colour-magnitude diagram of 47 Tuc showing the different branches of stellar evolution. Six key points with their respective values of T_{eff} and *log g* are shown.

The six points on the CMD shown in Figure 3.1 were selected to represent key stages of evolution of interest in *s*-process elemental abundance analysis. In particular, three points were selected on the giant branch (GB), one point on the subgiant branch (SG), and two on the main sequence (MS). The T_{eff} and *log g* values for each point are displayed.

The sets of T_{eff} and *log g* values were used to select stellar atmosphere models that were then used to generate synthetic spectra. The models and line lists used in the synthesis programme were sourced from the Kurucz grid of model atmospheres (Kurucz & Peytremann 1975; Kurucz 1979). Each model had a metallicity of [Fe/H] = −0.5 dex which is similar to the accepted metallicity of 47 Tuc ([Fe/H] = −0.76 dex, Harris 1996). A microturbulence of 2.0 kms^{-1} was used for all models. The line lists were calibrated as outlined in Section 2.3.

The spectrum synthesis programme MOOG (Sneden, 1973) was used to generate spectra for each of the points in Figure 3.1. The progression of the synthetic spectra from the RGB tip to the MS explores variations in the strength of weak metal lines with changes in T_{eff} and *log g*. Three spectral regions were synthesised based on lines used in Wylie et al. (2006). The key species in each of the spectral regions, and their neutron-capture classification, are set out in Table 3.1.

Table 3.1: Key *s*- and *r*-process features in synthesised regions.

Region (Å)	Feature (Å)	Species	Process
6139 - 6145	6140.46	Zr I	(light) *s*-
	6143.18	Zr I	(light) *s*-
5803 - 5807	5804.00	Nd II	(heavy) *s*-
	5805.77	La II	(heavy) *s*-
6644 - 6646	6645.13	Eu II	*r*-

In the following analysis model spectra were synthesised at high ($R \sim 60\ 000$) and medium ($R \sim 10\ 000$) resolving powers. The high resolving power provides comparison with a current instrument (UCLES) at the AAT (Wylie et al., 2006) and an equivalent instrument, SALT HRS, currently under construction (Buckley et al., 2006). The medium resolving power is the highest achievable with RSS on SALT and comparable to AAOmega's maximum resolving power on the AAT.

Each of Figures 3.2 to 3.7 corresponds to one of the six stellar models shown in the CMD of 47 Tuc in Figure 3.1. For each model the spectral regions from Table 3.1 were synthesised at high ($R \sim 60\ 000$) and medium ($R \sim 10\ 000$) resolving powers. In each spectral region the abundance of the key species was varied with respect to the model abundance. The dash-dot line represents a variation of −8.0 dex, simulating when essentially none of the species, X, is present. The solid line represents no variation of the species abundance from the model ([X/Fe]=0). The dashed line represents a variation of +0.5 dex and the dotted line represents a variation of +1.0 dex.

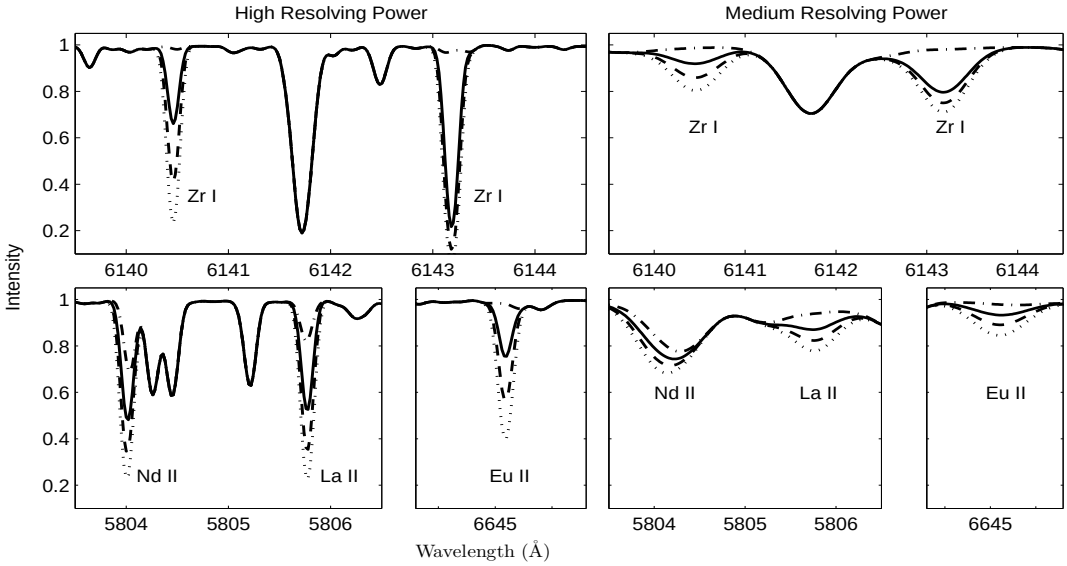

Figure 3.2: GB: $T_{eff} = 4000$ K, $log\ g = 1.0$.

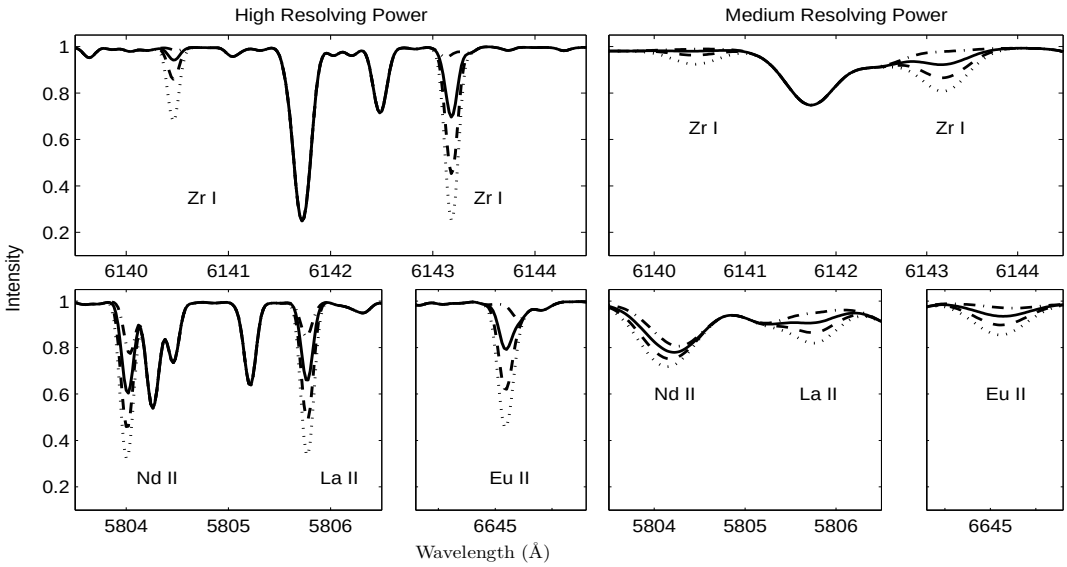

Figure 3.3: GB: $T_{eff} = 4500$ K, $log\ g = 1.5$.

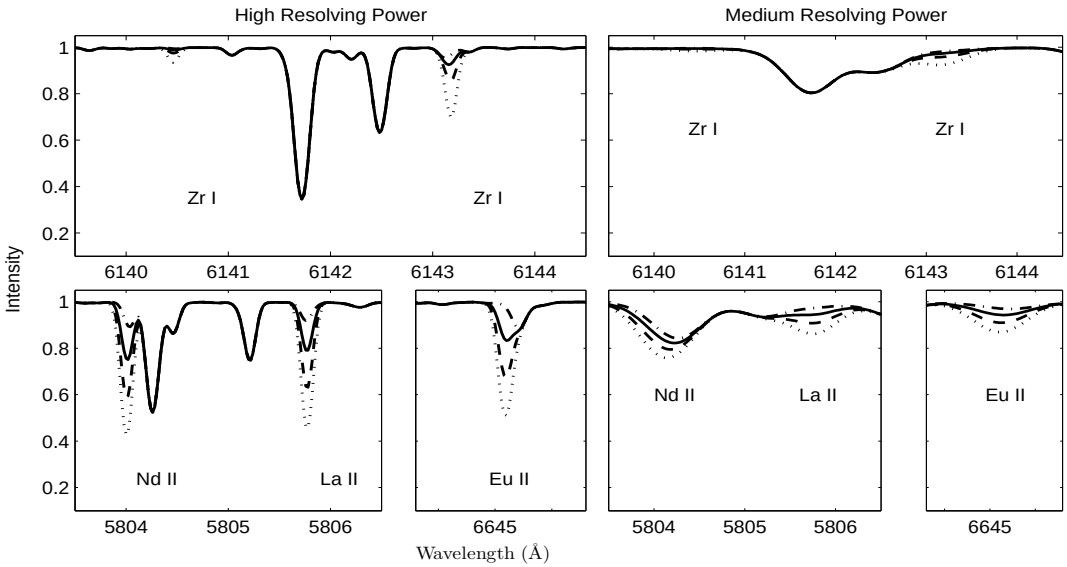

Figure 3.4: GB: $T_{eff} = 5000$ K, $log\ g = 2.0$.

By comparing the spectral regions between the models, and between the two resolving powers, the changes in line strength for the different species are very clear. The following analysis focuses on four effects observed in these comparisons.

3.2.1 Temperature & gravity effects on GB

Figures 3.2, 3.3 and 3.4 show the synthesised spectra for the three points on the various giant branches. The progression from the tip down the giant branch involves an increase in both T_{eff} and *log g*.

Comparing first the high resolving power synthesis for each model, both the neutral (Zr I) and ionised lines (La II, Nd II, Eu II) show a decrease in line strength down the giant branch. However the ionised lines are much less affected than the neutral lines. This is expected as the increased temperature is ionising the element, increasing the number of atoms contributing to the ionised lines and decreasing the number of contributors to the neutral lines. The increased temperature leads to an increase in the number of free electrons, increasing the H^- continuous opacity, which weakens both line species.

The increased pressure (increased *log g*) has more complicated effects as the neutral dominated populations are changing to ionised dominated populations due to the increased temperature. Initially the neutral lines will weaken with the increase in pressure, but as the population becomes ionised the effect becomes negligible. The ionised lines will initially weaken considerably with the increased pressure, but as the population becomes ionised this effect will lessen. Further exploration of temperature changes, and pressure changes, will allow comparison of the relative significance of temperature and pressure on line strength.

The key observable in this sequence is the weakening of Zr I lines as the temperature and pressure increase, while the La II, Nd II and Eu II lines are less affected. The medium resolving power synthesis echoes the above changes in line strength outlined for the high resolving power. All the features are identifiable and distinguishable at the +0.5 dex level, although the Zr I lines at the highest temperature have weakened considerably and would not be of use as Zr abundance indicators at medium resolving power.

The synthetic spectra along the giant branches show that abundance analysis at medium resolving powers is feasible, although as the temperature increases ionised lines will be the best candidates for analysis.

3.2.2 Temperature limit: SG

The spectra in Figure 3.5 were synthesised at *log g* = 3.5 and T_{eff} = 5500 K, the hottest model considered. Progressing from Figure 3.4, the increased temperature causes increased ionisation which strengthens the ionised lines due to the increased number of contributors.

There are two line weakening effects at work. First, the increase in continuous opacity due

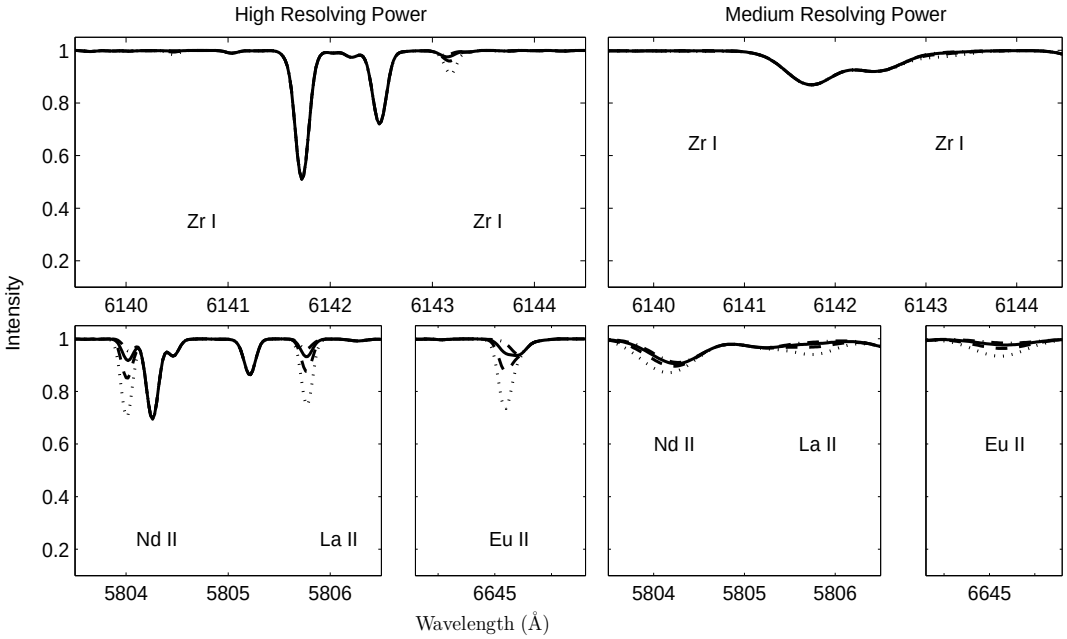

Figure 3.5: SG: $T_{eff} = 5500$ K, $log\ g = 3.5$.

to the increased ionisation, and second, the high pressure to which the ionised line strengths are now sensitive due to the element line and population being in the same ionisation state. Overall Figure 3.5 shows that the line strength of the ionised lines has reduced significantly in the high and medium resolving powers for the SG spectrum.

The effect on the neutral lines is much more dramatic. The increased ionisation and continuous opacity combine together to weaken the neutral lines. However, as the population is in the next higher ionisation state, the neutral lines are insensitive to pressure and so there is no weakening due to the increased pressure. Overall there is no effect strengthening the lines and they diminish considerably under the high temperature. In the high resolving power spectra the neutral lines are almost non-existent while in the medium resolving power spectra they have completely disappeared.

At this temperature, high resolving power spectra would be necessary to determine *s*-process elemental abundances. Only one Zr I feature remains visible, although considerably diminished. The abundance variations of the La II, Nd II and Eu II lines are still distinguishable in the high resolving power. For the medium resolving power the Zr I line has disappeared and the ionised lines are distinguishable only to the extent that upper limits on the abundances would be possible for SG stars.

3.2.3 Temperature effects on MS

Figures 3.6 and 3.7 show the synthesised spectra for the two points on the main sequence. The models have the same *log g* value, so there is no changes in pressure between the models, but the T_{eff} is lower for the point further down the MS. The differences in line strength between the models is due to the decrease in temperature. However the pressure

is very high and the change from an ionised to neutral dominated population increases the pressure sensitivity of both the ionised lines and neutral lines.

In the progression from the SG model (Figure 3.5) to the first MS model (Figure 3.6) the neutral lines start to experience the weakening effects of the high pressure as the population returns to being neutral dominated. However the decreased temperature means decreased ionisation and a decrease in continuous opacity. This acts to strengthen the neutral lines as there will be more neutral contributors available. This effect is most obvious in the progression further down the MS from Figure 3.6 to Figure 3.7. The Zr I features have become very pronounced in the lower temperature model.

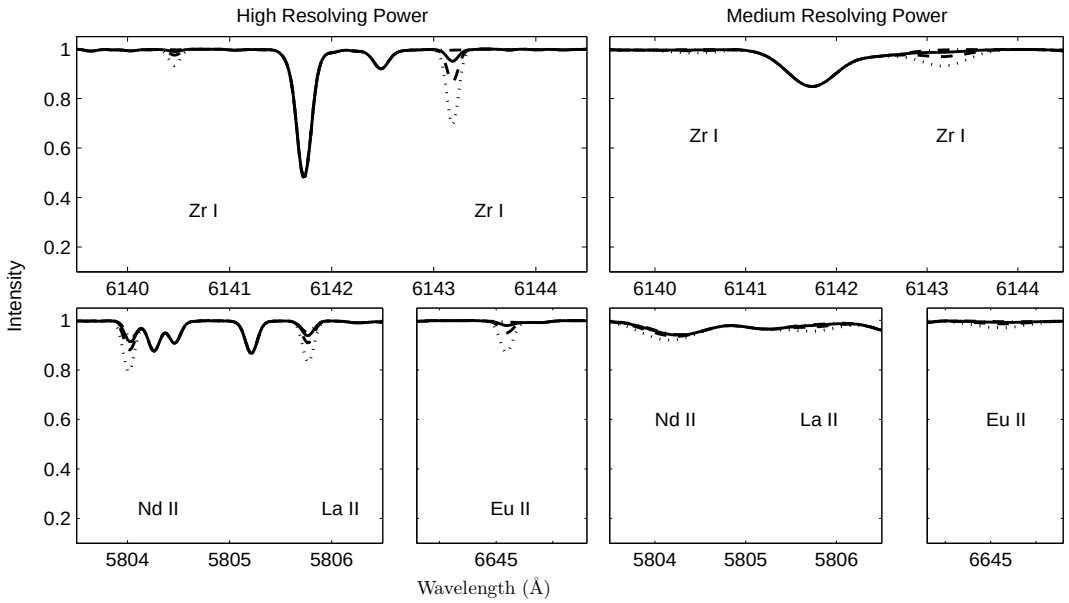

Figure 3.6: MS: $T_{eff} = 5000$ K, $log\ g = 4.5$.

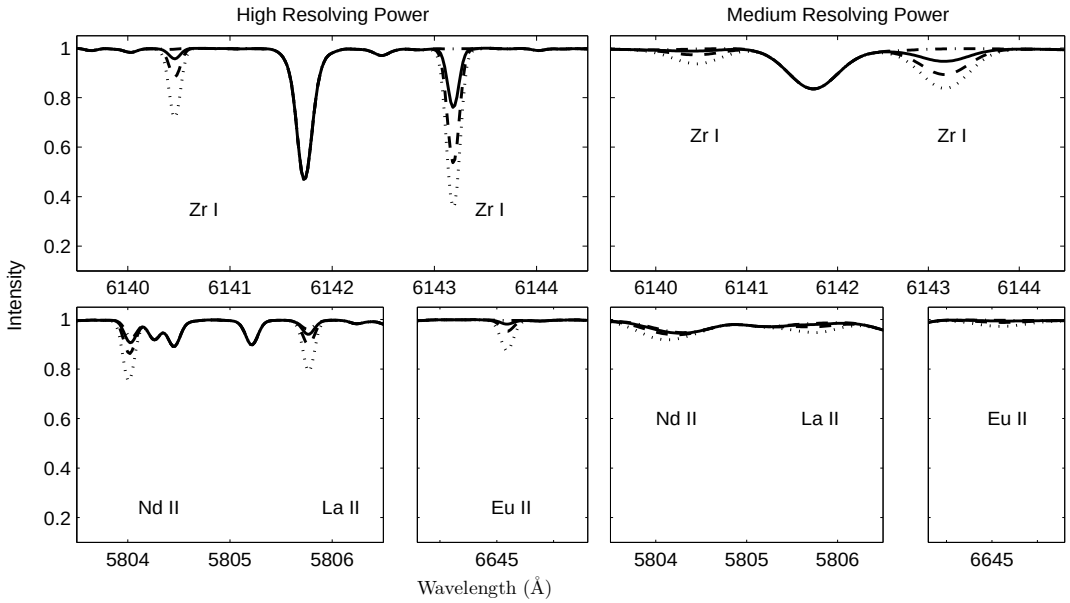

Figure 3.7: MS: $T_{eff} = 4500$ K, $log\ g = 4.5$.

The decreased continuous opacity also strengthens the ionised lines. However the reduction in ionised contributors, as the population becomes neutral dominated, simultaneously weakens the ionised lines. In the neutral dominated population the ionised lines become much more sensitive to the pressure than when the population was dominated by the ionised state of the species. The comparison between Figures 3.6 and 3.7 shows that overall there is some strengthening of the ionised lines due to the decrease in temperature but the strong pressure ensures it is a small effect.

This comparison indicates that neutral lines are the best candidates for abundance analysis of MS stars in both the high and medium resolving powers. The 6143 Å Zr I line is particularly strong. The ionised lines are very weak at high resolving power and even significant enhancements would be unobservable at medium resolving power. The resolving power of SALT HRS ($R \sim 60\,000$) will be required to test the hypothesis of intrinsic MS *s*-process element enhancements using these features.

3.2.4 Gravity effects: GB to MS

The synthesised spectra in Figures 3.4 and 3.6 (and separately Figures 3.3 and 3.7) have the same T_{eff} but different *log g* values. Comparing the hotter models, the increase in pressure from the GB to the MS weakens the ionised lines dramatically but, as the dominant population is in a higher state than the neutral lines, there is very little weakening of the neutral lines.

Comparison of the cooler models shows the same effect, although the decreased temperature corresponds to slightly stronger ionised lines as discussed above. This shows that, although temperature sensitivity dominates line strength variations, the high pressures on the MS make ionised lines unusable for abundance analysis at medium resolving power. Neutral features, such as the Zr I line at 6143 Å, would still provide a discriminant.

The success of using either RSS or AAOmega for the 47 Tuc survey is dependent upon selecting *s*- and *r*-process lines that are visible at medium resolving power for each of the different evolutionary stages.

This analysis shows that abundances for light and heavy *s*-process, and *r*-process elements should be able to be measured for stars on the giant branch to temperatures below the horizontal branch provided their enhancements are at the level ($\geq$ +0.5dex) indicated by Wylie et al. (2006). On the main sequence these abundances could also be measured for stars with sufficiently low temperatures. However the main limiting factor on those stars will be their brightness.

The SALT RSS limiting magnitude is expected to be $\sim$ 22 mag. For AAOmega observations of 47 Tuc stars the magnitude limit is $\sim$ 16 mag, which falls below the horizonal branch. Figure 3.8 shows the apparent magnitude limits of current (solid line) and future (dashed line) samples of 47 Tuc stars from high and medium resolving power instruments

on SALT and the AAT.

Observations of 47 Tuc using either AAOmega or RSS will be able to encompass the giant branches of that cluster. This will provide the opportunity to test whether there is evidence for TDU in 47 Tuc AGB stars by comparing their spectra to RGB spectra, which definitely do not experience TDU.

The exploration of the $T_{eff} - log\ g$ space in terms of line strength has significantly refined the line selection process for the abundance survey. The analysis shows that neutral lines are observable over a greater range of *log g* values than the ionised lines, but within a smaller range of T_{eff} values. Conversely the ionised lines are observable over a greater range of T_{eff} values than the neutral lines, but within a smaller range of *log g* values. This broadens the range of temperatures and gravities from which the survey star sample will be selected.

The characteristics of the instruments under consideration further limit the stellar sample. The medium resolving power of RSS and the magnitude limit of SALT do reduce the sample

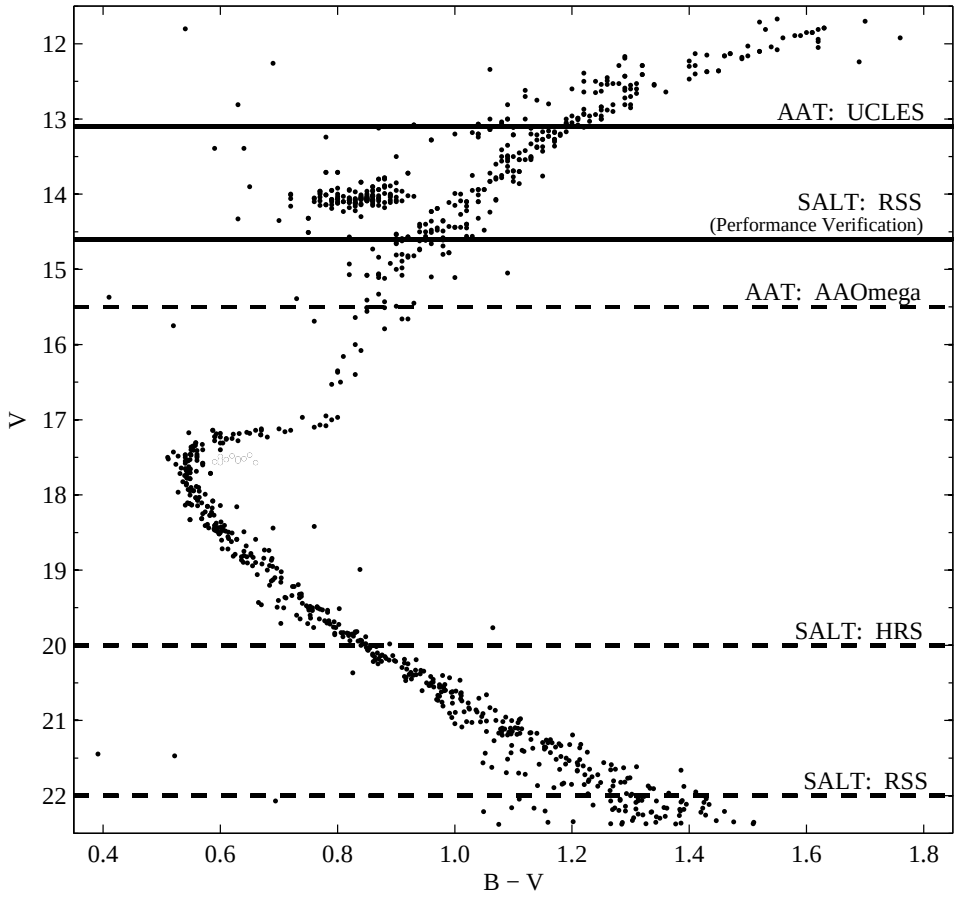

Figure 3.8: Telescope and instrument V limits on the 47 Tuc CMD. Both RSS on SALT and AAOmega on the AAT can observe the giant branches, though the main sequence is best observed using RSS on SALT.

options with regards to the MS. There is a small range on the MS where the temperatures are cool enough and the magnitudes are bright enough that abundances could be obtained using RSS. However, *s*-process element abundance analysis to just below the horizontal branch, which this analysis shows is quite possible using RSS or AAOmega, will provide definitive results on the nature of *s*-process element abundance variations in 47 Tuc. This is discussed in Section 3.3 for SALT RSS and in Chapter 4 for the AAOmega data.

This type of line strength feasibility study can be carried out for other GCs over a range of metallicities. These study could then be followed up in a series of medium resolution surveys in order to investigate *s*-process elemental abundance variations in GCs. This would be instrumental in determining what general and specific heavy element characteristics exist in these stellar systems.

3.3 SALT-RSS performance verification observations

In June and October of 2006 spectra for eleven giant branch stars in 47 Tuc were obtained during the performance verification (PV) commissioning stage of RSS on SALT. The camera settings used to obtain two overlapping wavelength regions are stated in Table 3.2.

Table 3.2: Camera Specifications for SALT-RSS performance verification (PV) observations.

Filter	Grating	Angle	Art	Region (Å)
PC04600	PG2300	48	96.26	6020 - 6860
PC04600	PG2300	41	82.01	5200 - 6150

These regions contain the key *s*- and *r*-process lines that were considered in the theoretical line strength analysis (see Section 3.2). The resolution obtained for these spectra was $R \sim 5,000$, although the maximum obtainable with RSS is expected to be $R \sim 10,000$. Signal to noise ratios per pixel between 50 and 140 were obtained.

Table 3.3 presents the effective temperatures and surface gravities for each star that were calculated from the stellar apparent magnitudes and colour indices using the calibration equations from Alonso et al. (1999). Giant branch classifications from Norris & Freeman (1979) have been included where possible.

Figure 3.9 shows the location of the eleven stars on the 47 Tuc CMD. The majority of the stars fall on the RGB, while the two stars classified as AGB clearly do fall on the AGB. The second star at the AGB tip is Lee 1513 which has been classified as an RGB.

Table 3.3: T_{eff} and *log g* derived from V and $B-V$ using calibration equations from Alonso et al. (1999) for each of the SALT-RSS PV Stars.

Lee No.	V	B-V	T_{eff} (K)	*log g*	AGB/RGB[a]
3512	11.79	1.63	4080	0.7	-
1513	12.41	1.32	4450	1.3	RGB
2525	12.43	1.29	4490	1.4	AGB
6519	12.81	1.27	4520	1.5	RGB
6524	13.08	1.21	4610	1.7	RGB
1506	13.27	1.15	4700	1.9	RGB
3510	13.63	1.09	4800	2.1	-
2604	13.07	1.04	4890	1.9	AGB
4514	14.35	0.98	5000	2.5	-
4515	14.49	0.98	5000	2.5	-
4513	14.59	0.98	5000	2.6	-

[a] Classification from Norris & Freeman (1979)

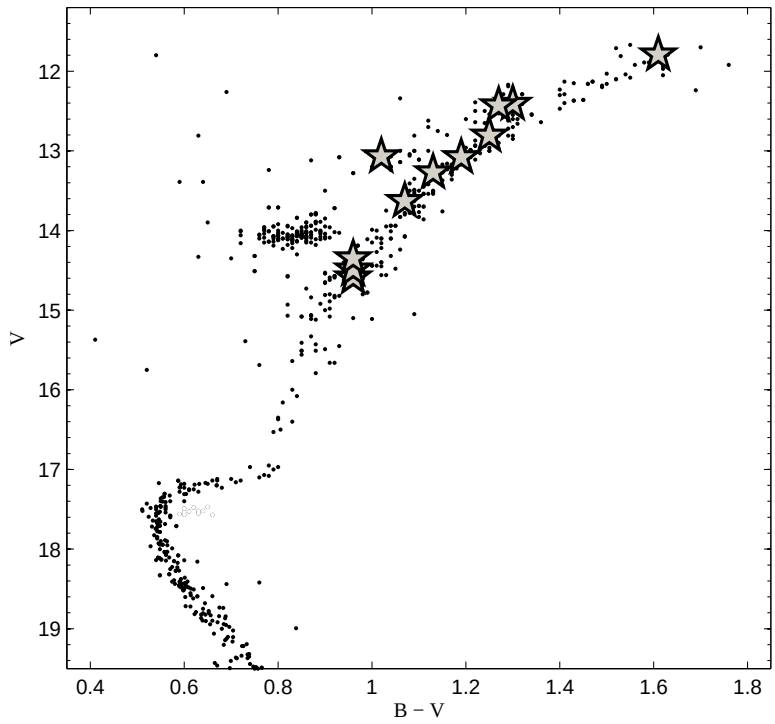

Figure 3.9: SALT-RSS PV stars on 47 Tuc CMD. The AGB/RGB classifications from Norris & Freeman (1979) agree with their placement on the CMD.

3.3.1 Temperature Sensitivity

Figure 3.10 shows both the observed spectra of the eleven stars and the synthesised spectra in the key Zr I region. As for Figures 3.2 to 3.7, the dash-dot line of the synthetic spectra indicates none of the species is present, the solid line indicates that the model abundance, the dashed line indicates +0.5 dex enhancement and the dotted line indicates +1.0 dex enhancement. The temperatures for each star are those listed in Table 3.3.

The spectra are presented with the temperature increasing down the panel, replicating the traverse down the giant branch. This region contains two Zr I features and one Ba II feature. The vertical lines trace these line locations in each spectrum.

In the coolest stars the neutral Zr features are quite distinct and, while growing weaker with increasing temperature, are apparent until a temperature of around 5000 K. The ionised Ba line, while it does weakens slightly, remains apparent through to the hotter temperatures.

This nicely replicates the theoretical analysis, showing the more dramatic weakening of neutral lines compared with ionised lines. It also is a good illustration of temperature sensitivity. The strength of the Zr I features provides a temperature scale that confirms the scale derived from the Alonso et al. (1999) equations. The temperature sensitivity is replicated in the synthetic spectra.

Figure 3.11 is a similar presentation of the key Nd II and Eu II features. In the observed spectra the Nd II features are very weak and not distinguishable above the noise for most of the spectra. In the synthesised spectra the Nd II and Eu II show a gradual decrease in strength with increasing temperatures as is expected. The Nd II lines would need to be enhanced by +1.0 dex to be measured at the hottest temperatures but the Eu II feature is still visible to the +0.5 dex limit.

3.3.2 Abundance analysis: Zr, Ba, La & Nd

Figures 3.12 and 3.13 present an abundance analysis of the two key spectral regions. Figure 3.12 shows the synthetic spectra overlaid onto the observed spectra for the Zr region for four of the stars. The stars were selected to represent the range of temperatures in the sample. The error bars give an indication of the uncertainty due to noise in these spectra. The location of each of the key spectral lines is indicated by a vertical line through the sequence of spectra.

The coolest star provides the best detail for analysis of each of the key spectral lines. The Zr features are prominent, again traced out by the vertical line. In terms of abundance this spectra best fits the model synthesis, indicating no Zr enhancement. The Ba also fitted best by the model synthesis.

For the next two spectra, both with $T_{eff} \sim 4500$ K, an enhancement of Zr to a +0.5 dex level is indicated, although the error does also bring these within the model abundance.

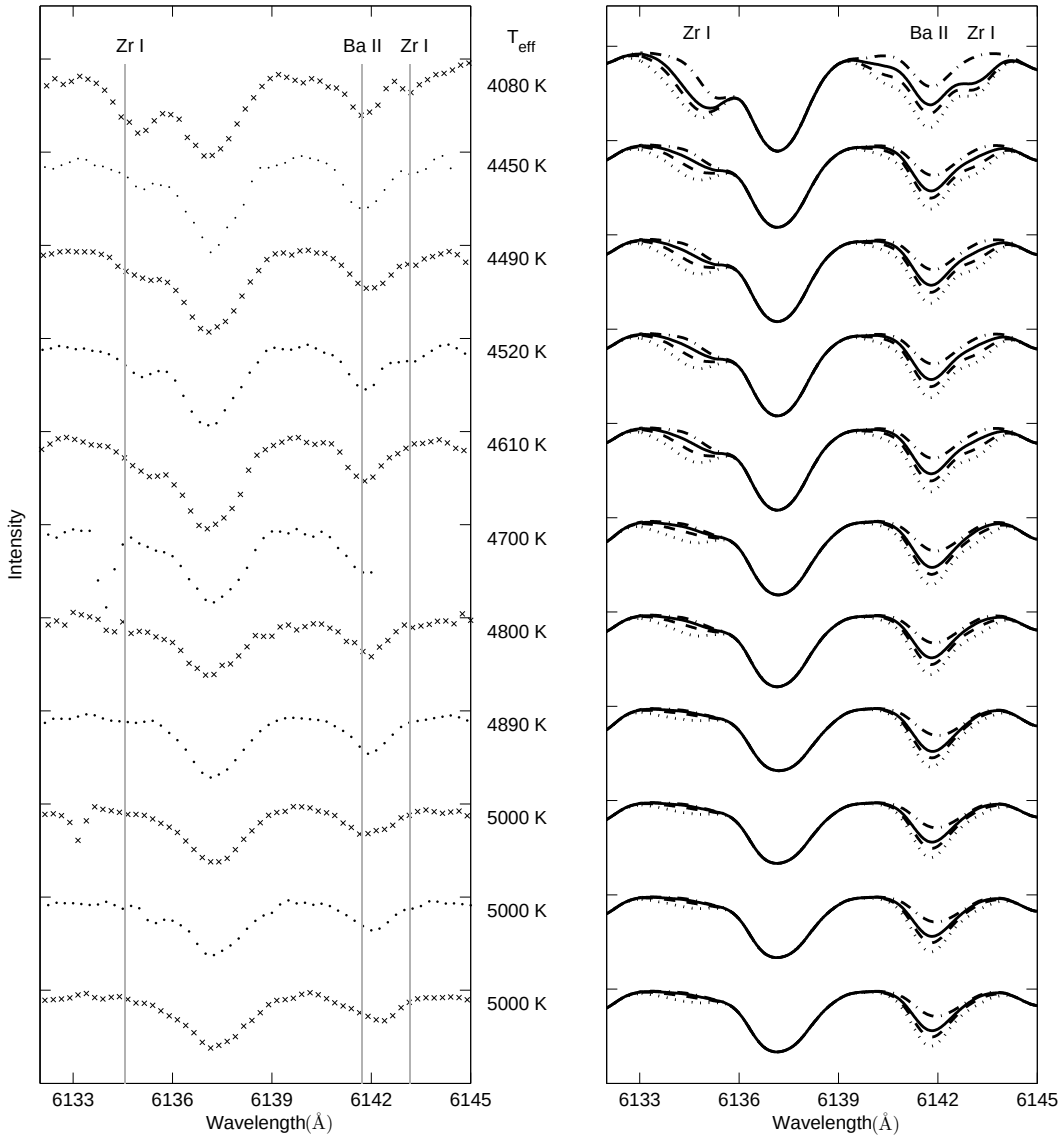

Figure 3.10: Temperature sensitivity in the Zr I and Ba II line region. Left: Observed spectra with key lines indicated. Right: Corresponding synthesised spectra with abundance variations of [Zr,Ba/Fe] = −8.0 dex (dash-dot line), [Zr,Ba/Fe] = 0.0 dex (solid line), [Zr,Ba/Fe] = +0.5 dex (dash line) & [Zr,Ba/Fe] = +1.0 dex (dotted line).

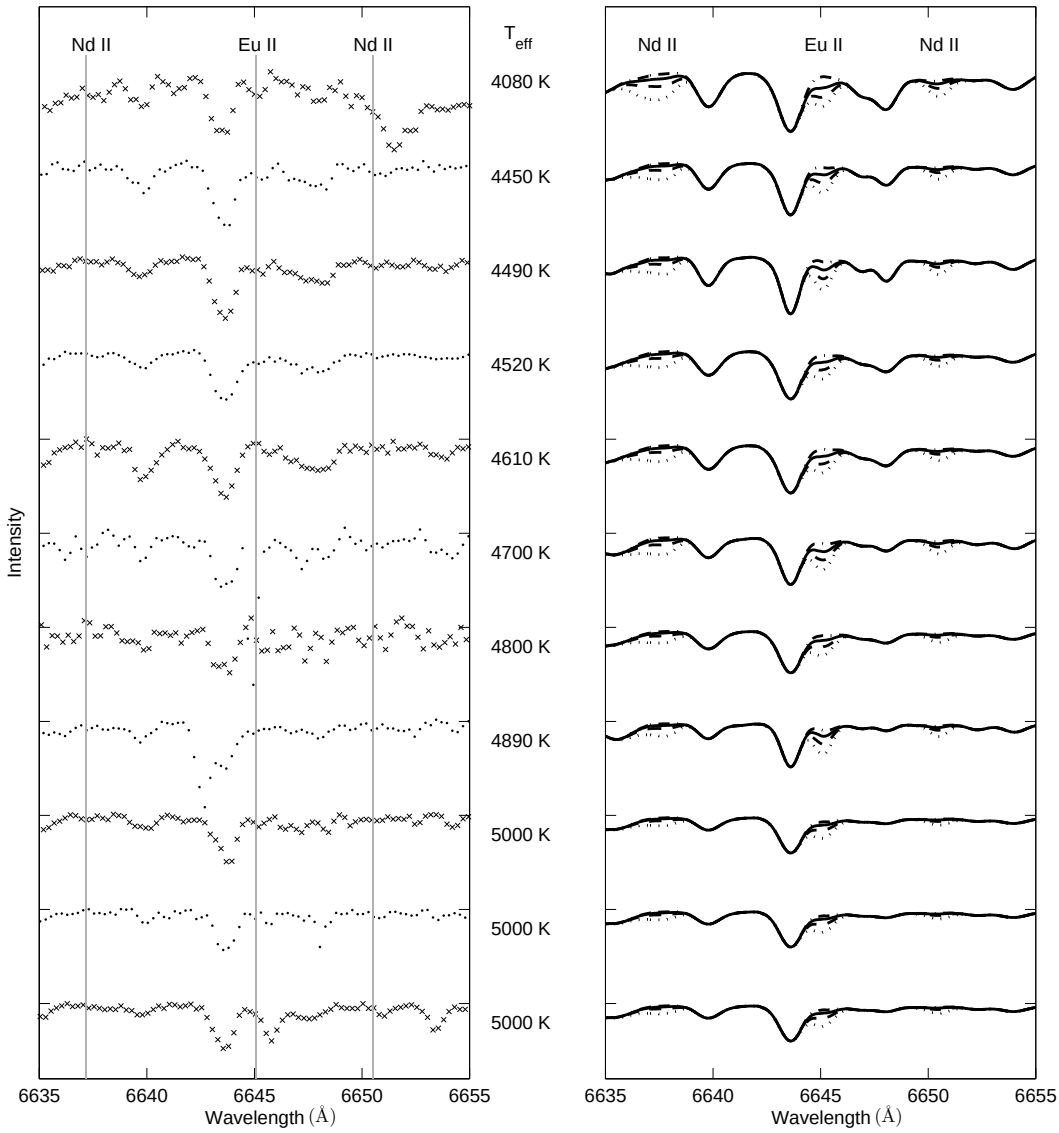

Figure 3.11: Temperature sensitivity in the Nd II and Eu I line region. Left: Observed spectra with key lines indicated. Right: Corresponding synthesised spectra with abundance variations of [La,Nd/Fe]= −8.0 dex (dash-dot line), [La,Nd/Fe]= 0.0 dex (solid line), [La,Nd/Fe]= +0.5 dex (dash line) & [La,Nd/Fe]= +1.0 dex (dotted line).

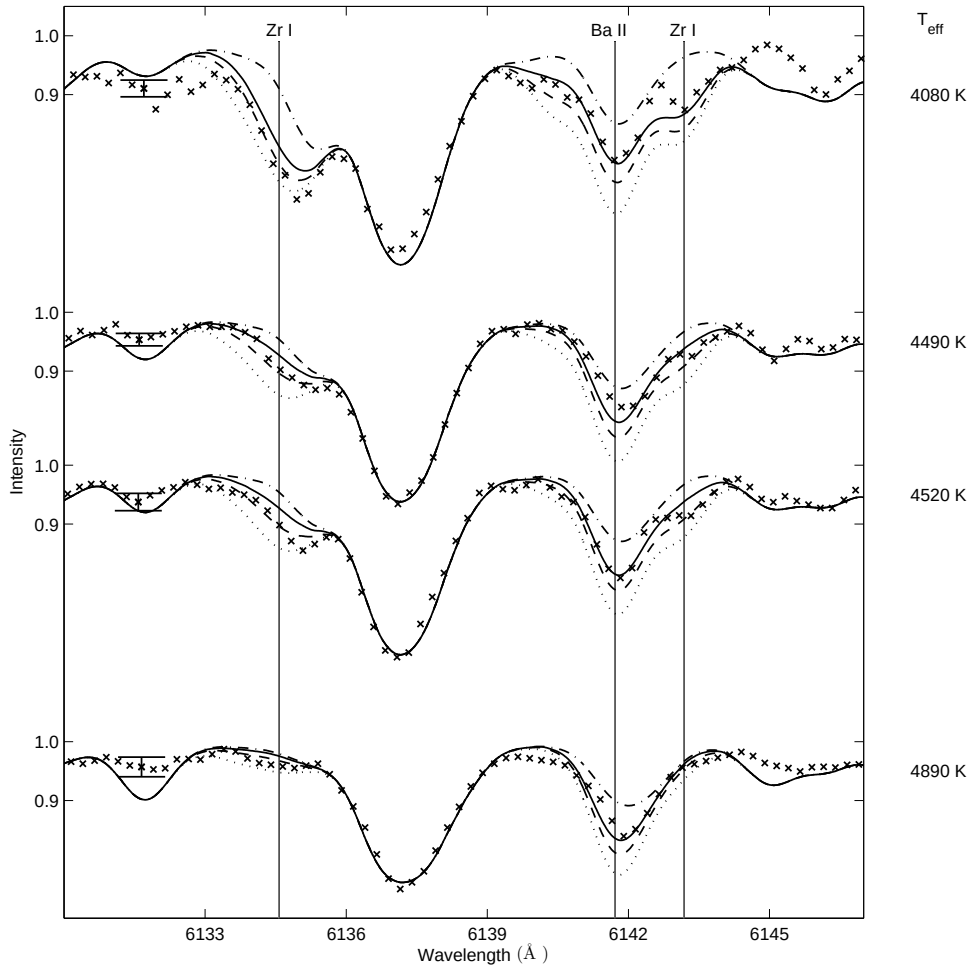

Figure 3.12: Observed abundances for the Zr I and Ba II lines. Synthesised spectra are overlaid on the observed spectrum with abundances varied by [Zr,Ba/Fe] = −8.0 dex (dash-dot line), [Zr,Ba/Fe] = 0.0 dex (solid line), [Zr,Ba/Fe] = +0.5 dex (dash line) & [Zr,Ba/Fe] = +1.0 dex (dotted line).

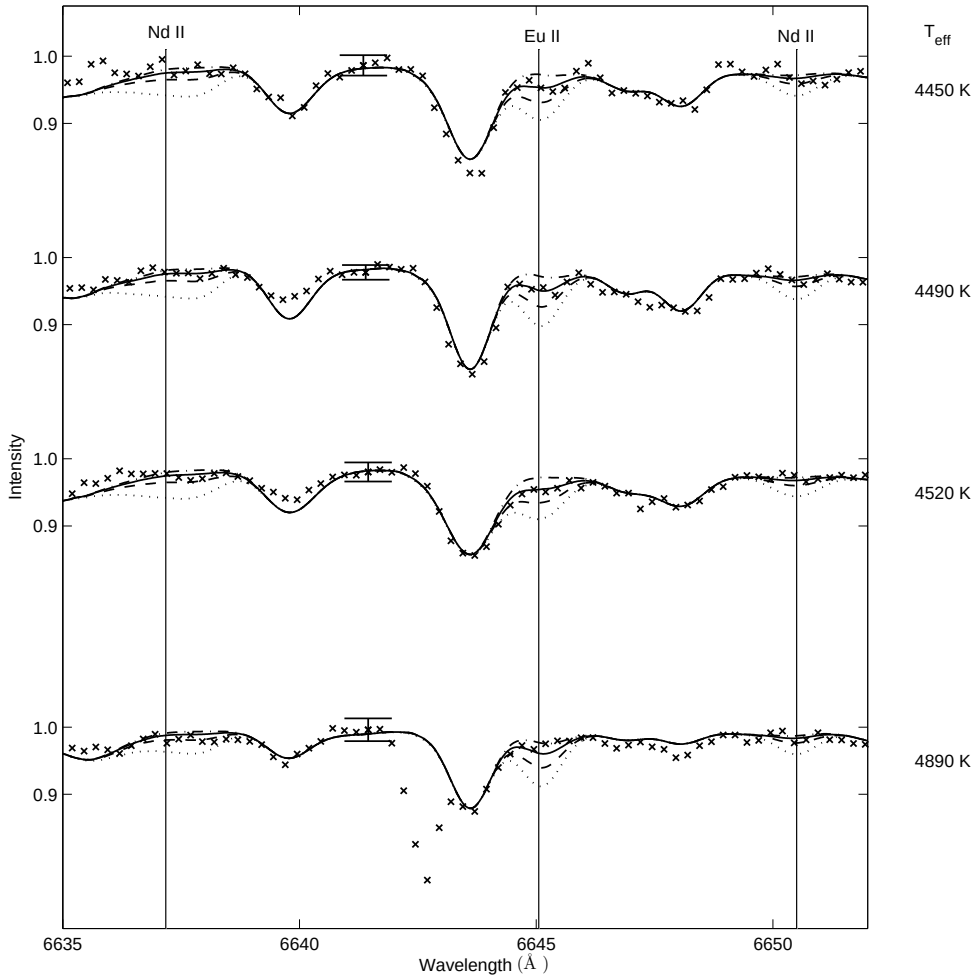

Figure 3.13: Observed abundances for the Nd II and Eu I lines. Synthesised spectra are overlaid on the observed spectrum with abundances varied by [La,Nd/Fe] = −8.0 dex (dash-dot line), [La,Nd/Fe] = 0.0 dex (solid line), [La,Nd/Fe] = +0.5 dex (dash line) & [La,Nd/Fe] = +1.0 dex (dotted line).

The spectra of the three hottest stars, which were not included in the figure, show that the Zr I features have diminished too much to observe any abundance variations. The Ba II feature is still prominent but the noise levels of these spectra do not give a convincing argument for anything other than the model abundance. In summary this sample of stars agree with a model abundance ([Zr/Fe]= 0.0 dex) with the extreme uncertainty giving [Zr/Fe]= +0.5 dex. The Ba II line also shows good agreement to the model abundance ([Ba/Fe]= 0.0 dex).

Figure 3.13 presents a similar abundance analysis of the Nd II/Eu II region. Even for the coolest star the Nd II features are too weak to be measured. The Eu II feature is more promising for the cooler stars at $T_{eff} \sim 4500$K as there is some evidence of enhancement. However, it is also in agreement with the model abundance within the uncertainties. As the stars get hotter this feature diminishes in strength and the noise levels increase such that only the model abundance provides a reasonable fit within the uncertainties. As such this sample of stars show model abundances for both Nd and Eu ([Nd/Fe]= 0.0 dex, [Eu/Fe]= 0.0 dex).

3.4 Conclusion

The *s*-process elemental abundance analysis of these spectra shows there may be enhancements in Zr for the cooler stars but the uncertainties puts this within the model abundance. Overall no enhancements in the *s*-process elemental abundances were found for this sample of 47 Tuc giant stars. However, upper limits could be placed on the Zr abundances of [Zr/Fe] = +0.5 dex. These spectra were not obtained at the maximum operating resolution for which RSS has been designed. Future observations at the maximum resolution of $R \sim 10,000$ will provide greater detail and a more realistic limit on the capabilities of this medium resolution instrument.

The line strength analysis shows that the success of using either RSS for the 47 Tuc survey is greatly enhanced by selecting *s*- and *r*-process lines that are visible at medium resolving power for each of the different evolutionary stages. The optimum line list for the MS may differ to that for the GB in order to take advantage of the effects of T_{eff} and $log\ g$ on the line strengths of ionised and neutral lines.

In the next chapter we will explore these ideas with AAOmega data observed on the AAT. The nature of these data, with blue and red wavelength data available simultaneously, provide additional opportunities

Chapter 4

Medium-resolution *s*-process element survey of 47 Tuc: AAOmega

The analysis of the medium-resolution SALT PV RSS stars has shown that heavy elemental abundances can be obtained above a limit of +0.5 dex using medium-resolution spectra. The survey of 47 Tuc was carried out on AAOmega to pursue these limits further with a larger sample of stars at slightly higher resolution. The choice of lines that were selected for observation in the survey was based on the analysis in the previous chapter, although the stellar sample was restricted to only those stars on the giant branches of 47 Tuc. Hence both neutral and ionised species of the elements could be observed with the expectation of being able to derived elemental abundances from either species.

This survey was carried out in service time observing and so the survey was limited to one set of targets for observation. The stars were selected so as to capture both AGB objects at the tip of the RGB and RGB objects below the horizontal branch. The target list included stars from previous studies in order to provide a comparison with previous results. The blue and red camera configuration of AAOmega allows observation of two distinct wavelength regions simultaneously. The wavelength regions for this survey were selected in the red to include key *s*-process features, and in the blue to include the CN and CH molecular bands at 4216 Å and 4315 Å. Several light element features were also included in the red wavelength region which provided the opportunity to investigate light elemental abundances as well.

4.1 Observations

In October 2008 ninety-seven giant stars in 47 Tuc were observed using AAOmega on the AAT (Sharp et al., 2006). The target stars were selected from the key studies this work is referencing: Lee (1977); Paltoglou & Freeman (1984); Brown & Wallerstein (1992); Wylie et al. (2006); and Worley et al. (2008). Photometry was provided through private communication with Gary Da Costa and Frank Grundahl and was derived where possible from the above papers. The co-ordinates of the sample were verified using 2MASS where J and K

magnitudes were also obtained.

Figure 4.1 shows the location of the 47 Tuc survey stars in RA and Dec about the cluster centre. The stars were selected so as to maximise the 2 degree field available on the AAT. The location of the stars from the SALT PV RSS observations analysed in Chapter 3 are indicated as well as the stars from Brown & Wallerstein (1992) and Wylie et al. (2006). The location of Lee 2525, in particular, is also shown. The star selection for the survey included many of the stars from these samples.

Figure 4.2 shows the location of these same stars in the V-$(B-V)$ colour-magnitude diagram (CMD). The mask configurations for AAOmega restricted stars to within a 2 magnitude range. In order to obtain stars on the tip of the AGB and on the RGB below the HB, the range of magnitudes for this survey was $12.5 \leq V \leq 14.5$. Hence there were stars that could not be observed from both Brown & Wallerstein (1992) and Wylie et al. (2006) as they were outside this range.

AAOmega has a red and a blue camera with which stars over two distinct wavelength ranges can be observed simultaneously. The wavelength regions observed for this survey and the key features analysed in each region are listed in Table 4.1. Other features of note, such as Sr II, were not analysed here but will be investigated as part of this ongoing research.

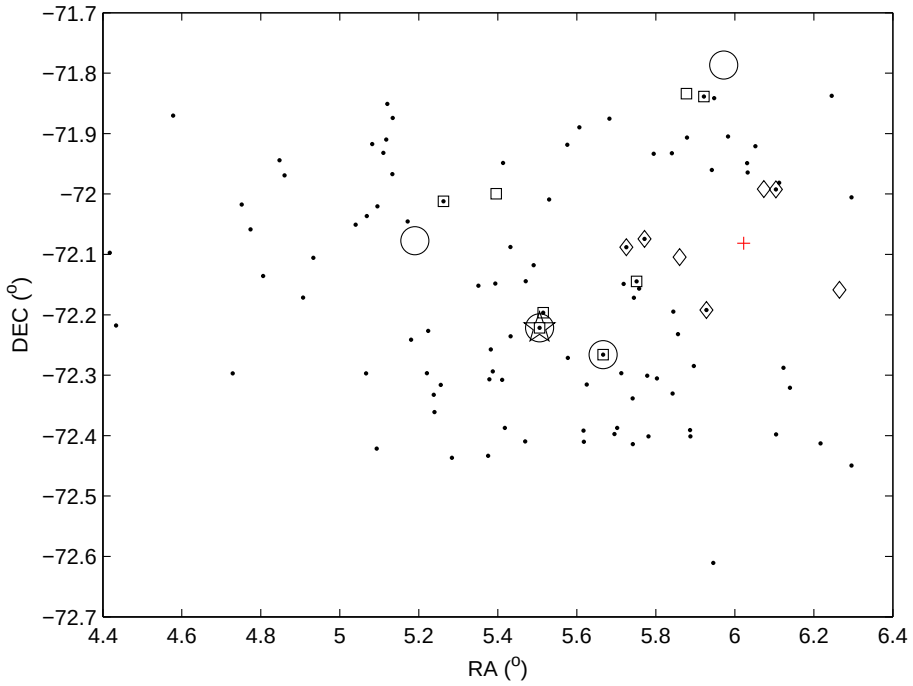

Figure 4.1: Location, in R.A. and Dec., of the 47 Tuc stars observed in the AAOmega medium-resolution survey (•). The stars from Brown & Wallerstein (1992) (◯), Wylie et al. (2006) (◊) and the SALT PV RSS observations of Worley et al. (2008) (□), as well as Lee 2525 (star) are shown. The cluster center is indicated also (+).

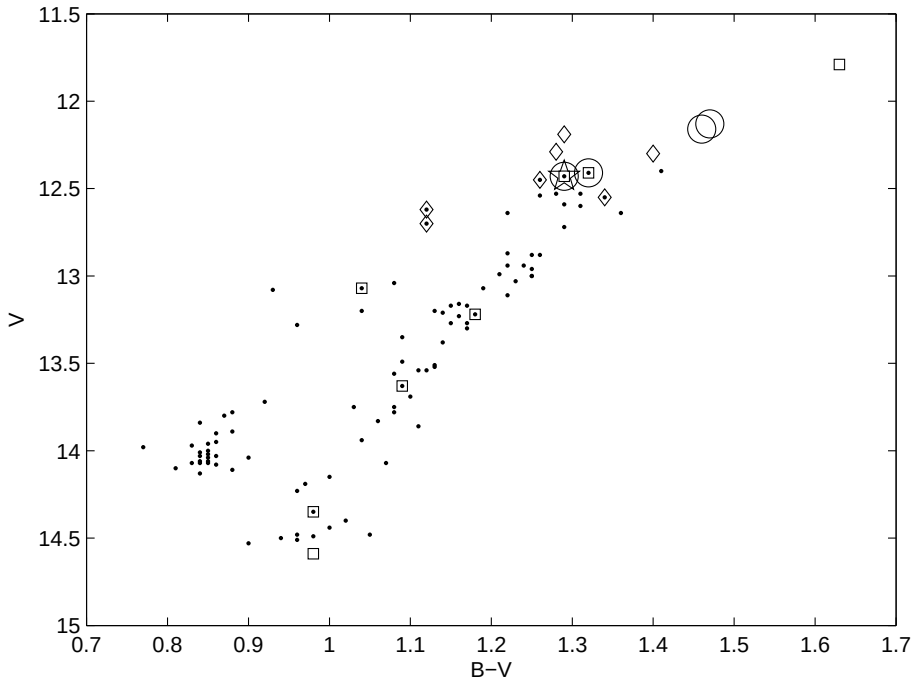

Figure 4.2: Colour-magnitude diagram of the 47 Tuc stars observed in the AAOmega medium resolution survey as for Figure 4.1.

The resolution of the spectra was $R \sim 6500$ and the signal-to-noise (SNR) per pixel ranged from $30 \leq SNR \leq 50$ for the blue arm, and $60 \leq SNR \leq 90$ for the red arm. The reduction of the spectra to the wavelength calibration stage was carried out by the duty observer, Dr. R. Sharp, using the reduction pipeline, 2dFdr.

Table 4.1: Wavelength regions and key spectral features observed in the AAOmega 47 Tuc survey. For the red arm spectra the elements are listed in increasing atomic number.

Camera	Regions (λ)	Grating	Species	Feature wavelengths (Å)
Blue	4040 - 4350 Å	3200B	CN	4142 - 4216
			CH	4305 - 4316 (G Band)
Red	5750 - 6200 Å	2000R	Na I	6154.226, 6160.747
			Fe I	6136.990, 6147.834, 6157.728
			Si I	6131.573, 6131.852, 6145.018, 6155.134
			Ca I	6156.023, 6166.439, 6169.563
			Zr I	6143.183
			Ba II	6141.728
			La II	5805.770
			Nd II	5811.572

The normalisation of the spectra was treated differently for each arm. The key features in the blue arm region are CN and CH bands, which obscure the location of the true continuum. In the red arm the molecular bands are not so prominent for these stellar temperature and so the continuum is not so obscured. In both cases comparison was made to the convolved spectrum of Arcturus but different methods were employed to order to locate the continuum.

4.1.1 Red arm spectra

An initial continuum fitting was carried out in IRAF where a simple spline fit was used in order to remove curvature in the spectra of the red arm. These spectra were then compared with the Arcturus spectrum to further normalise the spectrum.

The high resolution atlas of Arcturus (Hinkle & Wallace, 2005) was convolved using a simple MATLAB code to the same full-width-at-half-maximum (FWHM) as the red arm spectra. Figures 4.3(a) and (b) show the high resolution spectrum of Arcturus in the two key regions for the red arm. Figures 4.3(c) and (d) show the convolved medium resolution spectrum of Arcturus in the same two key regions. The key features for each region are shown. As expected the detail of the convolved spectrum is considerably reduced, although the key lines are sufficiently distinct for determining abundances using spectrum synthesis.

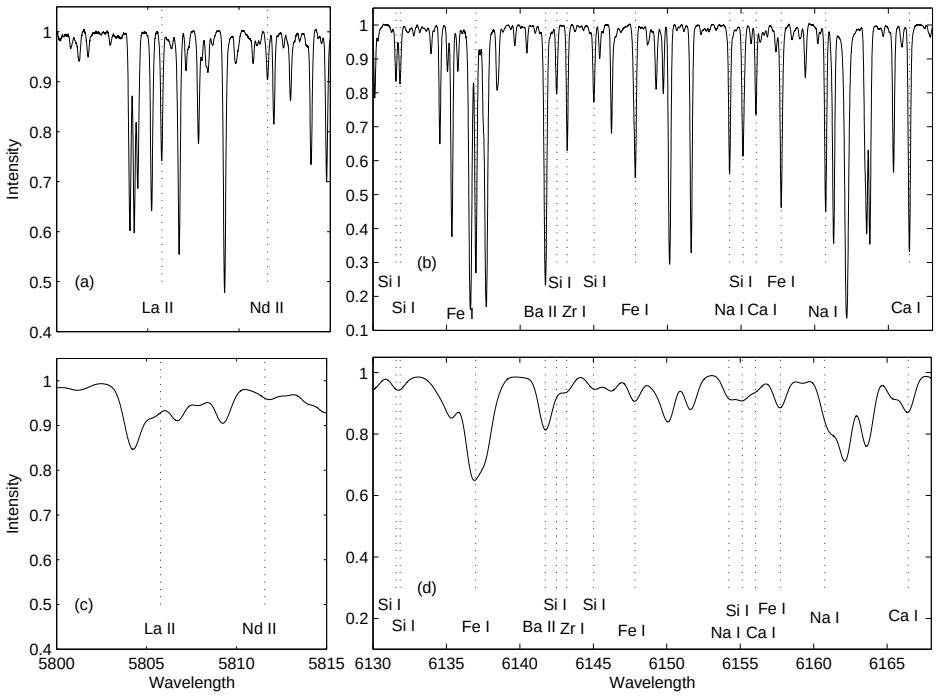

Figure 4.3: The high-resolution Arcturus spectrum was convolved to the same resolution as the hottest of the 47 Tuc survey stars. (a) Region of high-resolution Arcturus spectrum from 5800 Å to 5815 Å showing an La and Nd features. (b) Region of high-resolution Arcturus spectrum from 6130 Å to 6168 Å showing key spectral features. (c) and (d) as for (a) and (b) respectively but showing the convolved medium-resolution Arcturus spectrum.

The convolved Arcturus spectrum was then compared with synthesised spectrum generated using the Arcturus stellar model determined in Chapter 2 and the line list calibrated in Section 2.2.4. The line lists were originally calibrated for the synthesis of the heavy elements only and so for this analysis the line lists were adjusted if necessary to ensure the *log gf* values stated in Table 2.8 were being used for the light element lines. The abundances for each of the key lines were measured by spectrum synthesis for the high- and medium-resolution spectra of Arcturus. The abundances are listed in Table 4.2.

The Ba abundance shows the greatest change between the high-resolution and convolved spectra. The Ba line being measured is a very strong feature that is sensitive to changes in

Table 4.2: Elemental abundances derived from high and medium resolution spectra of Arcturus using spectrum synthesis.

Species	λ (Å)	High Resolution [Fe/H]	Medium Resolution [Fe/H]
Fe I	6136.990	0.22	-
Fe I	6147.834	-0.01	-0.01
Fe I	6157.728	0.07	0.10
	$\langle$[Fe/H]$\rangle$	0.03	0.04
	σ	0.06	0.08
Species	λ (Å)	[X/Fe]	[X/Fe]
Na I	6154.226	0.24	0.10
Na I	6160.747	0.33	0.23
	$\langle$[Na/Fe]$\rangle$	0.29	0.17
	σ	0.06	0.09
Si I	6131.573	0.22	0.28
Si I	6131.852	0.30	0.29
Si I	6145.018	0.25	0.25
Si I	6155.134	0.29	0.34
	$\langle$[Si/Fe]$\rangle$	0.27	0.29
	σ	0.04	0.04
Ca I	6156.023	0.25	0.23
Ca I	6166.439	0.37	0.22
	$\langle$[Ca/Fe]$\rangle$	0.31	0.23
	σ	0.08	0.01
Zr I	6143.180	0.00	-0.08
Ba II	6141.730	-0.26	0.10
La II	5805.773	0.07	0.07
Nd II	5811.572	0.01	-0.04

microturbulence. Lowering the resolution has greatly affected how this line is represented by the stellar model, in particular the microturbulence value. The remaining elements are in reasonable agreement to ≤ 0.10 dex between the high-resolution and convolved spectra. Iron and silicon, in particular, show very little change in abundance due to the convolution. The Ca line at 6166 Å and the two Na lines show a decrease of ≥ 0.1 dex for the convolved spectrum. The Zr and Nd abundance also decrease in the convolved spectrum while the La shows no change. These variations in abundance from the high-resolution spectrum to the convolved medium-resolution spectrum provide a gauge as to which lines will be most problematic for determining the abundances in the observed medium-resolution spectra.

Continuum regions were identified in the medium-resolution Arcturus spectrum about the key lines to be used in the spectrum synthesis (see Table 4.1). These were then used to normalise the spectra of the 47 Tuc survey stars. The continuum regions in Arcturus were measured for their relative height to the continuum at 1 in order to better represent the location of the continuum at medium resolution. Figure 4.4 shows the continuum regions used in each of the key regions. There are subtle differences in the heights of these regions. These ratios were used to reproduce the same relative heights for the continuum regions in the 47 Tuc survey stellar spectra.

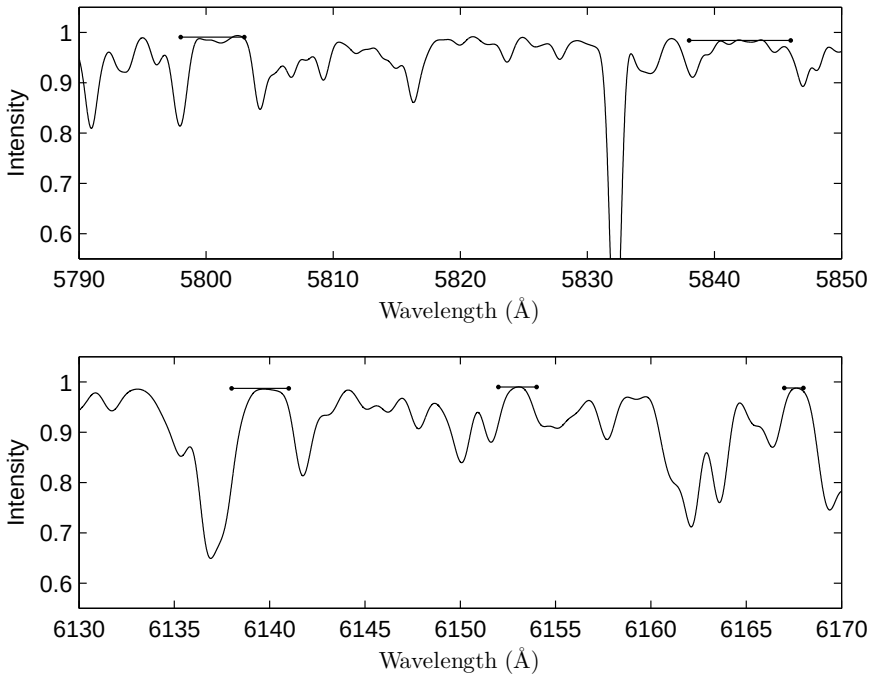

Figure 4.4: Arcturus convolved spectrum and continuum regions (bars) used in the normalisation of the 47 Tuc medium-resolution survey stars for the two key regions used in the spectrum synthesis.

4.1.2 Blue arm spectra

The Arcturus spectrum was again used to ensure appropriate normalisation of the AAOmega spectra. Figure 4.5 compares the high-resolution spectra to the convolved medium-resolution spectra in the region of the CN and CH molecular bands.

Due to the strong molecular bands in the blue arm spectra there were no clear continuum regions that could be used for normalisation. The primary quantity to be measured in this wavelength region is the CN index (see Section 4.2 for definition). The molecular and atomic linelists that are currently available also make spectrum synthesis a valid method of analysis for this region. In this preliminary analysis the CN index was used to determine CN band strength but the analysis is on going and spectrum synthesis of these regions will also be investigated.

One advantage of using CN indices is that the exact location of the continuum is not required as it is the difference between the strength of the molecular band region and the strength of the off-band region that is being measured. The section in common to both the on- and off-band regions is effectively canceled out. However, removing the shape of the

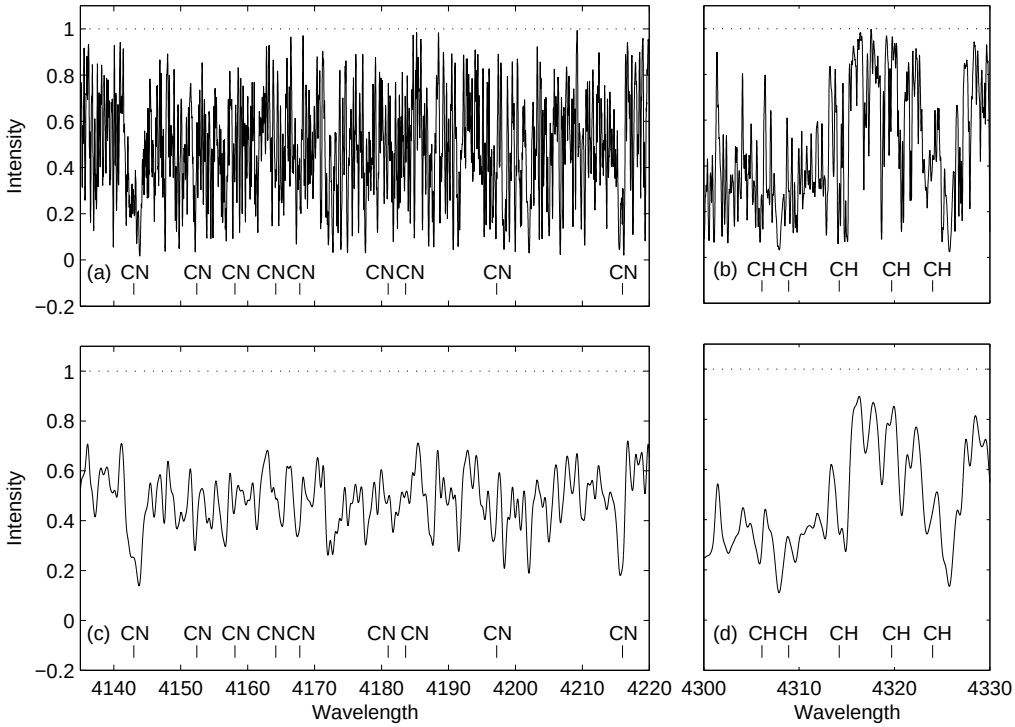

Figure 4.5: The high-resolution Arcturus spectrum was convolved to the same resolution as the hottest of the 47 Tuc survey stars. (a) Region of high-resolution Arcturus spectrum from 4135 Å to 4220 Å showing the CN molecular band. (b) Region of high-resolution Arcturus spectrum from 4300 Å to 4330 Å showing the CH molecular band. (c) and (d) as for (a) and (b) respectively but showing the convolved medium-resolution Arcturus spectrum.

instrument profile was pursued.

The spectrum of the hottest star in the survey, Lee 2311, was used to determine a continuum profile. This profile was divided out of all the spectra in order to remove residual curvature due to the instrument profile. Figure 4.6 illustrates the process. In Figure 4.6(a) the medium-resolution Arcturus spectrum is shown with the locations of the three pseudo-continuum regions used to to determine the continuum profile. In Figure 4.6(b) the raw and normalised spectrum of Lee 2311 is shown. Lee 2311 is the hottest star in the survey, with $T_{eff} \sim 5500$ K, and at this temperature the molecular bands in this region have minimal strength. The residual curvature in the raw spectrum is predominantly due to the instrument profile. The continuum profile shown in Figure 4.6(b) was determined using the pseudo-continuum regions in Arcturus and finding the relative heights of each region such that the spectrum of Lee 2311 was flattened. This profile was then used to normalise all the spectra in the survey. The wavelength region from 4100 Å to 4350 Å for each of the stars in the 47 Tuc survey are displayed in Appendix B. The high density of CN and CH bands in this region is shown.

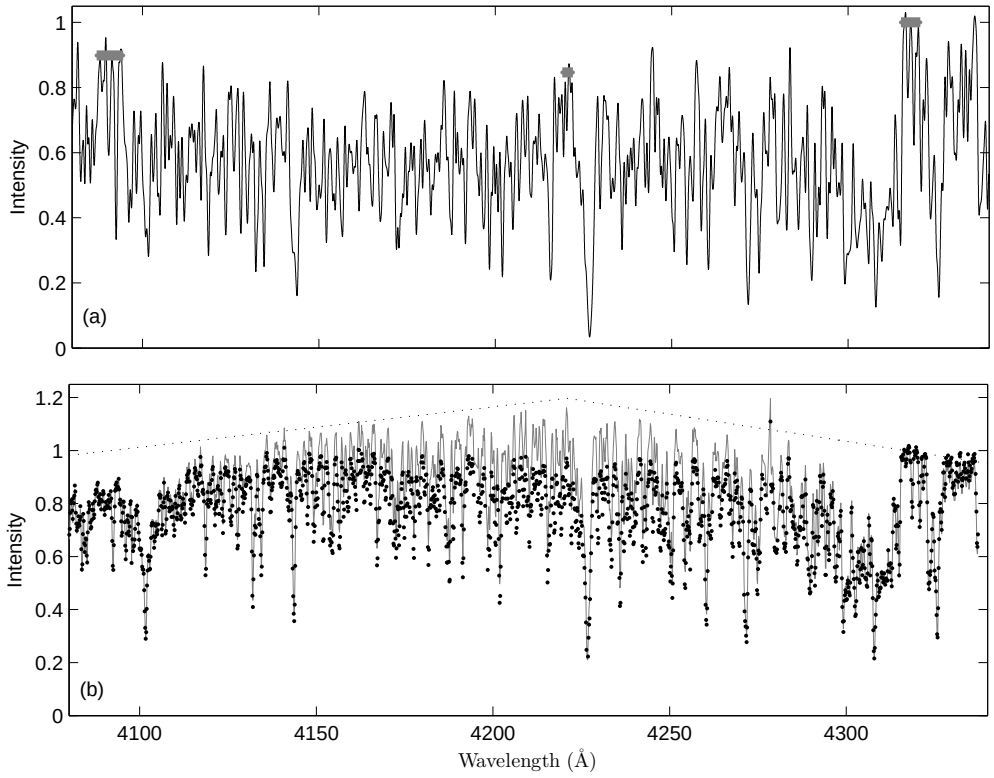

Figure 4.6: Continuum regions determined from Arcturus for normalisation about the CN and CH bands (a) Medium-resolution Arcturus spectrum with the three pseudo-continuum regions indicated in grey. (b) Spectra of the hottest star in the survey, Lee 2311. The raw spectrum (grey) is compared with the normalised spectrum (black). The profile used to normalise the spectrum is shown as the dotted line.

4.2 CN indices

CN indices for stars in 47 Tuc have been measured in several studies. A number of stars observed in this survey were previously observed by Norris & Freeman (1979) and Paltoglou & Freeman (1984), in which they were classified for their CN indices. The analysis of the stars here sought to replicate the CN indices and extend the analysis to the remaining stars in the sample. The CN index used here was as defined by Norris & Freeman (1979) and Paltoglou & Freeman (1984):

$$S(4142) \;=\; -2.5\; log_{10}\Big\{\; \frac{\int_{4120}^{4216} F_\lambda d\lambda}{\int_{4216}^{4290} F_\lambda d\lambda}\Big\} \tag{4.1}$$

In essence this is the sum of the spectral intensities between the two wavelength limits for each integral. The numerator in Equation 4.1 is the 'on-band' region which encompasses the CN bandhead. The denominator is the 'off-band' region which is the neighbouring section of wavelength clear of CN molecules. This was written as a MATLAB programme that then measured the S(4142) for all the survey stars. Norris & Freeman (1979) calibrated this line intensity version of the CN index to the previous photometric index, C(4142), using the following equation:

$$C(4142) \;=\; 0.742 \;\times\; S(4142) \;+\; 0.236 \tag{4.2}$$

In order to determine the CN excess, δC(4142) (hereafter δC), the CN indices were considered in C(4142)-V space in Norris & Freeman (1979), and in C(4142)-$B-V$ space in Paltoglou & Freeman (1984). The equations used to derive δC for these two studies were:

$$\delta C \;=\; C(4142) \;-\; 0.079 \;\times\; V \;+\; 1.123\;, \tag{4.3}$$

$$\delta C \;=\; C(4142) \;-\; (0.304 \;\times\; (B-V) \;-\; 0.275) \tag{4.4}$$

where Equation 4.3 is taken from Norris & Freeman (1979) and Equation 4.4 is taken from Paltoglou & Freeman (1984). As the C(4142) values were available in the literature the δC was recalculated for both studies using Equation 4.4. The stars were then classified as CN weak if $\delta C \leq 0.11$ or CN strong if $\delta C \geq 0.11$ (Paltoglou & Freeman, 1984). The CN index was then measured for each of the stars in the current survey directly from the AAOmega spectra using the above equations. Figure 4.7 shows the CN excess, δC, for the stars in common between this survey and the previous studies.

The two sets of indices are not in agreement in Figure 4.7. There is an distinct offset which indicates that there is systematic difference between the studies. This offset is due to the difference in placement of the continuum between the studies. The mean was determined for the previous CN indices and for the current CN indices. The difference between the means was then subtracted from the current CN excess in order to calibrate them to the previous studies. Figure 4.8 shows this adjustment to the current values (δC_{adj}). Overall there is very

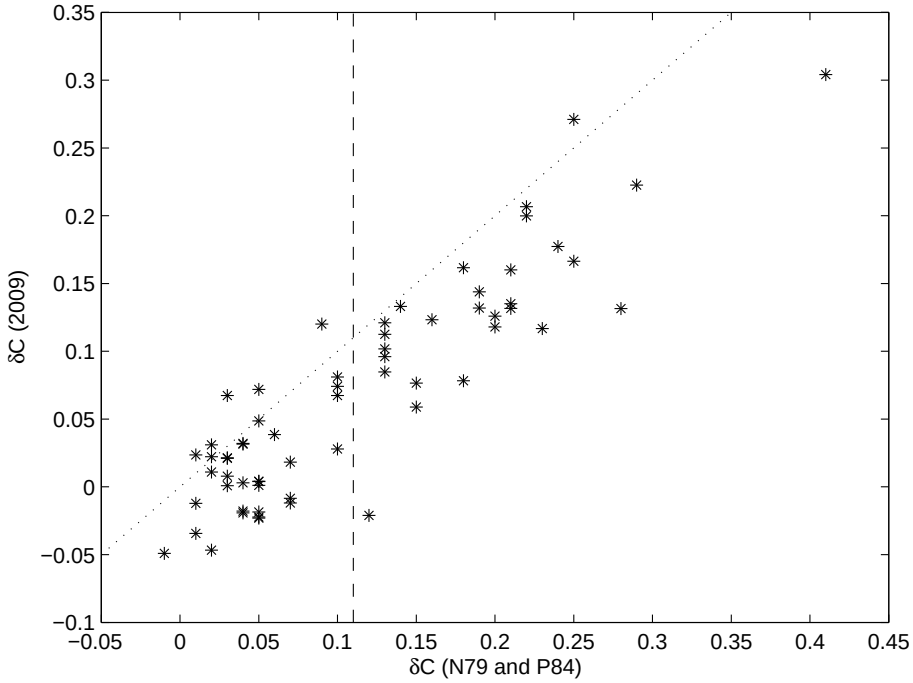

Figure 4.7: Comparison of CN excesses (δC), from Norris & Freeman (1979) (N79) and Paltoglou & Freeman (1984) (P84) (on abcissa) with the CN excess measure in this thesis (2009) (on ordinate). The dashed vertical line indicates the CN-weak, CN-strong separation value of δC = 0.11. Below this limit the stars are CN weak and above this limit the stars are CN strong. The data would lie along the dotted diagonal line if the indices were in agreement.

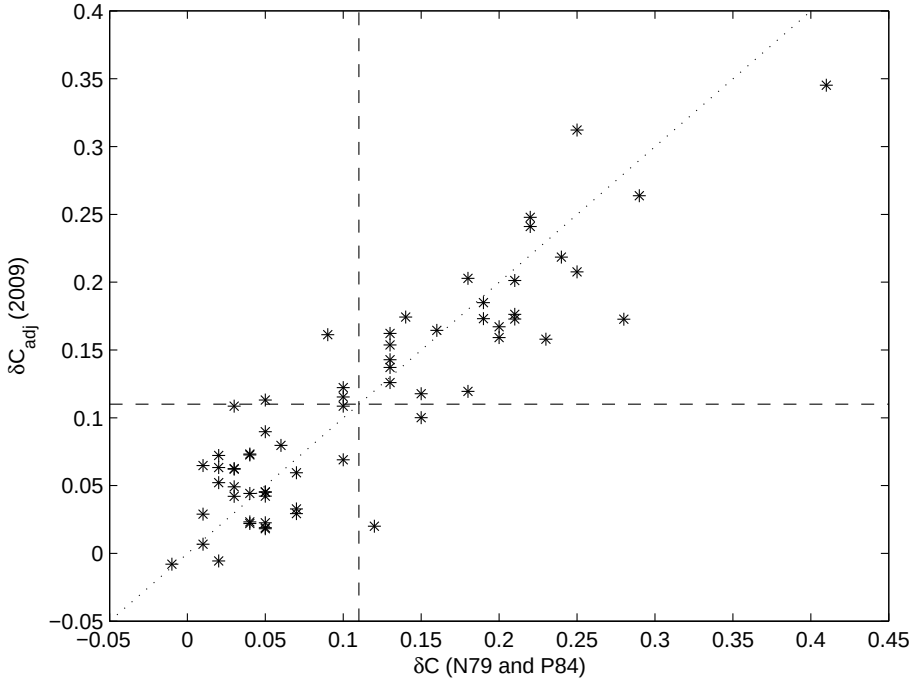

Figure 4.8: As for Figure 4.7 but with the current CN excesses calibrated to the previous studies (δC_{adj}). The δC separation value is included as a horizontal line also. For the majority of the stars the classification remains the same.

good agreement between the previous and current values for δC. Approximately six stars border the δC separation value. The calibration was sufficiently consistent for the purposes of this thesis.

Figure 4.9 reduces the raw CN excess measurements into a histogram using a bin interval of 0.02 and then smoothed using a gaussian filter with FWHM of 0.05. The CN bimodality is clearly seen as a peak in the CN-weak stars at $\delta C \sim 0.05$ and a peak in the CN-strong stars at $\delta C \sim 0.16$. In past studies evidence has been found for a radial gradient of CN strength in 47 Tuc (Norris & Freeman 1979; Freeman 1985; Paltoglou 1991).

Histograms were produced for the stellar sample divided into two distinct sections of cluster radius and are shown in Figure 4.10. The separation was made at a cluster radius of 0.6^o. As each radial subset comprised of a smaller sample than the total population a larger bin size (0.04) and FWHM (0.06) was required for smoothing the measurements. The histogram for the inner radii shows a greater number of CN-weak than CN-strong stars. The reverse is true for the outer radii where CN-strong stars dominate.

The sample analysed in this study was compared with the analysis carried out in Paltoglou & Freeman (1984), as a subset of the Paltoglou & Freeman (1984) sample was re-observed in this survey. Figure 4.11 compares the results for the Paltoglou & Freeman (1984) stars of radius greater than 17' with the results from the AAOmega survey for which the stars were also of radius greater than 17'. The two populations of CN-weak and CN strong stars are distinct in both stellar samples. However the Paltoglou & Freeman (1984) sample shows that the CN-weak population dominates the sample. Paltoglou & Freeman (1984) also analysed a sample of stars with radius between 2.5' and 6' for which the CN-strong population dominated. The combination of these two samples indicated a radial gradient in CN strength whereby the inner radii of the cluster are dominated by CN strong stars and the outer radii are dominated by CN weak stars.

The AAOmega sample analysed here included only stars with radius greater than 17'. The results from this sample are not so definitive as the Paltoglou & Freeman (1984) results and rather seem to imply that the CN-strong population dominates at outer radii.

Figure 4.12 compares the values of δC derived in each study for the Paltoglou & Freeman (1984) stars that were used in the AAOmega survey. The AAOmega values for the most part trace the overall result of the AAOmega survey but the CN-weak populations does dominate which is in agreement with the Paltoglou & Freeman (1984) values. The overall distribution of the two sets of values for these stars are quite different and this indicates some fundamental differences in the measurement of the CN strength between the studies. As the measurement of the CN index was preliminary for this study and further work is required to refine the indices, this analysis will be revisited at a later date.

The main discrepancy between the studies is that for radii greater that 17' Paltoglou & Freeman (1984) found that the CN-weak population dominated, while this survey found that

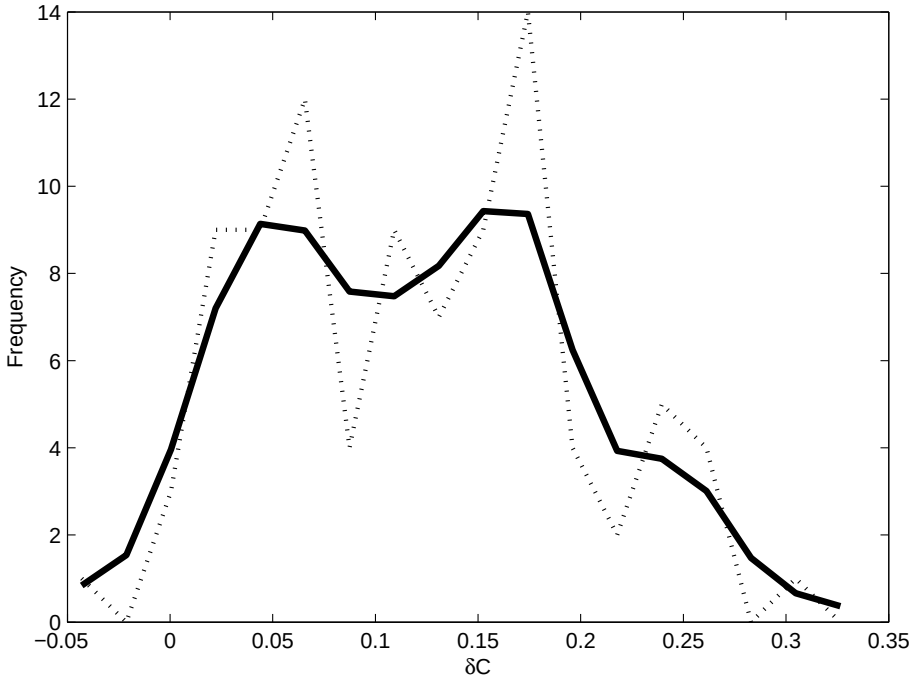

Figure 4.9: Histogram showing CN bimodality in the 47 Tuc survey using the δC measured in this analysis. The dotted line is the δC measurements binned to intervals of 0.02. The solid line is a gaussian smoothing of the raw measurements with a full-width-at-half maximum (FWHM) of 0.05.

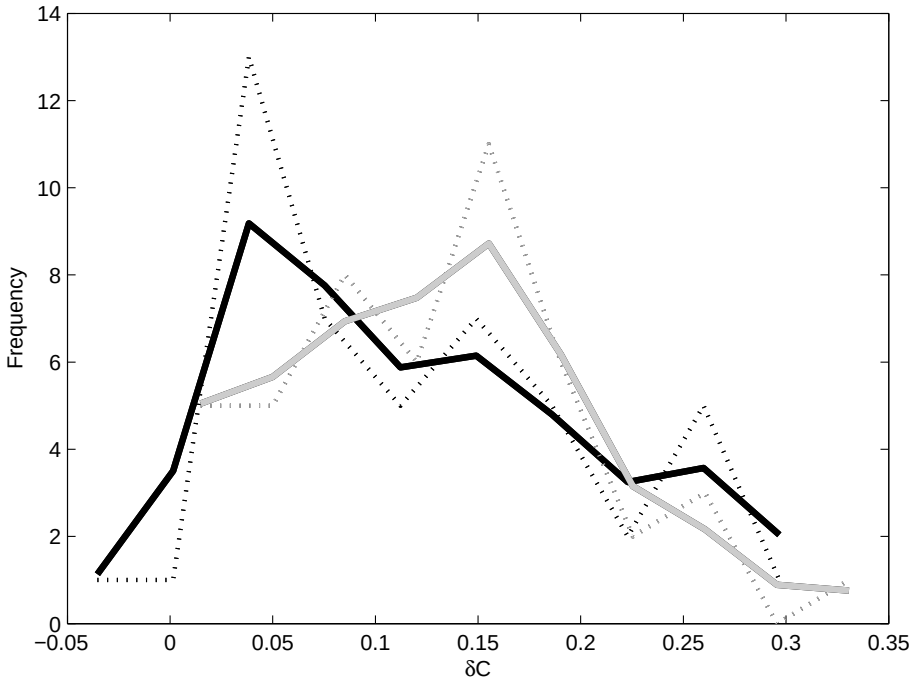

Figure 4.10: As for Figure 4.9, but showing the CN bimodality for two sections of cluster radius (R): R $\leq 0.6^o$ (black); R $\geq 0.6^o$ (grey). The δC measurements (dotted line) in both cases were binned in intervals of 0.04, then smoothed (solid line) with a FWHM of 0.06.

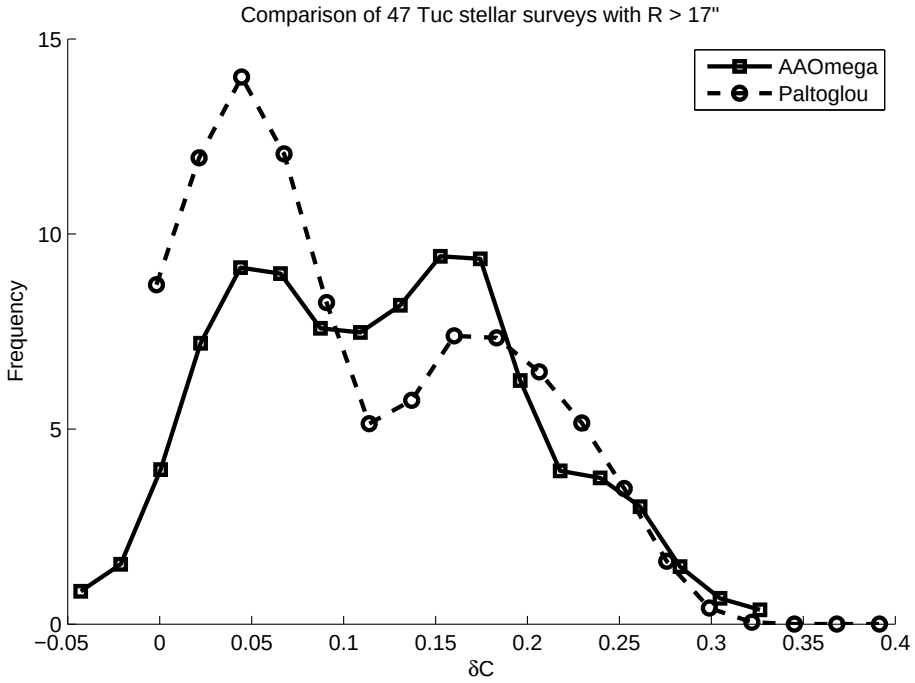

Figure 4.11: Histogram comparing the CN bimodality found in the AAOmega survey of 47 Tuc survey with that found in Paltoglou & Freeman (1984). The δC values displayed are those measured in the respective studies. The δC measurements were binned to intervals of 0.02 and full-width-at-half maximum (FWHM) of 0.05.

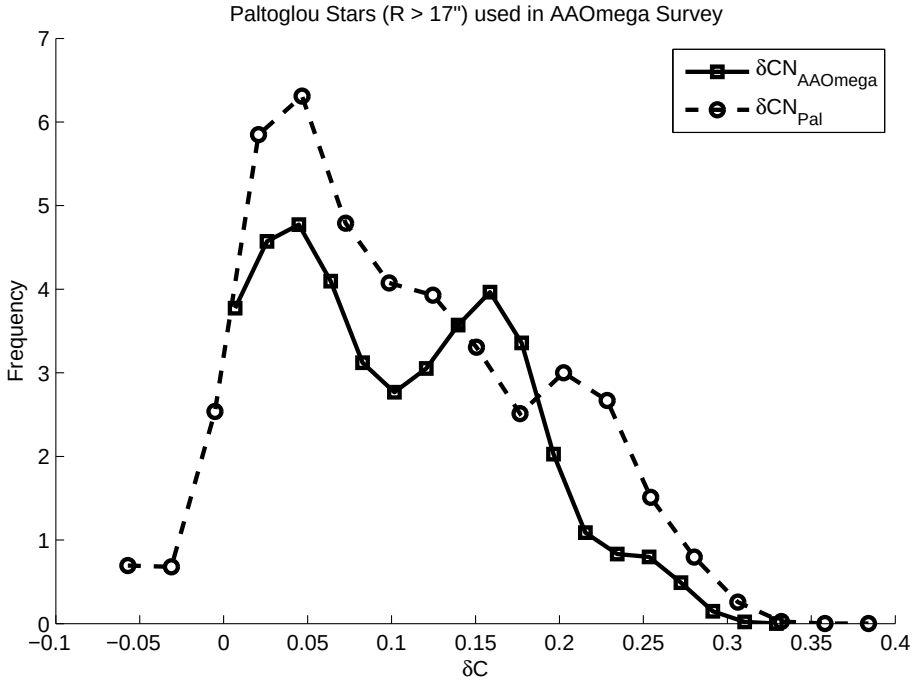

Figure 4.12: Histogram of CN Bimodality for the Paltoglou & Freeman (1984) stars used in the AAOmega survey comparing the δC_{Pal} with the $\delta C_{AAOmega}$. The δC measurements in both cases were binned in intervals of 0.02, then smoothed with a FWHM of 0.05.

the CN-strong population dominated. The radial analysis of the AAOmega sample shown in Figure 4.10 refines this result and shows that the CN-weak population dominates for radii greater than 17' but less than 36' (0.6^o) while the CN-strong population dominates for radii greater than 36'. This is not in disagreement with the Paltoglou & Freeman (1984) results but rather seems to refine the exact nature of the observed radial gradient in CN strength. However this is still preliminary work and further analysis is required, as well as follow up observations of the remaining stars in the Paltoglou & Freeman (1984) sample.

The CN-CH anti-correlation is a well known feature of 47 Tuc and other globular clusters (Cannon et al., 1998). In summary if a star is CN-strong its composition is enhanced in N and depleted in C, hence in a CN-strong star there are weak CH features. The effect was clearly seen in the stars in this sample. Figure 4.13 compares a CN-weak and a CN-strong star of similar T_{eff} and *log g*. In Figure 4.13(a) the CN band at 4216 Å shows the difference between the two stars for this feature where indeed the CN is strong in the CN-strong star. In Figure 4.13(b) the CH band at 4315 Å is also very different between the stars. As expected CH is weak in the CN-strong star. Further measurements of CH were not pursued in this thesis as the relationship between the two bands is well known.

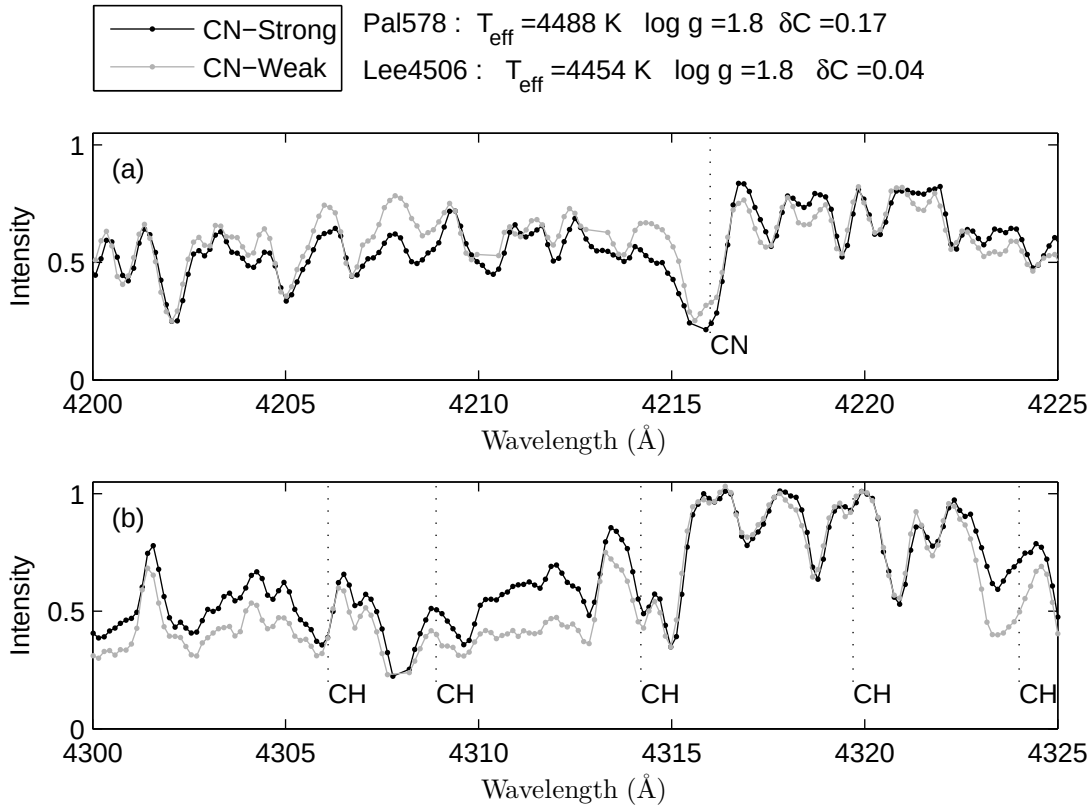

Figure 4.13: Comparison of a CN-weak star (grey) with a CN-strong star (black) from the 47 Tuc star survey. (a) CN bandhead at 4216 Å. (b) CH bandhead (G Band) at 4315 Å.

4.3 Photometric stellar atmosphere parameters

The stellar atmosphere models for each star were based on the T_{eff} and *log g* values derived from the photometry for each star. A range of photometry were available for all the stars in the survey. (see Appendix A) Temperatures and gravities were determined from the $(B-V)$, $(J-K)$ and $(V-K)$ values using the equations in Alonso et al. (1999). Figure 4.14 shows the three sets of values for the stars in the survey.

The $(B-V)$ and $(V-K)$ values are in reasonable agreement. The $(J-K)$ values are cooler by approximately ~ 200 K for the RGB. This is an effect that was reported in Alonso et al. (1999) for stars with $T_{eff} \leq 4500$ K. Stellar parameters based on $(V-K)$ photometry are reported to be a better representation of the star due to these colours being less affected by line absorption and less sensitive to metallicity (Bessell, 2004). Consequently the $(V-K)$ stellar parameters were used in this study rather than the $(B-V)$ parameters.

4.4 CN-Weak, CN-Strong Pairs

The relationship between CN-weak and CN-strong stars is best investigated through finding pairs at similar T_{eff} and *log g*. Based on the $(V-K)$ stellar parameters CN pairs were identified and are shown in T_{eff}−*log g* space in Figure 4.15. The sample contains several pairs on the RGB and HB, although the AGB is more sparsely populated.

The group of stars at $T_{eff} \approx 4200$ K and *log g* ≈ 1.3 includes the star Lee 2525, the high-resolution analysis of which will be discussed in Chapter 5. The stars in this group all have approximately the same stellar parameters and provide a good sample of comparable stars at different CN strengths. The stellar designations, CN excess, photometry, corresponding stellar parameters for ten of these stars are listed in Table 4.3. This table is replicated in Appendix A for all the stars in the 47 Tuc medium-resolution survey.

4.4.1 Lee 2525

Lee 2525 is a star that has been observed in several studies as part of this thesis. It has been observed in three separate datasets: SALT PV RSS medium resolution observations of eleven stars in 47 Tuc (Chapter 3); AAOmega 47 Tuc medium-resolution survey (this chapter); and high-resolution observation of Lee 2525 on the SSO 2.3 m telescope (Chapter 5). Figure 4.16 compares the spectra of Lee 2525 from all three observations. Also included is the convolution of the SSO high-resolution spectrum to a medium resolution comparable to AAOmega.

The Lee 2525 spectrum observed on RSS is at a lower resolution than the AAOmega spectra. The features in common between the high and medium-resolution spectra seem to agree in terms of their relative line depths. The convolved spectrum is used in the abundance analysis in the following sections. Lee 2525 was singled out in this thesis as a linking star

Table 4.3: Ten stars of similar stellar parameters are listed with their ID (past and current), CN excesses taken from Norris & Freeman (1979) (N79) and Paltoglou & Freeman (1984) (P84), and CN excesses calculated in this study (2009). The stellar parameters, T_{eff} and *log g*, were calculated for each star based on $(V-K)$, $(B-V)$ and $(J-K)$ photometry which are also listed.

		δC				T_{eff}	*log g*		T_{eff}	*log g*			T_{eff}	*log g*
ID1	Ref.	N79/P84	(2009)	V	$V-K$	$(V-K)$	$(V-K)$	$B-V$	$(B-V)$	$(B-V)$	J	$J-K$	$(J-K)$	$(J-K)$
Pal262	P84	0.25	0.21	12.72	1.29	4240	1.35	1.29	4207	1.33	10.42	0.84	4092	1.27
Pal661	P84	0.22	0.25	12.54	1.26	4233	1.28	1.26	4257	1.29	10.25	0.86	4041	1.17
Lee2525	N79	0.10	0.12	12.43	1.29	4232	1.23	1.29	4207	1.22	10.14	0.87	4033	1.13
Lee1513	N79	0.21	0.17	12.41	1.32	4242	1.23	1.32	4159	1.18	10.12	0.85	4059	1.13
Lee1747	N79	0.25	0.31	12.45	1.26	4284	1.27	1.26	4257	1.25	10.23	0.85	4072	1.15
W66	-	-	0.14	12.55	1.34	4181	1.25	1.34	4127	1.22	10.21	0.90	3951	1.15
Lee 3206	N79	0.05	0.02	12.59	1.29	4288	1.33	1.29	4207	1.28	10.35	0.83	4115	1.23
Pal 502	P84	0.02	-0.01	12.64	1.36	4158	1.27	1.36	4096	1.24	10.27	0.91	3935	1.19
Lee 3622	N79	0.03	0.06	12.60	1.31	4183	1.27	1.31	4175	1.26	10.25	0.89	3978	1.18
Lee 4628	N79	0.05	0.09	12.53	1.31	4241	1.28	1.31	4175	1.24	10.24	0.85	4057	1.18

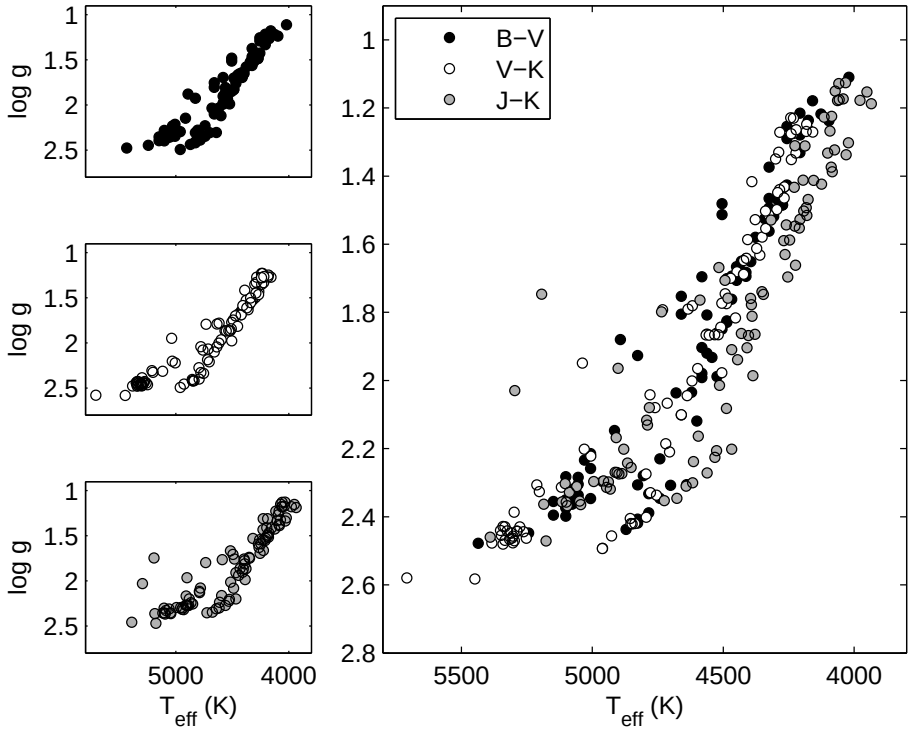

Figure 4.14: HR diagram of the 47 Tuc survey stars where T_{eff} and *log g* are derived from: $(B-V)$ (black circle); $(V-K)$ (white circle); and $(J-K)$ (grey circle).

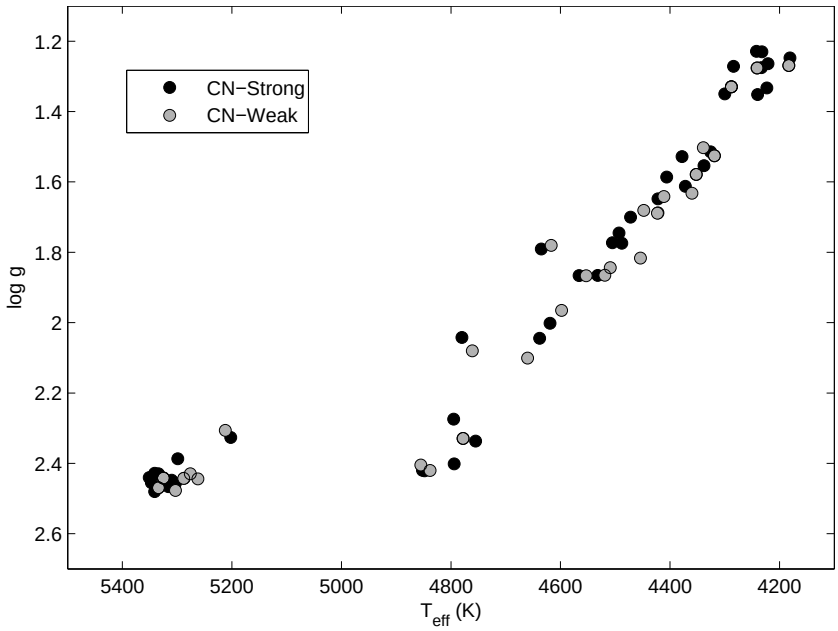

Figure 4.15: $T_{eff}-log\ g$ space for CN-weak (grey circle) and CN-strong (black circle) pairs based on $(V-K)$ photometry.

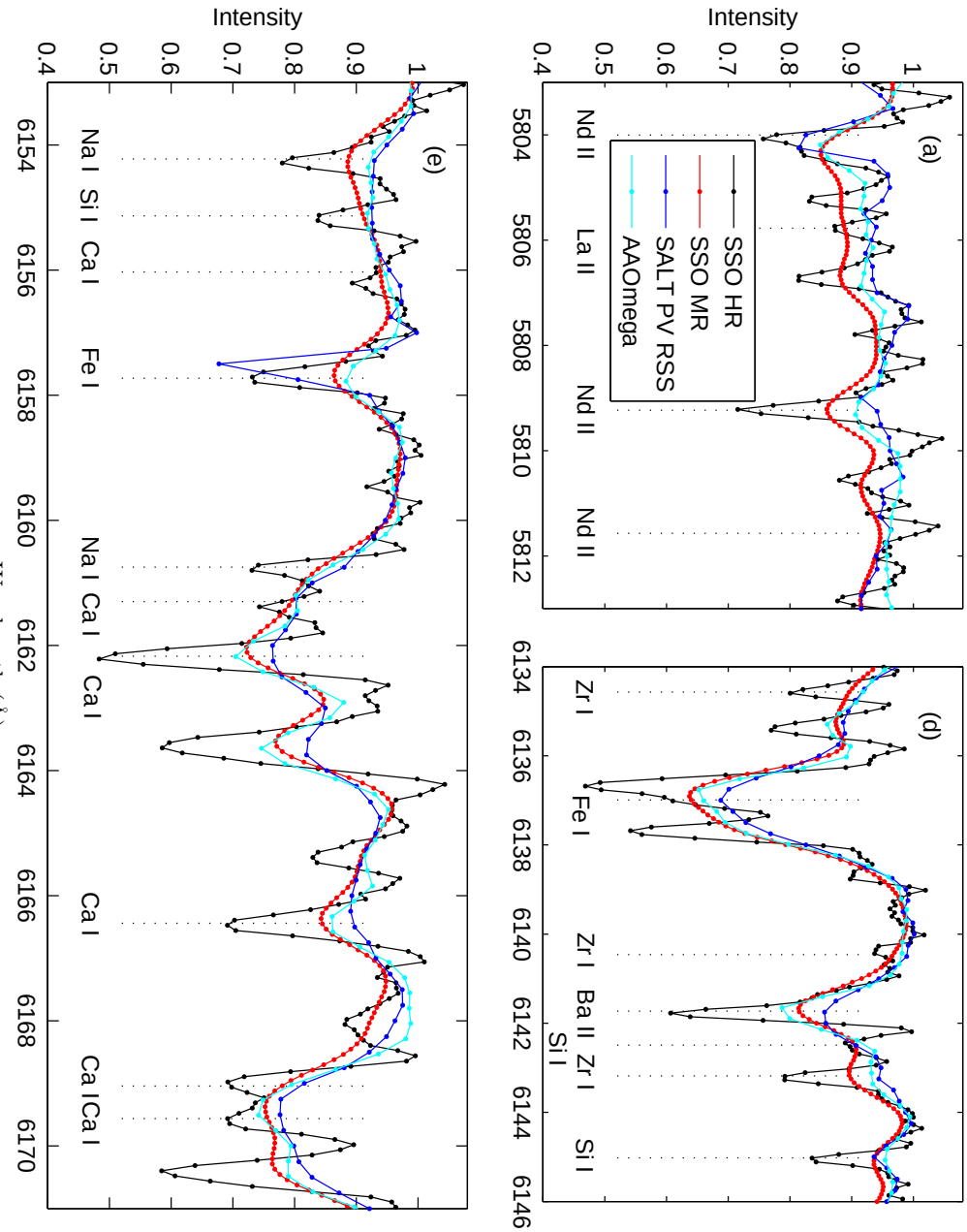

Figure 4.16: Comparison of the Lee 2525 spectra observed using RSS on SALT (blue), the SSO 2.3 m telescope (black), and AAOmega on the AAT (cyan). Also included is the convolution of the high-resolution spectra to a resolution comparable to the AAOmega observation (red). (a) Nd II and La II features in the 5800 Å region. (b) Si I, Fe I, Ba II and Zr I features in the 6140 Å region. (c) Na I, Si I, Ca I, and Fe I features in the 6160 Å region.

between two previous key studies (Brown & Wallerstein 1992 and Wylie et al. 2006) and is discussed in detail in Chapter 5. In the analysis of the 47 Tuc survey, it was selected to determine which elemental abundances could be obtained from these stars.

In Norris & Freeman (1979) Lee 2525 was found to be a CN-weak star with a δC = 0.10. Its CN-strong pair, in $(B-V)$ stellar parameters, was Lee 1513 which had a CN excess of δC = 0.21 (Brown & Wallerstein, 1992). In the current study Lee 2525 was re-classified as a CN-strong star (δC = 0.12) and Lee 1513 remained a CN-strong star (δC = 0.17). Although it was re-classified there was only a small change in measured CN excess for Lee 2525 compared with the previous study.

Figure 4.17 compares the spectra from these two stars, Lee 2525 and Lee 1513. Their respective stellar parameters, determined from $(V-K)$ photometry, and CN excess (δC) are listed in the legend to this figure. Figure 4.17(a) compares the spectra near the CN bandhead at 4216 Å. Lee 2525 is definitely weak in CN compared with Lee 1513 which is consistent with both the previous and new classifications. The CH bandhead in Figure 4.17(b) shows Lee 1513 to be depleted in CH compared to Lee 2525 which confirms the CN-CH anti-correlation for these two stars. Figures 4.17(c) to (e) compare the spectra of these two stars for wavelength regions in which there are key light and heavy element features. The two spectra are strikingly similar in all three figures. Given the similarity in stellar parameters this is not unexpected. These three regions will be analysed by spectrum synthesis in the following section to determine abundances based on these key features.

The re-classification of Lee 2525 as a CN-strong star in this analysis resulted in both Lee 2525 and Lee 1513 being paired with alternate CN-weak stars based on the $(V-K)$ stellar parameters. Figure 4.18 shows the same spectral regions as for Figure 4.17 but now Lee 2525 (δC = 0.12) is paired with Lee 3622 (δC = 0.06). The CN excesses for these stars have only a 0.06 difference between them. The small difference in CN strength can be seen in Figure 4.18(a). The key features in the spectral regions in Figure 4.18(c) to (e) are identical.

In Figure 4.19 Lee 1513 (δC = 0.17) is now paired with Lee 4628 (δC = 0.09). There is a difference of 0.08 between their respective CN excesses and the difference in CN and CH strength is clearly seen in Figure 4.19(a) and (b). The remaining spectral regions (Figure 4.19(c) to (e)) are also almost an exact match to each other. The Na feature at 6154 Å does look to be enhanced in the CN-strong spectra relative to the CN-weak spectra.

These pairings of Lee 2525 and Lee 1513 have CN excesses that are relatively similar in magnitude. Figure 4.20 compares two stars that are particularly well separated in CN excess value but have similar overall stellar parameters. Pal 262 is a CN-strong star with δC = 0.21 while Lee 2603 is a CN-weak star with δC = 0.02. The differences in CN and CH strength are particularly distinct when comparing these two stars (Figures 4.20(a) and (b)). What also becomes apparent is the difference in the line strength of the two Na I lines at 6154 Å and 6160 Å. The CN-strong star is considerably more enhanced in Na I than the CN-weak star. The correlation of Na I with CN strength has been noted in previous studies

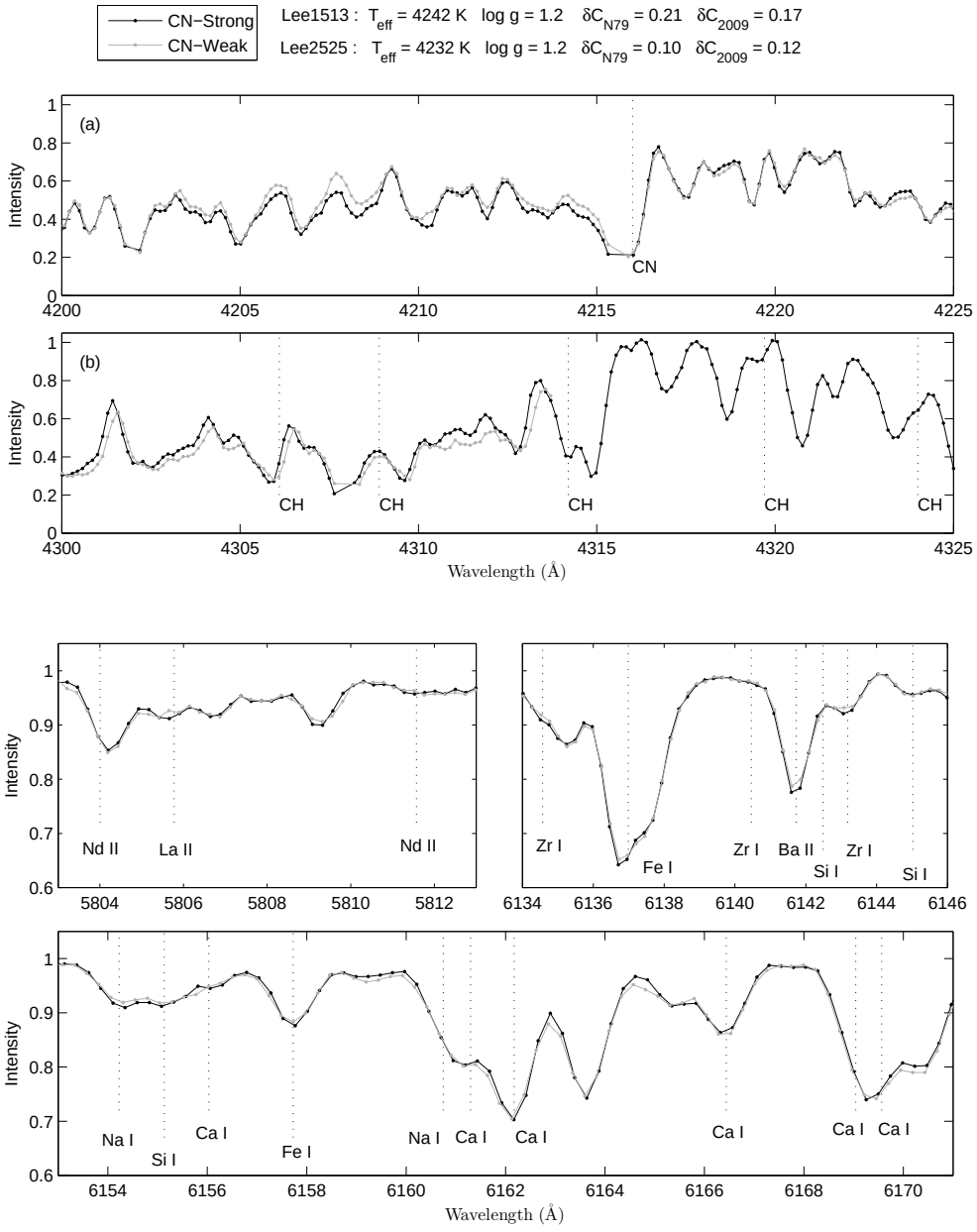

Figure 4.17: Comparison of Lee 2525 (grey) and Lee 1513 (black) spectra. The $(V - K)$ stellar parameters for each are listed, as well as the previous (δC_{N79}) and current (δC_{2009}) CN excess. (a) CN band at 4216 Å. (b) CH band at 4315 Å. (c) Nd II and La II features in the 5800 Å region. (d) Si I, Fe I, Ba II and Zr I features in the 6140 Å region. (e) Na I, Si I, Ca I, and Fe I features in the 6160 Å region.

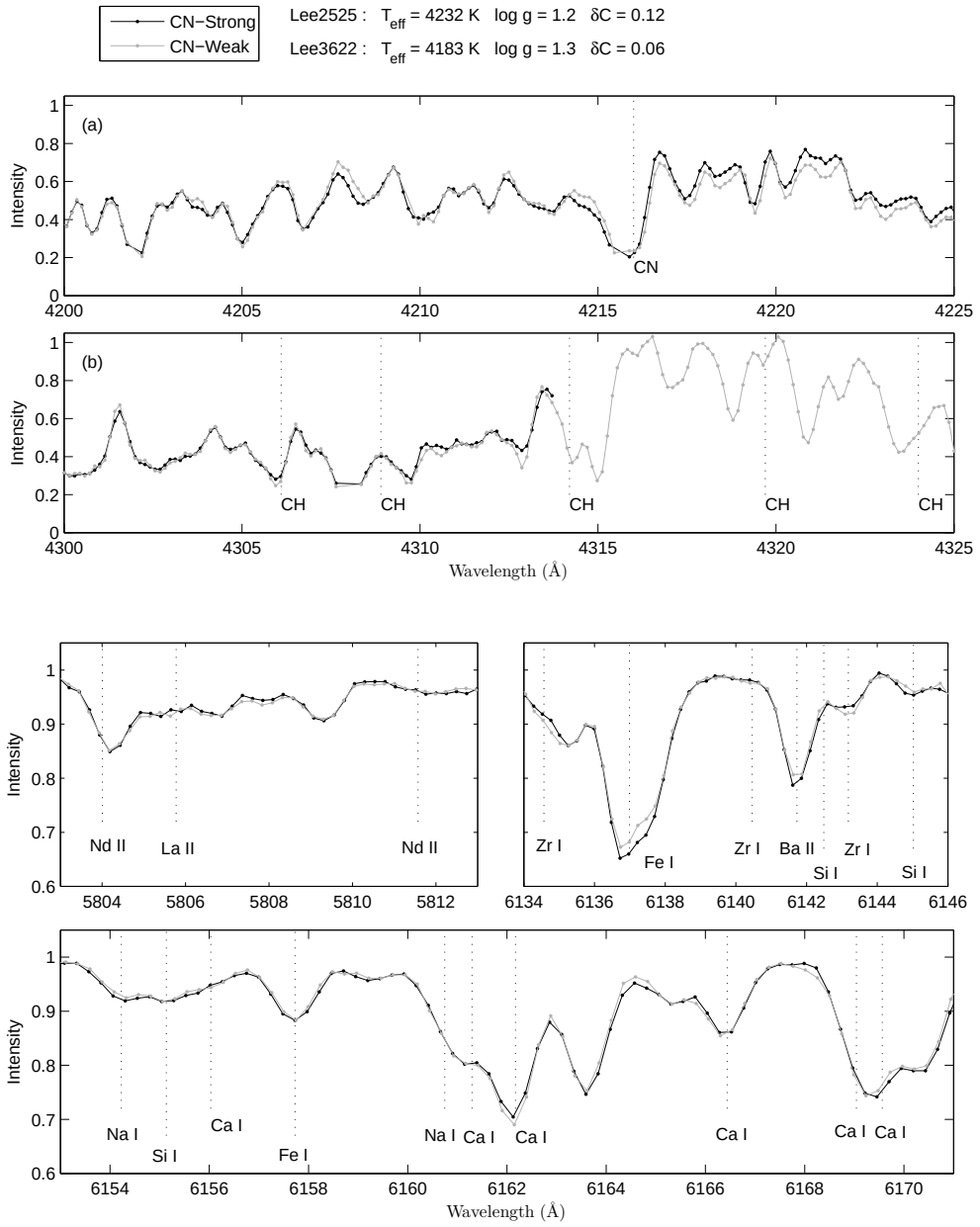

Figure 4.18: As for Figure 4.17, but comparing the spectra of Lee 2525 (black) and Lee 3622 (grey) spectra. The value for δC was determined in this study.

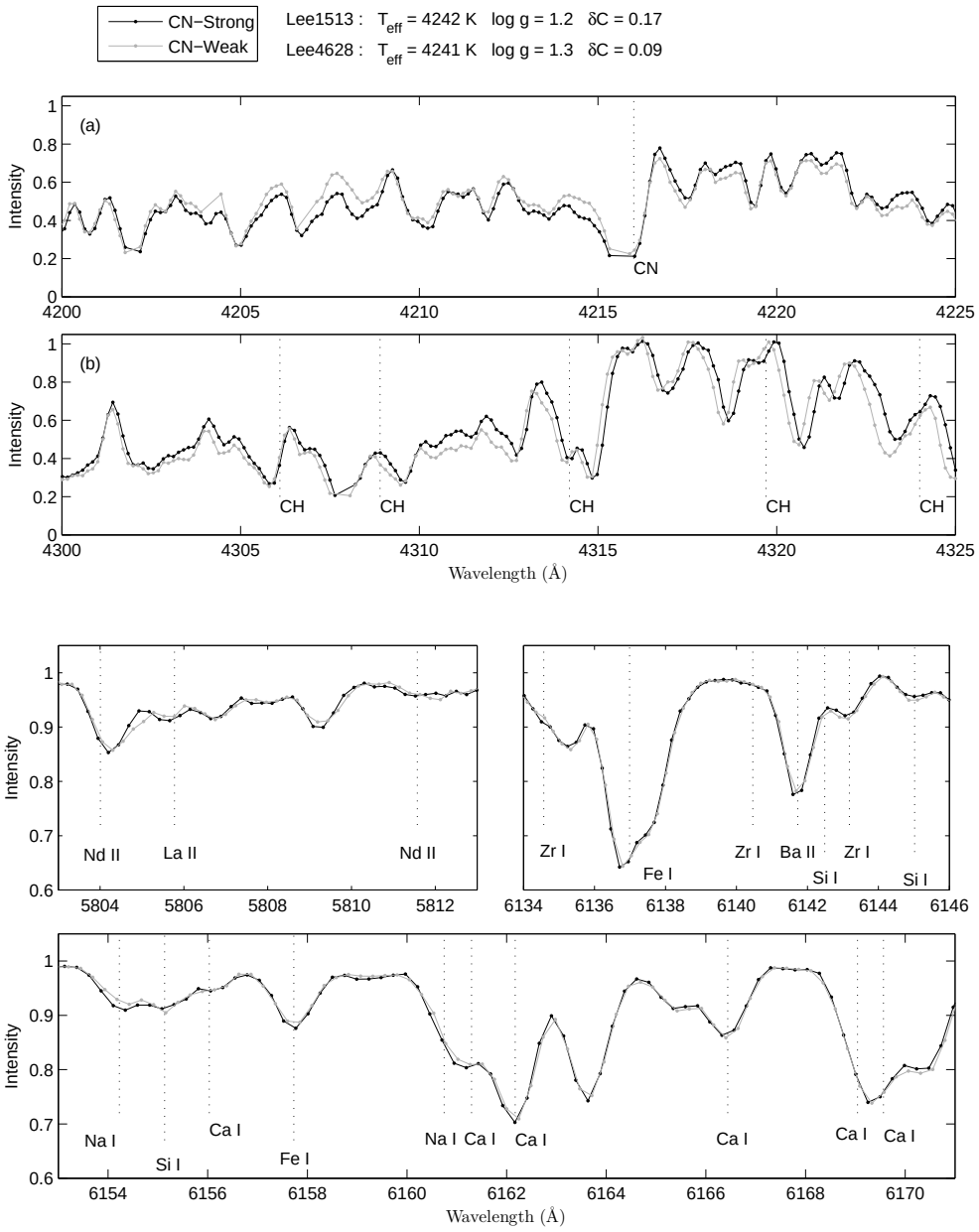

Figure 4.19: As for Figure 4.17, but comparing the spectra of Lee 1513 (black) and Lee 4628 (grey) spectra. The value for δC was determined in this study.

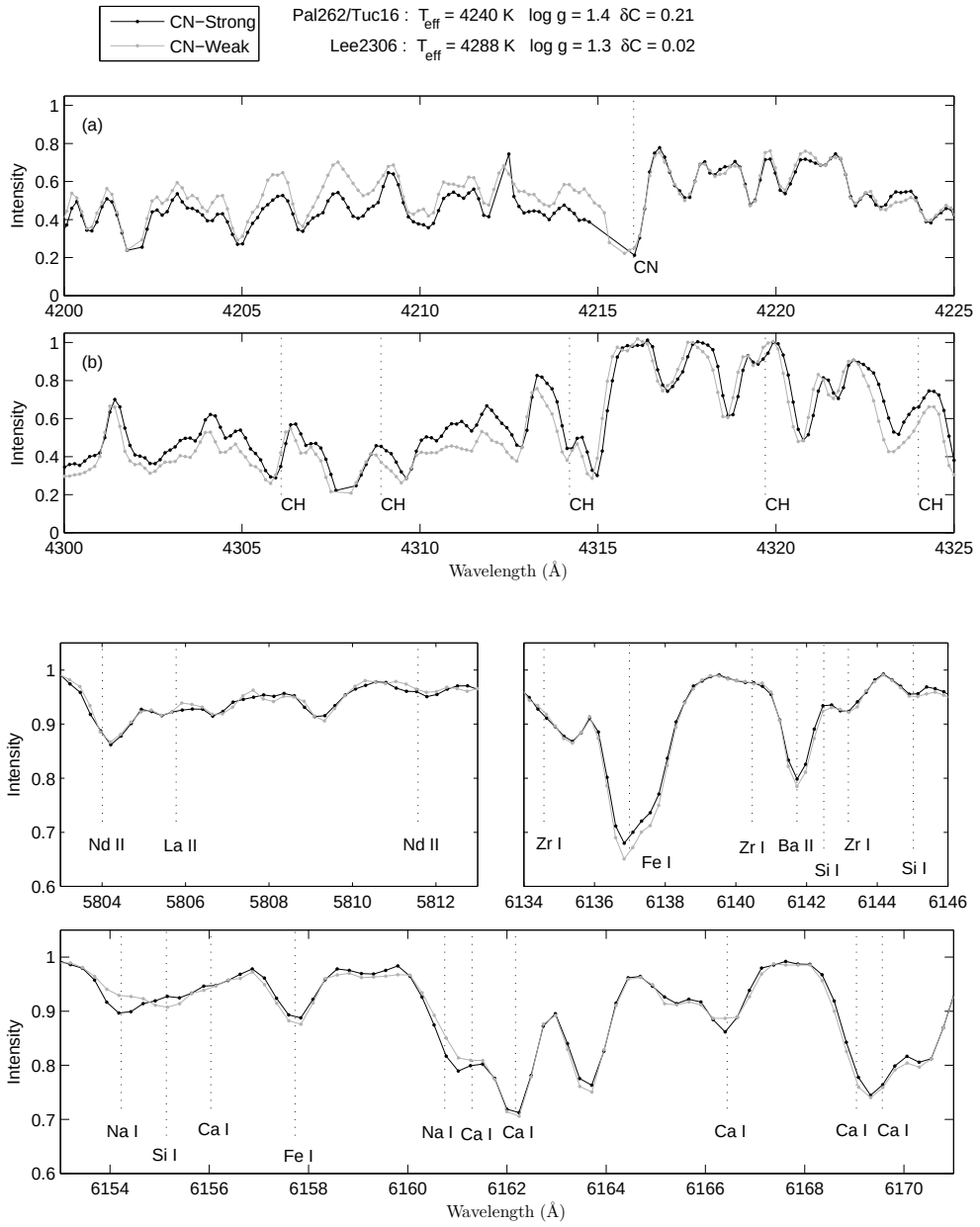

Figure 4.20: As for Figure 4.17, but comparing the spectra of Pal 262 (black) and Lee 2603 (grey) spectra. The value for δC was determined in this study.

and these spectra provide an excellent opportunity to investigate this correlation further (Cottrell & Da Costa, 1981). The remaining key features in these spectral regions show no distinct difference in line strength between these stars. The *s*-process element features in particular show no differences in line strength.

4.5 Abundance analysis of 47 Tuc survey stars

The subset of stars at $T_{eff} \approx 4200$ K and *log* $g \approx 1.3$ was used in a preliminary analysis of the survey to investigate the abundances of the light and heavy elements in 47 Tuc stars. In the high-resolution analysis of Lee 2525 that will be discussed in Chapter 5 the stellar atmosphere model for Lee 2525 was determined to have the parameters $T_{eff} = 4225$ K, *log* $g = 1.2$, $\xi = 1.8$ kms^{-1} and [Fe/H] $=-0.70$ dex. This model was used in the following abundance analysis of the medium-resolution observation of Lee 2525. It was subsequently used as the model for the remaining stars in the subset.

Figure 4.21 compares the observed spectrum of Lee 2525 with synthesised spectra that were used to determine the elemental abundances. The La II and Nd II features in Figure 4.21(a) are weak features and are blended with the surrounding lines. Model abundances for both of these is the best that can be determined for these lines within the noise. The wavelength region in Figure 4.21(b) includes several key heavy and light element features. In the analysis of Lee 2525, abundances could reliably be determined for the Si features at 6131 Å and 6145 Å, the Ba II feature, the Zr I feature at 6141 Å and the Fe I feature at 6147 Å. The Fe I feature at 6137 Å is comprised of three very strong Fe lines which are saturated. Obtaining abundances for these lines proved to be problematic.

Several of the light element features in the wavelength region in Figure 4.21(c) could also be used to obtain abundances. The feature at 6155 Å is comprised of an Na I, Si I and Ca I line, all of which were used to derive abundances. A second Na I line was also used at 6160 Å, as well as a second Ca I line at 6166 Å. The Fe I line at 6158 Å was also used to obtain an Fe abundance.

The synthesised spectra in these figures show key variations in the abundances of these elements. The dot-dash line shows how much of the element is responsible for these features by reducing the abundance of each by 8.0 dex. The model abundance is generally indicated by the solid line which clearly underestimates key elements such at Si, Ca and Ba, but it provides a reasonable fit for elements such as Zr and Na. The dashed line fits the enhanced elements; Si, Ca and Ba.

The elemental abundances determined from these lines for Lee 2525 are listed in Table 4.4. In order to make a direct comparison, the high-resolution Lee 2525 spectrum was convolved to the same resolution as the AAOmega spectrum and an abundance analysis was carried out. The results from that analysis and a spectrum synthesis analysis of the high-resolution Lee 2525 spectrum are also listed in Table 4.4.

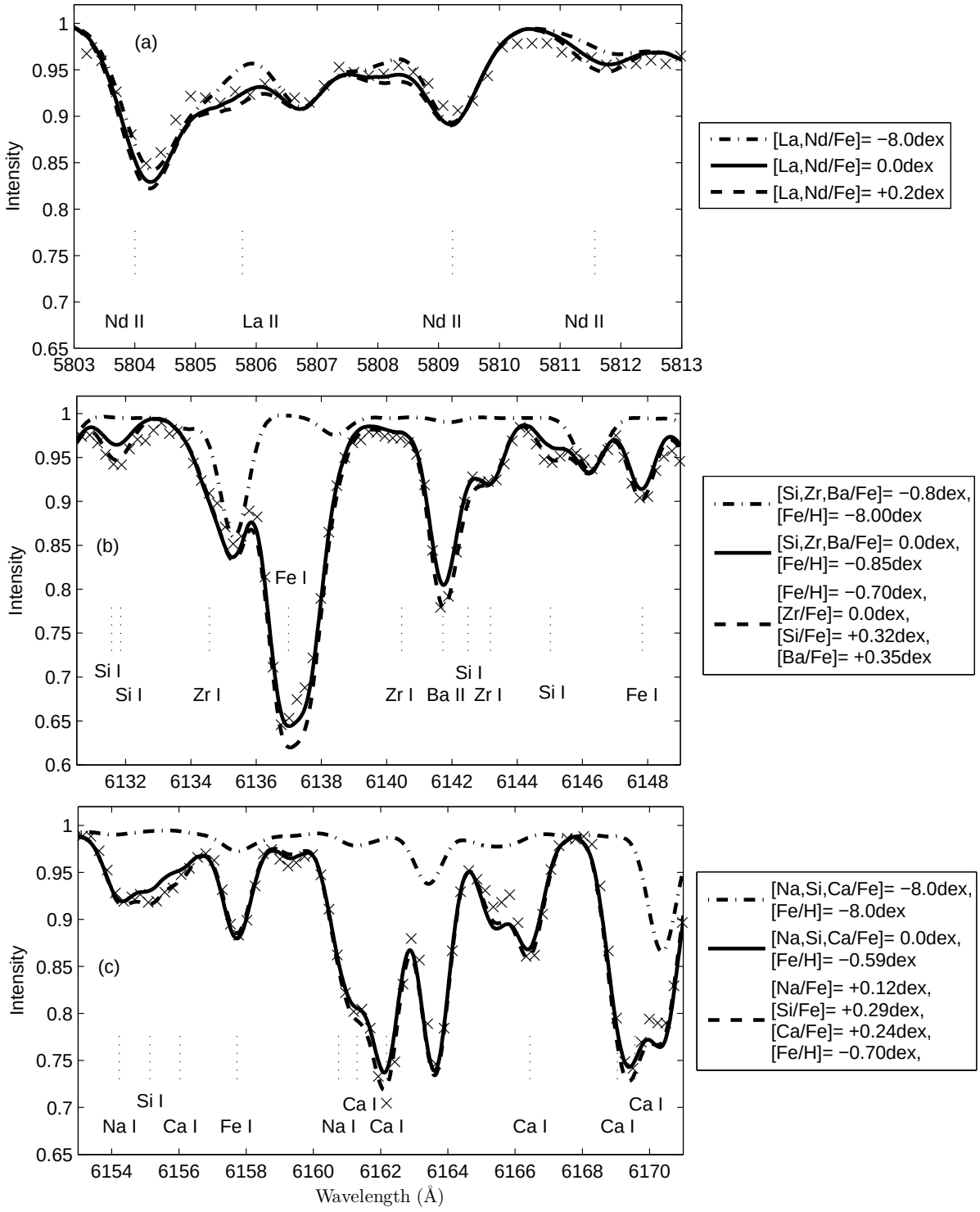

Figure 4.21: Spectrum of Lee 2525 as part of the AAOmega 47 Tuc survey compared with synthesised spectra. (a) The synthesised spectrum has the specified variations in abundance for La and Nd. An abundance of [X/Fe] = −8.0 dex corresponds to the element being completely depleted; [X/Fe] = 0.0 dex corresponds to no changes from the model abundance; positive [X/Fe] values correspond to an enhancement and negative [X/Fe] values correspond to a depletion of the element. (b) As for (a), but for Si, Zr, Ba and Fe. A value of [Fe/H] < −0.70 dex is a depletion of Fe while [Fe/H] > −0.70 dex is an enhancement of Fe. (c) As for (a) and (b), but for Na, Si, Ca and Fe.

Table 4.4: Elemental abundances derived for Lee 2525 from the medium-resolution AAOmega spectrum, from the spectrum convolved from the high-resolution SSO 2.3 m observation of Lee 2525 and from the high-resolution analysis itsself. Error analysis on the AAOmega medium-resolution spectrum is also included for the specified changes in stellar parameter.

	Instrument Resolution	AAOmega Medium	SSO 2.3 m Convolved	SSO 2.3 m High	Δ[Fe/H]		
					ΔT_{eff}	$\Delta log\ g$	$\Delta\xi$
	λ (Å)	[Fe/H]	[Fe/H]	[Fe/H]	+100 K	+0.5	+0.5
Fe I	6147.834	-0.70	-0.55	-0.73	-0.03	0.20	-0.08
Fe I	6157.728	-0.54	-0.50	-0.49	0.02	0.16	-0.21
	⟨[Fe/H]⟩	-0.62	-0.53	-0.61	0.01	0.15	-0.21
	σ	0.11	0.04	0.17	0.13	0.16	0.21
X		[X/Fe]	[X/Fe]	[X/Fe]	Δ[X/Fe]		
Na I	6154.226	0.12	0.42	0.40	0.06	-0.02	-0.09
Na I	6160.747	0.12	0.18	0.45	0.08	0.00	-0.12
	⟨[Na/Fe]⟩	0.12	0.30	0.43	0.07	-0.01	-0.11
	σ	0.00	0.17	0.04	0.01	0.01	0.02
Si I	6131.573	0.33	0.31	0.22	-0.02	0.13	0.01
Si I	6131.852	0.33	0.31	0.21	0.00	0.18	0.03
Si I	6145.018	0.32	0.36	0.39	-0.01	0.17	-0.04
Si I	6155.134	0.29	0.22	0.27	-0.03	0.14	-0.08
	⟨[Si/Fe]⟩	0.32	0.30	0.27	-0.02	0.16	-0.02
	σ	0.02	0.06	0.08	0.03	0.03	0.07
Ca I	6156.023	0.24	0.14	0.32	0.05	0.03	-0.07
Ca I	6166.439	0.24	0.37	0.27	0.13	0.09	-0.23
	⟨[Ca/Fe]⟩	0.24	0.26	0.30	0.09	0.06	-0.15
	σ	0.00	0.16	0.04	0.06	0.04	0.11
Zr I	6143.180	0.00	0.20	0.26	0.15	0.05	-0.10
Ba II	6141.730	0.35	-0.20	-0.40	0.00	0.17	-0.60
La II	5805.773	0.01	0.29	0.29	0.08	-0.08	-0.08
Nd II	5811.572	-0.11	-	-	0.10	0.03	0.03

There is reasonable agreement, particularly for Ca and Si, between the light elemental abundances for all three sets of results. Sodium, while enhanced in all three analyses, is less abundant in the AAOmega spectrum. For the Na line at 6154 Å, the abundance derived for the convolved spectrum agrees very well with the high-resolution abundance but not the medium-resolution abundance derived for that line. Conversely the abundance derived from the Na line at 6160 Å in the convolved spectrum agrees better with the medium-resolution abundance, not the high-resolution abundance. The 6154 Å line is part of a blend of similar strength Si and Ca lines. However, the 6160 Å line is on the edge of a set of strong Ca lines and is more heavily blended. Hence the greater difficulty in deriving it's abundance when convolved to medium-resolution. This is a good example of how the degradation of spectra at lower resolutions can obscure the true abundance of an element.

The heavy elemental abundances agree well between the convolved and the high-resolution spectra showing distinct enhancements in Zr and La. The medium-resolution spectrum shows no such enhancements in Zr or La, but an enhancement in Ba, which is depleted in the other two data sets. Barium is problematic due to the strong lines and the derived abundance being highly sensitive to microturbulence, as seen in Table 4.4. Further work on Ba is necessary to truly understand the abundances that are derived from these lines.

The error analysis in Table 4.4 shows changes in the elemental abundances on the order of 0.1 dex for reasonable changes in the stellar parameters. This reflects the difficulty in determining exact abundances for medium resolution spectra, hence placing limits on abundance variations is a more reasonable goal for this type of analysis.

Following this analysis of the medium-resolution Lee 2525 spectra the stars in the Lee 2525 subset were analysed for their elemental abundances. Table 4.5 lists the $(V-K)$ stellar parameters, CN excess and elemental abundances for each of the ten stars in this stellar subset.

The [*hs/ls*] ratio is included and derived simply as the difference between the Zr (light *s*-process) and Ba (heavy *s*-process) abundances ([*hs/ls*] = [Ba/Fe] − [Zr/Fe]). The sample mean and standard deviation for each element are also listed.

4.5.1 Light elemental abundances in 47 Tuc survey stars

The light elemental abundances are compared with [Fe/H] in Figure 4.22. There is a possible trend of Si with [Fe/H] but no such trend of Ca with [Fe/H]. Na has a much larger scatter in values than either Si or Ca but also shows no trend with [Fe/H]. Given the homogeneity in Si, and Ca, and that they have a similar scatter, if that scatter represents the systematic scatter in the analysis process then the range in values for Na far exceeds what can be expected from systematic uncertainties. This implies that the range in Na values is real and a Na abundance pattern exists in 47 Tuc stars. The addition of the remaining 87 stars from the survey will establish whether or not this trend exists over a larger sample of stars.

Table 4.5: Elemental abundances derived for ten stars in the 47 Tuc medium-resolution survey. The stars have similar stellar parameters to Lee 2525 and the Lee 2525 stellar atmosphere model was used to analyse the abundances for each. The $(V-K)$ stellar parameters for each star are listed as well as the CN excess. The mean abundance for the sample and standard deviation are also listed.

Star	Lee2525	Lee1513	Lee3622	Lee4628	Pal661	Pal262	Lee3206	Lee1747	W66	Pal502		
T_{eff} (K)	4230	4240	4180	4240	4230	4240	4290	1.3	4180	4160		
log g	1.2	1.2	1.25	1.3	1.3	1.35	1.2	1.2	1.25	1.3		
δC	0.12	0.17	0.06	0.09	0.25	0.21	0.02	0.31	0.14	0.02		
	$\langle$[Fe/H]$\rangle$										$\langle$[Fe/H]$\rangle$	σ
Fe	-0.67	-0.57	-0.71	-0.68	-0.59	-0.75	-0.59	-0.55	-0.63	-0.79	-0.65	0.08
X	$\langle$[X/Fe]$\rangle$										$\langle$[X/Fe]$\rangle$	σ
Na	0.06	0.15	-0.01	0.01	0.20	0.43	-0.01	0.38	0.28	0.12	0.16	0.16
Si	0.28	0.26	0.22	0.30	0.38	0.26	0.33	0.32	0.28	0.19	0.28	0.06
Ca	0.18	0.18	0.30	0.22	0.17	0.22	0.14	0.19	0.31	0.27	0.22	0.06
Zr	-0.01	0.08	0.08	0.08	-	-0.02	-0.02	-0.05	0.15	0.18	0.05	0.08
Ba	0.35	0.45	0.05	0.36	0.38	0.05	0.45	-0.05	0.09	0.15	0.23	0.19
X/Y	$\langle$[X/Y]$\rangle$										$\langle$[X/Y]$\rangle$	σ
hs/ls	+0.36	+0.37	-0.03	+0.28	-	+0.07	+0.47	0.00	-0.06	-0.03	+0.16	+0.21

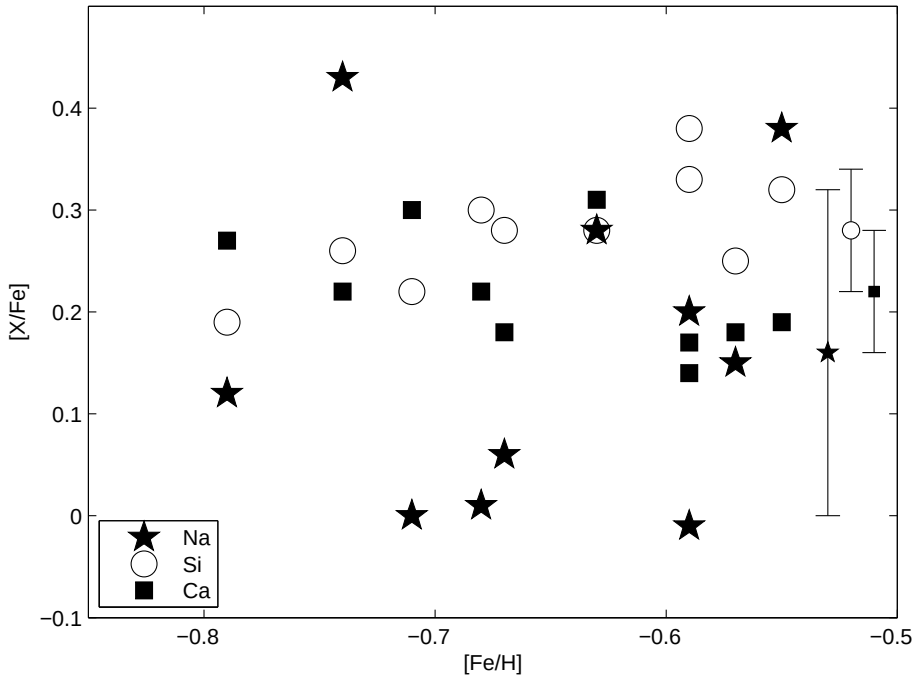

Figure 4.22: The element abundances for Na, Si and Ca against [Fe/H] determined for each of the ten stars similar in stellar parameters to Lee 2525. The mean and standard deviation for each elemental abundance is also shown.

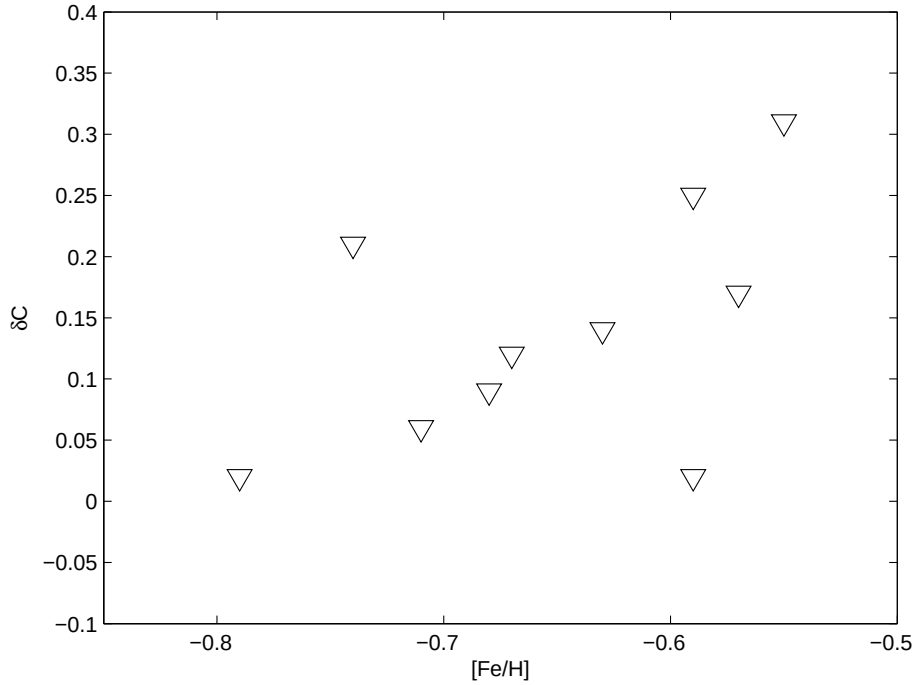

Figure 4.23: As for Figure 4.22, but the CN excess (δC) against [Fe/H].

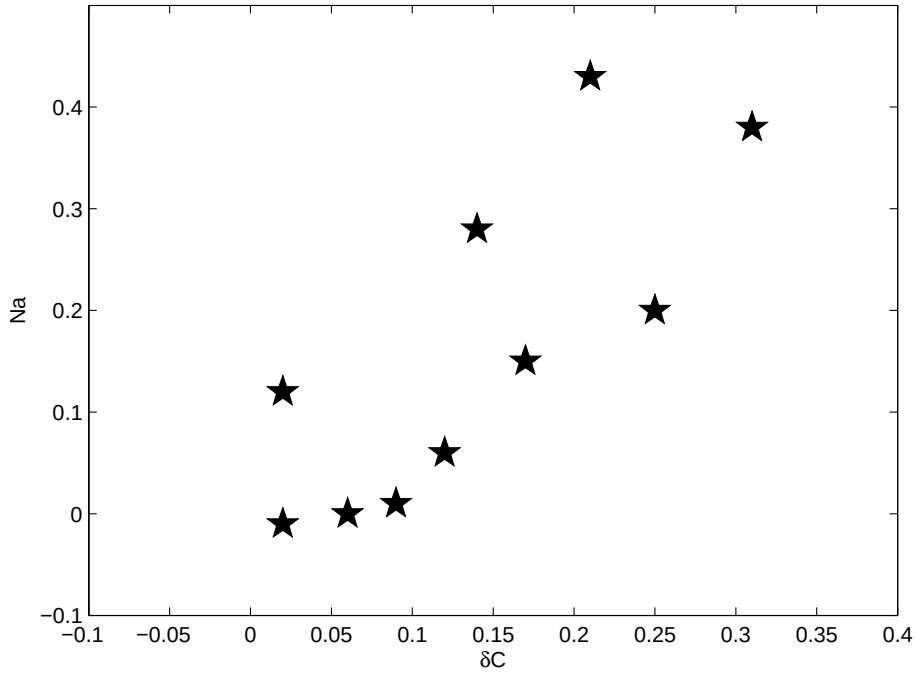

Figure 4.24: Na abundance against CN excess (δC) for each of the ten Lee 2525-like stars.

In Figure 4.23 the CN excess for each of the ten stars is compared with [Fe/H]. Two stars seem to disrupt what might otherwise be a trend of increasing CN excess with [Fe/H]. The addition of more stars when the rest of the survey is analysed will provide confirmation of whether or not a trend exists.

The Na-CN strength correlation is another well-documented abundance pattern in globular cluster stars (Cottrell & Da Costa, 1981). Figure 4.24 compares the Na abundances with CN strength and there is a clear correlation. There is some scatter but the increasing enrichment in Na corresponds to increasing CN strength. The trend seems continuous rather attributable to two distinct populations. Once again the results from the rest of the survey will enable this hypothesis to be tested.

4.5.2 Heavy elemental abundances in 47 Tuc survey stars

Figure 4.25 shows the abundances for each of Zr and Ba against [Fe/H]. The Zr abundances are reasonably consistent showing no particular trend with [Fe/H]. There is a large scatter in the Ba abundances, although again no trend with metallicity. The Lee 2525 model was used for all the stars in this subset and as such the microturbulence (ξ) was the same for each star. This provided a relative analysis between the stars in the subset for the majority of the lines. However, as Ba is very sensitive to ξ (see Table 4.4) the large spread in values could be caused by the poor fit of the microturbulence for some of these stars. For the remaining stars in the survey, a exact stellar atmosphere model will be determined based on the $(V-K)$ stellar parameters. The microturbulence will be adjusted in each case to ensure a proper fit to the spectrum. This should reduce the spread in the derived Ba abundances.

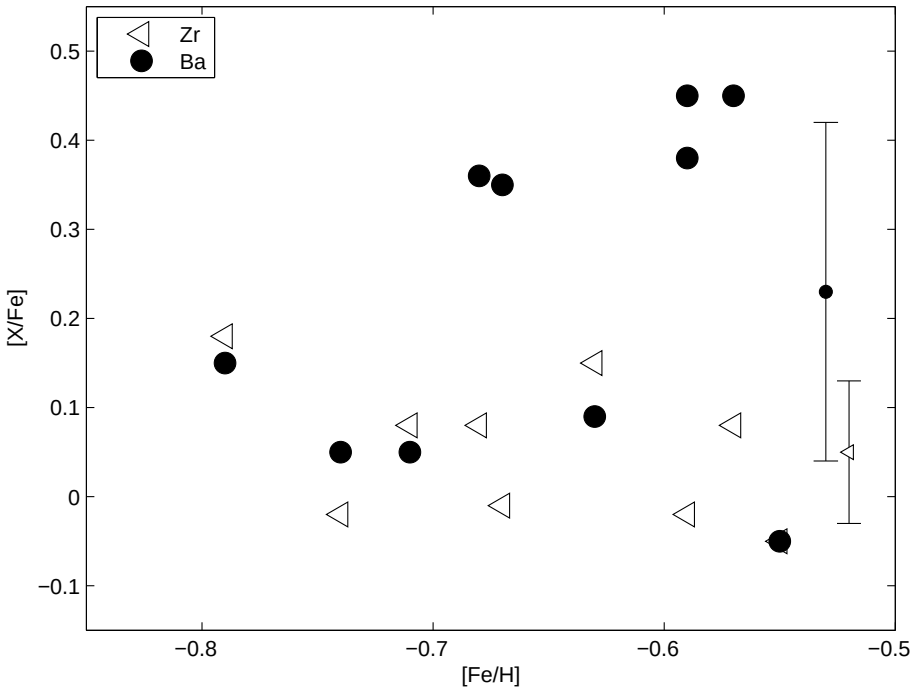

Figure 4.25: The abundances of the *s*-process elements, Zr and Ba, with [Fe/H] for the ten Lee 2525-like stars in the 47 Tuc medium-resolution survey. The mean and standard deviation for each elemental abundance is also shown.

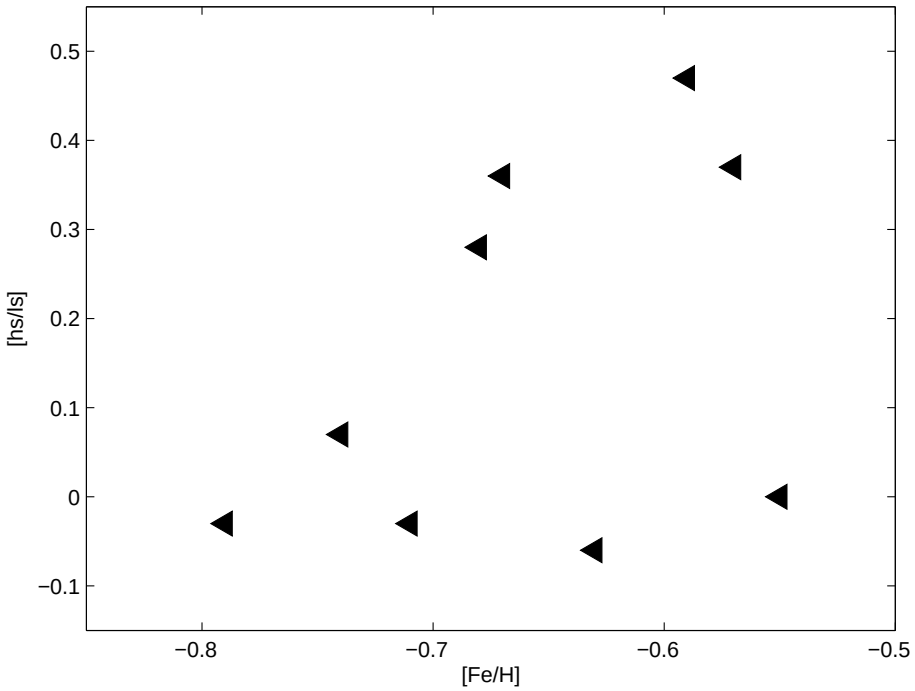

Figure 4.26: The [*hs/ls*] ratio against metallicity for each of the ten Lee 2525-like stars.

Bearing this issue with Ba in mind, the [*hs/ls*] ratio was calculated for each star and Figure 4.26 shows these values against [Fe/H]. There is no trend with metallicity. However there is a large scatter in the [*hs/ls*] values. Given the issues with Ba this is not unexpected. Further analysis of the [*hs/ls*] ratio in 47 Tuc stars is undertaken in Section 6.5.2. The results of this survey will be compared with the results from the 47 Tuc stars analysed in Chapters 5 and 6, and with previous studies of heavy elemental abundances in 47 Tuc stars.

4.6 Conclusion

The medium-resolution survey of 47 Tuc stars has provided a good sample with which to investigate several aspects of chemical abundances in globular clusters (GCs). The sample clearly shows the CN-CH anti-correlation which is well-documented for GCs (Norris & Freeman 1979; Cannon et al. 1998; Cannon et al. 2003; Briley et al. 2004). The bimodal distribution of CN-weak and CN-strong stars is also distinct in the sample and there is evidence of a radial gradient of CN strength in the cluster. CN-weak stars are predominantly located in the inner regions of the cluster, while CN-strong stars dominate the outer regions of the cluster. The current measurement of the CN indices of these stars were in good agreement with the previous studies of Norris & Freeman (1979) and Paltoglou & Freeman (1984), although the calibration to the previous studies requires further refinement.

The analysis of medium-resolution spectra is well suited to spectrum synthesis for determining chemical abundances. This technique was used to determine abundances for light and heavy elements in a subset of stars from the 47 Tuc stellar survey. The preliminary set of stars have similar stellar parameters and their representative star, Lee 2525, provided a link to high-resolution abundance analyses of 47 Tuc stars in this thesis and other key papers (Brown & Wallerstein 1992; Wylie et al. 2006; Worley et al. 2008).

The abundance analysis for these stars show a homogenous distribution of Fe ($\langle$[Fe/H]$\rangle = -0.65 \pm 0.08$ dex), Si ($\langle$[Si/Fe]$\rangle = +0.28 \pm 0.06$ dex) and Ca ($\langle$[Ca/Fe]$\rangle = +0.22 \pm 0.06$ dex) in 47 Tuc. There is a much larger scatter in the abundance derived for Na ($\langle$[Na/Fe]$\rangle = +0.16 \pm 0.16$ dex) and the Na abundance was found to correlate with CN strength. This is a phenomenon also previously observed in 47 Tuc stars (Cottrell & Da Costa 1981; Cannon et al. 2003).

The heavy elemental abundances proved difficult to obtain due to the weakness and blending of the feature from which the Zr abundance was derived, and the high microturbulence sensitivity of the abundances derived for the Ba II line. The analysis of the high-resolution spectrum of Lee 2525, which will be discussed in Chapter 5, determined an enhancement in the Zr abundance for this star. The medium resolution spectra did not reflect this enhancement. The mean Zr abundance for the survey subset showed a slight enhancement of $\langle$[Zr/Fe]$\rangle = +0.05 \pm 0.08$ dex. There was very little associated spread in Zr abundances

which is evidence for the homogeneity of this element in 47 Tuc stars. The mean abundance derived for Ba showed an overall enhancement in Ba ($\langle$[Ba/Fe]$\rangle$ = $+0.23 \pm 0.19$ dex) but the spread in the sample subset was very large. This is unlikely to be real but rather a consequence of the microturbulence value used in the stellar model. The resulting mean [*hs/ls*] ratio reflected this spread in the Ba abundances ($\langle$[*hs/ls*]$\rangle$ = $+0.16 \pm 0.21$ dex).

The preliminary results from the medium-resolution survey of the 47 Tuc giant stars are very promising, particular for the abundance patterns observed in the light elements. The heavy elements, Ba in particular, need further work before the derived abundances can be relied upon. The next stage for the survey is to determine the best stellar atmosphere model for each star and to then determine each star's elemental abundances by spectrum synthesis. The addition of the rest of the survey to the sample analysed here will clarify which of the observed trends in abundance are real. The high-resolution analysis of 47 Tuc giant stars in the following two chapters will provide more reliable abundances with which to compare the abundances derived in this survey. This will be particularly useful for the heavy elemental abundances for which there are currently contradictory results between the high-resolution and medium-resolution spectra.

Chapter 5

High-resolution studies: 47 Tuc giant star Lee 2525

The survey analysed in the previous chapter confirmed the homogeneity of heavy elemental abundances in 47 Tuc giant branch stars as well as the correlation of Na with CN strength. However, the exact nature of the heavy elemental abundance enhancements requires further investigation. High-resolution data provides a better measurement of these weak heavy element features, although comparison of previous high-resolution studies shows a varied and contradictory set of results.

This chapter seeks to resolve a discrepancy between two key studies (Brown & Wallerstein 1992 and Wylie et al. 2006) of *s*-process elemental abundances measured for giant stars in 47 Tuc. The giant star Lee 2525 was one of four 47 Tuc stars analysed in Brown & Wallerstein (1992). Similar stars were analysed in Wylie et al. (2006) and a comparison was made to the results from Brown & Wallerstein (1992). In order to provide a direct link between these two studies Lee 2525 was observed at high-resolution, using the AAO 2.3 m telescope, and is the subject of analysis in this chapter.

5.1 Observations and connection to previous work

In November 2007 the 47 Tuc giant branch star Lee 2525 was observed on the 2.3 m telescope at the Siding Spring Observatory by K.C. Freeman and E.C. Wylie de Boer. It was observed using the échelle spectrograph, obtaining wavelengths from 4500 Å to 6500 Å. The spectrum had a resolution of $R \sim 20,000$ with a signal-to-noise ratio per resolution element of ~ 35. The spectrum was reduced in IRAF and the normalised spectrum underwent the curve-of-growth analysis as outlined in Section 2.2 in order to derive the stellar atmospheric parameters. Lee 2525 had been observed previously in Brown & Wallerstein (1992), along with four other 47 Tuc giant branch stars. In Wylie et al. (2006) these stars were compared with seven more giant stars in 47 Tuc.

Figure 5.1 shows the placement of the stellar sample from both studies on the colour-magnitude diagram of 47 Tuc. Lee 2525 is also indicated on the diagram and all of the stars fall on the RGB or AGB as indicated by the fiducial lines (Hesser et al., 1987).

Lee 2525 has been studied in a number of papers. As a bright giant it was initially observed under this designation in Lee (1977). Subsequently it was studied in Norris & Freeman (1979) where it was determined to be a CN weak AGB star. It has also been part of a mass loss study for giant stars in 47 Tuc where it was determined to have no infrared excess (Ramdani & Jorissen, 2001). Lee 2525 was analysed in Brown & Wallerstein (1992) as the CN weak star in a CN weak-CN strong pair. Its counterpart was Lee 1513.

Worley et al. (2008) observed Lee 2525 as part of a study into the feasibility of medium resolution surveys of globular cluster stars to determine their *s*-process elemental abundances using the Robert Stobie Spectrograph (RSS) on the Southern African Large Telescope (SALT). This study was summarised in detail in Chapter 3. The resolution of the spectra in this study was determined to be too low (R∼5,000) to determine absolute *s*-process elemental abundances, although upper limits of +0.5 dex may be possible in future observations with RSS. For Lee 2525 in particular there was an indication of an enhancement in Zr, although this lay within the uncertainties of the model abundance (see T_{eff} = 4490 K spectrum in Figure 3.13 and associated text). Higher resolution was required in order to clearly ascertain the nature of the *s*-process elemental abundances.

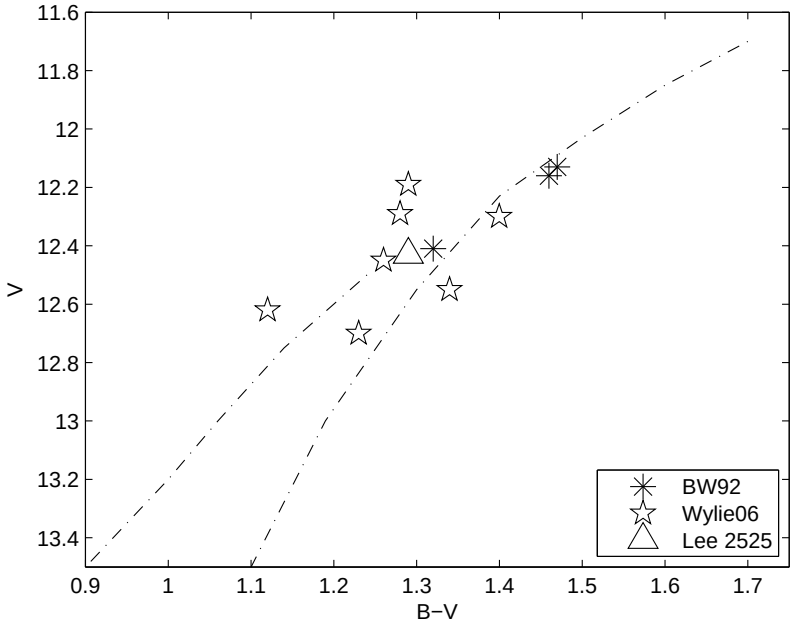

Figure 5.1: Colour-magnitude diagram of 47 Tuc showing the placement of the giant stars observed in Brown & Wallerstein (1992) and Wylie et al. (2006). The position of Lee 2525 is identified and the fiducial lines indicating the RGB and AGB branches of 47 Tuc are taken from Hesser et al. (1987).

The average heavy elemental abundances for the stellar samples reported in Brown & Wallerstein (1992) and Wylie et al. (2006) are listed in Table 5.1.

The sample in Wylie et al. (2006) show a general enhancement of the *s*-process elemental abundances across the sample, with the average enhancement for Zr being [Zr/Fe] = +0.64 dex. A similar abundance enhancement was found for several *s*-process elements (Y, La) in Brown & Wallerstein (1992), but Zr was found to be depleted with an average abundance of [Zr/Fe] = −0.43 dex. The *r*-process element Eu was enhanced in both studies.

The goal of this analysis of Lee 2525 is to link these two studies in an effort to consolidate the reported abundances of heavy elements in 47 Tuc giant branch stars.

Table 5.1: Comparison of the mean heavy elemental abundances from samples of AGB and RGB stars analysed in Brown & Wallerstein (1992) (BW92) and Wylie et al. (2006) (W06).

	BW92		W06	
No. Stars	4		7	
	Mean	σ	Mean	σ
[Fe/H]	−0.80	0.09	−0.62	0.06
[Y/Fe]	+0.51	0.28	+0.66	0.20
[Zr/Fe]	−0.43	0.10	+0.64	0.15
[La/Fe]	+0.17	0.09	+0.31	0.10
[Eu/Fe]	+0.31	0.10	+0.14	0.12

5.2 Comparison of Lee 2525 studies

A full chemical analysis of Lee 2525 was carried out in Brown & Wallerstein (1992). This analysis was replicated here with particular interest in the heavy elemental abundances. The stellar parameters were derived as outlined in Section 2.4. A comparison of the equivalent widths and stellar parameters derived here and in Brown & Wallerstein (1992) is made in the following two sections.

5.2.1 Lee 2525 equivalent widths

The equivalent widths of the Fe and other atomic lines measured in Brown & Wallerstein (1992) were obtained from those authors in order to compare them with the equivalent widths measured in this study.

Figure 5.2 compares the equivalent widths of the Fe lines in common between Brown & Wallerstein (1992) and this study. The resolution of the spectra was similar for both studies

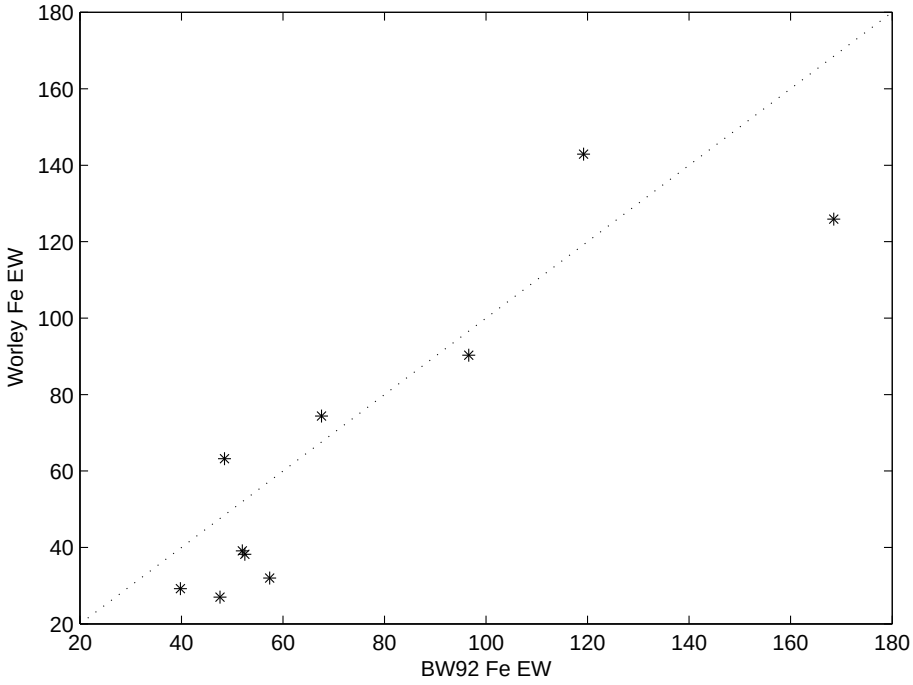

Figure 5.2: Comparison of the Fe equivalent widths measured in this research compared with those measured in Brown & Wallerstein (1992).

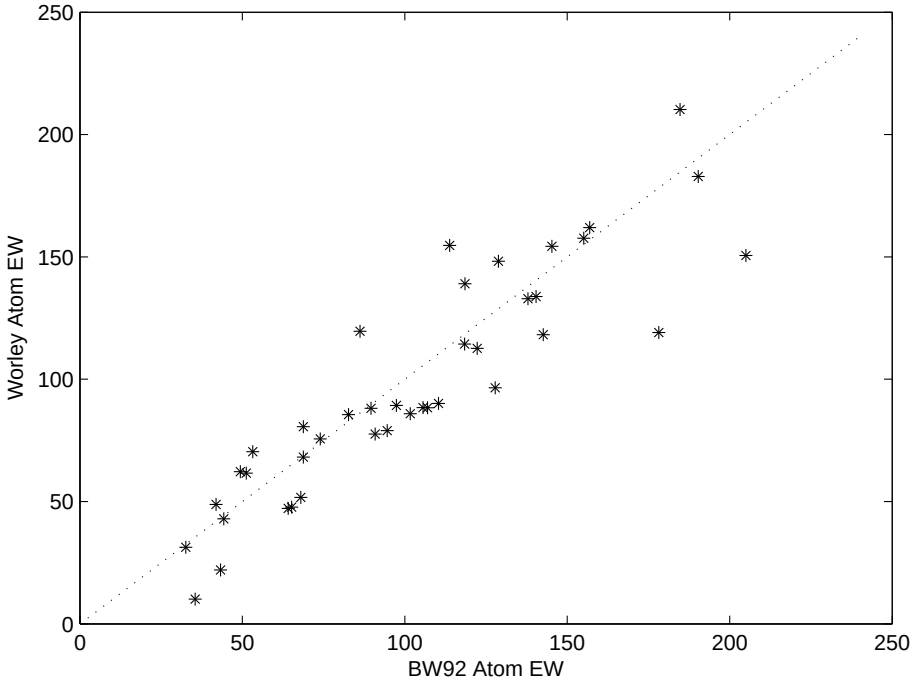

Figure 5.3: Comparison of the non-Fe equivalent widths measured in this research compared with those measured in Brown & Wallerstein (1992).

($R \sim 20,000$), but the signal-to-noise ratio (SNR) obtained here was much lower (SNR per pixel ~ 0.16) than that which was obtained in Brown & Wallerstein (1992) (SNR per pixel ~ 90). This limited the number of Fe lines that could be measured here in common with Brown & Wallerstein (1992). There is some scatter between the two studies but overall there is good agreement between both sets of measured equivalent widths.

Figure 5.3 compares the equivalent widths measured for the other atomic lines in common between the studies. The sample in common is more extensive than for the Fe lines and, while there is still some scatter, the agreement between the measurements is reasonable.

The Fe and atomic line lists were supplemented from the lines used to calibrate the analysis process. The exact lines used in this study in the analysis of Lee 2525 are noted in Tables 2.2 and 2.3.

5.2.2 Lee 2525 stellar atmosphere models

The stellar parameters for Lee 2525 in Brown & Wallerstein (1992) were determined to be T_{eff} = 4225 K, *log* g = 1.3, [Fe/H]= −0.82 dex and ξ = 2.0 kms^{-1}. In this analysis the $(B-V)$ photometric stellar parameters for Lee 2525 were calculated to be $T_{eff} \approx 4200$ K and *log* $g \approx 1.2$ based on the Alonso et al. (1999) equations and Equation 3.1. These stellar parameters were used as the starting point for determining the spectroscopic stellar model. An exploration in stellar parameter space was carried out in order to determine the best fit model. Table 5.2 lists the stellar parameters and resulting [Fe I,Fe II/H][1] values for each model permutation.

Table 5.2: Stellar model parameters and resulting values of [Fe I/H] and [Fe II/H] for Arcturus and a range of models for Lee 2525. Values at two different ξ values are also compared. The first model for Lee 2525 uses the Brown & Wallerstein (1992) parameters. The final model for Lee 2525 is the best fit determined in this study.

			Lee 2525 stellar models					
Star	Arcturus		BW92		interim		best fit	
T_{eff} (K)	4300		4225		4050		4225	
log g	1.6		1.3		0.8		1.2	
[Fe/H] (dex)	-0.60		-0.82		-0.65		-0.70	
ξ (kms^{-1})	1.5		1.5		1.5		1.8	
[Fe I/H]	-0.61	±0.12	-0.53	±0.18	-0.64	±0.17	-0.72	±0.16
[Fe II/H]	-0.56	±0.05	-0.71	±0.05	-0.60	±0.02	-0.74	±0.08
ξ (kms^{-1})	2.0		2.0		2.0		2.0	
[Fe I/H]	-0.90	±0.13	-0.86	±0.18	-0.98	±0.20	-0.84	±0.18
[Fe II/H]	-0.69	±0.10	-0.81	±0.09	-0.72	±0.06	-0.77	±0.09

[1] [Fe I,Fe II/H] refers to the Fe abundance derived from Fe I and Fe II lines respectively.

Figure 5.4 compares [Fe/H] against χ for Arcturus, the Brown & Wallerstein (1992) model for Lee 2525 and two prospective models for Lee 2525 derived in this study. In Figure 5.4a the small spread in values is obvious for Arcturus due to the much greater resolution and higher signal-to-noise ratio of that spectrum. The Arcturus models at $\xi = 2.0$ kms^{-1} and $\xi = 1.5$ kms^{-1} are compared showing that Arcturus clearly falls in the $\xi = 1.5$ kms^{-1} regime, illustrated by the smaller spread in [Fe/H] values (see Table 5.2).

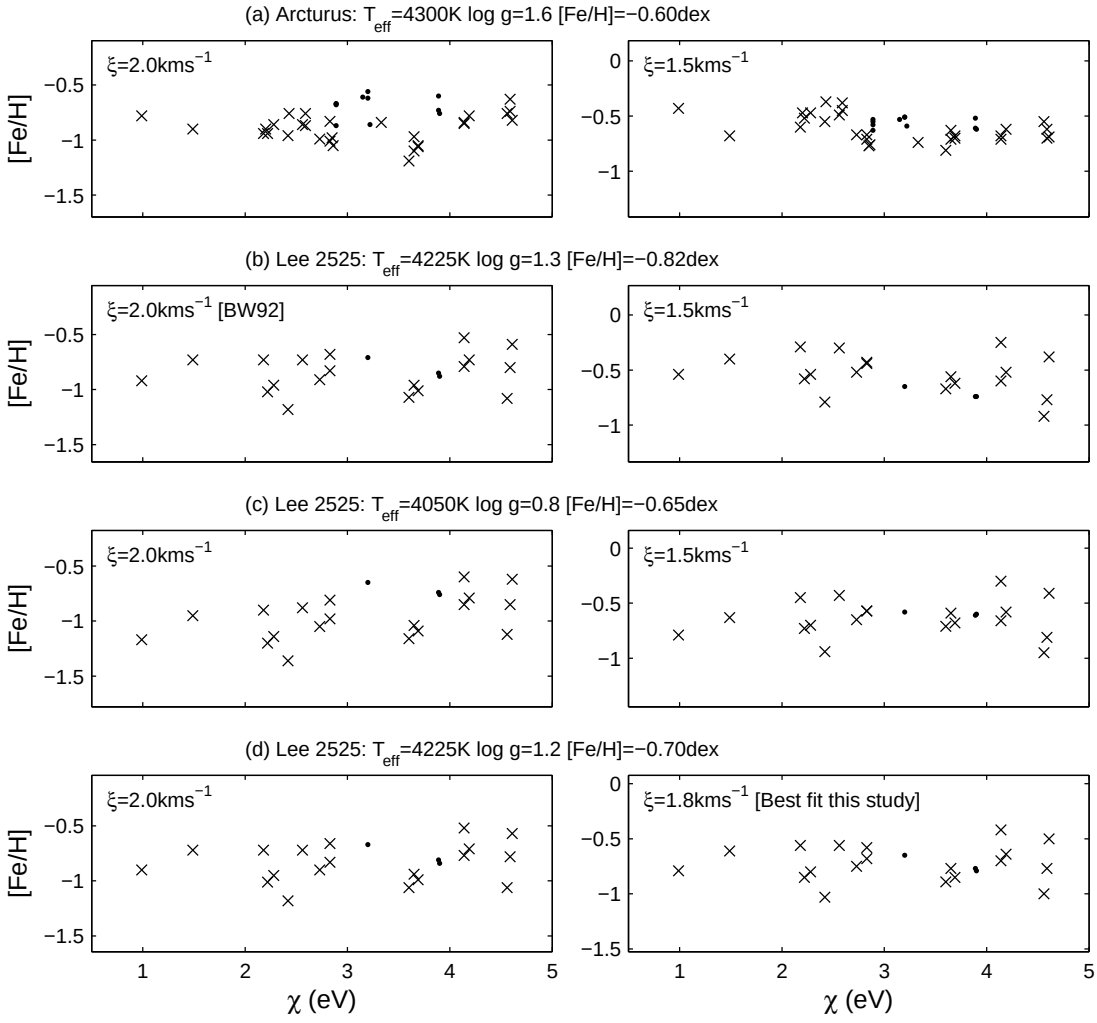

Figure 5.4: Comparison of [Fe/H] vs χ derived from Fe I ($\times$) and Fe II ($\bullet$) lines. (a) [Fe I/Fe II/H] derived for Arcturus using the measured Arcturus equivalent widths. (b) As for (a) but for the Brown & Wallerstein (1992) stellar model and the Lee 2525 measured equivalent widths. (c) As for (b), but for a high metallicity model and the Lee 2525 equivalent widths. (d) As for (b), but for the best fit stellar model determined for Lee 2525 in this study and the Lee 2525 equivalent widths. The figures in the lefthand column show the derived [Fe I/Fe II/H] values for the specified stellar atmosphere models at $\xi = 2.0$ kms^{-1}. The figures in the righthand column are the same but for $\xi = 1.5$ kms^{-1} except for the best fit model in (d).

The stellar model matching the Brown & Wallerstein (1992) stellar parameters for Lee 2525 (Figure 5.4b) show good agreement between the derived Fe I and Fe II abundance in the ξ = 2.0 kms^{-1} regime. For the ξ = 1.5 kms^{-1} regime the [Fe I,Fe II/H] values are out of equilibrium and the [Fe I/H] disagrees with the model [Fe/H] by $\sim$ 0.3 dex (see Table 5.2). Figure 5.4c uses a model for Lee 2525 at [Fe/H] = $-$0.65 dex which returns [Fe/H] = $-$0.62 dex for ξ = 1.5kms^{-1}. The spread in these values are reasonable and tighter than the spread in the ξ = 2.0 kms^{-1} regime.

Ultimately the best fit model, shown in Figure 5.4d, resides between the two ξ regimes at ξ = 1.8 kms^{-1}, where the spread in values is reasonable for both the Fe I and Fe II abundances. Hence the best fit model for Lee 2525 derived in this study returned values of T_{eff} = 4225 K, *log g* = 1.2, [Fe/H] = $-$0.70 dex and ξ = 1.8 kms^{-1} (see Table 5.2), which are in reasonable agreement with the values derived in Brown & Wallerstein (1992).

The best fit stellar model for this study returned an average [Fe/H] of $-$0.73 dex which is slightly more metal-rich than the Brown & Wallerstein (1992) value of $-$0.82 dex. Comparing these values to previous studies of RGB and AGB stars in 47 Tuc, both are more metal-poor than Alves-Brito et al. (2005), which found an average [Fe/H] of $-$0.68 dex, Carretta et al. (2004) ([Fe/H] = $-$0.67 dex), and Wylie et al. (2006) ([Fe/H] = $-$0.60 dex). However, a more recent paper, Koch & McWilliam (2008), derived an [Fe/H] of $-$0.76 dex for 47 Tuc with their stars having a range of values from $-$0.82 dex to $-$0.72 dex. Overall these studies provide reasonably similar metallicity values between the samples within the uncertainties. The analysis carried out in this study is also in good agreement within the uncertainties.

5.3 Elemental abundances in Lee 2525

Table 5.3 lists the light and heavy elemental abundances derived in this study for two models for Lee 2525, as well as the results from Brown & Wallerstein (1992). As outlined in Section 2.2.4, the light elemental abundances were derived using *abfind* in MOOG, while heavy elemental abundances were derived using MOOG's spectrum synthesis function, *synth*.

Given the similar nature of the stellar parameters for Lee 2525 derived in this study to those derived in Brown & Wallerstein (1992), element abundances using both models were calculated for a complete comparison. In Table 5.3 the abundances derived in Brown & Wallerstein (1992) are quoted in column 2 with associated uncertainties and the number of lines used. Column 5 lists the abundances derived in this study using the Brown & Wallerstein (1992) stellar model parameters, and column 7 lists the abundances derived using the best fit model determined in this study. Table 5.4 lists the changes in abundance associated with fixed changes in T_{eff}, *log g* and ξ.

Table 5.3: The light and heavy elemental abundances derived in this study from two stellar models for Lee 2525 compared with the values derived in Brown & Wallerstein (1992).

	BW92			This Study				
T_{eff} (K)	4225			4225		4225		
$log\ g$	1.3			1.3		1.2		
[Fe/H] (dex)	-0.82			-0.82		-0.70		
$\xi(kms^{-1})$	2.0			2.0		1.8		
Species	[X/H]	σ	N	[X/H]	σ	[X/H]	σ	N
Fe I	-0.83	0.16	22	-0.85	0.18	-0.72	0.16	19
Fe II	-0.82	0.17	5	-0.81	0.09	-0.73	0.08	3
	[X/Fe]	σ	N	[X/Fe]	σ	[X/Fe]	σ	N
O I	-	-	0	0.45	-	0.40	-	1
Na I	-0.01	0.06	2	0.15	0.06	0.05	0.05	2
Mg I	-	-	0	0.43	0.02	0.34	0.04	2
Al I	0.51	0.23	2	0.32	0.02	0.21	0.03	2
Si I	0.21	0.14	6	0.43	0.20	0.36	0.20	7
Ca I	-0.03	0.06	9	0.04	0.21	0.00	0.23	8
Sc I	-0.04	0.06	2	0.06	0.07	0.05	0.08	2
Ti I	0.17	0.09	7	0.24	0.19	0.14	0.18	9
Ti II	0.42	-	1	0.19	0.06	0.17	0.04	2
Zn I	0.14	0.03	2	0.04	0.15	0.05	0.16	2
Y I	0.58	-	1	0.60	0.25	0.51	0.28	2
Y II	0.41	0.47	2	0.44	-	0.54	-	1
Zr I	-0.51	0.24	3	0.37	0.04	0.36	0.04	3
Zr II	-	-	0	0.70	-	0.65	-	1
Ba II	-0.15	0.21	3	-0.32	0.02	-0.21	0.01	2
La II	0.10	0.40	2	0.34	0.01	0.31	0.03	3
Nd II	-	-	0	0.40	-	0.41	-	1
Eu II	0.44	-	1	0.48	-	0.40	-	1
	(X/Y)	σ		(X/Y)	σ	(X/Y)	σ	
ls/Fe	0.16	0.50		0.53	0.20	0.51	0.22	
hs/Fe	0.10	0.40		0.37	0.01	0.36	0.03	
hs/ls	-0.06	0.64		-0.16	0.15	-0.16	0.18	

Table 5.4: Variations in Lee 2525 abundances due to changes in the stellar parameters corresponding to ΔT_{eff} = +100 K, $\Delta log\ g$ = +0.5 and $\Delta\xi$ = +0.5 kms^{-1}.

		Δ[X/H]	
	ΔT_{eff}	$\Delta log\ g$	$\Delta\xi$
Species	+100K	+0.5	$+0.5 kms^{-1}$
Fe I	0.01	0.11	-0.23
Fe II	-0.12	0.32	-0.06
		Δ[X/Fe]	
O I	0.01	0.18	-0.01
Na I	0.09	0.01	-0.07
Mg I	0.01	0.05	-0.06
Al I	0.08	0.02	-0.08
Si I	-0.07	0.14	-0.06
Ca I	0.11	0.00	-0.24
Sc I	-0.03	0.22	-0.13
Ti I	0.17	0.05	-0.09
Ti II	-0.05	0.23	-0.11
Zn I	-0.08	0.16	-0.24
Y I	0.25	0.09	0.01
Y II	0.07	0.20	-0.50
Zr I	0.15	0.03	-0.12
Zr II	0.05	0.25	-0.03
Ba II	0.06	0.27	-0.49
La II	0.04	0.24	-0.05
Nd II	0.11	0.31	0.05
Eu II	0.12	0.38	0.11
		Δ(X/Y)	
ls/Fe	0.13	0.14	-0.16
hs/Fe	0.08	0.27	0.00
hs/ls	-0.05	0.13	0.16

5.3.1 Light elements: O to Zn

Comparing the abundances derived using the Brown & Wallerstein (1992) parameters with the Brown & Wallerstein (1992) results, there is reasonable agreement (to within 1 σ) for the majority of the light elements. The key differences were: Al I, which was less abundant in this study by 0.19 dex; Ti II, which was less abundant by 0.23 dex; Zn I, which was less abundant by 0.10 dex; and Sc II, which was over abundant by 0.10 dex.

Comparing the best fit model of this study with Brown & Wallerstein (1992), similar comments can be made. In general the light element abundances agree within 1 σ. Sc II and Zn I are also enhanced using this model compared to Brown & Wallerstein (1992), while Ti II is still significantly depleted. However, of the three sets of stellar atmosphere models, the best fit model in this study provided the best agreement between Ti I and Ti II abundances indicating a better choice of *log g*, at least in terms of Ti.

The error analysis in Table 5.4 shows that the strong lines of Sc II and Zn I used in this study are highly sensitive to changes in ξ as is the case for strong lines. Also both Sc II and Ti II are sensitive to changes in gravity as is expected for ionised lines.

This study found similar abundances patterns in this star as were previously observed in Brown & Wallerstein (1992), namely of Al and Na abundance with CN strength. Another key abundance anomaly is the Na-O anti-correlation observed in 47 Tuc (see Carretta et al. 2004 and references therein). An O abundance was not measured in Brown & Wallerstein (1992). However, it was obtained in this study using the forbidden O I line at 6300 Å. Lee 2525 is enhanced in O ([O/Fe] = +0.40 dex), while Na is not ([Na/Fe] = 0.05 ± 0.05 dex). These values fall clearly within the anti-correlated trend of [Na/Fe] to [O/Fe] shown in Figure 5 of Carretta et al. (2004).

The abundances of Mg and Al are both enhanced in agreement with previous studies. There is no indication of an anti-correlation between Mg and Al (Carretta et al. 2004; Koch & McWilliam 2008). As 47 Tuc is a metal-rich globular cluster this anomaly is not expected (Gratton et al., 2004).

With regard to Ca, previous studies have shown enhancements of this element in 47 Tuc stars (Carretta et al. 2004; Koch & McWilliam 2008). However the analysis of this star found a Ca abundance of [Ca/Fe] = 0.00 dex, in agreement with the value determined in Brown & Wallerstein (1992) ([Ca/Fe] = −0.03 dex).

The titanium abundance is slightly enhanced ($\sim$ +0.15 dex) in this study for both Ti I and Ti II. In Brown & Wallerstein (1992) Ti I was enhanced at this same level while Ti II was greatly enhanced ($\sim$ +0.42 dex). This implies either that there is a *log g* determination issue in their study due to the neutral and ionised species being out of equilibrium, or issues with the transition probabilities that were used for the Ti lines measured in their study.

The sample of five red giants in Alves-Brito et al. (2005) found the mean abundances for Ca to be [Ca/Fe] = 0.0 dex and Ti to be [Ti/Fe] $\sim$ 0.25 dex. The Ca and Ti abundances

derived in this study agree with Alves-Brito et al. (2005) within the uncertainties.

In Alves-Brito et al. (2005) a comparison of Ca abundances was made between Brown & Wallerstein (1992) and Carretta et al. (2004). The lack of enhancement in Ca in Brown & Wallerstein (1992) was noted. The stellar sample in Carretta et al. (2004) all had enhancements in Na and Ca, while the Alves-Brito et al. (2005) sample showed no enhancements in the mean abundances of both Na and Ca. While the correlation of Na with CN can be explained as leakage from the CNO cycle, a variation of Ca with Na or CN is not expected. Further investigation of Ca abundances is needed in order to clarify the reported abundances for this element in 47 Tuc.

Overall, this analysis of Lee 2525 confirms previous abundance anomalies within 47 Tuc giant branch stars with regards to Na and O, and the strength of the CN bands.

5.3.2 Heavy elements: Y to Eu

The comparison of the heavy elemental abundances in Table 5.3 show that the current analysis of Lee 2525 carried out using the Brown & Wallerstein (1992) stellar atmosphere model returns slightly higher abundances than the values found in the paper itself. Zr and La show enhancements relative to Brown & Wallerstein (1992), while Ba is depleted.

The best fit stellar model in this study also shows that Zr and La are enhanced compared with the Brown & Wallerstein (1992) values. However, there is better agreement between the Y I and Y II abundance values. There is also a large uncertainty in the Brown & Wallerstein (1992) La abundance within which the value from this study resides. While Ba is depleted here with respect to Brown & Wallerstein (1992), the effect is not so great. The Ba abundance agrees within the available uncertainties.

The Zr abundances are of particular interest as there is a significant difference between the two studies. Using the Brown & Wallerstein (1992) parameters an enhancement in Zr of [Zr I/Fe] = +0.37 dex and [Zr II/Fe] = +0.70 dex was determined in this study. The best fit model returned values of [Zr I/Fe] = +0.36 dex and [Zr II/Fe] = +0.65 dex compared with [Zr I/Fe] = −0.51 dex as determined in Brown & Wallerstein (1992). In order to investigate these differences further, Figure 5.5 shows the observed spectrum for Arcturus and Lee 2525 in a key region containing three Zr I lines used in this study, two of which were used in Brown & Wallerstein (1992).

In Figure 5.5b Lee 2525 is overlaid with a synthetic spectrum generated using the Brown & Wallerstein (1992) stellar model. The Zr abundance has been varied to show the spectrum when Zr is at the value calculated in Brown & Wallerstein (1992) ([Zr/Fe] = −0.51 dex); the Zr abundance expected from the model ([Zr/Fe] = 0.0 dex); and the best fit Zr abundance in this study for the line at 6134.57 Å ([Zr/Fe] = +0.33 dex). Similarly in Figure 5.5c, a synthesised spectrum of the best fit model in this study is overlaid on Lee 2525 with the same variations in Zr abundance, except the best fit Zr abundance for 6134.57 Å is

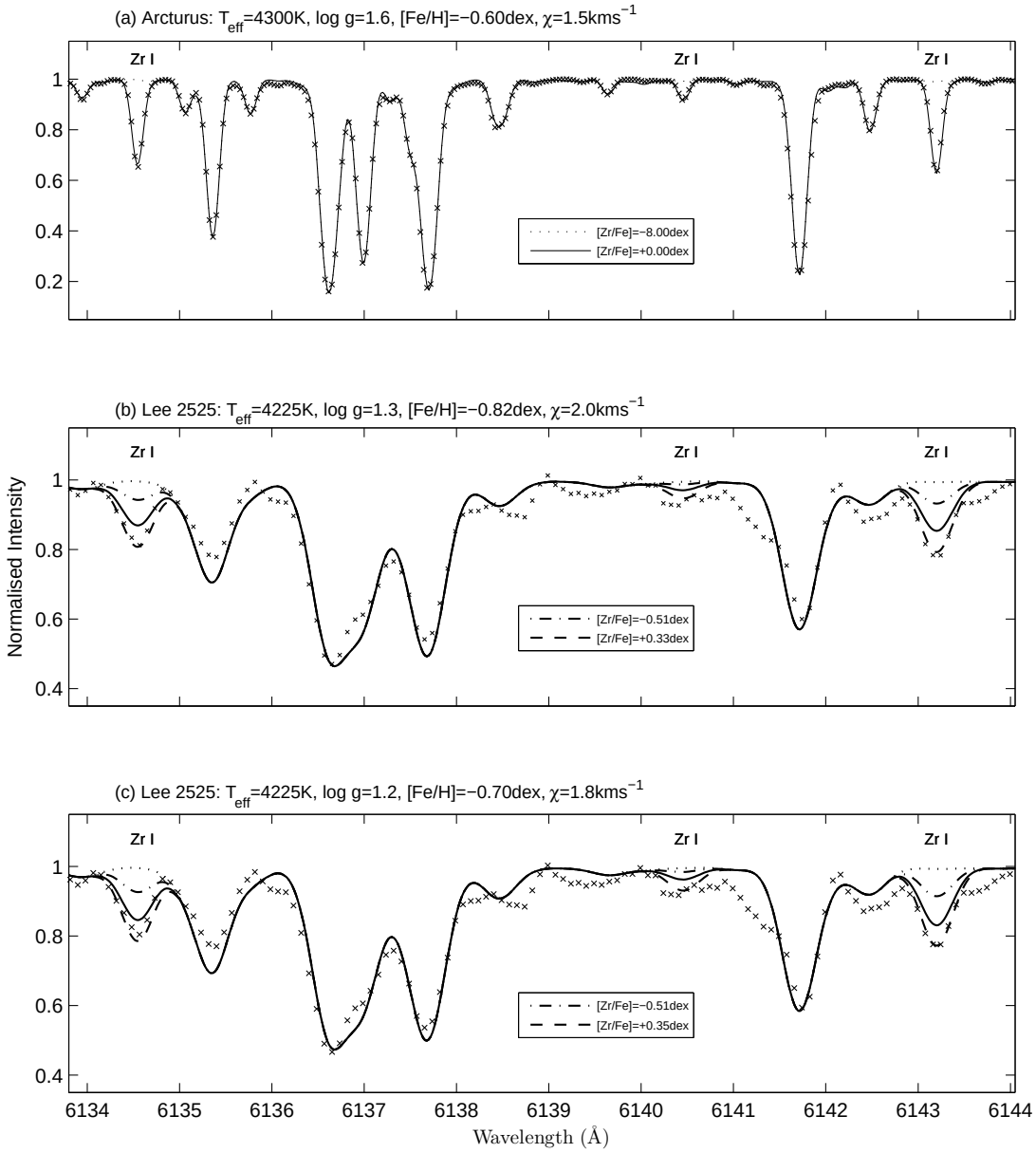

Figure 5.5: Wavelength region about 6140 Å showing the observed spectrum overlaid with spectra synthesised at different specified Zr abundances: (a) Arcturus spectrum where [Zr/Fe] = +0.00 dex provides the best fit to the Zr I lines; (b) Lee 2525 spectrum using the stellar model based on the stellar parameters specified in Brown & Wallerstein (1992). [Zr/Fe] = −0.51 dex is the best fit Zr abundance found in Brown & Wallerstein (1992). [Zr/Fe] = +0.33 dex is the best fit Zr abundance for this model in the current analysis; (c) Lee 2525 spectrum using the best fit stellar model parameters determined in this study. [Zr/Fe] = +0.35 dex is the best fit to the Zr abundance.

[Zr/Fe] = +0.36 dex. In both cases the Zr features are enhanced with respect to the model abundance, confirming the expected result of enhancements in Y coinciding with enhancements in Zr.

With Zr now similar to Y, these heavy elemental abundances fall within the spread of values determined for the *s*-process elemental abundances obtained in Wylie et al. (2006) confirming an enhancement of *s*-process elements in 47 Tuc (See Table 5.1).

5.3.3 Lee 2525 abundances with respect to Arcturus

In light of this result for Lee 2525 the [Fe/H] and [X/Fe] relative to the Sun listed in Table 5.3 were recalculated relative to Arcturus and are listed in Table 5.5. This was carried out in order to reduce any systematic errors within the analysis process by re-stating the abundances in Lee 2525 relative to a star of similar metallicity and atmospheric structure on which the process has been calibrated.

While Arcturus and Lee 2525 have similar stellar parameters, Table 5.5 shows the clear differences in their chemical make up. For the most part, Lee 2525 is less abundant in the light elements than Arcturus and more abundant in the heavy elements. Si and Sc are of similar abundance between the stars. However, Zn is greatly enhanced in Arcturus. Referring to the discussion on Sc and Zn above and their sensitivity to ξ, and bearing in mind Lee 2525 and Arcturus are in two distinct ξ regimes, their significance here should not be overstated.

Of the heavy elements, Ba II and Eu II show abundances similar to Arcturus, although the ξ sensitivity argument applies also to Ba II. As Eu is predominantly an *r*-process element, its abundance is a useful indication of how much pollution by supernovæ the gas clouds underwent prior to the formation of stars. The similar value between Lee 2525 and Arcturus implies some similar degree of exposure. The similarity in Eu abundances between globular cluster stars and field stars has been noted previously in James et al. (2004).

The comparison between the Lee 2525 and Arcturus results is a natural consequence of undertaking a differential analysis with a standard star. However, as Lee 2525 is a GC star and Arcturus is a field star, the comparison being made is really between two distinct stellar environments which is beyond the scope of this thesis. In the case of a larger set of stars within a GC a similar differential analysis would be more useful in order to reduce systematic errors within a study and thereby to produce more consistent results.

Table 5.5: [Fe/H] and [X/Fe] derived for Arcturus, and [Fe/H] and [X/Fe] calculated relative to Arcturus for the Brown & Wallerstein (1992) and best fit Lee 2525 stellar models. The results from Brown & Wallerstein (1992) are also re-calculated relative to Arcturus for comparison.

			This study	
Species	Arcturus [X/H]	BW92 $[X/H]_{Arc}$	BW $[X/H]_{Arc}$	Best Fit $[X/H]_{Arc}$
Fe I	-0.61	-0.22	-0.24	-0.11
Fe II	-0.56	-0.26	-0.22	-0.17
	[X/Fe]	$[X/Fe]_{Arc}$	$[X/Fe]_{Arc}$	$[X/Fe]_{Arc}$
O I	0.57	-	-0.12	-0.17
Na I	0.15	-0.16	0.01	-0.10
Mg I	0.34	-	0.08	-0.01
Al I	0.25	0.26	0.06	-0.04
Si I	0.20	0.01	0.23	0.16
Ca I	0.19	-0.22	-0.15	-0.19
Sc I	0.24	-0.28	-0.18	-0.20
Ti I	0.35	-0.18	-0.11	-0.21
Ti II	0.33	0.09	-0.14	-0.16
Zn I	-0.04	0.18	0.07	0.09
Y I	0.07	0.51	0.53	0.44
Y II	0.12	0.29	0.32	0.42
Zr I	0.01	-0.52	0.36	0.35
Zr II	0.12	-	0.58	0.53
Ba II	-0.19	0.04	-0.13	-0.02
La II	0.04	0.06	0.30	0.27
Nd II	0.10	-	0.31	0.32
Eu II	0.36	0.08	0.12	0.04
	(X/Y)	$(X/Y)_{Arc}$	$(X/Y)_{Arc}$	$(X/Y)_{Arc}$
ls/Fe	0.08	0.09	0.45	0.44
hs/Fe	0.07	0.06	0.30	0.29
hs/ls	-0.01	-0.03	-0.14	-0.14

5.4 [*hs*/*ls*] in 47 Tuc giant stars

The *hs* and *ls* indices were defined in order to include only the *s*-process element abundances that could be measured for this star:

$$[ls/\mathrm{Fe}] = \langle\ [\mathrm{Y/Fe}],\ [\mathrm{Zr/Fe}]\ \rangle$$
$$[hs/\mathrm{Fe}] = \langle\ [\mathrm{La/Fe}],\ [\mathrm{Nd/Fe}]\ \rangle$$

Barium was not included in the definition of [*hs*/Fe] due to the lines upon which the abundance was based being very sensitive to microturbulence (see Table 5.4). This extreme sensitivity makes the Ba abundance unreliable and a more detailed analysis of these features is necessary to reduce the uncertainties. The *hs* and *ls* indices derived for Lee 2525 in this study (see Table 5.3) were compared with Brown & Wallerstein (1992) and Wylie et al. (2006). Figure 5.6 shows the abundance ratio of the heavy *s*-process to light *s*-process elements ([*hs*/*ls*]) for Lee 2525, as well as for the other studies.

The *ls* indices for the Brown & Wallerstein (1992) stars were re-calculated to use only the Y I and Y II abundances in light of the above analysis of Zr. Considering the sample as a whole there appears to be no trend between the [*hs*/*ls*] ratio and [Fe/H]. Given these stars all exist in the same cluster and therefore have the same metallicity within some variance, if there was a spread in [*hs*/*ls*] values greater than the systematic spread on the [Fe/H] values, it would indicate that *s*-process elements were being produced in these stars.

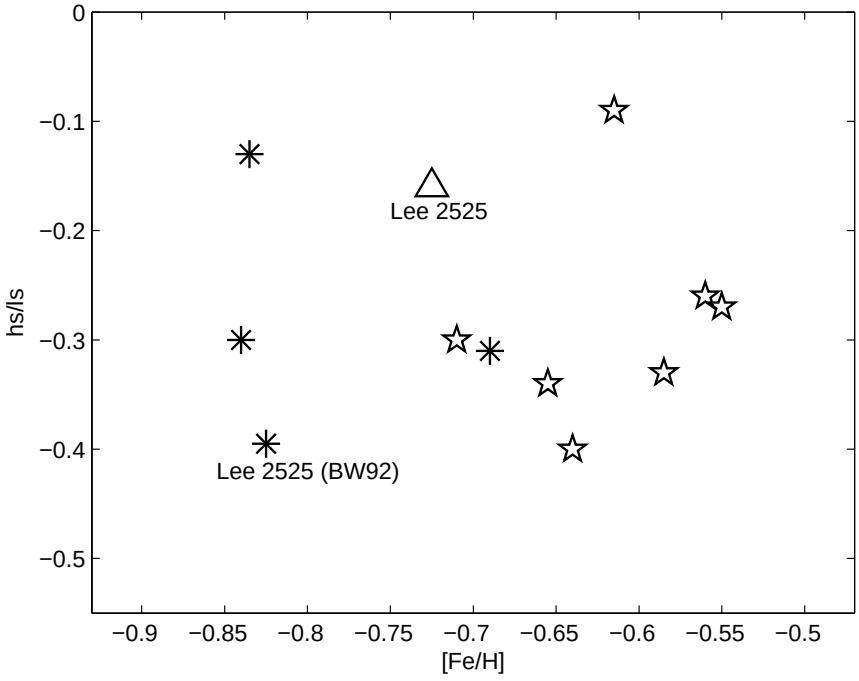

Figure 5.6: The ratio of the heavy to light *s*-process elemental abundance ([*hs*/*ls*]) for each star against [Fe/H]. (⋆) Wylie et al. (2006); (∗) Brown & Wallerstein (1992) using $[ls/\mathrm{Fe}] = \langle\ [\mathrm{Y\ I/Fe}],\ [\mathrm{Y\ II/Fe}]\ \rangle$; and (△) Lee 2525, this study.

Observational and theoretical studies have shown that for AGB stars undergoing third dredge-up the [*hs/ls*] ratio generally increases with decreasing metallicity, although the theoretical predictions are more complex (Busso et al., 2001). These will be discussed in greater detail in Chapter 6 when the entire sample of 47 Tuc stars analysed in this thesis can be considered as a whole. In the comparison of Lee 2525 with the remaining Brown & Wallerstein (1992) stars and the Wylie et al. (2006) there is no trend of [*hs/ls*] with [Fe/H] in this sample, and the spread in the [*hs/ls*] values does not exceed the spread in the [Fe/H]. This is evidence that the *s*-process elemental abundances in these stars are primordial and are not being produced internally in these stars.

5.5 Conclusion

Studies to date of *s*-process elemental abundances in 47 Tuc stars have concluded that the observed *s*-process element abundances are attributable to either the primordial chemical composition of the cluster or some pollution event early in the cluster's history, but are not due to internal nucleosynthesis within the observed stars. While within each study there is a small spread in the magnitude of the *s*-process elemental abundances, which supports the premise that these stars are not creating *s*-process elements, the magnitude of the abundances differ greatly between the respective studies. The analysis of Lee 2525 carried out here resolves a discrepancy between Brown & Wallerstein (1992) and Wylie et al. (2006) as to the magnitude of the Zr abundance in this star. This study found Lee 2525 to be enhanced in Zr at [Zr/Fe] = +0.51 dex, which is in agreement with the enhancement found for Y of [Y/Fe] = +0.53 dex, another light *s*-process element. This is in line with *s*-process element abundance enhancements found in 47 Tuc giant branch stars in Wylie et al. (2006). The Na-CN correlation reported in Brown & Wallerstein (1992) for Lee 2525 was also found here, as well as an Na-O anti-correlation in agreement with other studies of light elemental abundances in 47 Tuc stars (Carretta et al., 2004). Therefore, these results support the premise that the abundance anomalies observed in 47 Tuc have a primordial or pollution based-origin and are not being created internally within the currently observed stars, as was concluded by the other studies.

While this analysis has resolved a discrepancy between two key papers, the overall *s*-process elemental abundance distribution within 47 Tuc is still not clear. It is necessary to expand the sample of 47 Tuc stars analysed for their *s*-process element abundances in order to consolidate the results found here with those from other studies. This analysis was carried out differentially with respect to Arcturus in an effort to reduce systematic errors by calibrating the analysis process to a standard star of similar stellar parameters. This provides a solid framework for the chemical abundance analysis that is carried out in the following chapter of five 47 Tuc giant stars observed at high resolution on the VLT.

Chapter 6

High-resolution studies: AGB stars in 47 Tuc

This analysis builds on the work carried out in the previous chapter by investigating the heavy elemental abundances in five 47 Tuc AGB stars observed using UVES on the VLT. This sample of high resolution spectra provided the opportunity to measure accurate element abundances and compare them to the range of values already obtained for 47 Tuc giant stars in previous studies.

6.1 Observations and analysis

In July 2003 forty seven AGB stars were observed in six galactic gobular clusters (GCs) in a study of mass loss rates (McDonald & van Loon, 2007). The set contained nine stars in 47 Tuc which could potentially be analysed for their chemical abundances, in particular the *s*-process elemental abundances. The spectra covered the wavelength range 6100 Å to 9000 Å, with a gap of ∼80 Å around 8000 Å due to the split between the two CCDs. The spectra are of high resolution at $R \sim 110,000$ with good signal to noise ($70 \leq$ SNR per pixel ≤ 110).

Table 6.1 lists the observational details for McDonald & van Loon (2007) and other key high resolution studies, the results of which were discussed in Section 1.3.1 and compared in Section 6.5.2 with the results of this analysis.

The data were provided to the author as fully reduced spectra from the VLT reduction pipeline requiring only normalisation. McDonald & van Loon (2007) divided the sample into those with infra-red (IR) excess and those without. Cluster membership analysis was carried out and it was determined from radial velocities that all the stars in 47 Tuc were likely members of this cluster (see McDonald & van Loon (2007) for further discussion on variability and cluster membership). Five of the nine stars observed in 47 Tuc were analysed in this study. The remaining four stars were too cool and had large molecular features that made continuum placement and thus equivalent width measurement very difficult.

Table 6.1: Summary of the observations made for the key studies of heavy element abundances in 47 Tuc stars. Listed are the size of the 47 Tuc stellar sample, the telescope, spectrograph, resolution and signal to noise per pixel (S/N per pix) for Brown & Wallerstein (1992) (BW92); James et al. (2004) and Carretta et al. (2004) (J04/C04); Alves-Brito et al. (2005) (AB05); Wylie et al. (2006) (W06); McDonald & van Loon (2007) (McDvL07); Worley et al. (2009) (W09)

Paper	BW92	J04/C04	AB05	W06	McDvL07	W09
No. Stars	4	12	5	7	5	1
Telescope	CTIO 4 m	VLT	VLT	AAT	VLT	ANU 2.3 m
Spectrograph	échelle	UVES	UVES	UCLES	UVES	échelle
Resolution	$\sim 20,000$	$> 40,000$	$> 40,000$	$\sim 40,000$	$\sim 110,000$	$\sim 20,000$
S/N per pix	> 80	$20 - 40$	~ 200	> 40	$70 - 110$	> 20

Figure 6.1 shows the spectral region between 6120 Å and 6190 Å for all of the 47 Tuc stars. The stars have undergone the general normalisation, as outlined in Chapter 2, and are ordered in sequence with temperature increasing downwards. The key molecular bands for this region are indicated, as well as the Fe lines used in the analysis of these stars and the continuum regions used in the local normalisation about each Fe line. For the hottest stars the spectrum is reasonably flat. However, the four coolest stars show strong contamination, most likely due to the TiO bands, which makes continuum placement difficult. These stars

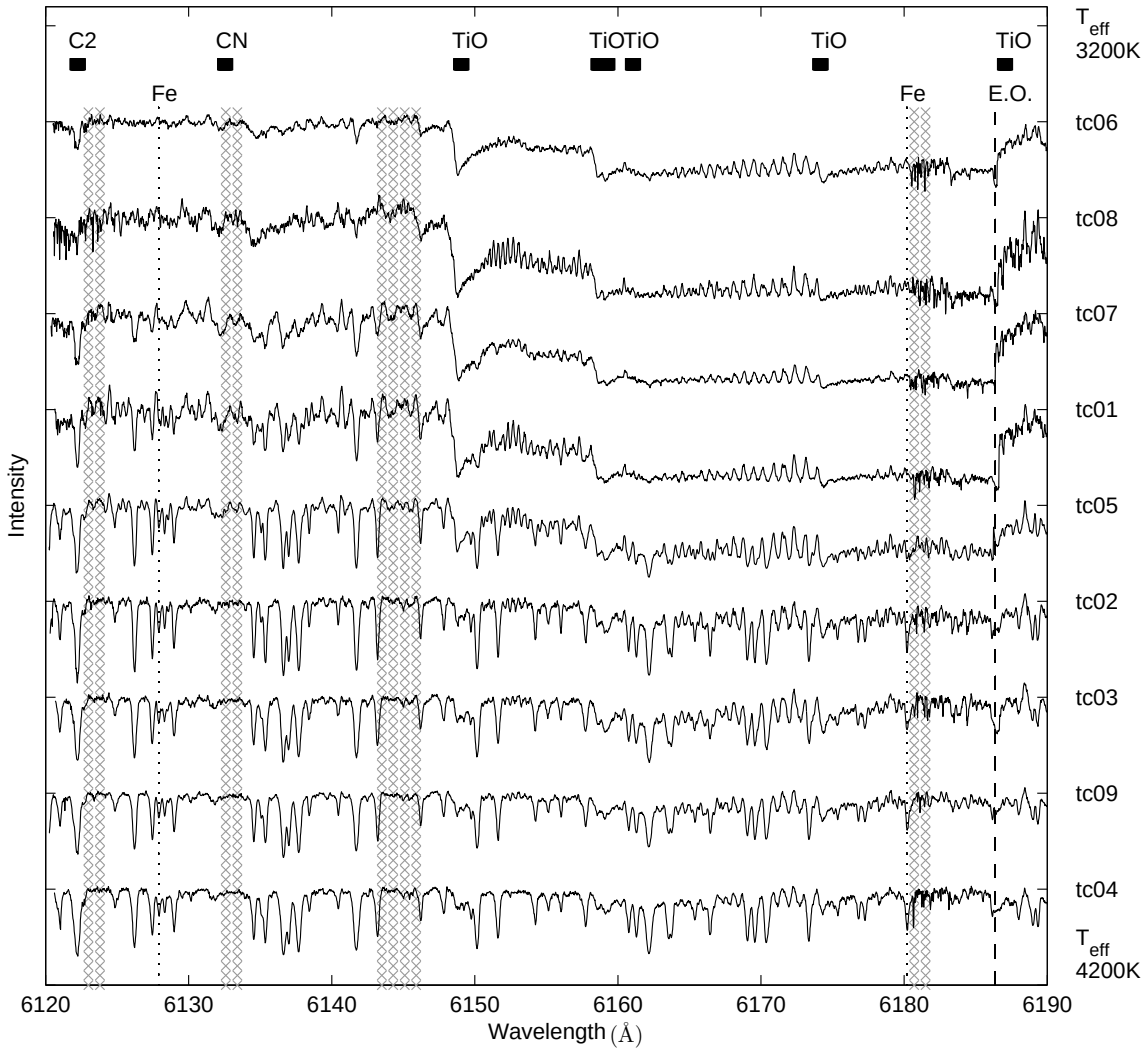

Figure 6.1: Section of spectra, from 6120 Å to 6190 Å, for each star in the 47 Tuc sample stacked in T_{eff} sequence increasing downwards. The location of C_2, CN and TiO bands are indicated at the top. The location of the Fe lines in this region that were used in the analysis are shown as dotted vertical lines. The échelle order break (E.O.) is indicated as a vertical dashed line. The vertical shaded regions are the continuum regions used for normalisation about each Fe line. The five hottest stars were analysed in this study (*tc*05, *tc*02, *tc*03, *tc*09 and *tc*04). The remaining stars were excluded as the spectral lines were considerably broader and the continuum of the spectra were contaminated by strong molecular bands.

were set aside in favour of the five hottest stars (*tc*05, *tc*02, *tc*03, *tc*09 and *tc*04) which provided a reasonable sample with which to pursue the heavy elemental abundance analysis for 47 Tuc. The star designated *tc*05 also shows substantial contamination by molecular bands. It was analysed to investigate the difficulties involved when deriving abundances from heavily contaminated spectra. Hence there an inherently greater uncertainty associated with the results from this star. The normalisation and analysis of these stars followed the procedure outlined in Section 2.4.

The stellar parameters for these stars were derived in McDonald & van Loon (2007) using spectral typing. The derived T_{eff} and corresponding *log g* found in that study are listed in Table 6.2 as well as the parameters determined for Arcturus (see Chapter 2), and those determined for Lee 2525 (see Chapter 5). The designations used for each star from McDonald & van Loon (2007) and any previous designations are listed. The IR colour index, $(\text{K-[12]})_o$, is also included for each star where possible (Ramdani & Jorissen 2001; Origlia et al. 2002). A star has an IR excess if $(\text{K-[12]})_o \geq 0.65$ (Origlia et al., 2002), which is the case for the five *tc* stars studied here.

In this analysis two sets of spectroscopic stellar parameters were derived for each star. This will be discussed in full in the following sections. However, the final parameters determined in this analysis are those listed as Spectroscopic 2 in Table 6.2.

6.1.1 T_{eff} and *log g* classification

McDonald & van Loon (2007) carried out an in-depth investigation to determine the atmospheric parameters of the stars based on their spectral type. The stellar sample covered a range of temperatures and the derived values for T_{eff} and *log g* (see Table 3 of McDonald & van Loon 2007), along with the uncertainties, are displayed in Figure 6.2. The 47 Tuc AGB star Lee 2525 that was analysed in Chapter 5 is also shown, along with two 12.5 Gyr isochrones at [Fe/H] = −1.0 dex and −0.5 dex for comparison (Dotter et al., 2007).

The placement of these stars in the $T_{eff}, log\ g$ space is problematic. The five stars analysed here appear to be in better agreement with the [Fe/H] = −1.0 dex isochrone and above the tip of the AGB. The remaining four stars are much cooler and of much lower gravity placing them well above the RGB tip for both isochrones. A further investigation was carried out into deriving stellar parameters from a variety of photometric values.

The temperatures and gravities derived in McDonald & van Loon (2007) were compared with values derived from a range of photometric colours using the equations derived in Alonso et al. (1999). The available photometry for each of the five stars are listed in Table 6.3.

A complete set of $(J - K)$ values was available from both McDonald & van Loon (2007) and 2MASS. There is some disagreement between these two sets for *tc*04 and *tc*09. As these are variable stars, differences between reported photometric magnitudes are not unexpected depending on when the observations were made.

Table 6.2: The stellar parameters for Arcturus and the 47 Tuc stars where *tc* identifies the stars from McDonald & van Loon (2007). The temperatures and gravities for the 47 Tuc stars derived in McDonald & van Loon (2007) are listed (McD07), while the photometric temperature and gravity for Lee 2525 is based on 2MASS $(V-K)$ photometry using the Alonso et al. (1999) calibration equations. The infra-red (IR) excess, defined as $(\text{K-[12]})_o^b \geq 0.65$, are included where possible. Two sets of spectroscopic parameters were derived in this study, the final parameters are listed as Spectroscopic 2. See Section 6.1.2 and 6.2 for discussion of the Spectroscopic 1 and 2 parameters.

		McD07			Spectroscopic 1				Spectroscopic 2			
Star ID	Other	T_{eff} (K)	*log g*	$(\text{K-[12]})_o^b$	T_{eff} (K)	*log g*	ξ (kms^{-1})	[Fe/H]	T_{eff} (K)	*log g*	ξ (kms^{-1})	[Fe/H]
Arcturus	α Boo	-	-	-	4300	1.6	1.5	−0.60	-	-	-	-
Lee 2525[a]		4200	1.30	−0.10[c]	4225	1.2	1.8	−0.70	-	-	-	-
*tc*02		4170	0.64	0.70	4100	1.0	2.0	−0.85	4060	0.50	1.5	−0.90
*tc*03		3985	0.30	0.76	3900	0.4	1.5	−0.75	4030	0.55	1.5	−0.90
*tc*04	LW8	4170	0.60	1.39	3950	0.5	1.5	−0.75	4060	0.60	1.5	−0.90
*tc*05	LW19	3775	0.10	2.14	4000	1.3	1.5	−0.85	3850	0.00	1.5	−0.95
*tc*09	V18	4170	0.15	1.37[c]	4100	0.9	1.5	−0.75	4100	0.10	1.5	−0.95

[a] 2Mass V-K Photometry
[b] Origlia et al. (2002)
[c] Ramdani & Jorissen (2001)

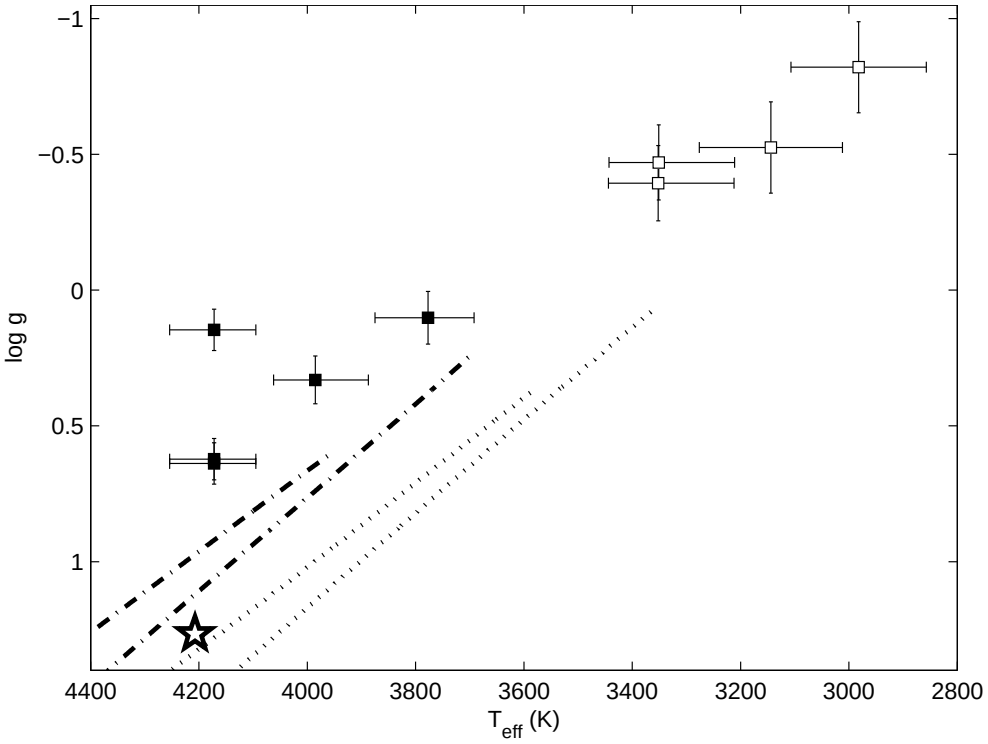

Figure 6.2: $T_{eff}, log\ g$ space of 47 Tuc showing the spectral stellar parameters and uncertainties from McDonald & van Loon (2007). The five stars analysed here (■) are shown, as well as the remaining four stars (□) from Figure 6.1 for comparison. Lee 2525 (star) is also included. The dash-dot lines represent the AGB and RGB of a 12.5 Gyr isochrone at [Fe/H] = −1.0 dex. The dotted lines represent the AGB and RGB of a 12.5 Gyr isochrone at [Fe/H] = −0.5 dex (Dotter et al., 2007).

Table 6.3: Reported photometry values for each of the five 47 Tuc AGB stars and Lee 2525. Two sets of J and $(J-K)$ values are listed, the first set from McDonald & van Loon (2007) (McD07) and second set was obtained from 2MASS. The V and $(B-V)$ values were obtained from SIMBAD for each star where possible. The V values were then used to derive $(V-K)$ values using the K values from McDonald & van Loon (2007) and 2MASS respectively.

	McD07		2MASS		SIMBAD		McD07	2MASS
	J	$(J-K)$	J	$(J-K)$	V	$(B-V)$	$(V-K)$	$(V-K)$
Lee 2525	-	-	10.14	0.87	12.43	1.29	-	3.16
*tc*02	8.80	1.01	8.80	1.01	-	-	-	-
*tc*03	8.37	1.02	8.37	1.02	-	-	-	-
*tc*04	8.77	1.02	8.02	0.94	11.82	-	4.07	4.75
*tc*05	8.30	1.14	8.29	1.18	11.85	-	4.69	4.73
*tc*09	8.67	2.11	8.50	1.07	11.67	1.88	5.11	4.24

The temperatures and gravities calculated from each set of photometric values are compared with the McDonald & van Loon (2007) values in Figure 6.3. The set of values for each star are connected by a line in order to clearly show the possible range of values. The McDonald & van Loon (2007) values appear to be considerably hotter than those derived from the photometric sets. Lee 2525 was included to compare the differences between photometric stellar parameters derived for a well-defined star. Lee 2525 falls on the AGB of the isochrone with [Fe/H] = −0.5 dex, although potentially could lie on the RGB for lower metallicities. The majority of the *tc* stars lie above the tip of the (Dotter et al., 2007) isochrones. However, while the RGB isochrones show the real tip of the RGB in each case, the AGB isochrone calculations stop before the thermally pulsing AGB phase begins and so the 'real' AGB extends beyond the limit indicated by the lines in Figure 6.2.

The parameters derived from $(V-K)$ and $(B-V)$ are in good agreement for Lee 2525 while the $(J-K)$ values are much cooler. Alonso et al. (1999) notes a divergence of ~ 200 K between temperatures derived from different colours for temperatures less than 4500 K. Stellar parameters derived from $(V-K)$ are expected to provide the best temperature

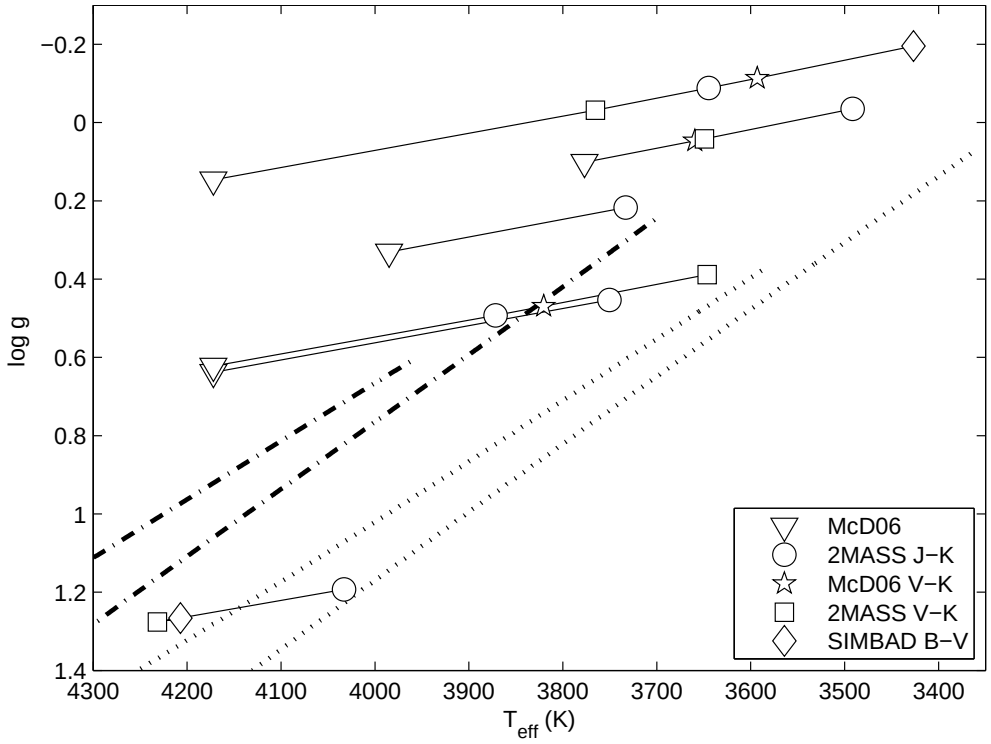

Figure 6.3: T_{eff}-*log g* space of 47 Tuc showing the spectral type stellar parameters from McDonald & van Loon (2007) compared with parameters derived from a range of photometric values. The set of values associated with each star are connected in a line. Lee 2525 is also included and has the highest gravity of the sample. The different sets correspond to the lists in Table 6.3. The dash-dot lines represent the AGB and RGB of a 12.5 Gyr isochrone at [Fe/H] = −1.0 dex. The dotted lines represent the AGB and RGB of a 12.5 Gyr isochrone at [Fe/H] = −0.5 dex (Dotter et al., 2007). The AGB, as calculated by Dotter et al. (2007), only covers the 'early AGB' phase. The 'real' AGB extends to the region in the top righthand corner of the figure.

determination due to these colours being less affected by line blanketing and convection. They also show little sensitivity to metallicity (Bessell, 2004).

The temperatures derived from the 2MASS $(J-K)$ values, which were available for all the stars, are much cooler than the McDonald & van Loon (2007) temperatures. Their location in the $T_{eff}-log\ g$ space is in better agreement with the [Fe/H] $= -0.5$ dex isochrone. The values from the other colours agree best with the 2MASS $(J-K)$ values. No colour stood out as being more consistent than the others but it was clear that the McDonald & van Loon (2007) values gave the hottest estimate for the stars. Given the associated uncertainties with the McDonald & van Loon (2007) values (see Figure 6.2), and the tendency for the $(J-K)$ photometry to under-estimate temperatures we decided to use these two results as upper and lower limits on the range of temperatures that could be used in the derivation of the stellar parameters for each star. Figure 6.4 shows the range of potential values for each star in T_{eff} and *log g* limited by the McDonald & van Loon (2007) and 2MASS $(J-K)$ temperatures.

All nine stars of the sample are shown in Figure 6.4 for comparison, although only the five hottest stars were analysed in the following sections. The range in temperature and gravity values for each star were used as the starting point for determining the spectroscopic stellar atmosphere models. The stars were then analysed for their chemical abundances using *synth* in MOOG (Sneden, 1973).

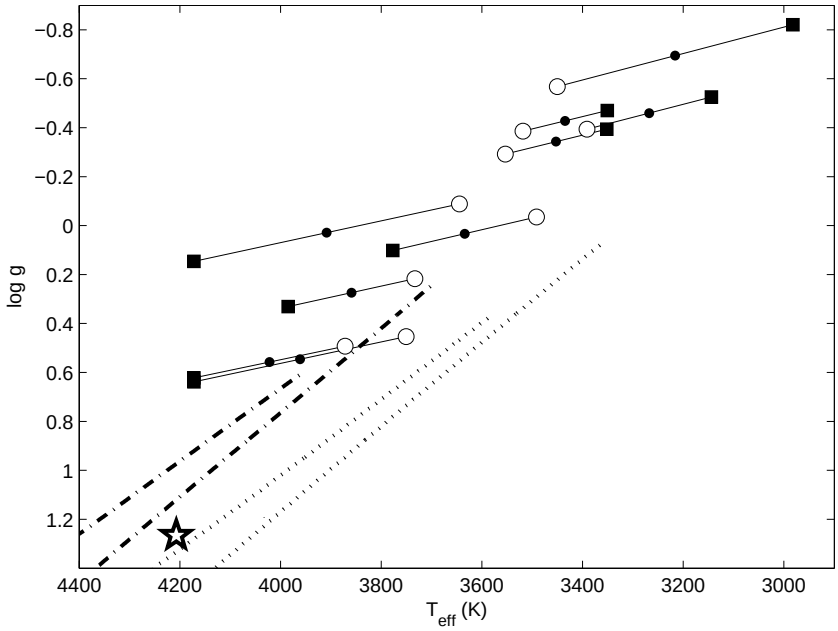

Figure 6.4: $T_{eff}-log\ g$ space of 47 Tuc showing the range of temperatures and gravities for each star limited by the McDonald & van Loon (2007) (■) and the 2MASS $(J-K)$ (◯) stellar parameters. The mean of the McDonald & van Loon (2007) and 2MASS $(J-K)$ parameters (•) are also indicated. Lee 2525 (star) and the isochrones as for Figure 6.3 are included for reference.

6.1.2 Spectroscopic derivation of stellar parameters

The sample of stars in this study were of sufficiently high resolution that determination of the spectral parameters of the stars could be carried out using a curve-of-growth analysis following the procedure outlined in Section 2.2. Section 2.4 summarises the specific normalisation required for this dataset. The equivalent widths for the Fe I and Fe II lines were measured in order to determine the stellar parameters for each of the stars. Spectrum synthesis was then used in order to determine the heavy elemental abundances following the procedure outlined in Section 2.2.4.

The stellar parameters were initially derived using the assumptions of LTE based on the equivalent width measurement of as many weak to medium strength Fe I and Fe II lines as possible. The initial estimates for the stellar parameters for these stars are listed as Spectroscopic 1 in Table 6.2. The stellar parameters for Arcturus and Lee 2525 that were derived in Chapters 2 and 5 respectively are also included.

The initial stellar models that were derived for the 47 Tuc AGB stars were more metal-poor than had been reported in previous studies. The range in metallicities for the Spectroscopic 1 stellar models was between -0.75 dex and -0.85 dex. Recent papers report more metal-rich values ~ -0.65 dex (Alves-Brito et al. 2005; Wylie et al. 2006). However, the most recent paper by Koch & McWilliam (2008) derived an [Fe/H] of -0.76 dex for 47 Tuc. Their stellar sample ranged in metallicity values from -0.82 to -0.72 dex. The Spectroscopic 1 models are in reasonable agreement with this result.

6.2 Non-LTE effects in Fe I lines

The stellar parameters for all the stars in this study were derived using MOOG which assumes LTE (Sneden, 1973). However, the cool temperatures and low gravities of these AGB stars means that LTE cannot be assumed for all species. Figure 6.5 shows [Fe I,Fe II/H] against χ derived using the best fit stellar atmosphere model in the curve-of-growth analysis for Arcturus, Lee 2525 and *tc*04. For Arcturus and *tc*04 the most appropriate choice of ξ was found to be 1.5 kms^{-1}, while $\xi = 1.8$ kms^{-1} provided the best fit for Lee 2525. These are shown in the figures in the righthand column of Figure 6.5. The figures in the lefthand column are of the same models but all with $\xi = 2.0$ kms^{-1} to show the effect of ξ on the Fe abundance derived from Fe I and Fe II lines.

The stellar parameters specified as Spectroscopic 1 in Table 6.2 were derived using Fe I lines with the range of χ from 0.0 eV to 5 eV. The mean of the Fe abundance derived from Fe I lines was required to balance with the Fe abundance from Fe II lines for the stellar parameters, in particular *log g*, to be correct.

Considering Arcturus in Figure 6.5a at $\xi = 2.0$ kms^{-1}, there is a distinct spread in the Fe abundance derived from the Fe I lines. That spread has been significantly reduced in

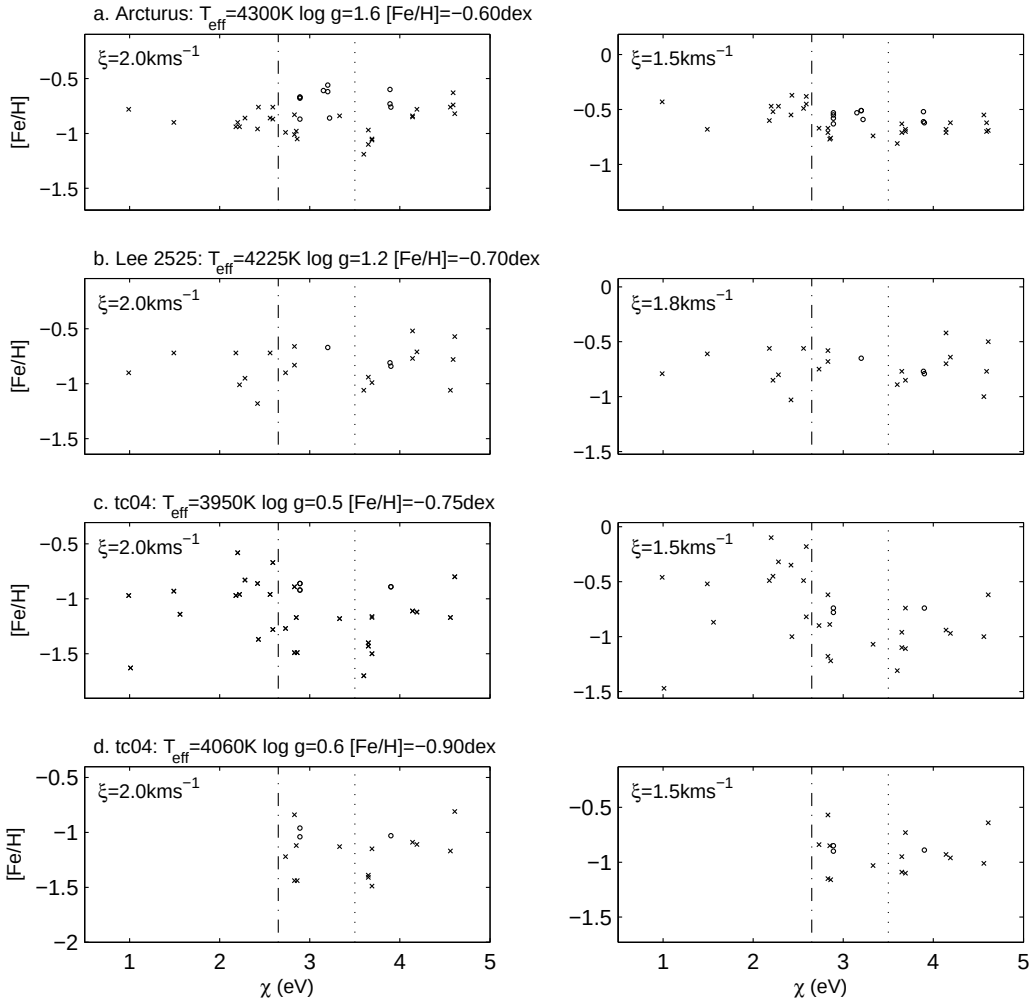

Figure 6.5: Plots of [Fe/H] vs χ for the Fe lines in each of Arcturus, Lee 2525 and two models for *tc*04. The lefthand column shows the derived values for the models at $\xi = 2.0$ kms^{-1}, while the righthand column is for $\xi = 1.5$ kms^{-1}, except for Lee 2525. Crosses indicate Fe I lines, circles indicate Fe II lines. The dash-dot line indicates an χ limit of 2.65 eV, the dotted line indicates an χ limit of 3.5 eV.

the $\xi = 1.5$ kms^{-1} model. The Fe abundance derived from the Fe II lines is also brought into balance with the abundance derived from the Fe I lines in the $\xi = 1.5$ kms^{-1} model. However, for the $\xi = 1.5$ kms^{-1} model, there is a distinct break in the derived abundances at $\chi \sim 2.65$ eV. The Fe I lines below this limit return a higher average Fe abundance than the Fe I lines above this limit, although both sets agree within the uncertainty of the derived [Fe I/H] for Arcturus of [Fe I/H] $= -0.61 \pm 0.12$ dex.

The discrepancy between derived abundances from high excitation potential compared with low excitation potential lines has been well documented. In a spectroscopic analysis of two giants, Pollux and Arcturus, Ruland et al. (1980) made a detailed investigation of departures from LTE in these stars. The primary effect that was noted was an underabundance of the element, assuming an LTE analysis, when derived from low excitation potential lines. This was attributed to overionisation of the element for low excitation levels. These lines are formed in high atmospheric layers and so are more susceptible to non-LTE effects, compared with the high excitation potential lines which form much deeper in the stellar atmosphere. This departure from LTE for low excitation potential lines skews the overall LTE abundance to a lower value than if the departures were taken into account. Ruland et al. (1980) recommended using element lines whose excitation potential (χ) is greater than the element's ionisation potential minus 4.4 eV. This was an arbitrary number which provides a reasonable sample of high excitation line for any particular element.

In the case of Fe I this limits the sample to lines with $\chi \geq 3.5$ eV, although it was specified in Ruland et al. (1980) that the exact division was not critical. This limit is indicated on each of the plots in Figure 6.5. However, based on Arcturus, a natural break occurs at $\chi = 2.65$ eV as noted above. No such break is seen in Lee 2525 but it is clearly seen in *tc*04. On the basis of the clear χ break seen in Arcturus it would be reasonable to expect to see a similar break in Lee 2525. However, the lower resolution and SNR of this observation of Lee 2525 compared to the Arcturus atlas is likely to be masking the effect. Follow up observation of this star at a higher resolution and SNR is necessary to investigate this further.

Table 6.4 lists the overall mean Fe abundance from Fe I lines, the mean Fe abundance from Fe II lines, and the mean Fe abundance from Fe I lines above and below the $\chi = 2.65$ eV limit for each model displayed in Figure 6.5. The models with $\xi = 1.5$ kms^{-1} ($\xi = 1.8$ kms^{-1} for Lee 2525) are listed first corresponding to the righthand column in Figure 6.5. The remaining rows in Table 6.4 list the same quantities for the same models but with $\xi = 2.0$ kms^{-1}, corresponding to the lefthand column in Figure 6.5.

Overall the $\xi = 2.0$ kms^{-1} results are much more metal poor than the $\xi = 1.5$ kms^{-1} results with a greater spread in values, particularly for the $\chi > 2.65$ eV subgroup. This is evident for all the stars including Lee 2525 and can be seen when comparing the two columns in Figure 6.5. Also the mean Fe abundance from Fe I lines are better balanced with the mean Fe abundance for Fe II lines for the lower values of ξ.

Closer consideration of the $\xi = 1.5$ kms^{-1} models in Figure 6.5 shows that the break

Table 6.4: Comparison of [Fe/H] against χ for Arcturus, Lee 2525 and two models for *tc*04.

			tc04 Best Fit Model	
Star	**Arcturus**	**Lee 2525**	χ(Fe I)<5eV	χ(Fe I)>2.65eV
T_{eff} (K)	4300	4225	3950	4060
log g	1.6	1.2	0.5	0.6
[Fe/H]	−0.60	−0.70	−0.75	−0.90
ξ (kms^{-1})	1.5	1.8	1.5	1.5
[Fe I/H] χ <5eV	−0.61 ±0.12	−0.72 ±0.16	−0.76 ±0.38	−0.93 ±0.18
[Fe I/H] χ <2.65eV	−0.49 ±0.09	−0.74 ±0.18	−0.53 ±0.40	-
[Fe I/H] χ >2.65eV	−0.69 ±0.06	−0.71 ±0.16	−0.98 ±0.20	−0.93 ±0.18
[Fe II/H]	−0.56 ±0.05	−0.74 ±0.08	−0.75 ±0.02	−0.88 ±0.03
ξ (kms^{-1})	2.0	2.0	2.0	2.0
[Fe I/H] χ <5eV	−0.90 ±0.13	−0.84 ±0.18	−1.10 ±0.35	−1.20 ±0.21
[Fe I/H] χ <2.65eV	−0.87 ±0.07	−0.89 ±0.18	−0.94 ±0.38	-
[Fe I/H] χ >2.65eV	−0.92 ±0.15	−0.82 ±0.18	−1.26 ±0.24	−1.20 ±0.21
[Fe II/H]	−0.69 ±0.10	−0.77 ±0.09	−0.89 ±0.03	−1.01 ±0.04

in abundance at $\chi = 2.65$ eV observed in Arcturus is also present for the *tc* star. The expected result is that the abundances derived from the low χ lines are underabundant with respect to the abundances derived from the high χ lines in an LTE analysis. The Fe I abundance subgroups for both Arcturus and *tc*04 are contrary to this expected result. Figure 6.5 and Table 6.4 show that in this analysis the low excitation potential lines return an LTE overabundance compared with the high excitation potential lines.

What is interesting to note is that for the best fitting models derived using all the Fe I lines with $\chi \leq 5$ eV, the Fe II abundance is in slightly better agreement with the mean abundance derived from the high excitation potential lines. This provides some confirmation that the high excitation potential lines provide a more reliable abundance than the low excitation potential lines. Also the scatter in the overall abundance is mainly due to the low excitation potential lines, as the high excitation lines have a relatively smaller spread in abundance for both Arcturus and particularly *tc*04 (see Table 6.4). However, there is still a reasonably large spread in the *tc*04 abundances of the high excitation Fe I lines compared to Arcturus, and even Lee 2525. The inherent uncertainties in the measurement of these lines due to continuum placement, as discussed previously, may be the cause and alternate methods to ensure correct continuum placement using synthetic spectra are being investigated.

For the $\xi = 2.0$ kms^{-1} models the mean Fe abundance derived from Fe II lines is higher than both Fe I subgroups showing that the $\xi = 1.5$ kms^{-1} regime is the more appropriate choice. The higher ξ does smooth out the discrepancy in χ, even for Arcturus, showing a better abundance agreement in general between the high and low excitation potential Fe I lines. However, the Fe abundances derived from the Fe I and Fe II lines are out of equilibrium at this ξ.

While changes in ξ seem to reduce the abundance discrepancy between the high and low excitation Fe I lines, it has been noted that increasing T_{eff} and *log g* will have the same effect and can bring the Fe I and Fe II abundances back into agreement. A detailed review of departures from LTE and the effect on stellar abundances was carried out in Asplund (2005). It was commented that an LTE analysis of late type stars using Fe I lines at all χ will overestimate T_{eff} by ~ 200 K in low [Fe/H] stars. Coaxing a best fit between the high and low excitation potential lines therefore leads to a derived model that is much hotter than the star being analysed.

The recommended course of action is to use 3D models that better represent the stellar atmosphere and the departures from non-LTE. This is an advancing field of research and such an analysis of these stars would be useful in future work. For the purposes of the current study the alternative course of action is to discard the low excitation potential lines and derive stellar parameters based solely on the high excitation potential Fe I lines. A differential analysis to a standard star of similar atmospheric structure and metallicity, in this case Arcturus, will help to reduce systematic errors introduced by the LTE analysis. This type of differential analysis between Arcturus and 47 Tuc giant stars has been carried

out recently in Koch & McWilliam (2008) who found the metallicity of 47 Tuc stars to be more metal poor, at [Fe/H]= −0.76 dex, than other recent studies (Alves-Brito et al. 2005; Wylie et al. 2006). In a study of similarly cool AGB stars Smith & Lambert (1990) also discarded the low excitation potential Fe I lines in order to minimise the effects of departures from LTE on the derived stellar parameters. A differential analysis was also carried out, but with respect to the cool giant α Tau, in order to reduce systematic errors.

In light of the literature on departures from LTE the stellar parameters for the AGB sample were re-derived repeating the procedure outlined in Chapter 2 but using only Fe I lines with $\chi \geq 2.65$ eV. The resulting parameters for each star are listed as Spectroscopic 2 in Table 6.2 and also included in Table 6.7.

The reduction of the Fe I line list to include only the lines with $\chi \geq 2.65$ eV meant that deriving a temperature using the [Fe/H] with χ calibration was no longer reliable due to the limited range in χ. It was necessary to return to the T_{eff} values listed in Table 6.2 and accept a temperature that fell between the McDonald & van Loon (2007) T_{eff} and the T_{eff} derived from the 2MASS $(J-K)$ photometry as discussed in Section 6.1.1. The derived [Fe/H] based on the reduced Fe I list are up to 0.2 dex more metal poor than the previously derived values, which was a result that could be predicted from the analysis of the Fe I subgroups carried out above. Arcturus was not re-analysed as the discrepancy between the high and low excitation potential Fe I lines, while apparent, was of a much smaller spread than that observed in the *tc* stars. A differential analysis between Arcturus and the *tc* stars was pursued to further reduce errors. However relying solely on a differential analysis between Arcturus and the *tc* stars, using the full Fe I list, would still have produced the spurious metallicities for these stars. The culled Fe I list was a necessary step in the derivation of the stellar atmospheric parameters for the *tc* stars.

Figures 6.5c and d compare the two spectroscopic models derived for *tc*04, Spectroscopic 1 and Spectroscopic 2 respectively. The full Fe I line list used in Spectroscopic 1 shows the lower metallicity for the high χ lines. It is this subset of Fe I lines that were then used to derive the Spectroscopic 2 model (see Table 6.2) and are displayed in Figure 6.5d. While not as metal poor as Figure 6.5c predicts, the resulting [Fe/H] derived for the Spectroscopic 2 model is much more metal poor than is expected for 47 Tuc. While Koch & McWilliam (2008) revises the 47 Tuc [Fe/H] to a more metal poor value than other recent papers it brings it back in line with previous published values, notably Harris (1996), of −0.76 dex. However, the values determined here are another $\sim$ 0.2 dex more metal poor. A possible cause for this very low metallicity is discussed in Section 6.4.

6.3 Non-LTE effects in Zr I lines

The *s*-process elemental abundances were determine by spectrum synthesis using the line lists that had been calibrated to Arcturus. In particular the key region of 6125 Å to 6150 Å was investigated for its four Zr I features.

Figure 6.6 shows this section of spectrum from 6134 Å to 6144 Å for Arcturus, Lee 2525 and the star designated *tc*04. Overlaid on each of the observed spectra are synthesised spectra generated using the specified stellar atmosphere model. *tc*04 is shown twice, first in Figure 6.6c using the Spectroscopic 1 parameters, and second in Figure 6.6d using the Spectroscopic 2 set.

In Figure 6.6a the Zr I lines in the Arcturus spectrum are clearly not enhanced as the synthesised spectra with no changes to the Zr abundance ([Zr/Fe] = 0.0 dex) is an excellent fit. Considering the same lines in the Lee 2525 spectrum in Figure 6.6b, there is a clear enhancement in the Zr abundance ([Zr/Fe]= +0.35 dex). An enhancement in Zr is also indicated for *tc*04, as shown in Figure 6.6c. However, there is a distinct disagreement between the Zr I lines as to the degree of enhancement. In particular, the weakest line at 6140 Å shows an enhancement of only 0.20 dex, but the two stronger lines at 6134 Å and 6143 Å are better represented by an enhancement of 0.80 dex.

Table 6.5 compares the abundance values derived from each Zr I line in the 6140 Å region for Arcturus, Lee 2525 and *tc*04. There is a clear decrease in abundance with χ for the Zr I lines in *tc*04. No such decrease can be seen for Arcturus nor for Lee 2525. This is emphasised by the large σ on [Zr/Fe] for *tc*04 compared with Arcturus and Lee 2525.

The obvious trend of Zr I abundance with χ in *tc*04 implies the temperature of the stellar model is incorrect. An investigation into the effect of changing the stellar parameters on the Zr abundances was carried out. Table 6.6 lists the variations on the stellar parameters, the resulting [Fe I/H] and [Fe II/H] values, and [Zr/Fe] values for each of the four Zr lines that were analysed in this study in the 6140 Å region for *tc*04. No Zr II lines could be measured in

Table 6.5: [Zr/Fe] for key lines in 6140 Å region for Arcturus and *tc*04.

Zr I		[Zr I/Fe]		
λ (Å)	χ (eV)	Arcturus	Lee 2525	*tc*04
6134.570	0.00	0.04	0.33	1.07
6143.180	0.07	0.00	0.49	0.80
6127.475	0.15	0.04	-	0.60
6140.460	0.52	0.00	0.43	0.20
<[Zr I/Fe]>		0.02	0.42	0.67
	σ	0.02	0.08	0.37

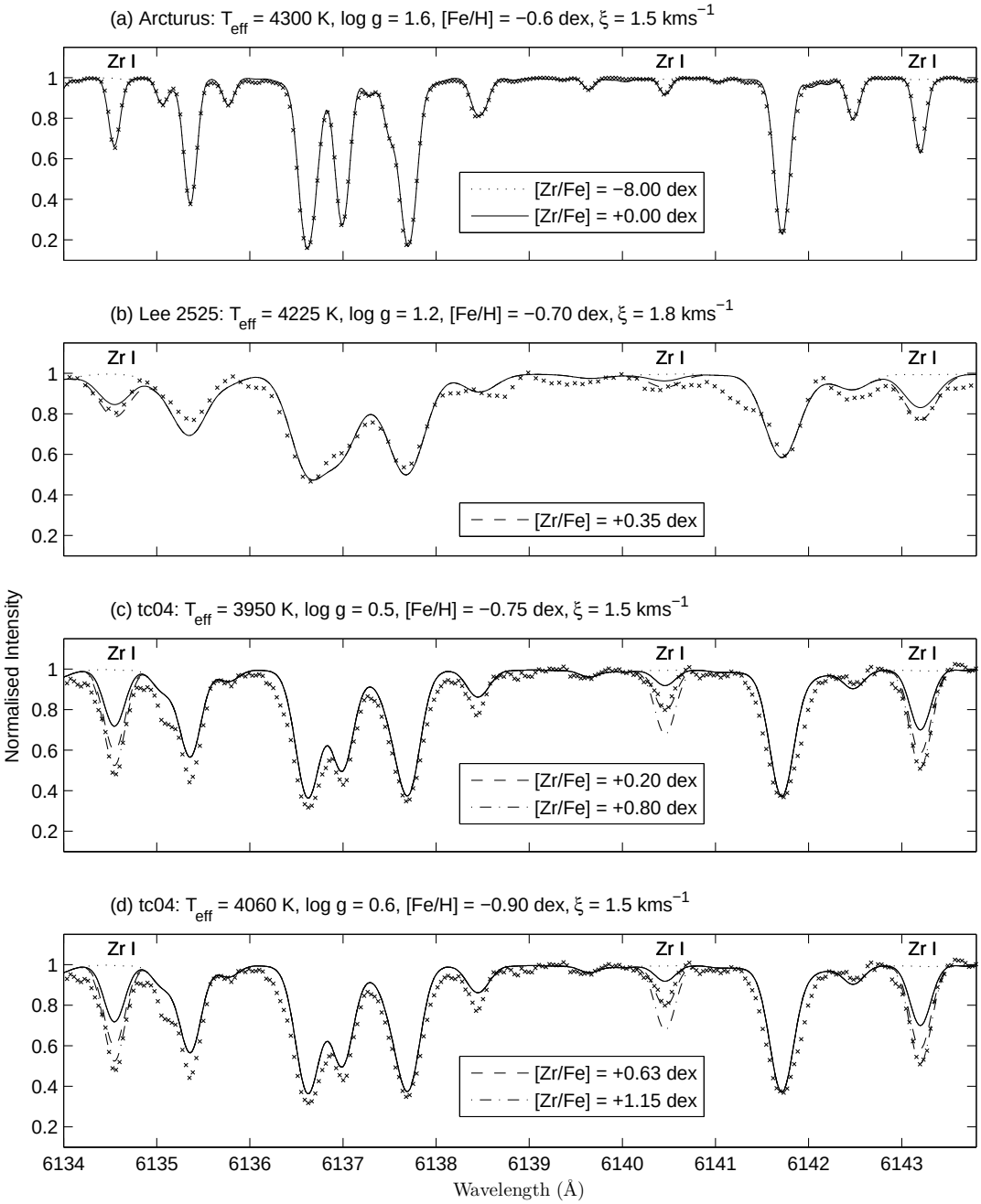

Figure 6.6: Observed and synthesised spectra showing the key Zr I features in the 6134 Å to 6144 Å region. (a) Arcturus spectrum compared with two spectra synthesised using the stated Arcturus stellar model. The dotted line represents depleted Zr at [Zr/Fe] = −8.0 dex and the solid line represents the Zr best fit abundance at [Zr/Fe] = 0.0 dex. (b) Lee 2525 spectrum compared with two spectra synthesised using the Lee 2525 stellar model. The dotted line is [Zr/Fe] = −8.0 dex. The dashed line is the Zr best fit at [Zr/Fe] = +0.35 dex. (c) *tc*04 spectra compared with three spectra synthesised using the Spectroscopic 1 stellar model for *tc*04. The dotted line is [Zr/Fe] = −8.0 dex. The dashed line is the best fit to the Zr feature at 6140.460 Å of [Zr/Fe] = +0.20 dex. The dash-dot line represents the best fit to the Zr features at 6134.570 Å and 6143.180 Å of [Zr/Fe] = +0.80 dex. (d) As for (c), but the three spectra are synthesised using the Spectroscopic 2 stellar model for *tc*04. The best fit to 6140.460 Å is [Zr/Fe] = +0.63 dex and the best fit to 6134.570 Å and 6143.180 Å is [Zr/Fe] = +1.15 dex.

these stars, which would have provided the opportunity for a similar analysis to that carried out between the Fe I and Fe II lines and compared with the analysis of Allen & Barbuy (2006).

While changes in T_{eff} and *log g* resulted in corresponding changes in [Zr/Fe] the spread in the abundance values did not change, remaining on the order of 0.4 dex. The parameter that succeeded in flattening out the [Zr/Fe] abundances was microturbulence (ξ). Figure 6.7 shows the effect of these changes in [Zr/Fe] against excitation potential (χ).

Increasing the microturbulence forced the Zr I abundances into agreement and a value of 2.5 kms^{-1} provided the best agreement at [Zr/Fe] = 0.06±0.10 dex. However, the Fe I and Fe II abundances were then forced out of agreement (see Table 6.6). Given the consistent set of [Zr/Fe] values that were obtained for Arcturus it was assumed that this discrepancy could not be explained solely by systematic errors within the derivation of equivalent widths and stellar parameters. An alternative explanation for the discrepancy between the Zr I abundances was required. The most likely explanation is once again the effects of departures from LTE on low excitation potential lines. The lower excitation potential lines for Zr I return higher

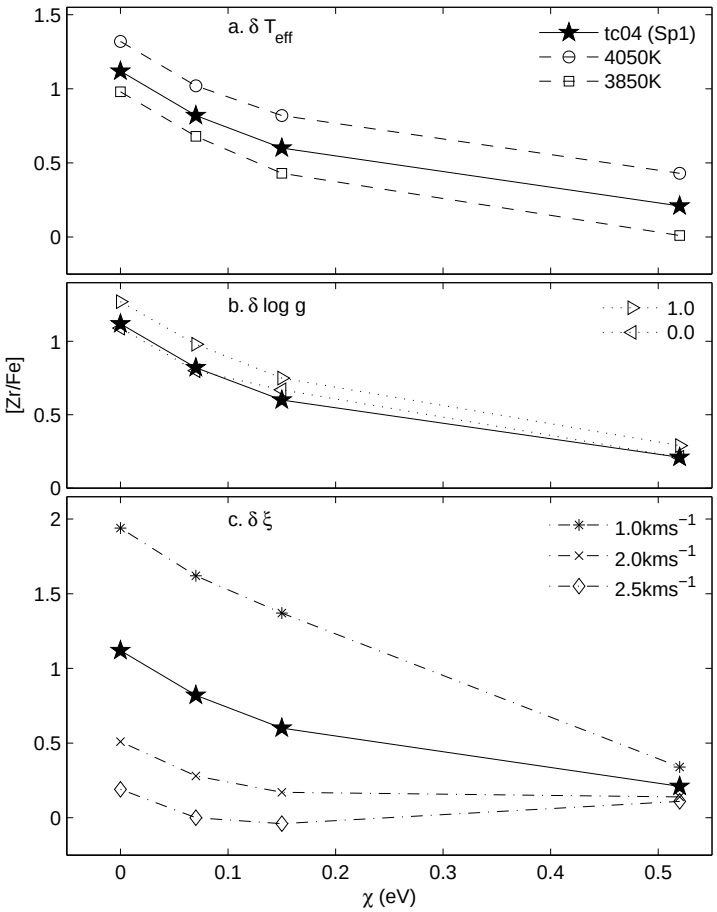

Figure 6.7: [Zr/Fe] vs χ for the Zr I lines listed in Table 6.6. [Zr/Fe] has been derived for each line in the best fit model (Spectroscopic 1 in Table 6.2) for *tc*04 and for models where the stellar parameters have been varied as specified in Table 6.6. Increasing ξ to 2.5 kms^{-1} provides the best agreement between the Zr I lines.

Table 6.6: Comparison of [Zr/H] against χ for $tc04$ showing the large spread in [Zr/Fe] for the stellar model derived using all the Fe I lines (Spectroscopic 1 in Table 6.2) and models with specified changes in T_{eff}, *log g* and ξ. An increase to $\xi = 2.5$ kms^{-1} produces reasonable agreement between the individual [Zr/Fe] values, but this is unrealistic when compared to the abundances derived from Fe I and Fe II lines.

χ(Fe I) < 5.0eV			T_{eff}	T_{eff}	*log g*	*log g*	ξ	ξ	ξ
Model		Best Fit	+100K	−100K	+0.5	−0.5	$+0.5 kms^{-1}$	$-0.5 kms^{-1}$	$+1.0 kms^{-1}$
T_{eff} (K)		3950	4050	3850	3950	3950	3950	3950	3950
log g		0.5	0.5	0.5	1	0	0.5	0.5	0.5
ξ kms^{-1}		1.5	1.5	1.5	1.5	1.5	2.0	1.0	2.5
[Fe/H]		−0.75	−0.75	−0.75	−0.75	−0.75	−0.75	−0.75	−0.75
[Fe I/H]		−0.76	−0.70	−0.75	−0.63	−0.58	−1.11	−0.35	−1.19
[Fe II/H]		−0.75	−0.84	−0.53	−0.46	−0.38	−0.89	−0.56	−0.63
λ (Å)	χ (eV)	[Zr/Fe]	[Zr/Fe]	[Zr/Fe]	[Zr/Fe]	[Zr/Fe]	[Zr/Fe]	[Zr/Fe]	[Zr/Fe]
6134.570	0.000	1.12	1.32	0.98	1.27	1.09	0.51	1.94	0.19
6143.180	0.070	0.82	1.02	0.68	0.98	0.8	0.28	1.62	0
6127.460	0.150	0.60	0.82	0.43	0.75	0.67	0.17	1.37	−0.04
6140.460	0.520	0.21	0.43	0.01	0.29	0.21	0.14	0.34	0.11
<[Zr I/Fe]>		0.69	0.90	0.53	0.82	0.69	0.28	1.32	0.06
σ		0.38	0.37	0.41	0.41	0.37	0.17	0.69	0.10

abundances similar to what was seen in the Fe I abundances in Arcturus and *tc*04. This is in good agreement with the analysis of Fe I lines over a range of χ in Section 6.2 which showed better agreement between individual [Fe I/H] for higher values of microturbulence (ξ).

The χ values for the four Zr lines considered here range from 0.0 eV to 0.52 eV. Of these the three lowest χ lines were discarded. The line at 6140.460 Å ($\chi = 0.52$ eV) along with another Zr I line at 6445.72 Å ($\chi = 1.0$ eV) were used where possible to determine the Zr I abundances of these 47 Tuc stars.

The other *s*-process elemental abundances were determined using the ionised species, except for Y which was based on one neutral and one ionised line. The neutral Y line was also of low χ so the same arguments as for the Zr I lines apply. The ionised Y line, as for other ionised lines, is not so affected by departures from LTE and as such its derived abundance can be regarded as being more reliable.

6.4 Effects of the circumstellar dust cloud

In attempting to reduce the effects of departures from LTE by constraining the Fe I line list to high excitation potential lines and to derive the 'true' stellar parameters another issue had been exposed. While Koch & McWilliam (2008) had measured a minimum [Fe/H] of -0.82 dex, the metallicity values derived here were significantly more metal poor (see Spectroscopic 2 models in Table 6.2. These could be attributed to systematic errors in the analysis process, but the analysis of both Arcturus and Lee 2525 provided reasonable results implying another effect at work. The nature of the AGB sample could well hold the solution. While Arcturus and Lee 2525 are reasonably 'hot' giant stars, the AGB sample are quite cool giants that were specifically selected by McDonald & van Loon (2007) in order to study mass loss rates. The 47 Tuc stars all have an infra-red (IR) excess which is indicative of circumstellar dust (see Table 6.2). The stars in this data set have an IR excess, $(K - [12])_o \geq 0.65$, which is based on the ISOCAM observations from which this sample was drawn (Origlia et al. 2002; McDonald & van Loon 2007).

A possible mechanism at work is 'veiling', the effects of which are discussed in Section 2.1.4. In summary, veiling introduces another layer of grey atmosphere such that when normalisation occurs the individual lines are scaled to smaller depths than if the veiling effect was not there. The measured equivalent widths are therefore smaller and give correspondingly lower metallicities. This affects all the observed lines, although it will have the greatest effect on strong lines. In this analysis the Fe I line list was restricted to lines of equivalent width less than 180 mÅ. Discarding Fe I lines of equivalent width greater than 100 mÅ did increase the abundance derived from the Fe I lines but only by a maximum of ~ 0.06 dex. This is well within the uncertainty for the abundance derived from this species (see Table 6.8) indicating the sample of Fe lines used here are being veiled to the same degree. The heavy

element abundances under consideration were mainly derived from weak lines which would be affected to the same degree as the Fe lines discussed above. As such, differentially the elemental abundances relative to the derived metallicity can still be considered to reflect the true abundance ratios within the star.

6.5 Chemical abundance results

The heavy elemental abundances derived for 47 Tuc stars are presented in Table 6.7. The derived abundances for Arcturus and Lee 2525 are also included for comparison.

The *tc* stars are more metal poor than what is expected for 47 Tuc stars. As the same process was used for all the stars in Table 6.7, Lee 2525 provides a benchmark as a 47 Tuc star with no IR excess for which a reasonable metallicity was derived. The *tc* stars show enhancements in Y, Zr, La, Nd and Eu in agreement with the enhancements observed in Lee 2525. Ba II is enhanced in the *tc* stars while it is depleted in Lee 2525.

Table 6.8 lists the uncertainties associated with changes in the stellar parameters for the representative star, *tc*04. As expected the two neutral species, Y I and Zr I, are both sensitive to temperature, while the remaining ionised species are sensitive to gravity. The Y I and Ba II abundances also show a sensitivity to ξ. The abundances for these elements were derived from strong lines which explains this sensitivity. In particular, the abundance determined for Ba was based on two very strong Ba II lines. The two lines provide consistent results between them, as seen in the small value for σ. However, the very high sensitivity to ξ means the abundance derived from these lines should be treated with caution. This may explain the difference between the Ba abundance derived for the *tc* stars and Lee 2525.

With this in mind the heavy *s*-process ratio, *hs*, was defined using only the La and Nd abundances. Also Sr could not be measured for these stars and so the definitions for *ls* and *hs* in this chapter are as follows:

$$\begin{aligned} [ls/\mathrm{Fe}] &= \langle\ [\mathrm{Y\ I/Fe}],\ [\mathrm{Y\ II/Fe}],\ [\mathrm{Zr\ I/Fe}],\ [\mathrm{Zr\ II/Fe}]\ \rangle \\ [hs/\mathrm{Fe}] &= \langle\ [\mathrm{La\ II/Fe}],\ [\mathrm{Nd\ II/Fe}]\ \rangle \end{aligned}$$

Returning to Table 6.7 the light *s*-process elements consistently show a greater enhancement than the heavy *s*-process elements in the *tc* stars, resulting in [*hs*/*ls*] ratios less than zero as for Lee 2525.

6.5.1 Abundances relative to Arcturus

The [Fe/H] and [X/Fe] relative to the Sun, listed in Table 6.7, were recalculated relative to Arcturus and are listed in Table 6.9.

Table 6.7: Final stellar atmospheric parameters (Spectroscopic 2), derived [Fe/H] and [X/Fe] for Arcturus, Lee 2525 and all the *tc* 47 Tuc stars. The number of lines (N) used to determine each abundance is also included.

Star	**Arcturus**		**Lee 2525**		**tc02**		**tc03**		**tc04**		**tc05**		**tc09**	
T_{eff} (K)	4300		4225		4060		4030		4060		3850		4100	
log g	1.60		1.20		0.50		0.55		0.60		0.00		0.10	
[Fe/H] (dex)	−0.60		−0.70		−0.90		−0.90		−0.90		−0.95		−0.95	
$\xi(kms^{-1})$	1.5		1.8		1.5		1.5		1.5		1.5		1.5	
X	[X/H]	N	[X/H]	N	[X/H]	N	[X/H]	N	[X/H]	N	[X/H]	N	[X/H]	N
Fe I	−0.61	29	−0.72	29	−0.92	14	−0.86	10	−0.93	14	−0.96	8	−0.98	12
Fe II	−0.56	11	−0.73	4	−0.88	3	−0.89	3	−0.88	3	−0.93	2	−0.97	3
X	[X/Fe]	N	[X/Fe]	N	[X/Fe]	N	[X/Fe]	N	[X/Fe]	N	[X/Fe]	N	[X/Fe]	N
Y I	0.07	3	0.51	2	0.56	1	0.43	1	0.64	1	0.55	1	0.62	1
Y II	0.12	5	0.54	1	0.38	1	0.64	1	0.52	1	-	0	0.43	1
Zr I	0.01	7	0.36	3	0.56	2	0.47	2	0.50	2	0.55	2	0.53	1
Zr II	0.12	3	0.65	1	-	0	-	0	-	0	-	0	-	0
Ba II	−0.19	2	−0.21	2	0.59	2	0.43	2	0.64	2	0.49	2	0.09	2
La II	0.04	6	0.31	3	0.28	1	0.36	1	0.35	1	0.41	1	0.22	1
Nd II	0.10	4	0.41	1	0.42	1	0.50	1	0.53	1	0.55	1	0.44	1
Eu II	0.36	2	0.40	1	0.49	1	0.32	1	0.51	1	0.55	1	0.49	1
X/Y	[X/Y]	σ	[X/Y]	σ	[X/Y]	σ	[X/Y]	σ	[X/Y]	σ	[X/Y]	σ	[X/Y]	σ
ls/Fe	0.08	0.05	0.51	0.12	0.50	0.10	0.51	0.11	0.55	0.08	0.55	0.00	0.53	0.10
hs/Fe	0.07	0.04	0.36	0.07	0.35	0.10	0.43	0.10	0.44	0.13	0.48	0.10	0.33	0.16
hs/ls	−0.01	0.06	−0.16	0.14	−0.15	0.14	−0.08	0.15	−0.11	0.14	−0.07	0.07	−0.20	0.18

Table 6.8: Uncertainties in [Fe/H] and [X/Fe] associated with changes in T_{eff}, $log\ g$ and ξ for the representative star $tc04$.

				Δ[X/H]		
				ΔT_{eff}	$\Delta log\ g$	$\Delta\xi$
X	N	[X/H]	σ	+100K	+0.5	$+0.5 kms^{-1}$
Fe I	14	−0.93	0.19	0.01	0.13	−0.27
Fe II	3	−0.88	0.02	−0.18	0.29	−0.13
X	N	[X/Fe]	σ		Δ[X/Fe]	
Y I	1	0.64	-	0.20	0.13	−0.24
Y II	1	0.52	-	−0.05	0.27	−0.02
Zr I	2	0.50	0.16	0.16	0.05	−0.07
Ba II	2	0.64	0.09	−0.01	0.21	−0.69
La II	1	0.35	-	0.02	0.23	−0.10
Nd II	1	0.53	-	0.07	0.26	0.00
Eu II	1	0.51	-	−0.02	0.23	−0.08

Table 6.9: [Fe/H] and [X/Fe] relative to Arcturus for the 47 Tuc stars where $[X/Y]_{Arc} = [X/Y]_{\star}$ - $[X/Y]_{Arcturus}$. The mean abundances with respect to the Sun and to Arcturus are also included.

Star	**Lee 2525**	**tc02**	**tc03**	**tc04**	**tc05**	**tc09**	**mean**		
X	$[X/H]_{Arc}$	$[X/H]_{Arc}$	$[X/H]_{Arc}$	$[X/H]_{Arc}$	$[X/H]_{Arc}$	$[X/H]_{Arc}$	<[X/H]>	$<[X/H]_{Arc}>$	σ
Fe I	−0.11	−0.31	−0.25	−0.32	−0.35	−0.37	−0.90	−0.29	0.10
Fe II	−0.17	−0.32	−0.33	−0.32	−0.37	−0.41	−0.88	−0.32	0.08
X	$[X/Fe]_{Arc}$	$[X/Fe]_{Arc}$	$[X/Fe]_{Arc}$	$[X/Fe]_{Arc}$	$[X/Fe]_{Arc}$	$[X/Fe]_{Arc}$	<[X/Fe]>	$<[X/Fe]_{Arc}>$	σ
Y I	0.44	0.49	0.36	0.57	0.48	0.55	0.55	0.48	0.08
Y II	0.42	0.26	0.52	0.40	-	0.31	0.50	0.38	0.10
Zr I	0.35	0.55	0.45	0.48	0.53	0.52	0.49	0.48	0.07
Zr II	0.53	-	-	-	-	-	0.65	0.53	-
Ba II	−0.02	0.78	0.62	0.83	0.68	0.28	0.34	0.53	0.33
La II	0.27	0.24	0.32	0.31	0.37	0.18	0.32	0.28	0.07
Nd II	0.32	0.33	0.41	0.44	0.46	0.35	0.48	0.38	0.06
Eu II	0.04	0.13	−0.04	0.15	0.19	0.13	0.46	0.10	0.08
X/Y	$[X/Y]_{Arc}$	$[X/Y]_{Arc}$	$[X/Y]_{Arc}$	$[X/Y]_{Arc}$	$[X/Y]_{Arc}$	$[X/Y]_{Arc}$	<[X/Y]>	$<[X/Y]_{Arc}>$	σ
ls/Fe	0.44	0.43	0.45	0.49	0.51	0.46	0.53	0.46	0.07
hs/Fe	0.29	0.28	0.36	0.37	0.41	0.26	0.40	0.33	0.11
hs/ls	−0.14	−0.15	−0.08	−0.11	−0.10	−0.20	−0.13	−0.13	0.13

This recalculation provided a subtle shift in the derived abundances. For better comparison Figures 6.8 to 6.15 show the derived abundances in groupings of [Fe/H], light *s*-process elements and heavy *s*-process elements for the stars in this study, as well as Lee 2525 and the stars in Wylie et al. (2006). Figures 6.8, 6.10 and 6.12 show the abundances relative to the metallicity of the star in question, while Figures 6.9, 6.11 and 6.13 show the abundances relative to Arcturus. For completeness the derived abundances reported in Wylie et al. (2006) were also recalculated with respect to Arcturus.

Figures 6.8 and 6.9 clearly show the lower metallicity for the *tc* stars compared with Lee 2525 and Wylie et al. (2006). Recalculating with respect to Arcturus does not improve matters between the studies. The stars are ordered by metallicity to show the spread between the studies and to compare with the following figures.

The light *s*-process abundances in Figure 6.10 also show a split at the *tc* stars, where they return lower Zr abundances than Lee 2525 and the Wylie et al. (2006) stars. Relative to Arcturus, Figure 6.11 shows the separation between studies is less distinct, although this is mainly due to a greater spread in the Wylie et al. (2006) values. There is a tighter agreement between the *tc* stars. However, there may still be residual systematic errors due to the above separation in [Fe/H].

The heavy *s*-process abundances in Figure 6.12 show a more consistent set of results with no residual with metallicity. Relative to Arcturus in Figure 6.13, there is an even tighter spread overall.

Both Y II and Ba II have the greatest spread between the stars which could be attributed to their ξ sensitivity discussed earlier. Otherwise there is reasonable agreement between the stars showing an overall enhancement in the *s*-process abundances. Eu II is also enhanced with a small spread comparable to the spread of the *s*-process enhancements. This supports the homogenous nature of the observed heavy element enhancements. Relative to Arcturus there is still significant enhancement for all but Eu II. The mean abundance of Eu is close, at the uncertainty limit, to the Arcturus Eu abundance, inline with previously derived Eu abundances for field stars being similar to those in globular cluster stars (James et al., 2004).

The average of all the 47 Tuc stars analysed in this study, including Lee 2525, are given in columns 7 to 9 of Table 6.9. There is a distinct enhancement in the abundances of both the light and heavy *s*-process elements, with the light *s*- being more enhanced than the heavy *s*-process elements.

6.5.2 [*hs*/*ls*] ratio in 47 Tuc AGB stars

The ratio of the heavy *s*- to light *s*-process element abundances with respect to a sample of stars of similar metallicity can be used to place the stars in the wider context of heavy element enrichment. AGB stars in 47 Tuc are not expected to be undergoing TDU as they are too low in mass. However, these elements have been enriched at some point in the history

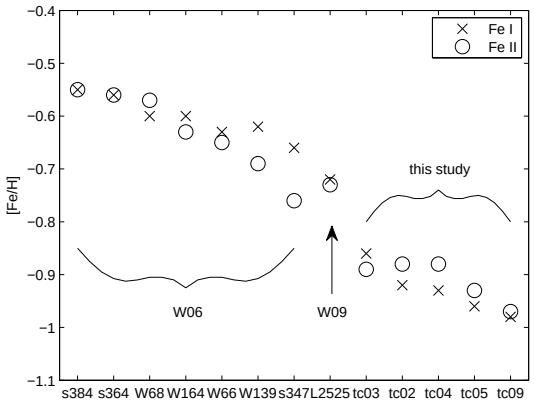

Figure 6.8: [Fe/H] relative to the Sun for each star in the sample for both Fe I and Fe II. The brackets and arrow indicate the samples from Wylie et al. (2006) (W06), Chapter 5 (W09) and this study.

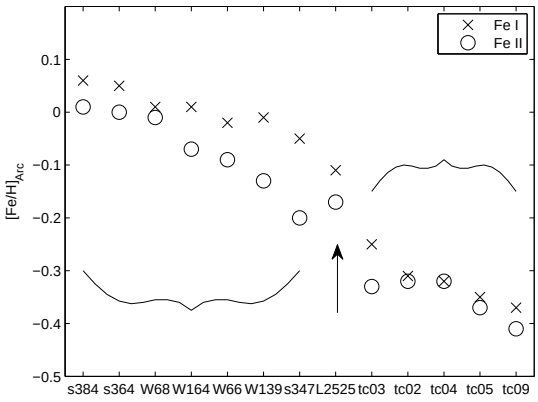

Figure 6.9: As for Figure 6.8 but the [Fe/H] is calculated relative to Arcturus, $[Fe/H]_{Arc}$.

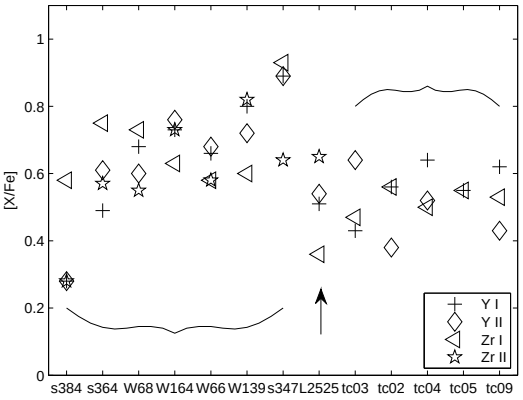

Figure 6.10: [X/Fe] relative to the Sun for each star in the sample for the light *s*-process elements, Y and Zr.

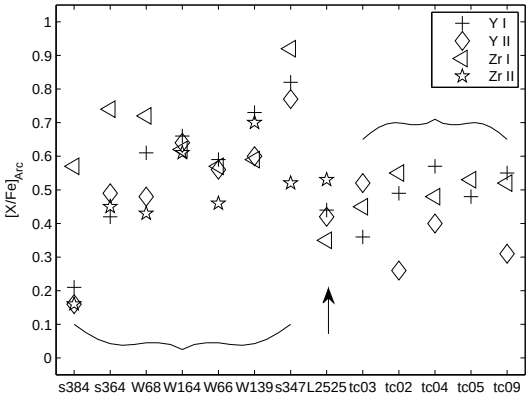

Figure 6.11: As for Figure 6.10 but the [X/Fe] is calculated relative to Arcturus.

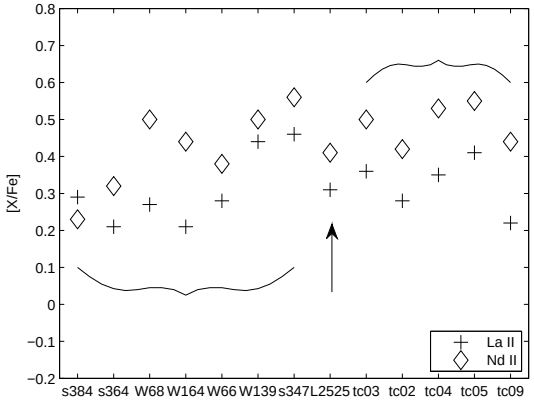

Figure 6.12: As for Figure 6.10 but for the heavy *s*-process elements, La and Nd.

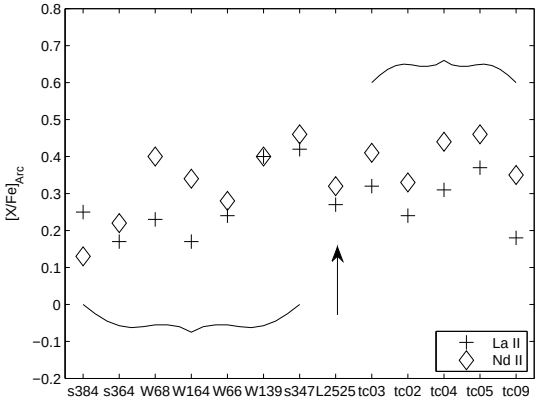

Figure 6.13: As for Figure 6.12 but the [X/Fe] is calculated relative to Arcturus.

of the GC. Comparing the [*hs/ls*] ratio here with values from other 47 Tuc studies and with expected [*hs/ls*] to [Fe/H] trends may assist in identifying the source of these enhancements.

As shown in Table 6.1, the previous high resolution studies considered here that involved heavy element abundances in 47 Tuc stars were carried out using spectra from a range of telescopes and instruments. The resolution ranged from 20,000 to 110,000 and the signal to noise per pixel ranged from 20 to 200 across the studies. Such a range in the quality of the spectra, and the subsequent differences in analysis techniques between the studies means the following comparisons of the results must be treated with some caution.

Figures 6.14 to 6.16 explore the [*hs/ls*] vs [Fe/H] space of the sample of stars in this analysis, including Lee 2525, the Wylie et al. (2006) stars and three of the 47 Tuc stars from Brown & Wallerstein (1992). Lee 2525 is the only star that has been observed in more than one of the high resolution studies considered here. The analysis of Lee 2525 that was carried out in Chapter 5 found enhancements in Zr for that star compared with a depletion in Zr that was found for that star and the three other 47 Tuc stars in Brown & Wallerstein (1992). In light of this, the [*hs/ls*] values used in Figures 5.6 to 6.16 for the three remaining Brown & Wallerstein (1992) stars were calculated using only the reported Y abundance for [*ls*/Fe].

Figure 6.14 shows the abundance ratio of the heavy *s*-process to light *s*-process elements with no adjustment with regard to Arcturus. The four different sets are indicated on the figure. The range in [Fe/H] is quite distinct with the *tc* stars returning higher [*hs/ls*] ratios than the higher metallicity samples. Disregarding the outlier in the Wylie et al. (2006) sample there is a trend of increasing [*hs/ls*] with decreasing metallicity as a result of the different analysis techniques.

Figure 6.15 shows the same picture but with the [*hs/ls*] and [Fe/H] for each star adjusted differentially with respect to Arcturus. The changes in the *tc* stars serve to diminish any hint of a trend between [*hs/ls*] and [Fe/H] within that set. The most dramatic effect is the elongating of the Wylie et al. (2006) results which effectively cancels out the potential trend observed in Figure 6.14.

If one accepts that each study is consistent within itself then the spread on the mean metallicity of each sample reflects the true spread within the cluster. It can be argued that each study is systematically offset in metallicity from the true mean metallicity of 47 Tuc if it is assumed that [Fe/H] is homogenous within a GC. This can particularly be argued for the *tc* stars which are significantly more metal poor than previous studies. By determining and removing the offset of the mean metallicity of each sample from the mean metallicity of 47 Tuc as determined by Koch & McWilliam (2008), the samples can be considered as a coherent whole.

Figure 6.16 shows each sample shifted such that the mean of the sample corresponds to the metallicity of 47 Tuc of [Fe/H] = -0.76 dex. Considered individually each sample shows no trend of [*hs/ls*] with [Fe/H] which is re-enforced when the samples are viewed as

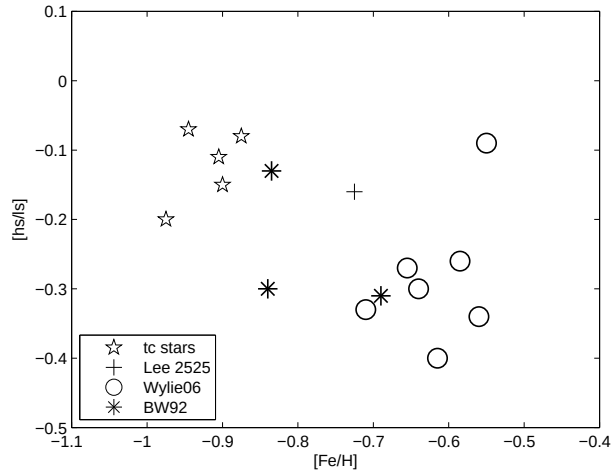

Figure 6.14: The ratio of the heavy to light *s*-process elemental abundance for each star against [Fe/H] with respect to the Sun.

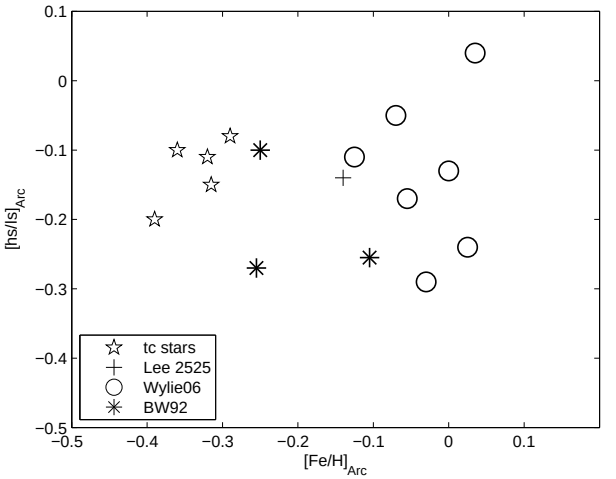

Figure 6.15: As for Figure 6.14 but with respect to the Arcturus.

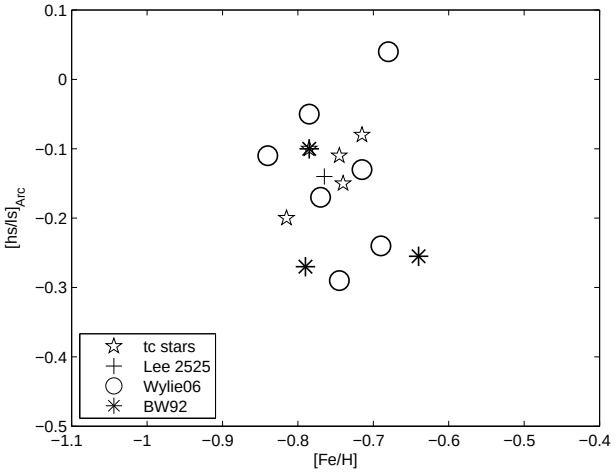

Figure 6.16: $[hs/ls]_{Arc}$ against [Fe/H] with respect to the Sun but with each data set shifted in [Fe/H] such that the mean [Fe/H] matches the reported 47 Tuc metallicity of −0.76 dex (Koch & McWilliam, 2008).

one sample with a single mean metallicity. The result is clear that there is no increase in [*hs/ls*] with decreasing [Fe/H] and the spread in [*hs/ls*] values is not greater than the spread in [Fe/H] values. A spread in [*hs/ls*] larger than the spread in [Fe/H] could indicate an internal production of *s*-process elements. No such spread is observed and this confirms the conclusion that the observed *s*-process enhancements are homogeneous throughout the sample and as such cannot have been produced within the stars themselves.

These results can be further compared with mean [*hs/ls*] value determined in the AAOmega medium resolution survey (see Chapter 4) and with the results from other studies. Only Zr and Ba could be measured in the AAOmega medium-resolution survey and based on those two abundances $\langle[hs/ls]\rangle = +0.16 \pm 0.21$ dex. Based on their derived abundances for Y, Zr and Ba, James et al. (2004) found $\langle[hs/ls]\rangle = +0.23 \pm 0.30$ dex for their sample of subgiant (SG) stars, and $\langle[hs/ls]\rangle = +0.05 \pm 0.23$ dex for their sample of turn-off (TO) stars. For their sample of giant stars Alves-Brito et al. (2005) found $\langle[hs/ls]\rangle = +0.35 \pm 0.24$ dex based on their abundances derived for Zr, Ba and La. These samples find that the *hs* peak is enriched with respect to the *ls* peak, whereas the sample considered here finds the *hs* peak depleted with respect to the *ls* peak at $\langle[hs/ls]\rangle = -0.13 \pm 0.14$ dex. However, the uncertainties between the studies do allow for some agreement between them.

Finally these results can be compared to theoretical predictions determined in Busso et al. (2001) that describe the expected [*hs/ls*] values produced by thermally pulsing AGB stars over a range of metallicities. The predictions are constructed at a certain stellar mass and for a certain amount of C^{13} in the C^{13} pocket. This measure of C^{13} is referred to as the C^{13} pocket parameter and is typically stated relative to the standard case (ST). The standard case was derived in Arlandini et al. (1999) as being the amount of C^{13} in AGB stars of mass between 1.5 and 3 $M_{\odot}$ at a metallicity of [Fe/H] $= -0.3$ dex that could explain the main solar component of the *s*-process elements (Busso et al., 2001). For alternative predictions the amount of C^{13} is varied with respect to the standard case by some scaling factor. As the efficiency of the *s*-process is sensitive to both the amount of C^{13} in the pocket, and to the metallicity of the star, by setting the C^{13} pocket parameter to a constant the [*hs/ls*] predictions for a certain mass can be explored over a range of metallicities.

Busso et al. (2001) defines AGB stars that are undergoing, or have undergone, TDU and the creation of *s*-process elements as being 'intrinsic'. Stars that bear the signature of TDU by some pollution or primordial event but are not creating *s*-process elements themselves are 'extrinsic'. An extrinsic signature may be produced by the pollution of the stellar atmosphere due to material ejected from evolved stars by stellar winds, or by pollution of the star forming gas cloud from which the extrinsic stars were formed. The analysis above shows that the AGB stars in 47 Tuc are extrinsic stars which bear the chemical signature of a previous generation of AGB stars that did undergo TDU. The homogeneity of the *s*-process element abundance results for these stars indicate that the source of the element abundances is external to the star, although the evidence is insufficient to distinguish between the possible scenarios of

pollution. As there are no variations between the stars no internal nucleosynthesis of these elements is occurring within them. Hence they are extrinsic giant stars.

If it is assumed that AGB stars are the source of the observed *s*-process elemental abundance enhancements then it follows that the [Fe/H] of the current extrinsic population of stars is the same as the [Fe/H] of the previous intrinsic population, as Fe is not produced within AGB stars. This may not actually be the case and more detailed scenarios are being considered in which material from both AGB stars and supernovæ are responsible for the observed abundance patterns in GC stars (Marcolini et al., 2009). But assuming intrinsic AGB stars to be the sole polluters the chemical composition of the extrinsic giant stars analysed here can be compared to the theoretical predictions in place of the original intrinsic stellar population. However, there is a certain amount of dilution of the chemical signature in the extrinsic stars due to internal mixing.

The prediction for the ST/1.5 case was used in Busso et al. (2001) as an average trend that compared well to the *s*-process element enhancements in intrinsic and extrinsic AGB stars, even taking into account the effects of mixing in the extrinsic stars. A mass of 1.5 $M_{\odot}$ was selected for the average trend, although it was noted that for low mass AGB stars the initial mass was not a critical criteria. It is important to note that the mass of 1.5 $M_{\odot}$ refers to the initial mass of the previous generation of intrinsic stars, not to the mass of the extrinsic stars. The extrinsic stars in the 47 Tuc stellar sample considered here have masses that are only $M \sim 0.85$ $M_{\odot}$ (Gilliland et al., 1998). However, there are timescale limits on the mass of the polluting star. A 3.0 $M_{\odot}$ star would need approximately ~ 1 billion years to evolve into a thermally pulsing AGB that is actively polluting the star-forming material within a globular cluster. A 1.5 $M_{\odot}$ star would need approximately ~ 4 billion years to evolve to the same stage. The star-formation epoch of a globular cluster occurs within the first billion years of its history, after which the intra-cluster gas is ejected from the cluster by supernovæ. It can be argued that 3.0 $M_{\odot}$ stars have sufficiently rapid lifetimes such that they may have been able to pollute the intra-cluster medium from which the extrinsic stars were formed before the gas was dispersed. However, stars of much lower mass are effectively ruled out as potential polluters.

Following the analysis in Busso et al. (2001) the prediction with a C^{13} pocket parameter of ST/1.5 and a mass of 1.5 $M_{\odot}$ was selected with which to compare the $\langle[hs/ls]\rangle$ values determined in this chapter, in Chapter 4 and in previous studies. The comparison is made in Figure 6.17.

The [Fe/H] realm in which 47 Tuc resides is on the cusp of a steep change in [*hs*/*ls*] values based on the theoretical prediction used in Figure 6.17. The low metallicities (~ -0.90 dex) derived in this study place this sample in the worst agreement with the theoretical prediction compared with the other studies, further adding to the argument that the derived metallicity is incorrect. Using instead the mean metallicity ([Fe/H] = -0.76 dex) of 47 Tuc derived in Koch & McWilliam (2008) provides a more reasonable agreement with the theoretical

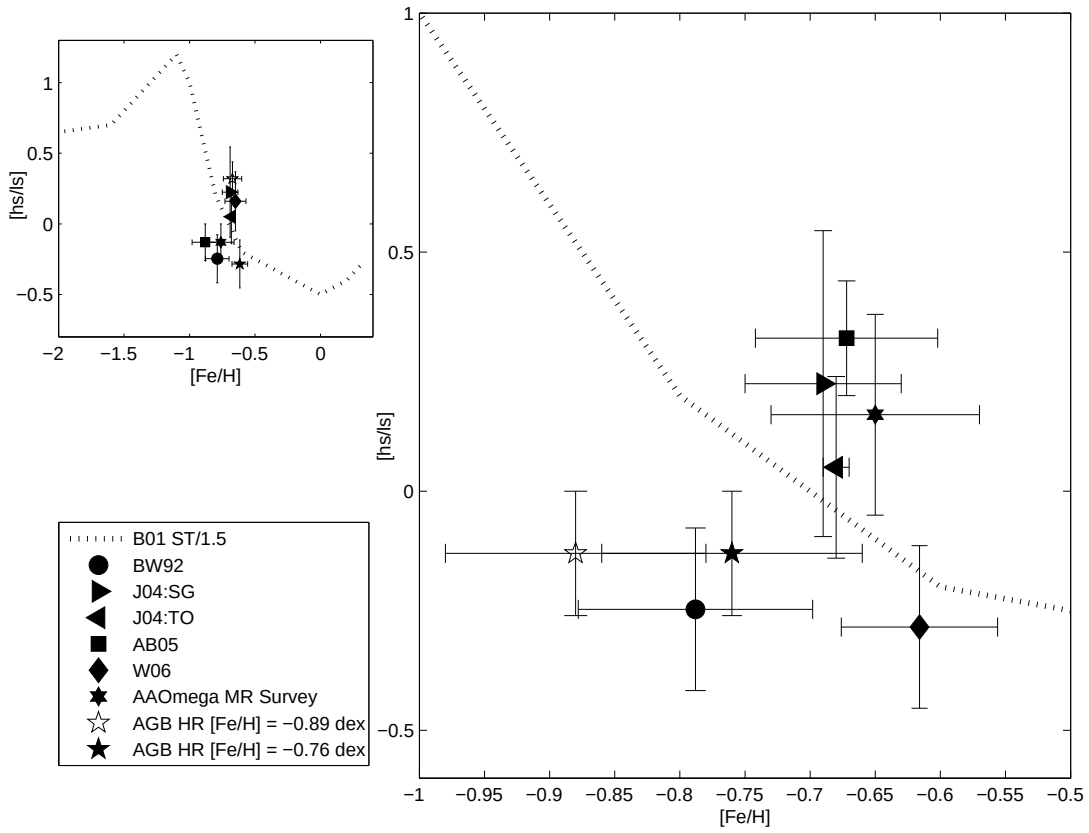

Figure 6.17: [*hs/ls*] against [Fe/H] with respect to the Sun for a C^{13} pocket parameter of ST/1.5 with mass of 1.5 $M_{\odot}$ as shown in Figure 7 of Busso et al. (2001) (B01). The full range of metallicities is shown in the top left panel while the right panel focusses on the 47 Tuc studies. The mean values and uncertainties for the samples in Brown & Wallerstein (1992) (BW92), James et al. (2004) (J04), Alves-Brito et al. (2005)(AB05) and Wylie et al. (2006) (W06) are shown as well as the values derived for the AAOmega medium-resolution (MR) survey in Chapter 4. The [hs/ls] mean and uncertainty for the AGB high resolution (HR) stars, including Lee 2525, are graphed at both the derived metallicity for this study ([Fe/H] = −0.89 dex) and the Koch & McWilliam (2008) metallicity ([Fe/H] = −0.76 dex).

prediction. The theoretical prediction agrees reasonably well with the majority of the studies identifying it as a good choice of mixing parameter for the intrinsic stars that are responsible for the heavy element pollution in this cluster. The spread in [*hs/ls*] is of similar magnitude to that of [Fe/H] for each study which further supports a homogeneous distribution of the heavy elements in 47 Tuc.

Overall these figures, combined with the clear homogeneity of the heavy elemental abundances shown in Figures 6.8 to 6.13, indicate that the *s*-process element abundance enhancements observed in 47 Tuc giant stars are of primordial or pollution origin and that these AGB stars are not undergoing TDU. The good agreement to the predicted [*hs/ls*] at the metallicity of 47 Tuc supports the scenario of a previous generation of intrinsic AGB stars as the source of the enhancements.

While this analysis has focused on the heavy elements, the light element abundances of these stars can provide further evidence regarding the likely sources of the abundance patterns within these stars. Thus far only Lee 2525 has been analysed for light element abundances. As outlined in Worley et al. (2009) the light element abundances within this star agree with previous analyses that found sodium (Na) to be enhanced while oxygen (O) was not. This pattern is the Na-O anti-correlation that is observed in many globular clusters, including 47 Tuc. In particular, the results of Worley et al. (2009) are in good agreement with Carretta et al. (2004), in which the light element abundance analysis of the stars in James et al. (2004) was carried out. This anti-correlation of Na and O is also indicative of pollution by thermally pulsing AGB stars, as the internal nucleosynthesis at this stage of evolution can produce this enhancement in Na without enhancing O. Considered in combination both the heavy and light element abundance distributions in 47 Tuc stars determined in these high resolution studies identify thermally pulsing AGB stars as key sources of pollution in the star forming history of 47 Tuc.

6.6 Conclusion

The analysis of these AGB stars has provided significant evidence as to the nature of *s*-process elemental abundance enhancements in 47 Tuc. However the analysis has also shown that departures from LTE plague the spectral determination of stellar parameters for cool, low gravity giants. A careful analysis is required in order to reduce the errors introduced by an LTE analysis of these types of stars.

The dust clouds that surround these variable stars, indicated by the high IR excesses, also introduce veiling effects that artificially lower the metallicity of these stars. However, this affects all the element spectral lines and as such, if the line list is constrained to weak high excitation lines, determining the chemical abundances relative to the derived metallicity of the star will provide a true representation of the relative abundances of the star.

A differential analysis to a star of similar atmospheric structure and metallicity is also instrumental in reducing the errors introduced by the above two effects. In this study the analysis process was calibrated to Arcturus in an effort to reduce any systematic errors.

The *s*-process elemental abundances determined in this study, and compared with previous studies, show a homogeneous enhancement of these elements within 47 Tuc. The cool giant stars analysed here show a very similar enhancement to hotter giant stars that have been analysed in 47 Tuc, such as Lee 2525 (see Chapter 5) and the stellar sample analysed in Wylie et al. (2006). This implies that, as 47 Tuc giant stars at different stages of evolution bear the same *s*-process signature, the enhancements observed here are not due to these AGB stars undergoing TDU. This is in line with the theory that 47 Tuc AGB stars are too low in mass for TDU to occur. For this sample of stars, includ-

ing Lee 2525, the mean abundance for the light *s*-process elements was determined to be $\langle$[ls/Fe]$\rangle = +0.53 \pm 0.09$ dex, while the heavy *s*-process elements were not as enhanced, with a mean abundance of $\langle$[hs/Fe]$\rangle = +0.40 \pm 0.11$ dex.

The [*hs/ls*] ratios of this sample, considered alongside the stars from Wylie et al. (2006) and Brown & Wallerstein (1992), showed no trend with [Fe/H]. This is expected given the homogeneity that was found for both [Fe/H] and the *s*-process elements in these stars. The mean value was found to be $\langle[hs/ls]\rangle = -0.13 \pm 0.13$ dex, which is in reasonable agreement with the predicted value assuming a C^{13} pocket parameter of ST/1.5 with an initial mass of $1.5 M_{\odot}$ as determined in Busso et al. (2001). [*hs/ls*] values from other studies also agree with this prediction within their uncertainties.

The results from the AAOmega medium-resolution survey are contradictory to the high resolutions results of this chapter, Brown & Wallerstein (1992) and Wylie et al. (2006). There was only a small enhancement in Zr ($\langle$[Zr/Fe]$\rangle = +0.05 \pm 0.08$ dex) compared to the greater *ls* enhancements for the high-resolution AGB stars of $\langle[ls/\mathrm{Fe}]\rangle = +0.53 \pm 0.07$ dex. The mean Ba abundance for the AAOmega survey ($\langle$[Ba/Fe]$\rangle = +0.23 \pm 0.19$ dex) was comparable to the *hs* enhancements found for the high-resolution AGB stars ($\langle[hs/\mathrm{Fe}]\rangle = +0.40 \pm 0.11$ dex). The difference in these results is likely to be due to the blending of the single Zr feature with the strong Ba/Fe feature in the medium-resolution spectra. This blending could be masking potential enhancements in Zr. This is seen in the comparison of the high resolution analysis of Lee 2525, which found [Zr/Fe] = +0.26 dex for the Zr I feature at 6143 Å, compared with the medium resolution analysis, which found [Zr/Fe] = 0.0 dex for the same feature (Table 4.4. The large range in Ba values for the AAOmega sample is most likely due to microturbulence effects which adds more uncertainty to the reported $\langle[hs/ls]\rangle$. A more detailed comparison between spectra of different resolutions for the same star would be instrumental in identifying which spectral features will provide consistent elemental abundance results. The stronger less blended light element features in Lee 2525 did provide consistent results between the two resolutions. Analysing a reasonable size sample of stars at high resolution, as was carried out for the AGB stars in this chapter, and then reanalysing them at medium resolution would then provide a benchmark for a larger medium resolution sample. This would produce consistent results for the *ls* and *hs* ratios.

This analysis of 47 Tuc AGB stars has confirmed the homogeneous enhancement of heavy elemental abundances in giant stars in 47 Tuc. The abundance of the *s*-process elements, as well as the *r*-process element, Eu, in 47 Tuc stars may be the signature of the primordial gas from which the cluster formed. Alternatively they are evidence of some pollution event early in the cluster's history. The good agreement of the results of this study with predicted *s*-process abundances supports AGB stars as a likely source of the enhancements in some primordial or pollution event. The observation of light element abundance patterns, such as the Na-O anti-correlation, in 47 Tuc stars also support the scenario of AGB stars as source of the observed abundance distribution. However, the timescales involved in the formation

of globular clusters indicate that an initial mass of approximately 3.0 $M_{\odot}$ is the minimum needed for pollution to occur in the time available. In order to discriminate between these two scenarios further investigation of the heavy elemental abundances in GCs is required. A large scale survey which extends down to the main sequence will provide the evidence needed to determine the origin of these enhancements and also to explain the abundance anomalies seen in the light elements. Alternatively, as will be pursued in the following chapter, similar analyses of stellar samples in other GCs can explore these abundance patterns over a range of metallicities.

Chapter 7

High-resolution studies: AGB stars in NGC 362 & NGC 6388

The analysis of the 47 Tuc stars in the previous chapter provided an in-depth investigation of the [*hs/ls*] ratio for a single metallicity. This chapter extends that work to consider clusters at other metallicities. Giant stars in NGC 362 and NGC 6388, observed as part of the McDonald & van Loon (2007) programme, were analysed in order to investigate the abundance distribution of heavy elements in globular clusters (GCs) at different metallicities. As the stars observed in these clusters were also cool, low gravity giants, the analysis of 47 Tuc was replicated for these two clusters to the extent of again considering the effects of departures from LTE and veiling on the stellar spectra.

7.1 Observations

The programme of stars observed for McDonald & van Loon (2007) included fifteen stars in NGC 362 and eighteen stars in NGC 6388. As for the 47 Tuc spectra analysed in the previous chapter, the spectra analysed here covered the wavelength range 6100 Å to 9000 Å, with a gap of ∼80 Å around 8000 Å. The spectra are of high resolution at $R \sim 110,000$ with signal-to-noise per pixel of $70 \leq \mathrm{SNR} \leq 120$.

Table 7.1 lists the observation details for McDonald & van Loon (2007) and other key high resolution studies undertaken in NGC 6388 and NGC 362, the results of which are discussed in Section 1.3.2 and compared in Section 7.3 with the results of this analysis.

The spectra of all of the NGC 6388 stars from 6120 Å to 6190 Å are shown in Figure 7.1. They are ordered in temperature sequence increasing downwards, replicating the descent down the giant branch. Similarly the NGC 362 stars are shown in Figure 7.2. As for Figure 6.1 the location of C_2, CN and TiO bands are indicated as well as the Fe lines, the continuum regions used for normalisation about the Fe lines and the échelle order break.

Table 7.1: Summary of the observations made for the key studies of heavy element abundances in NGC 6388 and NGC 362 stars. Listed for each study are the size of each stellar sample, the telescope, spectrograph, resolution and signal to noise per pixel (S/N per pix). For NGC 6388 the studies are Carretta et al. (2007) (C07); Wallerstein et al. (2007) (W07) and McDonald & van Loon (2007) (McDvL07) which is the original observing programme for the stars analysed here. For NGC 362 the studies are Pilachowski et al. (1983) (P87); Gratton (1987b) and Gratton (1987a); Shetrone & Keane (2000); and again McDonald & van Loon (2007) (McDvL07).

GC	NGC 6388			NGC 362			
Paper	C07	W07	McDvL07	P83	G87ab	S00	McDvL07
No. Stars	13	8	2	3	1	12	13
Telescope	VLT	CTIO 4 m	VLT	CTIO 4 m	ESO 3.6 m	CTIO 4 m	VLT
Spectrograph	UVES/FLAMES	échelle	UVES	échelle	CASPEC	échelle	UVES
Resolution	$\sim 40,000$	$\sim 35,000$	$\sim 110,000$	$\sim 30,000$	$\sim 15,000$	$\sim 30,000$	$\sim 110,000$
S/N per pix	$40-80$	$70-100$	~ 200	low to moderate	~ 50	$70-100$	~ 200

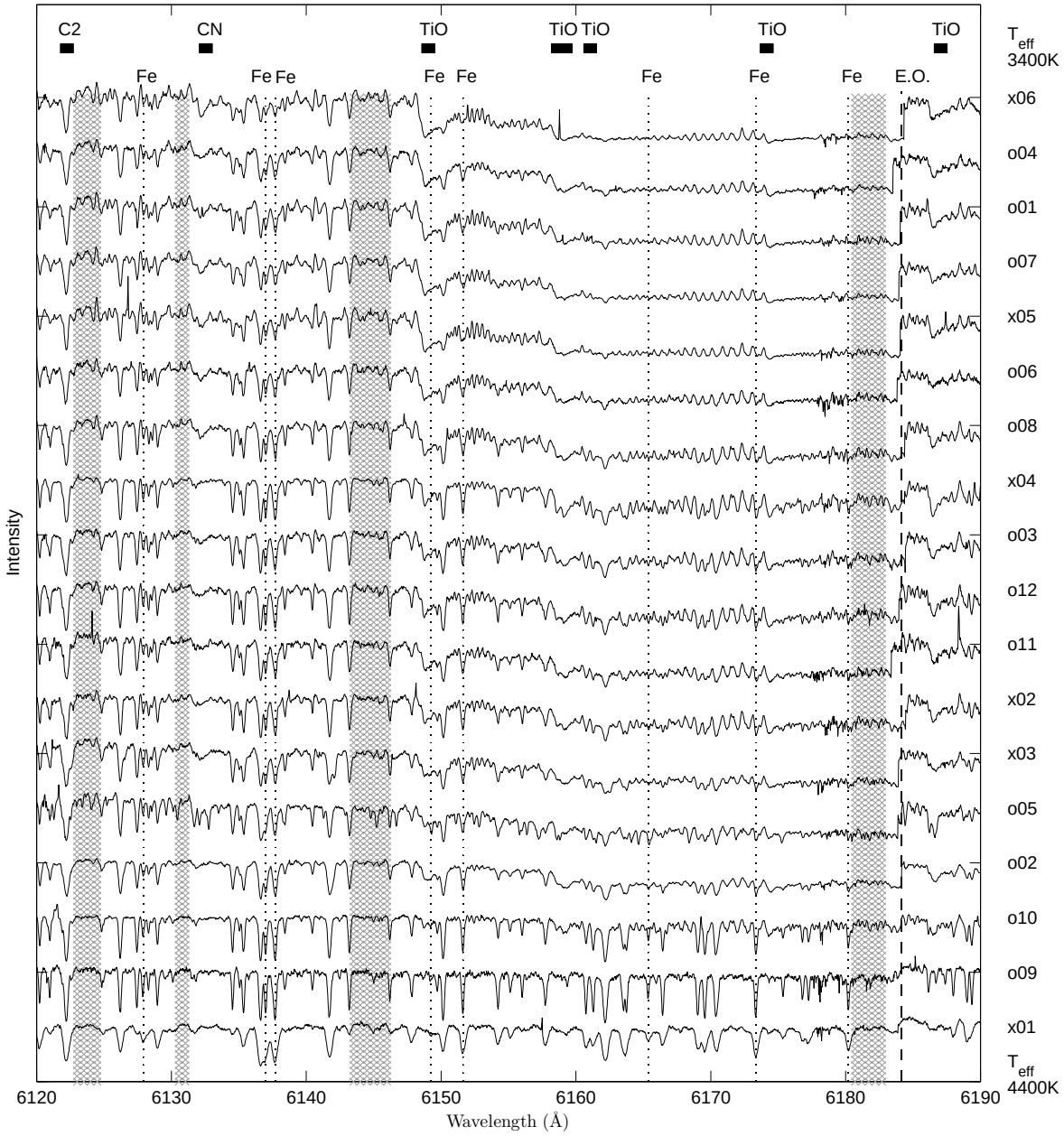

Figure 7.1: Section of spectra, from 6120 Å to 6190 Å, for each star in the NGC 6388 sample stacked in T_{eff} sequence increasing downwards. The location of C_2, CN and TiO bands are indicated at the top. The location of Fe lines in this region are shown as dotted vertical lines. The échelle order break (E.O.) is indicated as a vertical dashed line. The vertical shaded regions are the continuum regions used for normalisation about each Fe line. Only stars o09 and o10 were considered in this current analysis. x01 was excluded as its lines were considerably broader and all the cooler stars were contaminated by strong molecular bands.

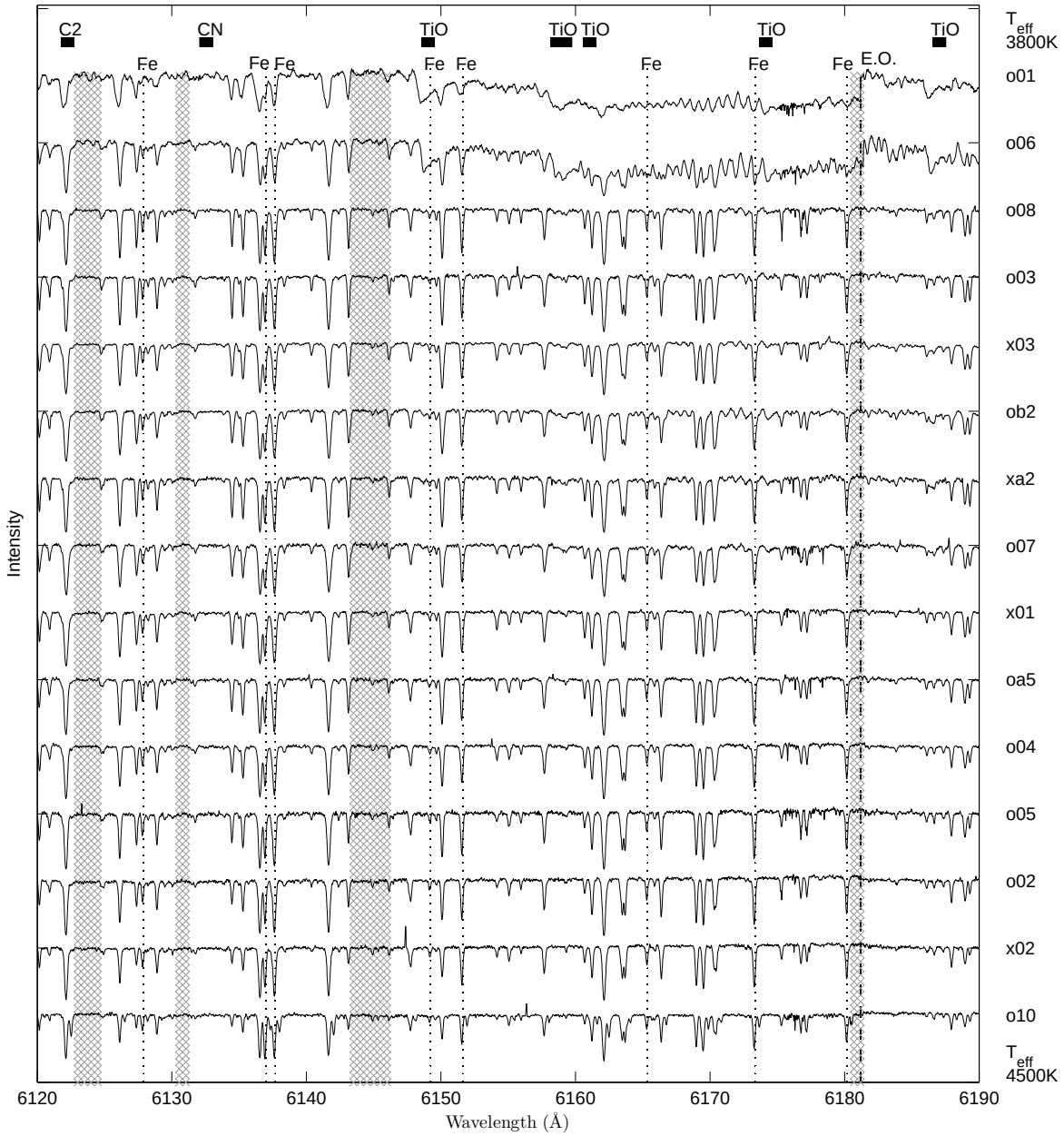

Figure 7.2: As for Figure 7.1 but for the NGC 362 stellar sample. Stars o01 and o06 were excluded due to strong contamination by molecular bands.

The molecular band issues that reduced the 47 Tuc sample from nine stars to five stars that could be analysed for chemical abundances also severely reduce the number of stars that can currently be analysed in the NGC 6388 sample. The three hottest NGC 6388 stars show the least contamination by the molecular bands, although the hottest star was discarded due to its very broad spectral features. Similarly in NGC 362 the two coolest stars show severe contamination by molecular bands. However, the remaining thirteen stars show very clear regions of continuum that can be used for normalisation about the Fe lines.

In terms of contamination by molecular bands, the five 47 Tuc stars that were analysed in Chapter 6 lie between NGC 6388 stars o10 and o02. The most contaminated of the 47 Tuc dataset, *tc*05, proved very difficult to analyse due to the greater uncertainty in the location of the continuum. Alternative methods to reliably locate the continuum in these stars need to be developed in order to accurately measure the equivalent widths of the spectral lines. Due to this only NGC 6388 stars o09 and o10 were analysed for the purposes of this research.

In Figure 7.3 a comparison of the NGC 6388 o09 spectrum, convolved to the resolution of the 47 Tuc observations, is made with the 47 Tuc star *tc*04 spectrum.

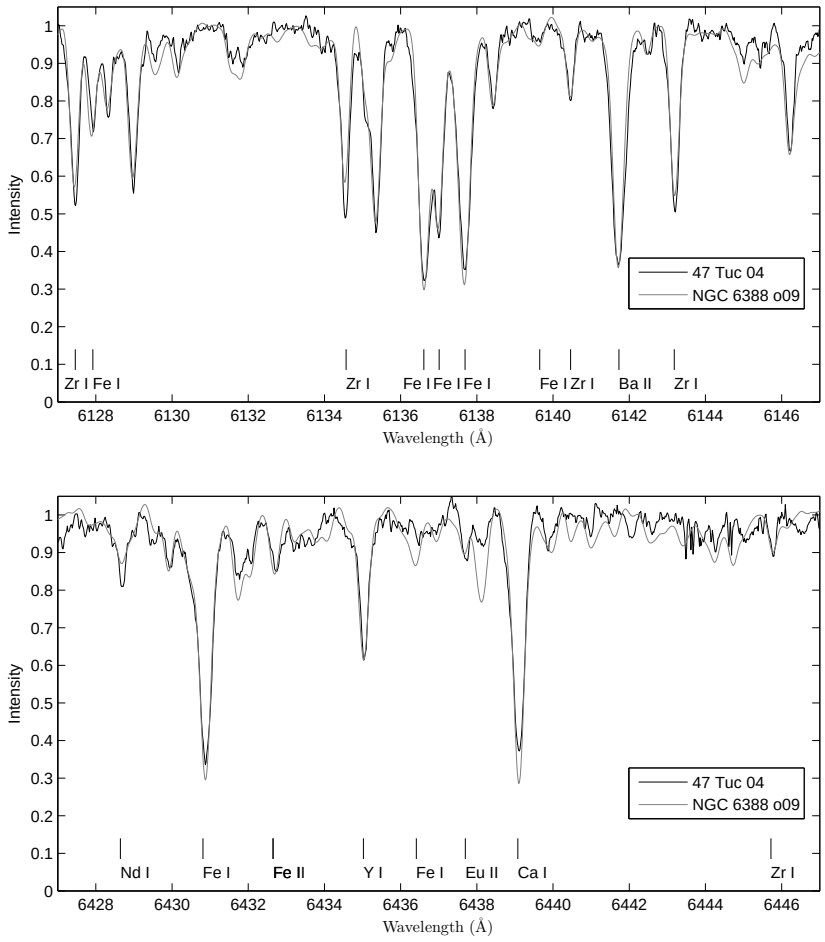

Figure 7.3: Comparison of the 47 Tuc star *tc*04 spectrum (black) with the NGC 6388 star o09 spectrum (grey). Top: Region from 6127 Å to 6147 Å with key lines indicated. Bottom: Region from 6427 Å to 6447 Å.

Similar temperatures ($T_{eff} \sim 4000$) K and gravities ($log\ g \sim 0.5$) were derived for both of these stars. At the same resolution the stellar spectra are in good agreement, although the strong lines appear stronger in NGC 6388 o09. Given the similarity of the spectra a similar metallicity is expected for the two stars. The very metal-poor results for 47 Tuc was attributed to veiling effects, evidence of which could be the difference in line depth seen in Figure 7.3. However, the very strongest of the Fe I lines were not used in the abundance analysis and the veiling effect seems minimal for the medium strength lines in Figure 7.3. The lower quality of the 47 Tuc star's spectra, and the greater molecular band contribution to the continuum of those stars, may have a more significant effect than in the NGC 6388 stars. A detailed line by line comparison between the 47 Tuc and NGC 6388 spectra of the Fe I lines used in the stellar derivation may help to pinpoint the exact cause of the lower metallicity. However, this comparison of the spectra argues in favour of shifting the mean [Fe/H] of the 47 Tuc sample to the more metal-rich value, relying on the differential analysis to have produced the correct relative abundances.

Figure 7.4 shows the entire NGC 6388 sample in the $T_{eff} - log\ g$ space using the temperatures and gravities from McDonald & van Loon (2007). The two stars that have been analysed in this study are indicated as black stars. The remaining stars are included in order to compare the entire sample with the AGB and RGB branches for both the [Fe/H] $= -1.0$ dex and -0.5 dex isochrones that are taken from the grid of Dotter et al. (2007). The majority of the stars in the NGC 6388 samples lie above the tip of the (Dotter et al., 2007) isochrones. However, while the RGB isochrones show the real tip of the RGB in each case, the (Dotter et al., 2007) AGB isochrone calculations stop before the thermally pulsing AGB phase begins and so the real AGB extends beyond the limits indicated in Figure 7.4.

The sample includes stars that are much cooler than those in 47 Tuc (see Figure 6.1) and the stellar parameters place the majority of the stars on the AGB relative to the [Fe/H] $= -0.5$ dex isochrone at the tip of the red giant branch. Only J and K photometry was available for these stars so no comparison between photometric temperatures could be made. However the temperature uncertainties derived in McDonald & van Loon (2007) are reasonably large ($\pm$100 K), as seen in Figure 7.4. The analysis of the 47 Tuc stars showed the McDonald & van Loon (2007) temperatures seemed to be overestimated. Hence the temperatures considered here in the derivation of the stellar parameters ranged from an upper limit of the McDonald & van Loon (2007) temperature to the lower limit of their uncertainties.

Figure 7.5 replicates Figure 7.4 but for the NGC 362 sample. In this case the isochrones are at [Fe/H] $= -1.5$ dex and -1.0 dex. This sample is hotter and of higher gravities than the NGC 6388 stars. If they are RGB stars they fit well to the isochrone at [Fe/H] $= -1.5$ dex, although their position can be interpreted as AGB stars relative to the [Fe/H] $= -1.0$ dex isochrone. The temperature uncertainties for these stars are on the order of $\pm$250 K. As above, the temperatures derived in McDonald & van Loon (2007) were used as the upper limit and the uncertainties as the lower limit in the range of potential temperatures used in

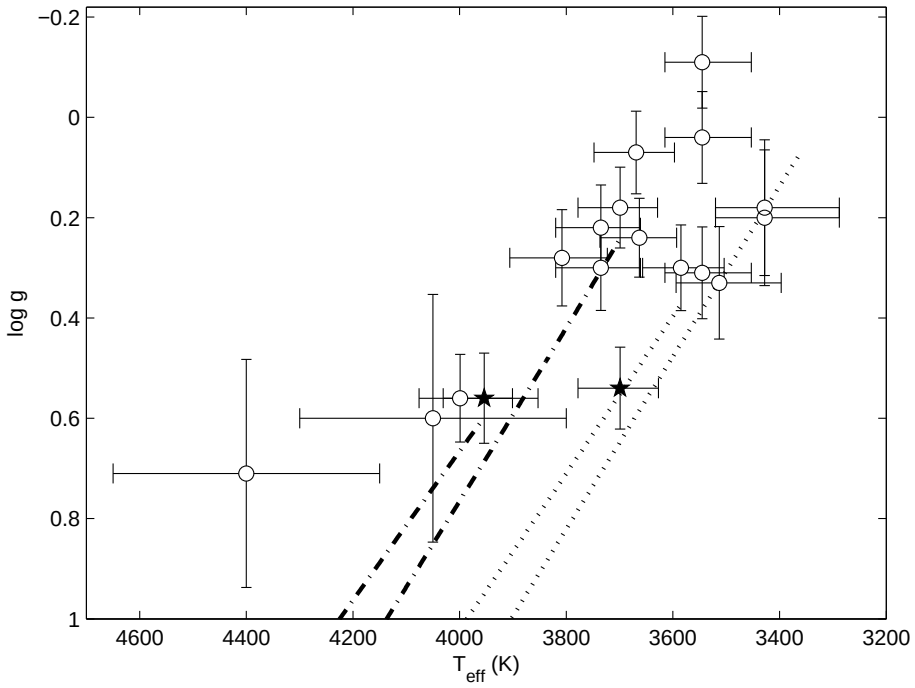

Figure 7.4: $T_{eff}-$ *log g* space for the stars in NGC 6388. The two stars analysed in this study are indicated as black stars ($\star$). The remaining stars in the sample ($\circ$) are included for reference. The dotted lines are AGB and RGB isochrones at [Fe/H] $= -0.5$ dex from Dotter et al. (2007). The dot-dash lines are AGB and RGB isochrones at [Fe/H] $= -1.0$ dex.

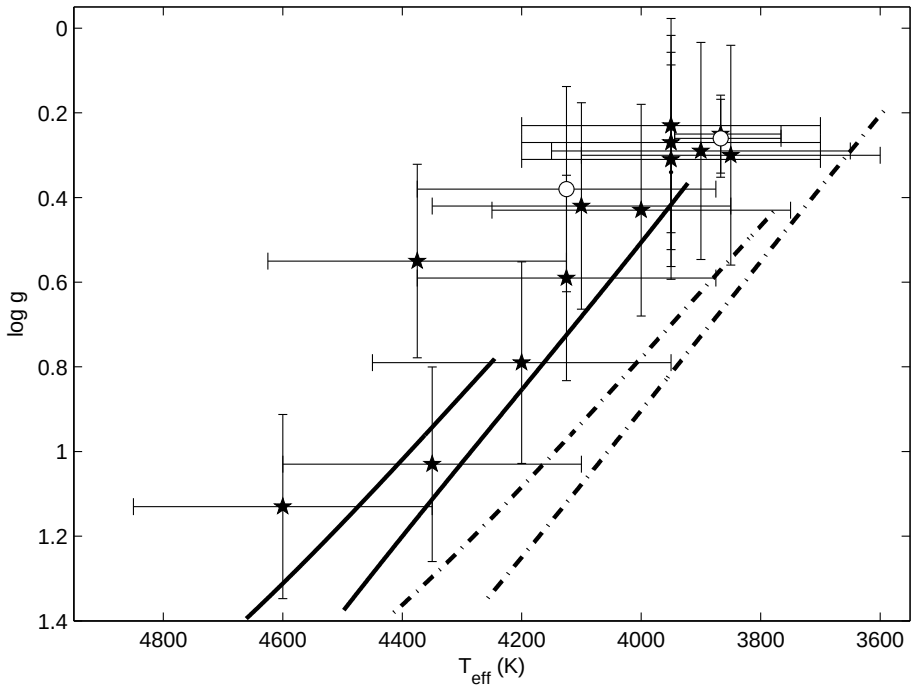

Figure 7.5: As for Figure 7.4 but for the stars in NGC 362. The dot-dash lines are AGB and RGB isochrones at [Fe/H] $= -1.0$ dex from Dotter et al. (2007). The solid lines are AGB and RGB isochrones at [Fe/H] $= -1.5$ dex.

the derivation of the stellar parameters for each star.

The two stars in NGC 6388 and the thirteen stars in NGC 362 were analysed following the process outlined in Chapter 2.

7.2 Derivation of stellar parameters

The stellar parameters of the two NGC 6388 stars that were analysed in this study are listed in Table 7.2. The temperature and gravity based on the values derived in McDonald & van Loon (2007), as well as whether or not the star has an infra-red excess, are also included. The spectroscopic parameters derived in this study are also listed.

Table 7.3 lists the same information as in Table 7.2 but for the thirteen stars in NGC 362 that were analysed for their heavy elemental abundances.

Bearing in mind the issues that were encountered with interpolating low gravity, low temperature MARCS models in the analysis of the 47 Tuc stars it was decided to forego interpolating models to derive the exact parameters. We preferred to use the best fit 'gridpoint' model for each star in the determination of the stellar abundances. The microturbulence was also restricted to intervals of 0.25 kms^{-1}.

The distinct continuum in the NGC 362 stars (see Figure 7.2) resulted in a very straightforward analysis in comparison to the 47 Tuc stars. Often two gridpoint models presented reasonable agreement, where one gridpoint model was higher in both gravity and temperature than the other. An abundance analysis was carried out in both cases and the level of agreement between the Y I and Y II lines was used to discriminate which model was the better fit. This analysis was also carried out for the two stars in NGC 6388.

NGC 6388 o10 and NGC 362 o01 both proved difficult in determining the best stellar model, and both resulted in lower microturbulence values than the other stars. Further investigation of these stars using lighter elements such as Ti to determine the stellar models, in combination with Fe, would clarify the stellar parameters for these stars. However the models determined from the Fe lines were reasonably consistent with the spectral parameters and the abundances that were derived showed no extreme departure from the rest of the sample (see Section 7.3).

7.2.1 Effects of departures from LTE on [Fe/H]

The departures from LTE that were seen between the high and low excitation potential Fe I lines in 47 Tuc were also found in both the NGC 362 and NGC 6388 samples. The same analysis was carried out investigating the mean abundances of the various Fe I subgroups for both NGC 362 and NGC 6388.

Considering first the thirteen stars in NGC 362, it was useful to see the effect of departures from LTE over a larger number of stars and with a greater range in temperatures. The high resolution of these stars also allowed them to be compared to departures from LTE that were seen in Arcturus.

Table 7.2: Star ID and stellar parameters for the two NGC 6388 stars as determined by spectral type in McDonald & van Loon (2007), and by spectroscopic analysis in this study. Neither star has an infra-red (IR) excess.

	McD07			Spectroscopic			[Fe/H]	
Star ID	T_{eff} (K)	*log g*	IR Excess[a]	T_{eff} (K)	*log g*	ξ (kms^{-1})	model[b]	derived[c]
o09	3699	0.54	N	4000	0.5	1.50	−0.5	−0.58
o10	3954	0.56	N	4000	0.5	1.25	−0.5	−0.62

[a] Origlia et al. (2002) designation of IR excess
[b] stellar model metallicity
[c] derived [Fe/H] as the mean of the Fe I and Fe II abundances

Table 7.3: As for Table 7.2, but for the thirteen NGC 362 stars.

	McD07			Spectroscopic			[Fe/H]	
Star ID	T_{eff} (K)	*log g*	IR Excess[a]	T_{eff} (K)	*log g*	ξ (kms^{-1})	model[b]	derived[c]
x02	3950	0.27	Y?	3900	0.0	1.50	−1.0	−1.18
o08	3850	0.30	N	4000	0.0	1.50	−1.0	−1.23
o03	3900	0.29	N	4000	0.0	1.50	−1.0	−1.24
ob2	3950	0.23	Y?	4000	0.0	1.50	−1.0	−1.32
o07	3950	0.31	N	4000	0.0	1.50	−1.0	−1.23
x01	4000	0.43	Y	4000	0.0	1.75	−1.0	−1.28
oa5	4100	0.42	N	4000	0.0	1.75	−1.0	−1.26
x03	3950	0.34	Y	4000	0.5	1.50	−1.0	−1.10
o05	4125	0.38	N	4250	0.5	1.50	−1.0	−1.20
xa2	4375	0.55	Y	4250	0.5	1.50	−1.0	−1.28
o04	4125	0.59	N	4250	1.0	1.50	−1.0	−1.06
o02	4200	0.79	N	4250	1.0	1.50	−1.0	−1.12
o10	4600	1.13	N	4250	1.0	1.00	−1.0	−1.27

[a] Origlia et al. (2002)
[b] stellar model metallicity
[c] derived [Fe/H] as the mean of the Fe I and Fe II abundances

Figures 7.6 to 7.8 show [Fe/H] against χ for the abundances derived from Fe I and Fe II lines in each of the NGC 362 stars. Within these figures each star has three associated figures investigating the $\chi - T_{eff}$ space, referred to as the left, middle and right column in each of the figures.

The stellar atmosphere model specified for each star was the best fitting model derived using the high χ Fe I lines only. The corresponding [Fe I/H] and [Fe II/H] values determined for that model using just the high χ Fe I lines for each star are shown in the figures in the righthand column. The ξ value specified in the those figures is the best fitting microturbulence value for each star. The best fitting model was then used to derive Fe I and Fe II abundance values based on the entire Fe I sample. These are shown in the figures in the middle column for the best fitting value of ξ, and the figures in the lefthand column show the values for the whole Fe I sample derived using the best fit model but with $\xi = 2.0 kms^{-1}$. The figures show the progression of the derived abundances from high to low ξ and the progression from the entire Fe I sample to the high χ Fe I sample.

For the hottest stars in Figure 7.6 there is no separation between the high and low χ Fe I lines at a $\xi = 2.0 kms^{-1}$. This is similar to what was seen in Arcturus. What is clear is the larger scatter in values at this ξ and the Fe II lines are, for the most part, at a higher abundance.

In the $\xi = 1.5 kms^{-1}$ regime the scatter in the high χ Fe I lines is much less and any trend with χ is reduce considerably indicating an appropriate choice of T_{eff}. This is more clearly seen when just the high χ lines are displayed in the right column.

As the stars move to lower temperatures and gravities (Figures 7.7 and 7.8), the separation between high and low χ lines becomes distinct in the $\xi = 2.0 kms^{-1}$ regime, although the high ξ also shows a trend of increasing abundance with χ. Lower values of ξ flatten out this trend but push the low χ lines to higher abundances. These figures show the effect of deriving stellar parameters from Fe lines over a large range of χ values for stars of low gravity and temperature. It further supports the need for careful line selection that minimises the errors introduced by departures from LTE and strong lines that are highly sensitive to changes in microturbulence.

Tables 7.4 and 7.5 quantify the observations made for Figures 7.6 to 7.8. The mean abundances for the Fe I subgroups and Fe II lines for each star at the specified ξ are listed, as well as the σ for each subset of lines.

The best fit values based on the high χ Fe I subgroup are listed first. The uncertainties for both the Fe I and Fe II lines reflect the small spread in values at this best fitting ξ. For the most part there is good agreement between the Fe I and Fe II abundances despite the decision not to use interpolated models to gain a more exact balance.

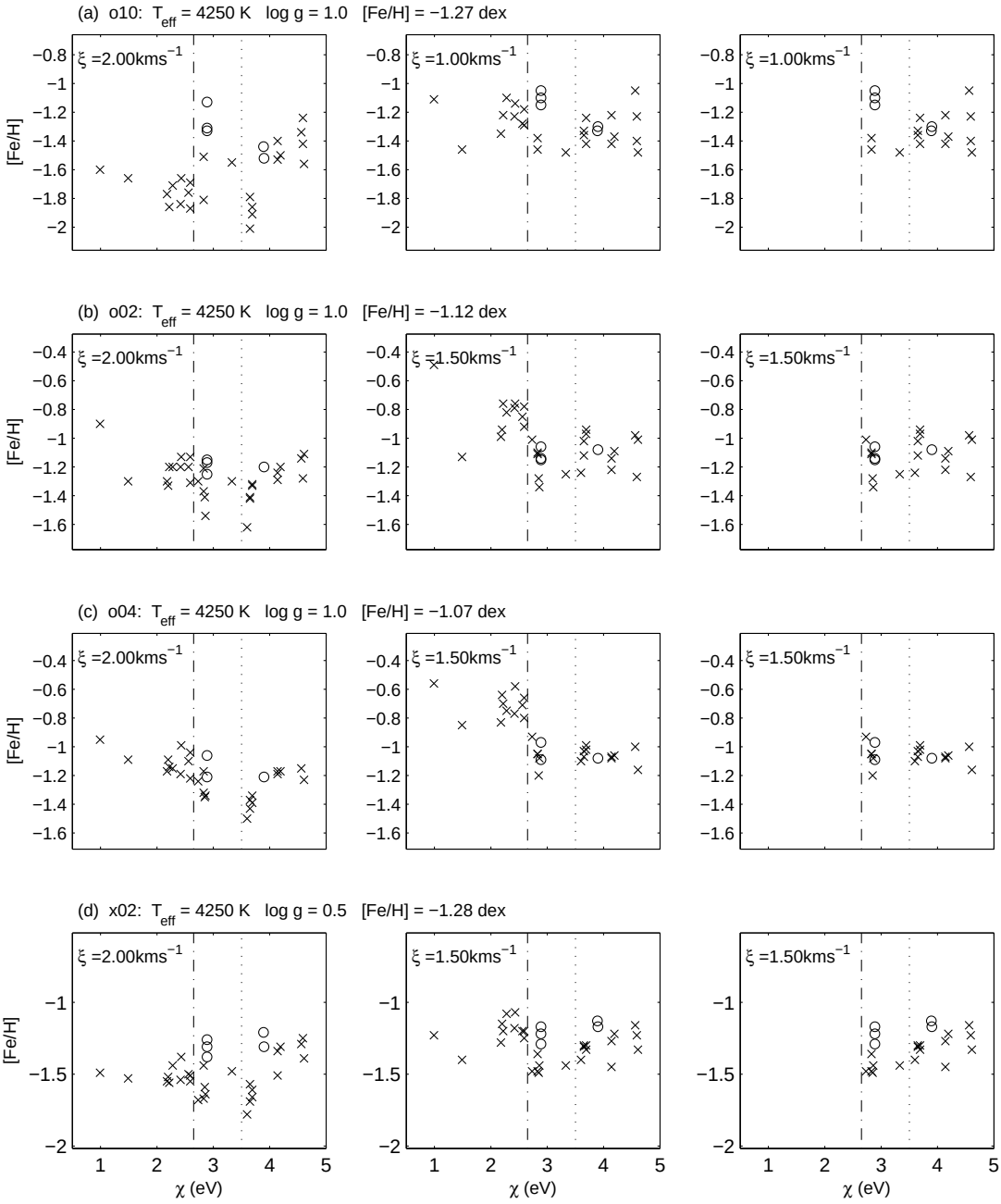

Figure 7.6: [Fe/H] against χ for the four hottest NGC 362 stars that were analysed in this study. The abundance values derived for both the Fe I ($\times$) and Fe II ($\circ$) lines are shown. The left column shows the complete sample of Fe I lines at all χ using the best fit $T_{eff}/log\ g$/[Fe/H] model, as specified, but using $\xi = 2.0$ kms^{-1}. The middle column shows the best fit model with best fit ξ for the whole Fe I sample. The right column shows the best fit model with best fit ξ for the Fe I lines of $\chi > 2.65$ eV only. The χ limit at 2.65 eV is indicated by the dash-dot line, the $\chi = 3.5$ eV limit by the dotted line.

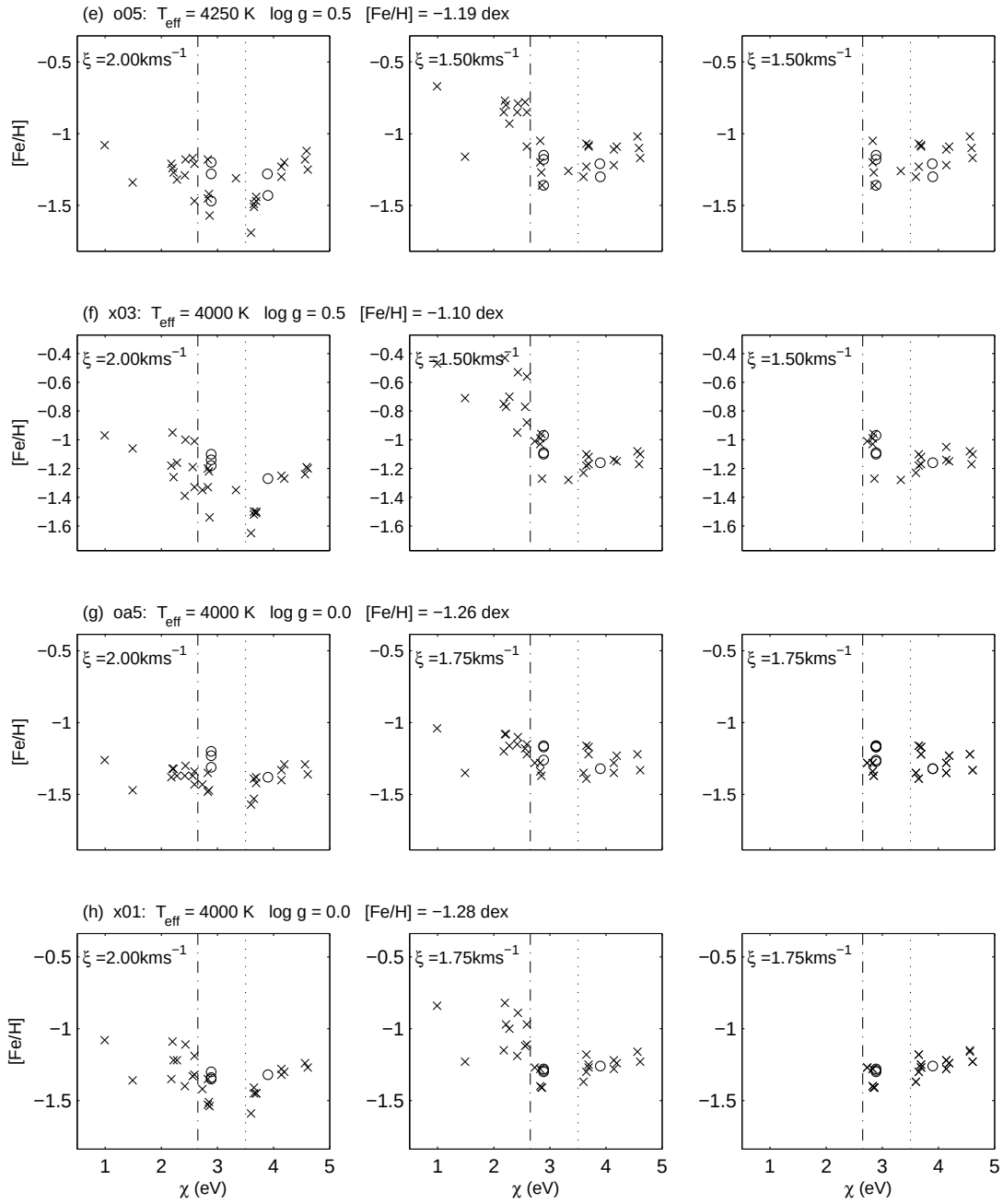

Figure 7.7: As for Figure 7.6 but for the four medium T_{eff} stars that were analysed in NGC 362.

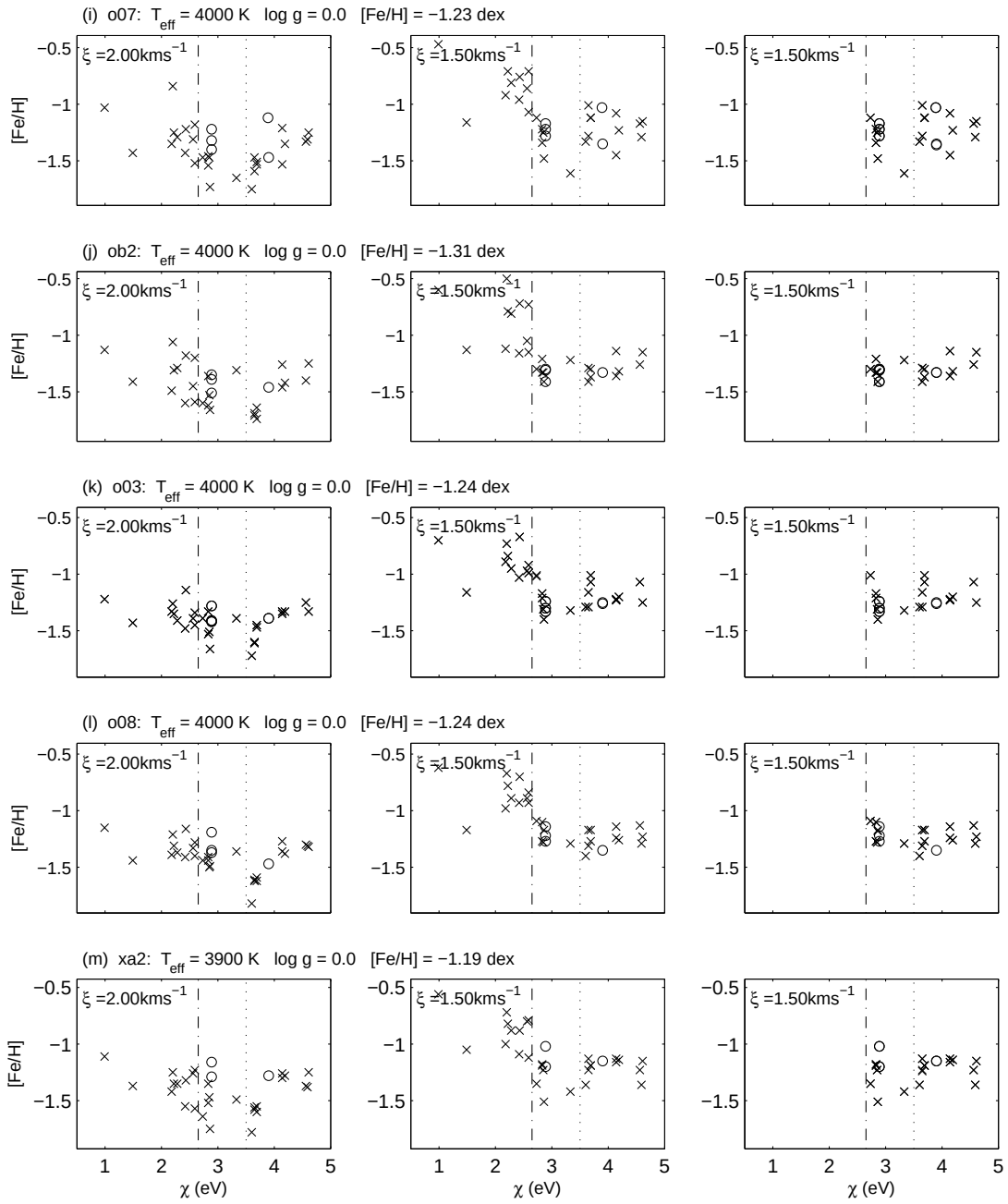

Figure 7.8: As for Figure 7.6 but for the five coolest T_{eff} stars that were analysed in NGC 362.

Table 7.4: Mean [Fe I/H] and [Fe II/H] values determined from the best fit model for the hottest seven stars at different values of ξ. Row 6 is the result using only the Fe I lines with $\chi > 2.65$ eV at the best fitting value for ξ, corresponding to the right column in Figures 7.6 to 7.8. Rows 9 to 11 are the results from the entire Fe I line list using the best fitting ξ value, corresponding to the middle column in Figures 7.6 to 7.8. Rows 14 to 16 are the results from the entire Fe I line list using $\xi = 2.0$ kms^{-1}, corresponding to the left column in Figures 7.6 to 7.8. The mean [Fe II/H] for each ξ sub-group are included in rows 7, 12 and 17.

Row														
1	Star ID	o10		o02		o04		xa2		o05		x03		oa5
2	T_{eff} (K)	4250		4250		4250		4250		4250		4000		4000
3	*log g*	1.0		1.0		1.0		0.5		0.5		0.5		0.0
4	[Fe/H]	−1.27		−1.12		−1.06		−1.28		−1.20		−1.10		−1.26
	Fe I lines for $\chi > 2.65$ eV													
5	ξ (kms^{-1})	1.00		1.50		1.50		1.50		1.50		1.50		1.75
6	[Fe I/H] $\chi > 2.65$ eV	−1.35	±0.12	−1.12	±0.12	−1.06	±0.07	−1.35	±0.10	−1.16	±0.10	−1.12	±0.09	−1.28	±0.07
7	[Fe II/H]	−1.19	±0.12	−1.11	±0.04	−1.05	±0.07	−1.20	±0.06	−1.24	±0.09	−1.08	±0.08	−1.23	±0.07
	Fe I lines at all χ													
8	ξ (kms^{-1})	1.00		1.50		1.50		1.50		1.50		1.50		1.75
9	[Fe I/H] $\chi < 5$ eV	−1.30	±0.13	−1.01	±0.20	−0.91	±0.19	−1.29	±0.12	−1.04	±0.19	−0.94	±0.25	−1.23	±0.10
10	[Fe I/H] $\chi < 2.65$ eV	−1.24	±0.11	−0.84	±0.16	−0.71	±0.10	−1.20	±0.09	−0.87	±0.14	−0.68	±0.17	−1.16	±0.09
11	[Fe I/H] $\chi > 2.65$ eV	−1.35	±0.12	−1.12	±0.12	−1.06	±0.07	−1.35	±0.10	−1.16	±0.10	−1.12	±0.09	−1.28	±0.07
12	[Fe II/H]	−1.19	±0.12	−1.11	±0.04	−1.05	±0.07	−1.20	±0.06	−1.24	±0.09	−1.08	±0.08	−1.23	±0.08
13	ξ (kms^{-1})	2.00		2.00		2.00		2.00		2.00		2.00		2.00
14	[Fe I/H] $\chi < 5$ eV	−1.66	±0.20	−1.27	±0.14	−1.21	±0.14	−1.52	±0.13	−1.32	±0.15	−1.27	±0.19	−1.38	±0.08
15	[Fe I/H] $\chi < 2.65$ eV	−1.74	±0.09	−1.20	±0.12	−1.10	±0.08	−1.51	±0.05	−1.25	±0.10	−1.14	±0.15	−1.36	±0.06
16	[Fe I/H] $\chi > 2.65$ eV	−1.60	±0.23	−1.32	±0.13	−1.29	±0.11	−1.52	±0.16	−1.36	±0.16	−1.36	±0.15	−1.41	±0.08
17	[Fe II/H]	−1.35	±0.15	−1.19	±0.04	−1.16	±0.09	−1.29	±0.06	−1.33	±0.11	−1.17	±0.07	−1.28	±0.08

Table 7.5: As for Table 7.4, but for the remaining six NGC 362 stars analysed in this study.

Row													
1	Star ID	x01		o07		ob2		o03		o08		x02	
2	T_{eff} (K)	4000		4000		4000		4000		4000		3900	
3	*log g*	0.0		0.0		0.0		0.0		0.0		0.0	
4	[Fe/H]	−1.28		−1.23		−1.32		−1.24		−1.23		−1.18	
	Fe I lines for $\chi > 2.65$ eV												
5	ξ (kms^{-1})	1.75		1.50		1.50		1.50		1.50		1.50	
6	[Fe I/H] $\chi > 2.65$ eV	−1.28	±0.08	−1.25	±0.15	−1.29	±0.08	−1.20	±0.11	−1.22	±0.08	−1.24	±0.11
7	[Fe II/H]	−1.28	±0.02	−1.21	±0.12	−1.34	±0.05	−1.28	±0.04	−1.24	±0.09	−1.12	±0.08
	Fe I lines at all χ												
8	ξ (kms^{-1})	1.75		1.50		1.50		1.50		1.50		1.50	
9	[Fe I/H] $\chi < 5$ eV	−1.18	±0.17	−1.06	±0.29	−1.14	±0.27	−1.08	±0.20	−1.07	±0.22	−1.10	±0.23
10	[Fe I/H] $\chi < 2.65$ eV	−1.03	±0.14	−0.79	±0.24	−0.89	±0.24	−0.90	±0.15	−0.85	±0.15	−0.88	±0.17
11	[Fe I/H] $\chi > 2.65$ eV	−1.28	±0.08	−1.24	±0.15	−1.32	±0.11	−1.20	±0.11	−1.22	±0.09	−1.25	±0.11
12	[Fe II/H]	−1.28	±0.02	−1.21	±0.11	−1.30	±0.08	−1.28	±0.04	−1.19	±0.14	−1.01	±0.16
13	ξ (kms^{-1})	2.00		2.00		2.00		2.00		2.00		2.00	
14	[Fe I/H] $\chi < 5$ eV	−1.34	±0.14	−1.39	±0.20	−1.44	±0.19	−1.41	±0.13	−1.40	±0.15	−1.43	±0.17
15	[Fe I/H] $\chi < 2.65$ eV	−1.24	±0.12	−1.26	±0.19	−1.34	±0.18	−1.35	±0.10	−1.31	±0.10	−1.34	±0.14
16	[Fe I/H] $\chi > 2.65$ eV	−1.41	±0.11	−1.48	±0.15	−1.51	±0.17	−1.45	±0.14	−1.46	±0.15	−1.48	±0.17
17	[Fe II/H]	−1.33	±0.02	−1.31	±0.14	−1.43	±0.07	−1.37	±0.06	−1.34	±0.12	−1.24	±0.07

The next set of values are the mean abundances and σ derived using the best fit model on the entire Fe I line list. For the hottest stars there is ~ 0.1 dex difference between the derived Fe I abundances above and below the χ limit of 2.65 eV, which is on the order of the σ for these subgroups. However, moving to the cooler, lower gravity stars shows the abundances increasing to as much as 0.4 dex which lies well outside the associated uncertainties. As expected, departures from LTE increase with decreasing temperature and gravity, and accounting for these effects becomes very important.

The mean abundance from the entire Fe I line list derived using the best fitting model shows how the metallicity can be underestimated if departures from LTE are not taken into account. For the hotter models the difference is well within the uncertainties of the high χ Fe I subgroup, but for the cooler stars it is not. Consequently, the lack of equilibrium in terms of the curve-of-growth analysis would result in the selection of a different model, which studies have shown are typically much hotter than if the departures from LTE were taken into account (Asplund, 2005).

In Figure 7.9 the two NGC 6388 stars also show the separation in derived Fe I abundance between high and low χ lines. The same model was used for both stars, with o10 requiring a lower value of ξ. The larger scatter in Fe I abundance values for this star contributed to the difficulty in determining its best fit model.

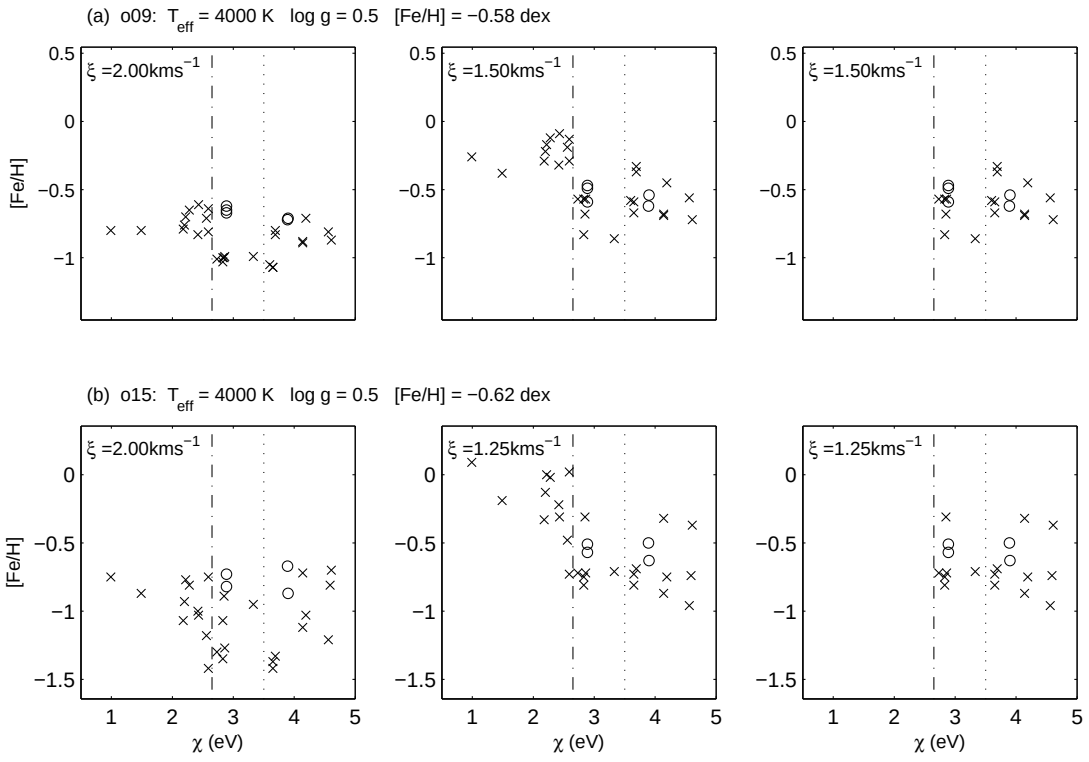

Figure 7.9: [Fe/H] against χ for the two NGC 6388 stars that were analysed in this study. All other details as in Figure 7.6.

Table 7.6 lists the associated abundances for the Fe I subgroups in Figure 7.9. Given the low temperatures and gravities of these stars the discrepancy between abundances derived from high and low χ lines would result in the selection of an incorrect stellar model if the departures from LTE were not taken into account.

Table 7.6: As for Table 7.4, but for the two NGC 6388 stars analysed in this study.

Star ID	o09		o10	
T_{eff} (K)	4000		4000	
log g	0.50		0.50	
[Fe/H]	−0.58		−0.62	
Fe I lines for $\chi > 2.65$ eV				
ξ (kms^{-1})	1.5		1.25	
[Fe I/H] $\chi > 2.65$ eV	−0.61	±0.14	−0.68	±0.19
[Fe II/H]	−0.54	±0.06	−0.55	±0.06
Fe I lines at all χ				
ξ (kms^{-1})	1.5		1.25	
[Fe I/H] $\chi < 5$ eV	−0.45	±0.23	−0.48	±0.32
[Fe I/H] $\chi < 2.65$ eV	−0.22	±0.09	−0.21	±0.24
[Fe I/H] $\chi > 2.65$ eV	−0.61	±0.14	−0.68	±0.19
[Fe II/H]	−0.54	±0.06	−0.55	±0.06
ξ (kms^{-1})	2.0		2.0	
[Fe I/H] $\chi < 5$ eV	−0.86	±0.14	−1.04	±0.24
[Fe I/H] $\chi < 2.65$ eV	−0.74	±0.08	−0.96	±0.21
[Fe I/H] $\chi > 2.65$ eV	−0.94	±0.11	−1.10	±0.24
[Fe II/H]	−0.67	±0.04	−0.77	±0.09

7.2.2 Effects of departures from LTE on Zr I lines

The NGC 362 sample presented a good range of temperatures over which to investigate in more detail how departures from LTE affects the strength of the Zr I lines that were discussed in Section 6.3.

Figure 7.10 shows the changes in Zr abundance as the stars in the sample become cooler and of lower gravity. The Zr abundances were normalised to provide a better comparison of the effects. For the hottest stars the Zr abundances from each line are in good agreement, and as for the Fe abundances, using the whole sample of lines would not produce a spurious result. However, as the stars become cooler the spread in Zr values becomes greater, with the

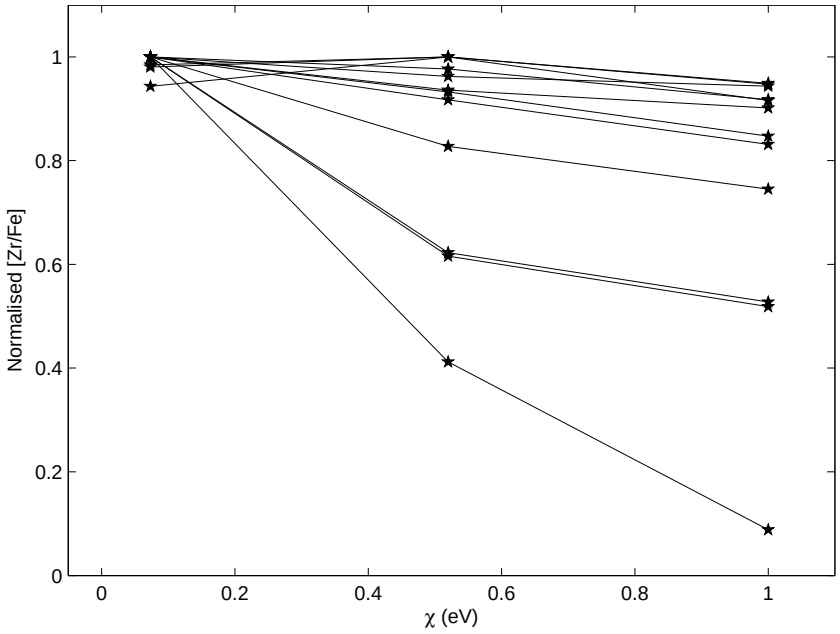

Figure 7.10: Variations in [Zr/Fe] derived for Zr I lines over a range of excitation potentials. The [Zr/Fe] values are normalised for better comparison. Each set of three datapoints ($\star$) connected by lines represents one of the NGC 362 stars with stellar temperature decreasing downwards. The datapoint at ~ 0.1 eV is the mean Zr abundance of the three lowest χ Zr I lines. The other two datapoints represent the abundances for the Zr I lines at 6140 Åand 6445 Å.

low excitation Zr I lines returning much higher abundances than the high excitation lines. This is the effect that was seen in the Fe I lines in the previous section. At these cooler temperatures and lower gravities line selection becomes very important. The investigation of the 47 Tuc star *tc*04 showed that increasing the microturbulence can force the Zr abundances into equilibrium. However, this can have a detrimental effect on the Fe I - Fe II equilibrium. For the hotter stars in the NGC 362 sample the majority of the Zr lines were used to derived the abundance as they were all in good agreement. For the cooler stars the low excitation lines ($\chi \leq 0.2$ eV) were discarded.

7.2.3 Veiling Effects

With the exception of Lee 2525, the 47 Tuc stars were found to have much lower metallicity than is expected for that cluster. As discussed in Section 6.4 these stars all had IR excesses, which indicates the presence of a circumstellar dust cloud. This dust cloud veils the absorption features of the star and artificially lowers the derived metallicity as outlined in Section 2.1.4. The derived metallicity for Lee 2525 was in good agreement with the accepted cluster metallicity and this object also has no IR excess. This supports the argument that veiling is at work in the rest of the 47 Tuc stars analysed here. Further investigation of this effect can be made using the stars in NGC 362 and NGC 6388.

Table 7.7 lists each of the stars analysed in this study over the three clusters including

their derived metallicity, whether or not they have an IR excess and, if so, its magnitude as represented by the index, $(K - [12])_o$. The difference of the star's metallicity with respect to the cluster metallicity is also included.

The two NGC 6388 stars that were analysed for chemical abundances have no IR excess and so no internal comparison could be made within that cluster. However, as NGC 6388 and 47 Tuc are of similar metallicity (-0.60 dex and -0.76 dex respectively), the stars in NGC 6388 can be compared with the 47 Tuc stars.

Table 7.7: The stars, for each of the three clusters, ordered in increasing metallicity. The difference of the star's metallicity from the mean cluster metallicity is compared with the reported IR excess, $(K - [12])_o$.

Star ID	[Fe/H]	IR Excess?	$[Fe/H]_\star - [Fe/H]_{GC}$	$(K-12)_o$ [a]
47 Tuc	−0.76			
tc09	−0.98	Y	−0.22	1.37
tc05	−0.95	Y	−0.19	2.14
tc04	−0.91	Y	−0.15	1.39
tc02	−0.90	Y	−0.14	0.70
tc03	−0.88	Y	−0.12	0.76
Lee2525	−0.73	N	+0.03	−0.10[b]
NGC 6388	−0.60			
o10	−0.62	N	−0.02	-
o09	−0.58	N	+0.02	-
NGC 362	−1.16			
ob2	−1.32	Y?	−0.16	?
x01	−1.28	Y	−0.12	1.75
xa2	−1.28	Y	−0.12	1.11
o10	−1.27	N	−0.11	-
oa5	−1.26	N	−0.10	-
o03	−1.24	N	−0.08	-
o07	−1.23	N	−0.07	-
o08	−1.23	N	−0.07	-
o05	−1.20	N	−0.04	-
x02	−1.18	Y?	−0.02	?
o02	−1.12	N	+0.04	-
x03	−1.10	Y	+0.06	0.99
o04	−1.06	N	+0.11	-

[a] Origlia et al. (2002)
[b] Ramdani & Jorissen (2001)

Table 7.7 shows that the IR excess stars of 47 Tuc returned metallicities that were significantly more metal poor than the accepted metallicity value for that cluster. The stars with the highest IR excess also differed the greatest from the cluster's accepted metallicity. The non-IR excess star, Lee 2525, differed from that cluster metallicity by only 0.03 dex. The non-IR excess stars of NGC 6388 returned metallicities in very good agreement with the accepted metallicity of that cluster. This limited sample presents a definite correlation between IR excess and metallicity.

NGC 362 presented a complete sample within a single cluster that had both IR and non-IR excess stars. Three of the thirteen stars have a reported IR excess while two more have suspected IR excesses. Table 7.7 shows that the three most metal-poor stars differ from the cluster metallicity to the same magnitude as the IR excess 47 Tuc stars. Two of these definitely have an IR excess, while the third is a suspected IR excess object. Of the two remaining IR excess stars in NGC 362, one is only slightly more metal poor than the cluster mean with a suspected IR excess, while the other is more metal rich by 0.06 dex, although it has a reported IR excess. Also at least two non-IR excess stars are almost as metal-poor as three metal-poor IR excess stars. So the case is not conclusive for NGC 362.

This is an issue that can be better addressed with further refinement of the stellar models for these stars. These stars were selected for observation by McDonald & van Loon (2007) because they are variable stars undergoing mass loss and so they present an excellent sample for a more detailed study into the relation between dust, IR excess and metallicity. However, other than the discussion noted above as a possible explanation for the derived low metallicities, a more detailed investigation is beyond the scope of this research until the other issues with stellar model determination have been satisfactorily resolved.

7.3 Element abundance results

The results of the chemical abundance analysis for the NGC 362 and the NGC 6388 stars are listed in Tables 7.8 to 7.14. A detailed discussion of these results is presented with the pertinent figures in the following sections.

Tables 7.8 and 7.9 list the derived Fe and heavy element abundances for each of the NGC 362 stars. The 1 σ variation in [Fe I,Fe II/H] are $\pm$0.09 dex and $\pm$0.08 dex respectively. The particular light *s*-process elements that could be measured in these stars differed for the analysis of the 47 Tuc stars by the inclusion of Sr. Hence the *ls* and *hs* ratios were defined for both the NGC 362 and NGC 6388 analyses as:

$$[ls/\mathrm{Fe}] = \langle\ [\mathrm{Sr\ I/Fe}],\ [\mathrm{Y\ I/Fe}],\ [\mathrm{Y\ II/Fe}],\ [\mathrm{Zr\ I/Fe}],\ [\mathrm{Zr\ II/Fe}]\ \rangle$$
$$[hs/\mathrm{Fe}] = \langle\ [\mathrm{La\ II/Fe}],\ [\mathrm{Nd\ II/Fe}]\ \rangle$$

Table 7.8: Abundance results for Fe I, Fe II and the heavy elements for seven stars analysed in the NGC 362 sample starting with the hottest stars. The stellar parameters are also specified, as well as the light *s*- and heavy *s*-process ratios where $ls \equiv$ Y I, Y II, Zr I, and $hs \equiv$ La II, Nd II. The uncertainty in [Fe I,Fe II/H] values are $\pm$0.09 dex and $\pm$0.08 dex respectively.

Star ID	o10		o02		o04		xa2		o05		x03		oa5	
T_{eff} (K)	4250		4250		4250		4250		4250		4000		4000	
log g	1.0		1.0		1.0		0.5		0.5		0.5		0.0	
ξ (kms^{-1})	1.00		1.50		1.50		1.50		1.50		1.50		1.75	
X	[X/H]	N	[X/H]	N	[X/H]	N	[X/H]	N	[X/H]	N	[X/H]	N	[X/H]	N
Fe I	−1.35	14	−1.12	17	−1.06	15	−1.35	17	−1.16	13	−1.12	17	−1.28	14
Fe II	−1.19	5	−1.11	4	−1.05	3	−1.20	5	−1.24	3	−1.08	4	−1.23	4
X	[X/Fe]	N	[X/Fe]	N	[X/Fe]	N	[X/Fe]	N	[X/Fe]	N	[X/Fe]	N	[X/Fe]	N
Sr I	0.26	1	0.33	1	0.33	1	0.46	1	0.46	1	0.29	1	0.24	1
Y I	0.19	1	0.31	2	0.45	2	0.17	1	0.60	2	0.22	2	0.09	2
Y II	0.22	1	0.45	1	0.30	1	0.33	1	0.24	1	0.18	1	-	0
Zr I	0.18	4	0.47	5	0.48	2	0.33	5	0.54	2	0.32	2	0.24	2
Ba II	0.28	2	0.51	2	0.66	2	0.57	2	0.91	2	0.24	2	0.72	2
La II	0.29	1	0.35	1	0.47	1	0.37	1	0.50	1	0.35	1	0.23	1
Nd II	0.47	3	0.68	3	0.63	3	0.57	3	0.59	2	0.52	3	0.48	3
Eu II	0.78	2	0.85	2	0.81	2	0.82	2	0.87	2	0.75	2	0.73	2
	[X/Y]	σ	[X/Y]	σ	[X/Y]	σ	[X/Y]	σ	[X/Y]	σ	[X/Y]	σ	[X/Y]	σ
ls/Fe	0.21	0.04	0.39	0.08	0.39	0.09	0.33	0.12	0.46	0.16	0.25	0.06	0.19	0.09
hs/Fe	0.38	0.13	0.52	0.23	0.55	0.11	0.47	0.14	0.55	0.07	0.44	0.07	0.36	0.18
hs/*ls*	0.17	0.11	0.13	0.22	0.16	0.14	0.14	0.18	0.09	0.16	0.18	0.09	0.17	0.19

Table 7.9: As for Table 7.8, but for the remaining six stars analysed in the NGC 362 sample.

Star ID	x01		o07		ob2		o03		o08		x02	
T_{eff} (K)	4000		4000		4000		4000		4000		3900	
log g	0.0		0.0		0.0		0.0		0.0		0.0	
ξ (kms^{-1})	1.75		1.50		1.50		1.50		1.50		1.50	
X	[X/H]	N	[X/H]	N	[X/H]	N	[X/H]	N	[X/H]	N	[X/H]	N
Fe I	−1.28	15	−1.25	17	−1.29	15	−1.20	16	−1.22	17	−1.24	17
Fe II	−1.28	4	−1.21	5	−1.34	4	−1.28	4	−1.24	4	−1.12	3
X	[X/Fe]	N	[X/Fe]	N	[X/Fe]	N	[X/Fe]	N	[X/Fe]	N	[X/Fe]	N
Sr I	0.38	1	0.24	1	-	0	0.55	1	0.35	1	0.28	1
Y I	0.22	1	0.24	2	0.39	1	0.62	1	0.19	2	0.17	2
Y II	-	0	0.27	2	0.30	1	0.28	1	-	0	-	0
Zr I	0.31	5	0.23	2	0.43	2	0.48	2	0.26	2	0.17	2
Ba II	0.01	2	0.43	2	0.87	2	1.12	2	0.48	2	0.52	2
La II	0.27	1	0.32	1	0.41	1	0.67	1	0.24	1	0.25	1
Nd II	0.53	3	0.53	3	0.65	3	0.62	3	0.49	2	0.46	3
Eu II	0.73	2	0.78	2	0.76	2	0.79	2	0.74	2	0.73	2
	[X/Y]	σ	[X/Y]	σ	[X/Y]	σ	[X/Y]	σ	[X/Y]	σ	[X/Y]	σ
ls/Fe	0.30	0.08	0.25	0.02	0.38	0.06	0.48	0.15	0.27	0.08	0.21	0.06
hs/Fe	0.40	0.18	0.42	0.15	0.53	0.17	0.64	0.04	0.36	0.17	0.36	0.15
hs/*ls*	0.10	0.19	0.18	0.12	0.15	0.17	0.16	0.13	0.09	0.18	0.15	0.15

As each ratio is the mean of the specified elemental abundances, the uncertainties for [*ls*/Fe] and [*hs*/Fe] are the standard deviation on that mean. The [*hs/ls*] ratio is the difference between the two means and so the [*hs/ls*] uncertainty is the sum of the standard deviations for each mean divided by $\sqrt{2}$.

Following the same analysis techniques as for the 47 Tuc stars the derived abundances for NGC 362 were re-calculated relative to Arcturus. These abundances are listed in Table 7.10.

NGC 362 x03 was used as the basis of the error analysis for the sample. Table 7.11 lists the uncertainties for each elemental abundance and the changes in abundances for associated changes in T_{eff}, *log g* and ξ. The variations are similar to those noted for Arcturus and the 47 Tuc stars. The barium abundance is the most sensitive to microturbulence due to the strength of the lines upon which the abundance was derived. The neutral species show the greatest sensitivity to changes in T_{eff}. The majority of the ionised species show abundance changes of similar magnitude for changes in all three parameters, although the degree of sensitivity is only on the order of the uncertainties in the Fe lines.

The average abundances for the NGC 362 sample are listed in Table 7.12. The uncertainties here are the standard deviation of the mean of each elemental abundance over the stellar sample. This definition for the uncertainty was also used for each of the [*ls*/Fe], [*hs*/Fe] and [*hs/ls*] values, and represents the spread of these indices across the sample, rather than deriving these from the stellar sample means. Both the abundances relative to the Sun and Arcturus are shown.

Table 7.13 lists the derived iron and heavy elemental abundances for the two NGC 6388 stars with respect to the Sun. The mean abundance of the two stars for each element is also included, as well as the *hs* and *ls* ratios.

Table 7.14 lists the abundances calculated relative to Arcturus. The metallicity derived for these stars is almost identical to the metallicity derived in this study for Arcturus. However these results clearly show that these stars are considerably more enriched in *s*-process elements than Arcturus, despite the similarity in metallicity. The *r*-process element, Eu, is also enriched with respect to Arcturus to a level that is outside the uncertainties. The 47 Tuc stars were also enriched in *s*-process elements compared to Arcturus, although the Eu abundances were comparable. This is indicative of the different enrichment processes that have occurred for the globular cluster stars compared with the field star Arcturus.

NGC 6388 o09 was used as the basis of the error analysis for the NGC 6388 sample and the results are listed in Table 7.15. The uncertainties in the derivation of each elemental abundance, as well as changes in abundance associated with changes in the stellar parameters, are shown. Again the results are similar to what was observed in the previous error analyses of NGC 362 and 47 Tuc stars.

Table 7.10: Abundances for Fe I, Fe II and the heavy elements for each star analysed in the NGC 362 sample calculated relative to the derived abundances for Arcturus. The *ls* and *hs* ratios were also recalculated using these abundances relative to Arcturus. The resulting uncertainty in [Fe I,Fe II/H] values are ±0.15 dex and ±0.09 dex respectively.

Star	o10	o02	o04	xa2	o05	x03	oa5	x01	o07	ob2	o03	o08	x02
X	$[X/H]_{Arc}$	$[X/H]_{Arc}$	$[X/H]_{Arc}$	$[X/H]_{Arc}$	$[X/H]_{Arc}$	$[X/H]_{Arc}$	$[X/H]_{Arc}$	$[X/H]_{Arc}$	$[X/H]_{Arc}$	$[X/H]_{Arc}$	$[X/H]_{Arc}$	$[X/H]_{Arc}$	$[X/H]_{Arc}$
Fe I	−0.74	−0.51	−0.45	−0.74	−0.55	−0.51	−0.67	−0.67	−0.64	−0.68	−0.59	−0.61	−0.63
Fe II	−0.63	−0.55	−0.49	−0.64	−0.68	−0.52	−0.67	−0.72	−0.65	−0.78	−0.72	−0.68	−0.56
X	$[X/Fe]_{Arc}$	$[X/Fe]_{Arc}$	$[X/Fe]_{Arc}$	$[X/Fe]_{Arc}$	$[X/Fe]_{Arc}$	$[X/Fe]_{Arc}$	$[X/Fe]_{Arc}$	$[X/Fe]_{Arc}$	$[X/Fe]_{Arc}$	$[X/Fe]_{Arc}$	$[X/Fe]_{Arc}$	$[X/Fe]_{Arc}$	$[X/Fe]_{Arc}$
Sr I	0.32	0.39	0.38	0.52	0.52	0.35	0.30	0.44	0.30	-	0.61	0.41	0.34
Y I	0.12	0.24	0.38	0.11	0.54	0.16	0.03	0.15	0.17	0.33	0.55	0.12	0.10
Y II	0.10	0.33	0.18	0.22	0.12	0.06	-	-	0.15	0.19	0.16	-	-
Zr I	0.17	0.46	0.46	0.32	0.53	0.31	0.23	0.30	0.22	0.42	0.47	0.25	0.16
Ba II	0.47	0.70	0.85	0.76	1.10	0.43	0.91	0.20	0.62	1.06	1.31	0.67	0.71
La II	0.25	0.31	0.43	0.33	0.46	0.31	0.19	0.23	0.28	0.37	0.63	0.20	0.21
Nd II	0.38	0.59	0.53	0.47	0.50	0.43	0.39	0.43	0.43	0.56	0.52	0.39	0.37
Eu II	0.42	0.49	0.45	0.46	0.51	0.39	0.37	0.37	0.42	0.41	0.43	0.38	0.37
X/Y	$[X/Y]_{Arc}$	$[X/Y]_{Arc}$	$[X/Y]_{Arc}$	$[X/Y]_{Arc}$	$[X/Y]_{Arc}$	$[X/Y]_{Arc}$	$[X/Y]_{Arc}$	$[X/Y]_{Arc}$	$[X/Y]_{Arc}$	$[X/Y]_{Arc}$	$[X/Y]_{Arc}$	$[X/Y]_{Arc}$	$[X/Y]_{Arc}$
ls/Fe	0.18	0.36	0.35	0.29	0.43	0.22	0.19	0.30	0.21	0.31	0.45	0.26	0.20
hs/Fe	0.31	0.45	0.48	0.40	0.48	0.37	0.29	0.33	0.36	0.46	0.58	0.30	0.29
hs/*ls*	0.13	0.09	0.13	0.11	0.05	0.15	0.10	0.03	0.15	0.15	0.13	0.03	0.09

Table 7.11: Variations in the derived abundances with associated changes in T_{eff}, *log g* and ξ for NGC 362 star x03.

				Δ[X/H]		
Species				ΔT_{eff}	$\Delta log\ g$	$\Delta\xi$
X	N	[X/H]	σ	-100K	-0.5	$+0.5 kms^{-1}$
Fe I	17	-1.12	0.09	+0.02	-0.12	-0.23
Fe II	4	-1.08	0.08	+0.19	-0.27	-0.09
		[X/Fe]		Δ[X/Fe]		
Sr I	1	0.29	-	-0.21	+0.17	+0.18
Y I	2	0.22	0.01	-0.31	+0.05	+0.12
Y II	1	0.18	-	-0.11	-0.15	+0.16
Zr I	2	0.32	0.21	-0.27	+0.10	+0.16
Ba II	2	0.24	0.08	-0.06	-0.06	-0.48
La II	1	0.35	-	-0.13	-0.05	+0.07
Nd II	3	0.52	0.06	-0.09	-0.02	+0.15
Eu II	2	0.75	0.02	-0.08	-0.02	+0.10

Table 7.12: Mean abundances for the NGC 362 sample. Columns 1 and 2 are the mean and σ calculated with respect to the Sun. Columns 3 and 4 are the mean and σ calculated with respect to Arcturus.

X	$\langle$[X/H]$\rangle$	σ	$\langle$[X/H]$_{Arc}\rangle$	σ
Fe I	-1.22	0.09	-0.61	0.09
Fe II	-1.20	0.09	-0.64	0.09
X	$\langle$[X/Fe]$\rangle$	σ	$\langle$[X/Fe]$_{Arc}\rangle$	σ
Sr I	0.35	0.10	0.41	0.10
Y I	0.30	0.17	0.23	0.17
Y II	0.29	0.08	0.17	0.08
Zr I	0.34	0.12	0.33	0.12
Ba II	0.56	0.30	0.75	0.30
La II	0.36	0.12	0.32	0.12
Nd II	0.56	0.07	0.46	0.07
Eu II	0.78	0.05	0.42	0.05
X/Y	$\langle$[X/Y]$\rangle$	σ	$\langle$[X/Y]$_{Arc}\rangle$	σ
ls/Fe	0.32	0.10	0.29	0.09
hs/Fe	0.46	0.09	0.39	0.09
hs/*ls*	0.14	0.03	0.10	0.04

Table 7.13: Individual and mean Fe and heavy elemental abundances for the two NGC 6388 stars analysed in this study.

Star ID	o09		o10			
T_{eff} (K)	4000		4000			
log g	0.5		0.5			
ξ (kms^{-1})	1.5		1.25		mean	
X	[X/H]	N	[X/H]	N	⟨[X/H]⟩	σ
Fe I	−0.61	14	−0.68	15	−0.65	0.05
Fe II	−0.54	5	−0.55	4	−0.55	0.01
X	[X/Fe]	N	[X/Fe]	N	⟨[X/Fe]⟩	σ
Sr I	0.37	1	0.73	1	0.55	0.25
Y I	0.59	2	0.72	2	0.65	0.09
Y II	0.57	1	-	0	0.57	-
Zr I	0.40	2	0.55	2	0.47	0.10
Ba II	1.12	2	0.82	2	0.96	0.21
La II	0.40	1	0.38	1	0.39	0.02
Nd II	0.28	3	0.51	3	0.40	0.16
Eu II	0.50	2	0.63	2	0.57	0.09
X/Y	[X/Y]	σ	[X/Y]	σ	⟨[X/Y]⟩	σ
ls/Fe	+0.49	0.11	+0.67	0.11	+0.58	0.13
hs/Fe	+0.34	0.08	+0.44	0.09	+0.39	0.07
hs/*ls*	−0.14	0.14	−0.23	0.14	−0.18	0.06

Table 7.14: Individual and mean Fe and heavy element abundances calculated with respect to Arcturus for the two NGC 6388 stars analysed in this study.

Star ID	o09	o10		
T_{eff} (K)	4000	4000		
log g	0.5	0.5		
ξ (kms^{-1})	1.5	1.25	mean	
X	$[X/H]_{Arc}$	$[X/H]_{Arc}$	$\langle[X/H]_{Arc}\rangle$	σ
Fe I	0.00	0.01	0.01	0.01
Fe II	0.02	−0.07	−0.02	0.06
X	$[X/Fe]_{Arc}$	$[X/Fe]_{Arc}$	$\langle[X/Fe]_{Arc}\rangle$	σ
Sr I	0.43	0.79	0.61	0.25
Y I	0.52	0.65	0.59	0.09
Y II	0.45	-	0.45	-
Zr I	0.39	0.53	0.46	0.10
Ba II	1.31	1.01	1.16	0.21
La II	0.36	0.34	0.35	0.02
Nd II	0.19	0.41	0.30	0.16
Eu II	0.14	0.27	0.21	0.09
X/Y	$[X/Y]_{Arc}$	$[X/Y]_{Arc}$	$\langle[X/Y]_{Arc}\rangle$	σ
ls/Fe	+0.45	+0.66	+0.56	0.15
hs/Fe	+0.28	+0.37	+0.33	0.07
hs/ls	−0.17	−0.29	−0.23	0.08

Table 7.15: Variations in the derived abundances with associated changes in T_{eff}, *log g* and ξ for NGC 6388 o09.

Species	N	[X/H]	σ	Δ[X/H] ΔT_{eff} -100K	$\Delta log\ g$ -0.5	$\Delta\xi$ $+0.5 kms^{-1}$
Fe I	14	-0.61	0.14	+0.07	-0.10	-0.32
Fe II	5	-0.54	0.07	+0.21	-0.29	-0.13
	N	[X/Fe]	σ	Δ[X/Fe]		
Sr I	1	0.37	-	-0.23	+0.16	+0.21
Y I	2	0.59	0.25	-0.30	=0.06	+0.03
Y II	1	0.57	-	-0.13	-0.26	+0.23
Zr I	2	0.40	0.04	-0.28	+0.09	+0.18
Ba II	2	1.12	0.13	-0.14	-0.03	-0.27
La II	1	0.40	-	-0.14	-0.09	+0.06
Nd II	3	0.28	0.11	-0.14	-0.03	+0.22
Eu II	2	0.50	0.04	-0.16	+0.01	+0.17

7.4 Discussion of the derived chemical abundance

The analysis of the heavy elemental abundances for NGC 6388 and NGC 362 allowed investigation of the nature of *s*-process element abundances for globular clusters (GCs) of different metallicity. NGC 362 provided the largest sample for consideration. However, as NGC 6388 is quite similar to the metallicity of 47 Tuc, the two NGC 6388 stars also provide a comparison to that cluster.

7.4.1 Abundances in NGC 362 stars

Table 7.16 lists the Fe and heavy element abundances derived in previous studies of NGC 362 (Pilachowski et al. 1983; Gratton 1987a,b; Shetrone & Keane 2000) with the results from this analysis.

As shown in Table 7.1, these high resolution studies were carried out using spectra from a range of telescopes and instruments. The resolution ranged from 15,000 to 110,000 and the signal to noise per pixel ranged from 20 to 200 across the studies. This range in resolution and signal to noise, combined with systematic differences in analysis techniques between the studies, implies some caution must be observed in a comparison of these results. The mean metallicity determined here for the NGC 362 stars compares well to the accepted metallicity of this cluster of −1.16 dex (Harris, 1996). The other reported metallicities for this cluster range from −0.87 dex (Pilachowski et al., 1983) to −1.33 dex (Shetrone & Keane, 2000).

Table 7.16: Comparison of the heavy element abundances derived for this sample of NGC 362 stars with previous studies by Pilachowski et al. (1983) (P83), Gratton (1987a) & Gratton (1987b) (G87ab), and Shetrone & Keane (2000) (S00). The number of stars (N) for each study is listed.

Study	P83	G87ab	S00	this analysis
N	3	1	12	13
		$\langle$[Fe/H]$\rangle \pm \sigma$		
Fe	-0.87 ± 0.2	-1.18 ± 0.04	-1.33 ± 0.03	-1.21 ± 0.09
X		$\langle$[X/Fe]$\rangle \pm \sigma$		
Sr				$+0.35 \pm 0.10$
Y				$+0.29 \pm 0.18$
Zr				$+0.34 \pm 0.12$
Ba	-0.30 ± 0.4	-0.17 ± 0.23	$+0.28 \pm 0.22$	$+0.56 \pm 0.30$
La	$+0.30 \pm 0.3$			$+0.36 \pm 0.12$
Nd				$+0.56 \pm 0.07$
Eu			$+0.57 \pm 0.08$	$+0.78 \pm 0.05$

Only abundances of Ba, La and Eu were available in the previous studies for comparison with the results in this study. The large range in Ba abundances is as expected given the issues discussed earlier. The La abundance from this study agrees well with the abundance derived in Pilachowski et al. (1983). The Eu abundance derived in this study is higher by ~ 0.2 dex than the abundance derived in Gratton (1987a). The limited sample of derived abundances in the previous studies meant that [*hs*/*ls*] ratios could not be compared.

Figures 7.11 and 7.12 show the abundances derived from the Fe I and Fe II lines for each star relative to the Sun and Arcturus respectively. The stars are ordered in temperature sequence from hottest to coolest as listed in Table 7.3. In Figure 7.11 there is good agreement between the Fe I and Fe II values for each star and between the stars. Recalculating the Fe I and Fe II abundances relative to Arcturus, as shown in Figure 7.12, has a very small effect on the values. The uncertainty in each mean remains the same at 0.09 dex (see Table 7.12), although there is a slightly greater separation (0.03 versus 0.02) between the mean values for the sample. However the decision to use only gridpoint models has meant that the Fe I-Fe II equilibrium, and therefore the derived abundances, could be improved with further refinement of the stellar atmosphere models. With this in mind the uncertainty in the sample mean for each of Fe I and Fe II is reasonable.

Figures 7.13 and 7.14 display the light *s*-process elemental abundances that were derived for each star in temperature sequence relative to both the Sun and Arcturus. The abundances for Sr I, Y I, Y II and Zr I were obtained where possible for each of the stars. The Sr I and Zr I abundances are consistently higher than the Y I and Y II abundances for these stars. The mean values and uncertainties for each of the light *s*-process elements are given in Table 7.12 with the average of the *ls* to iron ratio being $\langle[ls/\mathrm{Fe}]\rangle = 0.32 \pm 0.10$ dex. The individual uncertainties for each *ls* elemental abundance are on the order of 0.10 dex, although Y I has a much larger uncertainty due to the range of values from the individual stars as seen in Figures 7.15 and 7.16.

Most notable are the spread in the individual *ls* element abundances for each of the two stars NGC 362 o05 and o03. Both show higher values for Sr I, Y I and Zr I than the rest of the sample, but the Y II value is much lower. This indicates a gravity issue as the Y I and Y II are out of equilibrium. Figure 7.11 shows that the Fe I and Fe II abundance equilibrium for these two stars could be improved. While the stated models are the best fitting of the grid-point models for each of these stars, further refinement will be possible when the interpolation issues are resolved.

Figure 7.14 shows the same as Figure 7.13, but for the *ls* element abundances relative to Arcturus. The average *ls* abundance relative to Arcturus is $\langle[ls/\mathrm{Fe}]_{Arc}\rangle = 0.29 \pm 0.09$ dex, which is lower in both mean and uncertainty compared to the values calculated relative to the Sun. However, the individual means for each of the *ls* element abundances show a larger disparity between them (see Table 7.12) which can be seen in the greater spread of values in Figure 7.14 compared with Figure 7.13. Relative to Arcturus there is better agreement

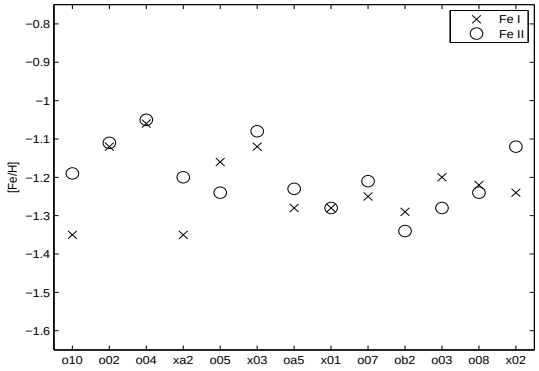

Figure 7.11: [Fe/H] relative to the Sun for each NGC 362 star in T_{eff} sequence for Fe I and Fe II.

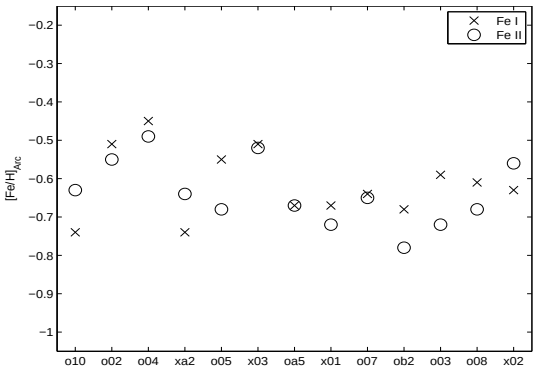

Figure 7.12: As for Figure 7.11 but the [Fe/H] is calculated relative to Arcturus.

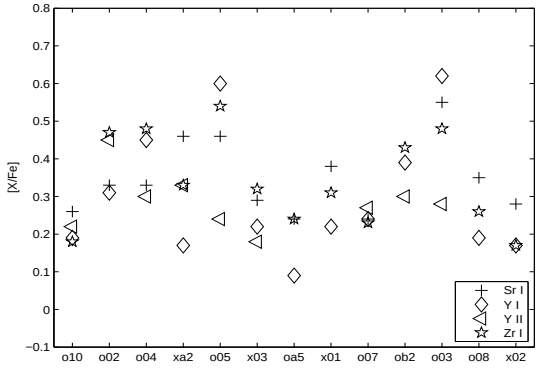

Figure 7.13: [X/Fe] relative to the Sun for each NGC 362 star in the sample for the light *s*-process elements, Sr, Y and Zr.

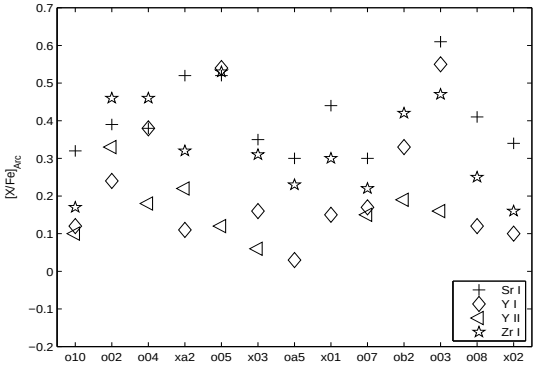

Figure 7.14: As for Figure 7.13 but the [X/Fe] is calculated relative to Arcturus.

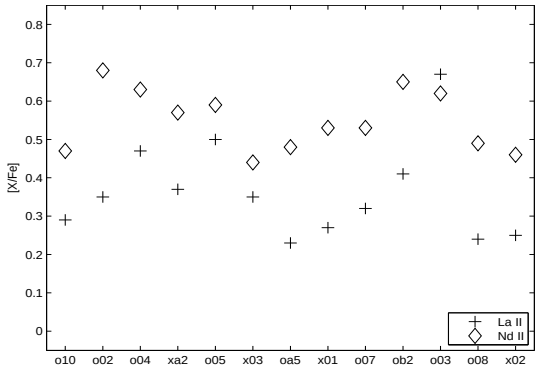

Figure 7.15: As for Figure 7.13 but for the heavy *s*-process elements, La and Nd.

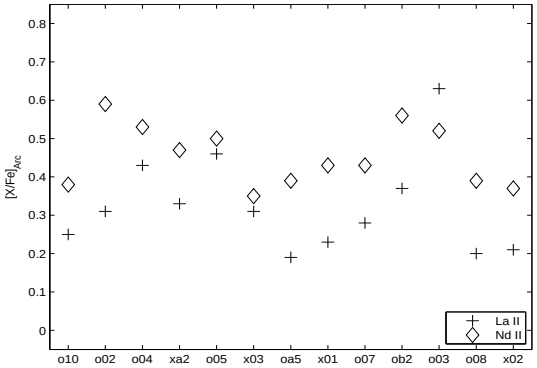

Figure 7.16: As for Figure 7.15 but the [X/Fe] is calculated relative to Arcturus.

between the stars for the *ls* elements as a whole.

The heavy *s*-process elements abundances, derived for each star relative to the Sun, are shown in Figure 7.15. The La abundances are consistently lower than the Nd abundances. The exception is NGC 362 o03 for which both the La and Nd abundances are high. This star was discussed earlier with regard to the separation of the Y I and Y II abundances, which indicates that the gravity may be incorrect. As both Nd and La abundances were derived from ionised species, which are more sensitive to changes in gravity, this may explain the discrepancy (see Table 7.11). For the heavy *s*-process elements $\langle[hs/\mathrm{Fe}]\rangle = 0.46 \pm 0.09$ dex which is approximately two σ greater than $\langle[ls/\mathrm{Fe}]\rangle$.

Figure 7.16 is the same as for Figure 7.15 but the abundances are calculated relative to Arcturus. In this instance the La and Nd abundances are in better agreement compared to the abundances relative to the Sun. Overall there is a reduction in the mean *hs* index where $\langle[hs/\mathrm{Fe}]_{Arc}\rangle = 0.39 \pm 0.09$ dex.

The two remaining elements, Ba and Eu, represent the extremes of the sample in terms of their uncertainties. As has been discussed in previous chapters, the two Ba II lines used in this study to determine the Ba abundances are very strong lines that are blended with iron lines. This makes them very susceptible to changes in T_{eff}, *log g* and ξ. Given the non-LTE and microturbulence issues that have been encountered during the course of this work, the Ba abundances found here have been treated with caution and not used in the calculation of the *hs* index. For the NGC 362 stellar sample the mean abundance was found to be $\langle[\mathrm{Ba/Fe}]\rangle = 0.56 \pm 0.30$ dex. While this is only 0.1 dex greater than $\langle[ls/\mathrm{Fe}]\rangle$ there is a very significant spread in this sample which, given the homogeneity in the other heavy elemental abundances, is unlikely to be real. Re-calculating relative to Arcturus considerably increased the abundance which is contrary to the overall, and minor, reduction that occurred for the other heavy elements. As La and Nd abundances could be readily obtained for these stars, and given the large uncertainties associated with the Ba lines, the pursuit of Ba abundances was not investigated further.

Europium on the other hand has a mean abundance of $\langle[\mathrm{Eu/Fe}]\rangle = 0.78 \pm 0.05$ dex. The uncertainty on this mean is very small indicating the very good agreement within the stellar sample. This abundance for Eu is enhanced compared to the more metal-rich stellar sample in 47 Tuc. The summary of [Eu/Fe] for GCs in Gratton et al. (2004) finds that $\langle[\mathrm{Eu/Fe}]\rangle = +0.42 \pm 0.05$ dex for clusters of $[\mathrm{Fe/H}] < -1$. The results here suggest NGC 362 is more enhanced in Eu than other clusters of similar metallicity. In Figure 6 of Gratton et al. (2004), this cluster mean would be placed above the GC sample but not excessively so. A reasonable number of GCs lie in the +0.6 dex realm for $\langle[\mathrm{Eu/Fe}]\rangle$. Refinement of the stellar models may bring this cluster within the trend observed in Gratton et al. (2004).

Figures 7.17 and 7.18 examine [*hs/ls*] against [Fe/H] derived relative to the Sun and Arcturus respectively. The mean and standard deviation of [*hs/ls*] and [Fe/H] for the sample is included in each figure.

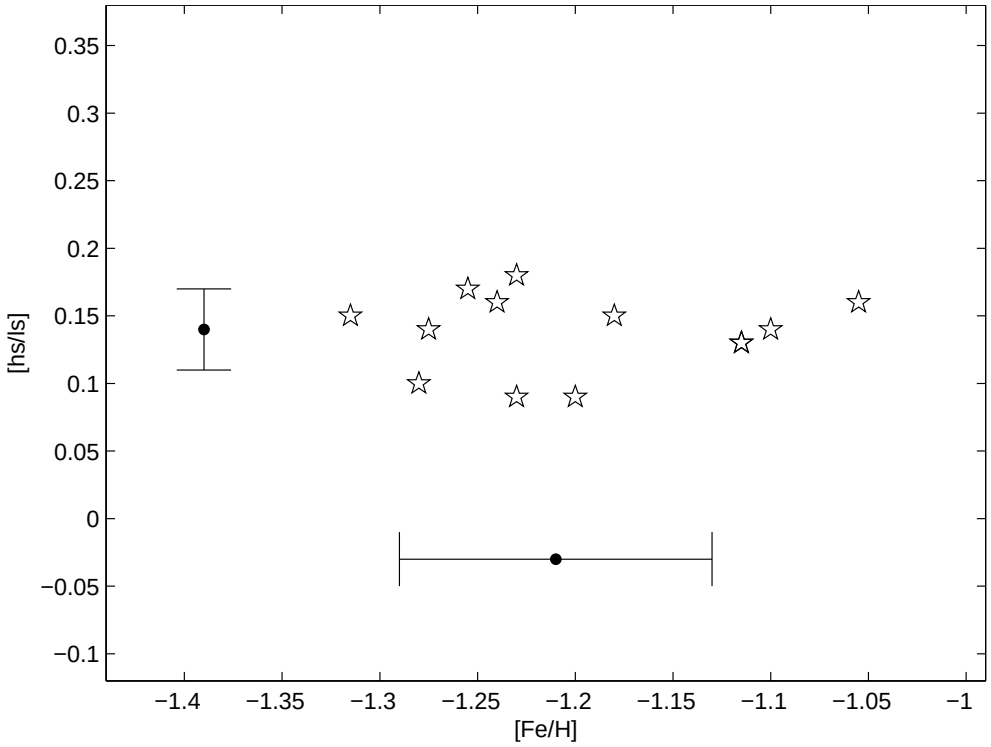

Figure 7.17: The ratio of the heavy to light *s*-process elemental abundance for each NGC 362 star against [Fe/H] with respect to the Sun. The mean and uncertainty for [*hs/ls*] and [Fe/H] are also indicated with values of $\langle[hs/ls]\rangle = +0.14 \pm 0.03$ dex and $\langle[\mathrm{Fe/H}]\rangle = -1.21 \pm 0.09$ dex

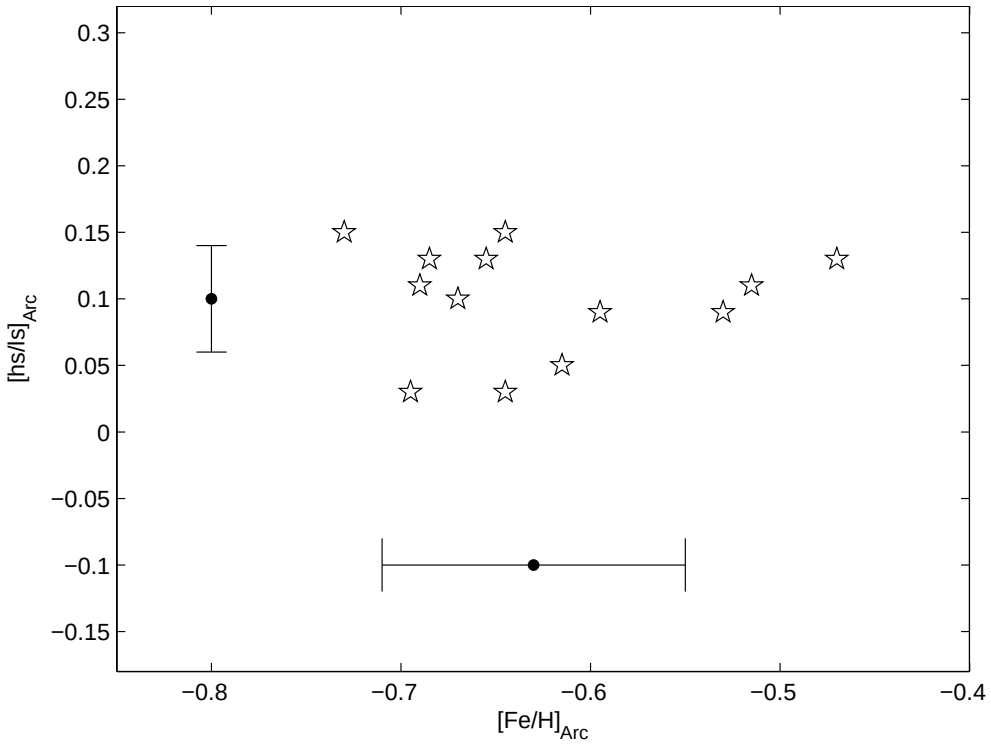

Figure 7.18: As for Figure 7.17, but with respect to Arcturus such that $\langle[hs/ls]_{Arc}\rangle = +0.10 \pm 0.04$ dex and $\langle[\mathrm{Fe/H}]_{Arc}\rangle = -0.63 \pm 0.09$ dex

With respect to the Sun, the sample shows a smaller spread in [*hs/ls*] than in [Fe/H] with $\langle[hs/ls]\rangle = +0.14 \pm 0.03$ dex and $\langle[\text{Fe/H}]\rangle = -1.21 \pm 0.08$ dex. [Fe/H] was calculated as the mean of the [Fe/H] values in the stellar sample, where [Fe/H] for each star is the mean of the abundances derived from the Fe I and Fe II lines. This is indicative of a very homogenous sample in terms of *ls* and *hs*. The [*hs/ls*] is lowered relative to Arcturus but the small spread in both values is retained. The low spread in both [*ls*/Fe] and [*hs*/Fe], and the lack of trend of [*hs/ls*] with metallicity, indicates a clear homogeneity in the *s*-process elemental abundance enhancements for NGC 362. It also indicates that the spread in the overall derived metallicity for these stars is simply due to the analysis rather than intrinsic difference between the stars.

7.4.2 Abundances in NGC 6388 stars

The two stars analysed for NGC 6388 cannot give a comprehensive picture of *s*-process elemental abundances in this cluster. However the similarity in metallicity to 47 Tuc means the stars can be compared to the results from that cluster.

There are two key studies that have investigated heavy element abundances in NGC 6388 stars. The summary of the mean abundances found for each study and the values determined in this analysis are summarised in Table 7.17. As for the NGC 362 samples, there is a range of resolution and signal to noise across these datasets which must be taken into account when comparing their results (see Table 7.1).

The mean [Fe/H] for the two NGC 6388 stars was found to be $\langle[\text{Fe/H}]\rangle = -0.60 \pm 0.02$ dex, so despite the issues with the models the derived metallicities agree well with the accepted metallicity of NGC 6388 of [Fe/H] = −0.60 dex (Harris, 1996). The cluster has been recently reported as being more metal-rich with a metallicity of $\langle[\text{Fe/H}]\rangle = -0.44 \pm 0.03$ dex (Carretta et al., 2007). However, in Wallerstein et al. (2007) two sets of metallicities were determined based on spectroscopic and photometric measurements. The spectroscopic curve-of-growth measurement found a mean metallicity of $\langle[\text{Fe/H}]\rangle = -0.79 \pm 0.08$ dex, while the photometrically derived metallicity agreed with previous values at a mean of $\langle[\text{Fe/H}]\rangle = -0.58 \pm 0.09$ dex.

It is interesting to note that the stars analysed in Wallerstein et al. (2007) were very cool low gravity giants and the very low metallicities of the spectroscopic analysis were derived by comparing line depths of high and low excitation potential Fe I lines. It is not clear if departures from LTE were taken into account and if so how they were treated. But given the very low metallicities derived for the 47 Tuc stars in Chapter 6, which are of similarly low temperature and gravity to the Wallerstein et al. (2007) NGC 6388 stars, it could be argued that the same effect is being seen in both datasets. Clearly further investigation into how best to treat these low temperature, low gravity stars is essential for future abundance analyses.

Table 7.17: Comparison of the heavy element abundances derived for this sample of NGC 6388 stars with previous studies by Carretta et al. (2007) (C07), and two sets of abundances from Wallerstein et al. (2007) (W07). The first set, designated W07p, was derived using a photometrically determined stellar model and the second set, W07s, was derived using a spectroscopically determined stellar model. The number of stars (N) for each study is also listed.

	C07	W07p	W07s	this analysis
N	13	8	8	2
		$\langle$[Fe/H]$\rangle \pm \sigma$		
Fe	-0.44 ± 0.03	-0.58 ± 0.09	-0.79 ± 0.08	-0.60 ± 0.02
X		$\langle$[X/Fe]$\rangle \pm \sigma$		
Rb		-0.27 ± 0.38	-0.09 ± 0.38	
Sr				$+0.55 \pm 0.25$
Y	-0.16 ± 0.19	-0.40 ± 0.23	-0.25 ± 0.24	$+0.61 \pm 0.09$
Zr	-0.18 ± 0.14	0.00 ± 0.26	-0.09 ± 0.16	$+0.47 \pm 0.10$
Ba	$+0.12 \pm 0.03$	$+0.21 \pm 0.19$	$+0.16 \pm 0.22$	$+0.96 \pm 0.21$
La	$+0.36 \pm 0.10$	$+0.13 \pm 0.23$	$+0.08 \pm 0.27$	$+0.30 \pm 0.02$
Ce	-0.27 ± 0.16	-0.10 ± 0.12	-0.15 ± 0.15	
Nd		$+0.39 \pm 0.10$	$+0.34 \pm 0.11$	$+0.40 \pm 0.16$
Eu	$+0.29 \pm 0.08$	$+0.26 \pm 0.23$	$+0.19 \pm 0.21$	$+0.57 \pm 0.09$
		$\langle$[X/Y]$\rangle \pm \sigma$		
ls/Fe	-0.17 ± 0.12	-0.28 ± 0.32	-0.18 ± 0.29	$+0.58 \pm 0.13$
hs/Fe	$+0.07 \pm 0.08$	$+0.16 \pm 0.09$	$+0.11 \pm 0.12$	$+0.39 \pm 0.07$
hs/*ls*	$+0.25 \pm 0.10$	$+0.44 \pm 0.33$	$+0.28 \pm 0.32$	-0.18 ± 0.06

Figures 7.19 and 7.20 show the Fe I and Fe II abundances for each star relative to the Sun and Arcturus respectively. The derived Fe I and Fe II abundances for NGC 6388 o10 are not in good agreement which implies that the gravity that has been used could be improved upon once the interpolation issues are resolved. NGC 6388 o09 has more consistent results, and both sets are improved when calculated relative to Arcturus.

The abundances of the light *s*-process elements for the NGC 6388 stars are shown in Figure 7.21 relative to the Sun and in Figure 7.22 relative to Arcturus. The respective means are $\langle[\mathrm{ls/Fe}]\rangle = 0.58 \pm 0.13$ dex and $\langle[\mathrm{ls/Fe}]_{Arc}\rangle = 0.56 \pm 0.15$ dex. The *ls* elemental abundances for NGC 6388 o09 are in better agreement when calculated relative to Arcturus.

In comparison to the analysis of the high-resolution 47 Tuc AGB stars, for which the sample mean relative to the Sun for the high-resolution AGB stars was $\langle[ls/\mathrm{Fe}]\rangle = 0.53 \pm 0.02$ dex, the similar metallicities have similar *ls* abundances. The NGC 6388 sample is in better agreement with the high resolution analysis of 47 Tuc stars, than with the results from the AAOmega medium-resolution 47 Tuc stars. This provides good support for the high-resolution analysis being more indicative of the heavy elemental abundances in the GCs. The medium-resolution analysis will be refined for future comparisons.

Comparing the high-resolution results of both 47 Tuc and NGC 6388 to the metal poor NGC 362 stars, for which the sample mean relative to the Sun was $\langle[ls/\mathrm{Fe}]\rangle = 0.32 \pm 0.10$ dex, shows a trend of decreasing *ls* abundance with decreasing metallicity. The NGC 6388 heavy *s*-process elements abundances in Figures 7.23 and 7.24 have corresponding means of $\langle[hs/\mathrm{Fe}]\rangle = 0.39 \pm 0.07$ dex and $\langle[hs/\mathrm{Fe}]_{Arc}\rangle = 0.33 \pm 0.06$ dex.

Making the comparison of the heavy *s*-process elements between clusters, the mean abundance relative to the Sun for 47 Tuc was $\langle[hs/\mathrm{Fe}]\rangle = 0.40 \pm 0.06$ dex, while for NGC 362 it was $\langle[hs/\mathrm{Fe}]\rangle = 0.46 \pm 0.09$ dex. Again 47 Tuc and NGC 6388 are in excellent agreement. The value for NGC 362 is also of similar magnitude, though slightly more enhanced, showing a general increase of $[hs/\mathrm{Fe}]$ with decreasing [Fe/H].

The Ba and Eu abundances (Tables 7.13 and 7.14) show a variation between the two NGC 6388 stars. However the Ba abundances are very high with a large spread and for the reasons discussed previously cannot be relied upon. Eu is again enhanced and there is reasonable agreement between the two stars, $\langle[\mathrm{Eu/Fe}]\rangle = 0.57 \pm 0.09$ dex and $\langle[\mathrm{Eu/Fe}]_{Arc}\rangle = 0.21 \pm 0.09$ dex. The abundances of Ba and Eu relative to Arcturus do not reduce the spread in either mean.

The values of Ba are so disparate within and between the clusters that making a comparison is not useful until those abundances are better understood. However, Eu provides an excellent comparison of the abundances of an *r*-process element between clusters. In 47 Tuc $\langle[\mathrm{Eu/Fe}]\rangle = 0.46 \pm 0.08$ dex, while for NGC 362 $\langle[\mathrm{Eu/Fe}]\rangle = 0.77 \pm 0.06$ dex. All three values are at the upper limits of the uncertainties when compared to GCs of similar metallicity in Figure 6 of Gratton et al. (2004). So while each sample has a small spread

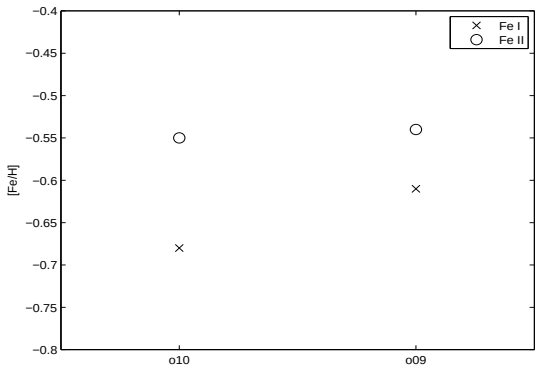

Figure 7.19: [Fe/H] relative to the Sun for each star in the NGC 6388 sample for Fe I and Fe II.

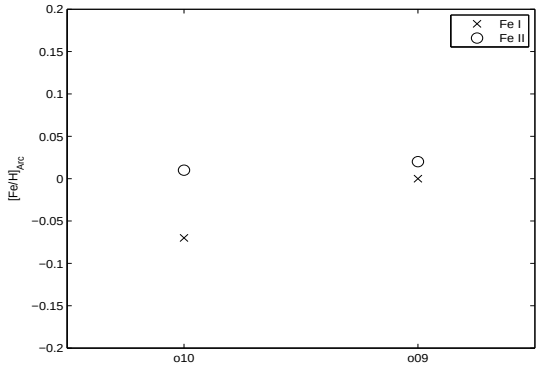

Figure 7.20: As for Figure 7.19, but the [Fe/H] is calculated relative to Arcturus.

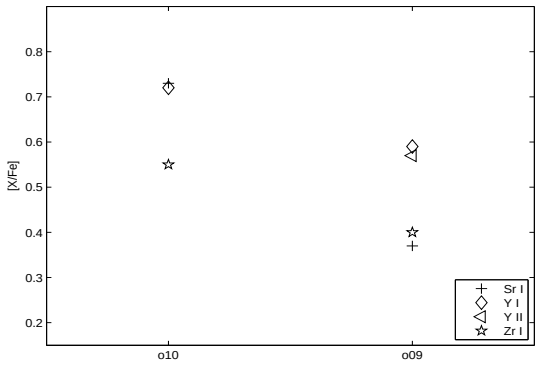

Figure 7.21: [X/Fe] relative to the Sun for each NGC 6388 star in the sample for the light *s*-process elements, Sr, Y and Zr.

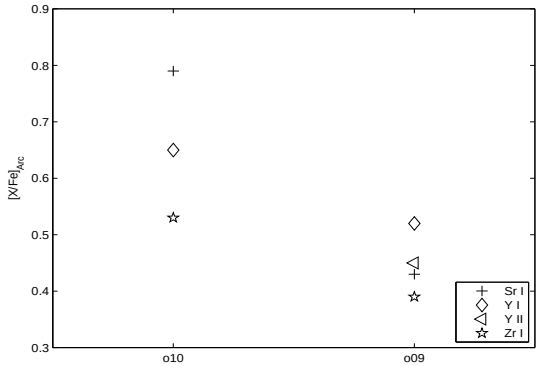

Figure 7.22: As for Figure 7.21, but the [X/Fe] is calculated relative to Arcturus.

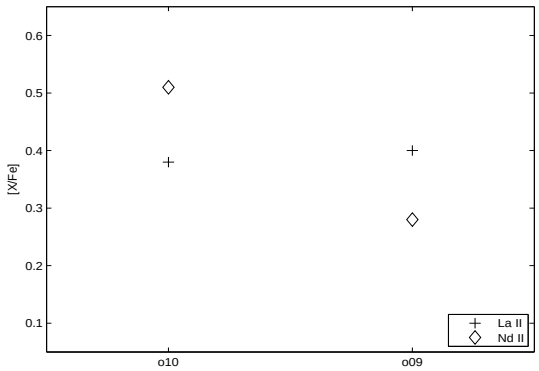

Figure 7.23: As for Figure 7.21, but for the heavy *s*-process elements, La and Nd.

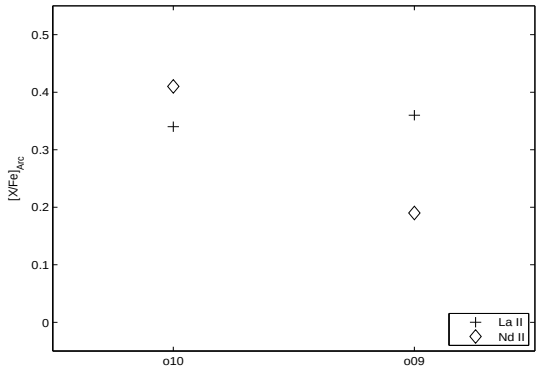

Figure 7.24: As for Figure 7.23 but the [X/Fe] is calculated relative to Arcturus.

within the cluster, confirming the homogeneity of Eu abundances within GCs, there may be some systematic offset that has occurred in the derivation of the abundances. There is still reasonable agreement between the NGC 6388 and 47 Tuc Eu abundances, as has been observed for the other heavy elements.

Figures 7.25 and 7.26 show [*hs/ls*] against [Fe/H] relative to the Sun and Arcturus for the NGC 6388 stars,. The mean ratio in each case is $\langle[hs/ls]\rangle = -0.18 \pm 0.06$ dex and $\langle[hs/ls]_{Arc}\rangle = -0.23 \pm 0.08$ dex. As a sample of two this cannot be said to show any trend. The values relative to the Sun are in better agreement than the values relative to Arcturus. The ratio relative to the Sun is comparable to that of the 47 Tuc stars, $\langle[hs/ls]\rangle = -0.13 \pm 0.05$ dex.

This analysis has determined a general enrichment of the heavy elements in the two NGC 6388 stars. The results from previous work (see Table 7.17) show a general depletion in the heavy elements. Only the Nd and Eu abundances are in reasonable agreement between all three studies. The two sets of results from Wallerstein et al. (2007) are in reasonable agreement with each other, despite the difference in metallicity, due to the differential analysis that was carried out that reduced the effects of any systematic errors.

The main difference between the studies is that both Carretta et al. (2007) and Wallerstein et al. (2007) have measured their abundances using equivalent width techniques. The analysis here pursued spectrum synthesis to determine heavy elemental abundances in order to take account of blending that is present for key weak heavy element lines. Some spectrum synthesis was undertaken in Wallerstein et al. (2007) for the Rb abundances which they then noted as being enriched in one star. Deriving elemental abundances from the equivalent widths of the heavy element lines in the NGC 6388 stars analysed here would provide a better comparison with these two studies.

With this difference in techniques in mind, Figure 7.27 compares [*hs/ls*] ratios of these studies with the theoretical predictions for four C^{13} pocket parameters at an initial mass of 1.5 $M_{\odot}$. (Stars of this initial mass are required in the GC formation scenario as they provide a sufficiently short timescale for an initial generation of stars to progress through their thermally pulsing AGB phase and hence produce heavy elements that can be incorporated into the currently observed generation of stars.) The predictions are constructed at a certain stellar mass and for a certain amount of ^{13}C in the ^{13}C pocket. The ^{13}C pocket parameter is typically stated relative to the standard case (ST). The standard case was derived in Arlandini et al. (1999) as being the amount of ^{13}C in AGB stars of initial mass between 1.5 and 3 $M_{\odot}$ at a metallicity of [Fe/H] = −0.3 dex that could explain the main solar component of the *s*-process elements (Busso et al., 2001). For alternative predictions the amount of ^{13}C is varied with respect to the standard case by some scaling factor. As the efficiency of the *s*-process is sensitive to both the amount of ^{13}C in the pocket, and to the metallicity of the star, by setting the ^{13}C pocket parameter to a constant the [*hs/ls*] predictions for a certain mass can be explored over a range of metallicities.

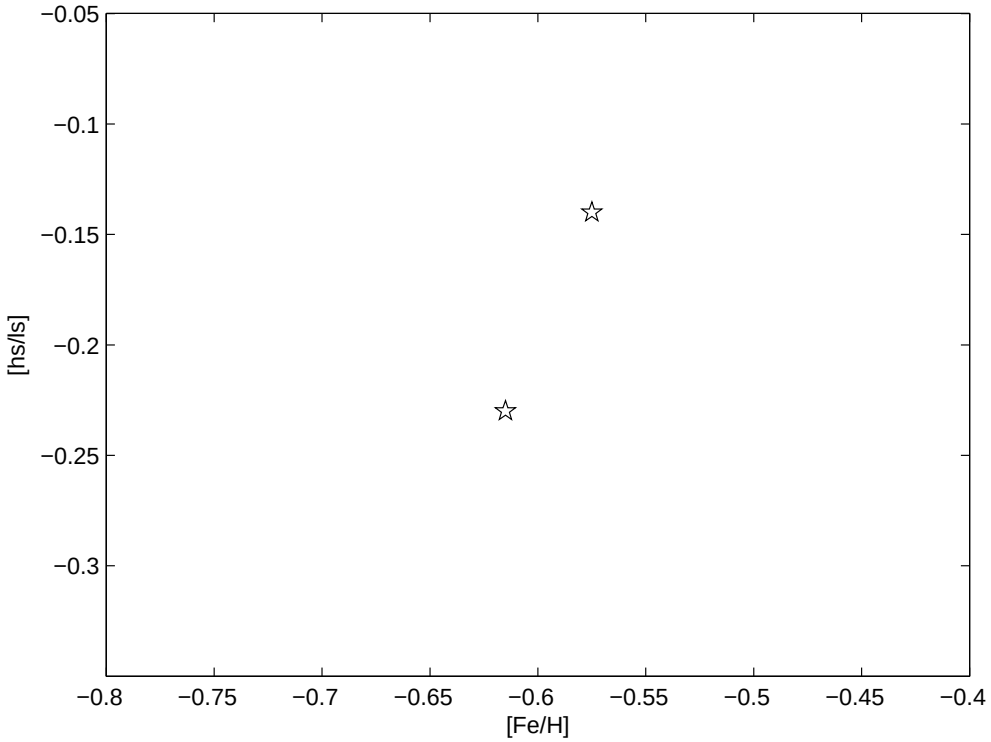

Figure 7.25: The ratio of the heavy to light *s*-process elemental abundance for each NGC 6388 star against [Fe/H] with respect to the Sun.

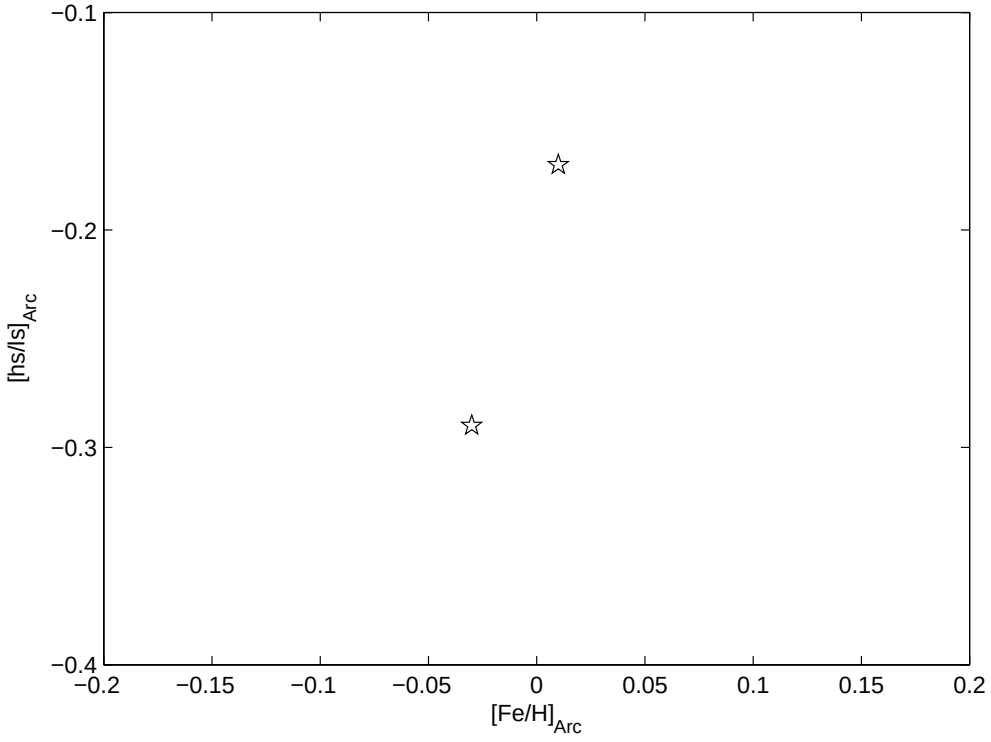

Figure 7.26: As for Figure 7.25 but with respect to the Arcturus.

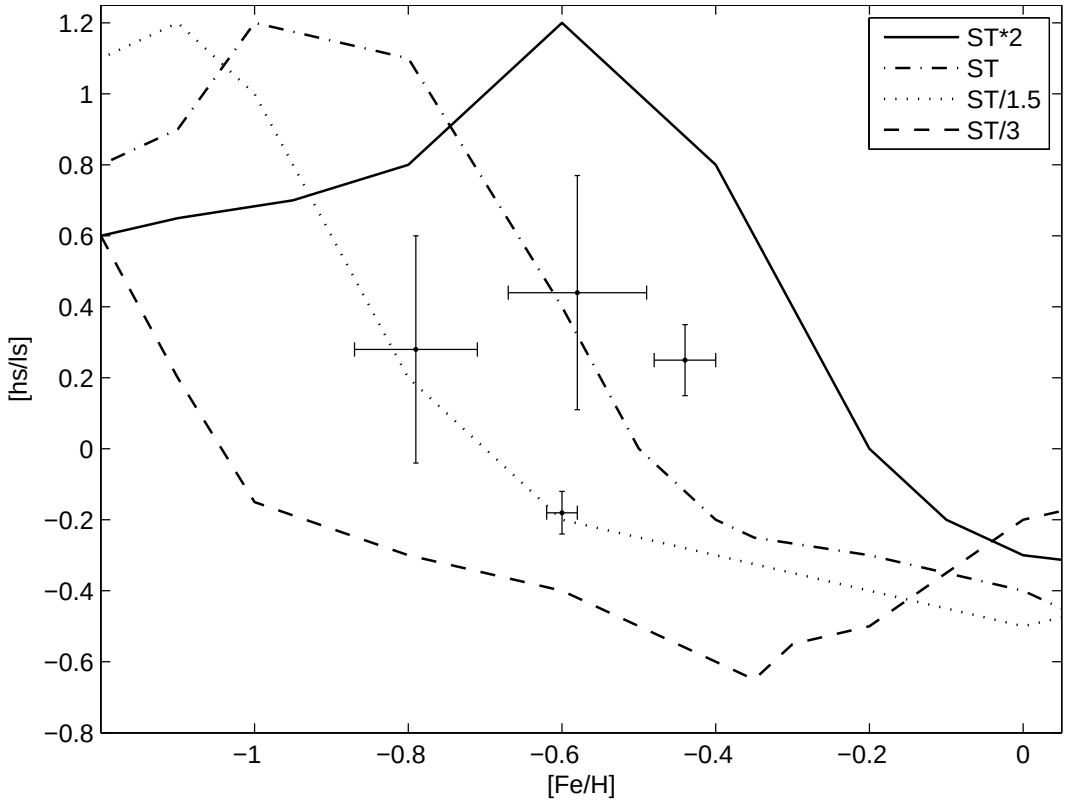

Figure 7.27: Heavy to light *s*-process abundance ratios, as sample means and standard deviations, derived here for the NGC 6388 stars and compared with the results from Carretta et al. (2007) and Wallerstein et al. (2007). Theoretical predictions from Busso et al. (2001) with the stated C^{13} pocket parameters and initial mass of 1.5 $M_{\odot}$ are also shown.

The stars analysed here produced the lowest [*hs/ls*] value with the smallest spread. However, it clearly falls on the ST/1.5 theoretical prediction. The spectroscopic [*hs/ls*] values from Wallerstein et al. (2007) also fall on the ST/1.5 theoretical prediction. The photometric Wallerstein et al. (2007) [*hs/ls*] values are better described by the standard case (ST), as is the result from Carretta et al. (2007).

A more detailed discussion regarding [*hs/ls*] and [Fe/H] is made in the following section. However, overall the heavy element abundances of the NGC 6388 stars agree closely with the results of the 47 Tuc analysis.

7.4.3 Comparison of NGC 6388 and NGC 362 with 47 Tuc

Comparing the 47 Tuc and NGC 6388 results ($\langle[ls/\mathrm{Fe}]\rangle = 0.53 \pm 0.07$ dex and $\langle[ls/\mathrm{Fe}]\rangle = 0.58 \pm 0.13$ dex) to the metal-poor NGC 362 stars, for which the sample mean relative to the Sun was $\langle[ls/\mathrm{Fe}]\rangle = 0.32 \pm 0.10$ dex, shows a trend of decreasing *ls* abundance with decreasing metallicity.

Making the comparison of the heavy *s*-process elements between clusters, the mean abundance relative to the Sun for 47 Tuc was $\langle[hs/\mathrm{Fe}]\rangle = 0.40 \pm 0.06$ dex and for NGC 6388 it

was $\langle[hs/\mathrm{Fe}]\rangle = 0.39 \pm 0.07$ dex, while for NGC 362 it was $\langle[hs/\mathrm{Fe}]\rangle = 0.46 \pm 0.09$ dex. Again 47 Tuc and NGC 6388 are in excellent agreement. The value for NGC 362 is also of a similar magnitude, but showing a general increase of [*hs*/Fe] with decreasing [Fe/H].

The values of Ba are so disparate within and between the GCs that making a comparison is not useful until those abundances are better understood. However, Eu provides an excellent comparison of the abundances of an *r*-process element between clusters. In 47 Tuc and NGC 6388 $\langle[\mathrm{Eu/Fe}]\rangle = 0.46 \pm 0.08$ dex and $\langle[\mathrm{Eu/Fe}]\rangle = 0.57 \pm 0.09$ dex respectively, while for NGC 362 $\langle[\mathrm{Eu/Fe}]\rangle = 0.77 \pm 0.06$ dex. All three values are at the upper limits of the uncertainties when compared to GCs of similar metallicity in Figure 6 of Gratton et al. (2004). So while each sample has a small spread within the cluster, confirming the homogeneity of Eu abundances within GCs, there may be some systematic offset that has occurred in the derivation of the abundances. There is still reasonable agreement between the NGC 6388 and 47 Tuc Eu abundances, as has been observed for the other heavy elements.

The [*hs/ls*] ratios for each of these three clusters can be considered in comparison to theoretical predictions of [*hs/ls*] with [Fe/H]. The homogeneity of the iron abundance and the *s*-process elemental abundances in these clusters is clear evidence that these stars are not producing *s*-process elements internally but rather the observed abundances are the signature of some external pollution that occurred at some point in the cluster's history.

The lack of trend of [*hs/ls*] with metallicity in any of these clusters means that these stars can be classified as extrinsic, in that their *s*-process elements were obtained externally. Where they are placed with respect to the Busso et al. (2001) theoretical predictions represents the original intrinsic stars that polluted the gas cloud from which the stars analysed in this thesis were formed. Hence the mass and C^{13} pocket parameter of the theoretical predictions refers to the intrinsic stars that have long since disappeared from the cluster, not to the stars that currently exist within the cluster and from which these *s*-process elemental abundances have been derived. It is the signature of the intrinsic stars that has been measured.

While this analysis has focused on the heavy element abundance distribution within each of these clusters, the distribution of the light element abundances also provides important evidence regarding the likely sources of the elemental abundances within these stars. The previous studies considered here found the well-known Na-O anti-correlation for the stars analysed in both NGC 362 and NGC 6388. Thermally pulsing AGB stars are one of the potential sources of this anti-correlation between Na and O, as the internal nucleosynthesis at this stage of evolution can produce this enhancement in Na without enhancing O. Considered in combination, both the heavy and light element abundance distributions determined for the stars in these three clusters stars provide evidence that supports thermally pulsing AGB stars as key sources of pollution in the star forming history of these GCs.

Figure 7.28 uses the predictions from Figure 3a of Busso et al. (2001) for 1.5 $M_\odot$ AGB stars at the end of their thermally pulsing stage. It compares them to the three clusters under consideration. In these figures the 47 Tuc star sample has been shifted in [Fe/H]

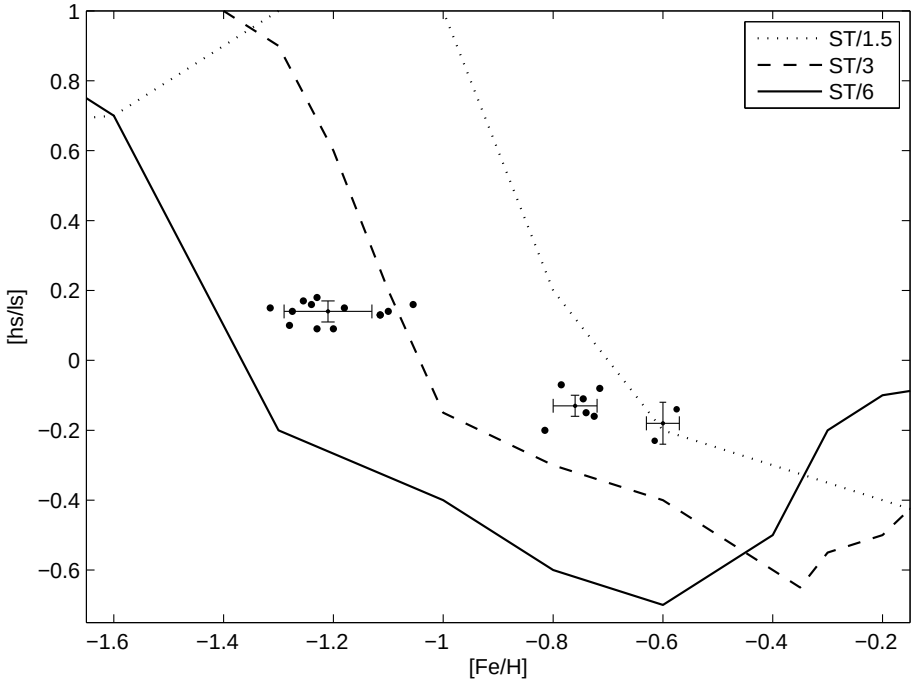

Figure 7.28: [*hs/ls*] against [Fe/H] for the NGC 6388, 47 Tuc and NGC 362 stellar samples including the mean and uncertainty. Three theoretical predictions for AGB mass of $1.5M_{\odot}$ are shown for comparison at C^{13} pocket parameters of ST/1.5, ST/3 and ST/6.

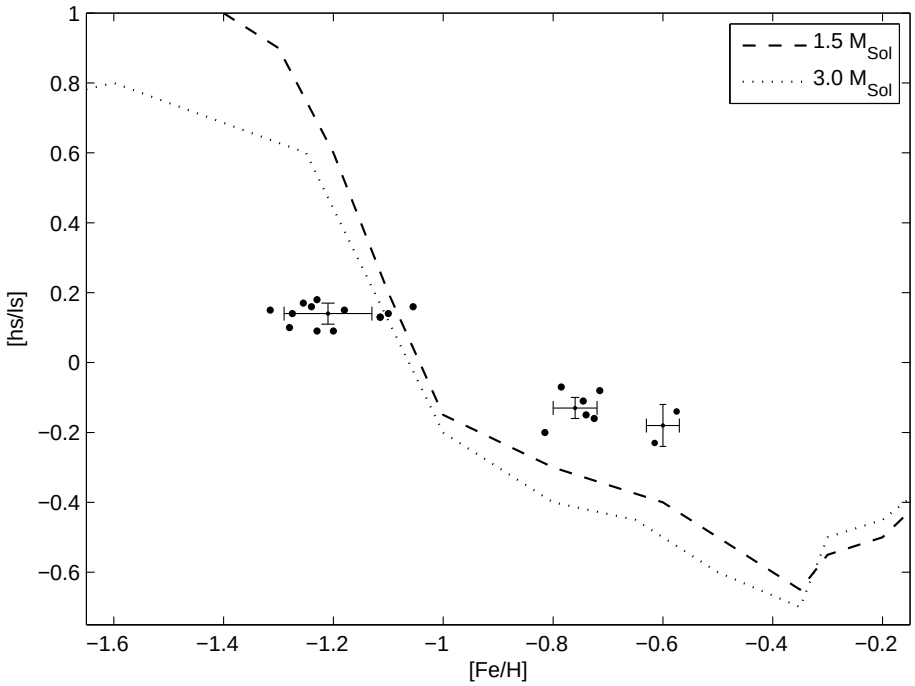

Figure 7.29: As for Figure 7.28, but the dotted line represents an AGB mass of 3.0 $M_{\odot}$ and a C^{13} pocket parameter of ST/3.0. The dashed line is for an AGB mass of 1.5 $M_{\odot}$ and a C^{13} pocket parameter of ST/3.0.

such that the mean [Fe/H] of the sample coincides with the cluster metallicity of −0.76 dex (Section 6.5.2).

As expected from the analysis in the previous section, the samples from 47 Tuc and NGC 6388 fall close together in the [*hs/ls*]-[Fe/H] space. The two NGC 6388 stars agree very well with a C^{13} pocket parameter of ST/1.5. The 47 Tuc star sample falls between this relation and that with a C^{13} pocket parameter of ST/3.0. If the sample were placed at its derived metallicity mean of [Fe/H]= -0.92 ± 0.05 dex the latter parameter would be a more appropriate choice. The [*hs/ls*] for NGC 362 is too low to be any sort of match for ST/1.5 and is better suited to a parameter between ST/3.0 and ST/6.0. The standard case scaled by the division of increasing values implies that less material needs to be mixed to the surface of the star in order to reproduce the same s-process element abundance signature as in the standard case. Hence the material is more enriched and so the s-processing has been more efficient. This is also related to the seed nuclei becoming less abundant in the metal-poor stars and so more heavy s-process elements are created.

Figure 7.28 shows that the [*hs/ls*] of the three clusters can be fitted by the [*hs/ls*]-[Fe/H] predictions for a relatively low mass progenitor AGB star. Figure 7.29 compares the ST/3.0 relation of an AGB with a mass of 1.5 $M_\odot$ to one of 3.0 $M_\odot$ (see Figure 4a of Busso et al. 2001). There is a small change in the [Fe/H] location of the loci with the change in mass, although the most distinct change is the smaller peak in [*hs/ls*] at [Fe/H]~ -1.6 dex. This may prove important for the most metal-poor cluster of the three, NGC 362, in determining which mass and mixing parameter can best reproduce the results presented in this study.

It is important to note that the specified mass of 1.5 or 3.0 $M_\odot$ refers to the initial mass of the previous generation of thermally pulsing AGB stars that produced the heavy element abundance signature. The mass does not refer to the currently observed stars which now bear this signature. The homogeneity of the heavy element abundance distribution determined for these three clusters in this study indicate that these stars are not producing the heavy elements themselves but have obtained them through some pollution event. If the origins of these heavy elements are thermally pulsing AGB stars that have polluted the star forming material prior to the formation of the currently observed stars, limits can be placed on the mass of these polluters due to the timescales involved in GC formation. A star with an initial mass of 3.0 $M_\odot$ would need approximately ~ 1 billion years to evolve into a thermally pulsing AGB that is actively polluting the star forming material within a GC. To evolve to the same stage a star with an initial mass of 1.5 $M_\odot$ would need approximately ~ 4 billion years. The star formation epoch of a GC occurs within the first billion years of its history, after which the star forming material is ejected from the cluster by supernovæ. The lifetimes of 3.0 $M_\odot$ stars may be sufficiently rapid such that they could pollute the intra-cluster medium from which the currently observed stars were formed before the gas was dispersed. However, lower mass stars evolve too slowly and so are effectively ruled out as potential polluters.

7.5 Conclusion

The analysis of the stars in NGC 362 and NGC 6388, as well as the stars in 47 Tuc, have successfully constructed a distribution pattern for heavy elemental abundances in globular cluster stars over a range of metallicities.

The large sample of stars that were analysed in NGC 362 produced a comprehensive analysis of heavy elements for that cluster. The NGC 362 stars showed comparable enhancements in the light and heavy *s*-process elements for the sample of 13 giants stars with values of $\langle[ls/\mathrm{Fe}]\rangle = 0.32 \pm 0.10$ dex and $\langle[hs/\mathrm{Fe}]\rangle = 0.46 \pm 0.09$ dex. The small spread in the metallicity ($\langle[\mathrm{Fe/H}]\rangle = -1.21 \pm 0.09$ dex) also confirms the homogeneity of that element. Compared to [Fe/H] the smaller spread in the abundances of the *ls* and *hs* elements is further confirmation that heavy elements are not varying within the cluster. The location of these stars in $T_{eff} - log\ g$ space places them high on the AGB. However, the lack of heavy elemental abundance variation with metallicity and the small spread of values confirms that these stars are not undergoing third dredge-up and so are not producing the observed *s*-process enhancements internally.

The two stars analysed in NGC 6388 showed enhancements in the light and heavy *s*-process elements with values of $\langle[\mathrm{ls/Fe}]\rangle = 0.58 \pm 0.13$ dex and $\langle[hs/\mathrm{Fe}]\rangle = 0.39 \pm 0.07$ dex. The light *s*-process elements are more enhanced in this metal-rich cluster compared to the heavy *s*-process elements. The derived metallicity was in good agreement between the two stars with the mean value for the cluster of $\langle[\mathrm{Fe/H}]\rangle = -0.60 \pm 0.02$ dex. This agrees well with accepted values. These two stars could be compared to the 47 Tuc sample due to the comparable metallicities of the two clusters. Indeed the heavy element enhancements between the two clusters were found to be very similar.

The previous light element abundances that have been determined for stars in all three GCs showed, in particular, the well-known Na-O anti-correlation. This abundance pattern is indicative of pollution by thermally pulsing AGB stars, which is also the potential source of the heavy element abundances determined in this study. Further analysis of the stars considered here for their light element abundances, combined with this heavy element abundance analysis, will refine the nature of the polluters that have contributed to the observed abundance patterns.

Another element that showed homogeneity within all three clusters was europium. As a predominantly *r*-process element this homogeneity indicates that the cluster material was well mixed prior to the formation of the currently observed stars. However the values derived here for NGC 362 and NGC 6388 were higher than the general globular cluster trend of [Eu/Fe] with [Fe/H]. This may imply some systematic issues in the analysis process which will need to be addressed.

The spectra for these two clusters were analysed so as to minimise abundance errors due to departures from LTE in the stellar atmosphere, and systematic uncertainties due

to the analysis process. NGC 362 in particular provided an extended sample over a range of temperatures and gravities in which the abundance issues due to low excitation Fe I lines could be investigated. The effect was particularly significant for the cooler, lower gravity stars. The effects of veiling on the spectra were also explored with some evidence of decreasing metallicity with increasing IR excess.

The key comparative analysis of these clusters was the relationship between the cluster [*hs/ls*] ratios and metallicity. The analysis focused on how the values derived in this research compared to theoretical predictions of *s*-process element enhancements from AGB stars, and comparisons to the values derived in other studies. The values derived in this study for 47 Tuc and NGC 6388 stars showed consistently lower values of [*hs/ls*] when compared to other studies. However, the analysis technique used to determine the heavy *s*-process elemental abundance seemed to play a major role in the contradictory results. Determining heavy elemental abundances by curve-of-growth analysis consistently returned solar or depleted *s*-process abundances. The spectrum synthesis techniques used in this research generally found enhancements in the *s*-process for the three clusters. The elements used in the definition for the [*hs/ls*] ratio also affected the results. Barium, which is often measured and has strong features, showed a large range of values in this analysis due to its abundance being derived from these strong features which are sensitive to changes in stellar parameters, in particular microturbulence. Despite this it was often included in the definition for *hs* in other studies.

The results from the three clusters analysed here were also compared with the theoretical predictions. In general the clusters showed a trend of increasing [*hs/ls*] with decreasing metallicity. The ratio is very similar for NGC 6388 and 47 Tuc ($\langle[hs/ls]\rangle = -0.18 \pm 0.06$ dex and $\langle[hs/ls]\rangle = -0.13 \pm 0.05$ dex, respectively) but for NGC 362 the ratio is much higher ($\langle[hs/ls]\rangle = +0.14 \pm 0.03$ dex). This is reflective of the lower metallicity of that cluster and is predicted by the theoretical models. This observed trend of [*hs/ls*] with cluster metallicity is indicative of greater s-process element enrichment due to more efficient processing of seed nuclei into s-process elements when fewer seed nuclei are available.

The homogeneity determined for the s-process element abundances between the stars in all three clusters is evidence that these stars are not creating the s-process elements themselves but that they merely bear the chemical signature of a previous generation of AGB stars that underwent third dredge-up. As such it is this signature that is being compared to the theoretical predictions and the estimates of mass and mixing parameters based on these predictions apply to that previous generation that polluted the star-forming material. However, while thermally pulsing AGB stars with an initial mass of 3.0 $M_{\odot}$ could have polluted the intra-cluster medium within the GC formation timescale, lower mass stars can be ruled out. The exploration of theoretical chemical abundance predictions, stellar evolution theory and observed chemical abundance signatures in GC stars provide the basis with which to constrain the characteristics of the polluters that produced the observed element abundance distribution.

Chapter 8

Conclusion & future work

The exploration that was undertaken in this thesis has produced key results as to the nature and extent of chemical abundances in globular cluster (GC) stars. The range of data that was analysed at both medium- and high-resolution has resulted in a comprehensive analysis process that seeks to reduce systematic errors and provide consistent results between stellar samples.

The main sequence (MS) provides the best candidates for determining the original chemical composition of the gas cloud from which GC stars formed as there has been no internal mixing in these stars that would contaminate the primordial composition of their atmospheres. Stars on the red giant branch (RGB) that are located below the horizontal branch (HB) may have undergone some mixing due to the first dredge-up. The chemical signature of this mixing is simpler to identify in these stars and disentangle from the original chemical composition than in the more evolved stars in which extensive mixing has occurred. As stars evolve through the RGB, HB and asymptotic giant branch (AGB) the chemical composition of their atmospheres is modified by the mixing up of H-burning products. It becomes more difficult to determine which abundances are due to internal nucleosynthesis and which are due to the original chemical composition of the gas cloud. The chemical signatures of different nuclear processes are well-known, and the sites that produce these signatures have been postulated. The goal of chemical abundance analyses is to identify these various signatures within stars to determine how these stars, and clusters of stars, came to be. Comparing the abundances of GC stars at different stages of evolution is an invaluable aid to disentangling these chemical signatures and determining the scenarios that produced the observed GCs.

This research sought to derive elemental abundances from medium- and high-resolution spectra. To this end a robust analysis procedure was established which provided an overlap between the different techniques required for each resolution. The standard star Arcturus was used to calibrate both the high- and medium-resolution techniques. The stellar parameters determined for Arcturus in the course of this calibration were found to be $T_{eff} = 4300 \pm 50$ K, $log\ g = 1.6 \pm 0.2$, $\xi = 1.5 \pm 0.25$ kms^{-1}, and [Fe/H] $= -0.59 \pm 0.12$ dex, which are in good

agreement with previous studies. The subsequent analyses were carried out differentially with respect to Arcturus in an effort to reduce systematic errors by calibrating the analysis process to a standard star of similar stellar parameters.

8.1 The medium-resolution studies

The goal of the analysis of the medium-resolution spectra obtained using RSS on SALT was to determine the capability of RSS, and other medium-resolution instruments, to survey *s*-process elemental abundances in GC stars.

The line strength analysis served as a feasibility study that compared synthesised spectra at different resolutions and in different locations in the 47 Tuc $T_{eff}-$ *log g* space. From this analysis it was determined which heavy element spectral lines can be used to derive elemental abundances at medium-resolution for various stellar parameters. The ionised and neutral species of an element behave differently for variations in T_{eff} and *log g*. The ionised lines are visible over a greater range of T_{eff} than the neutral lines, while the neutral lines are visible over a greater range of *log g* than the ionised lines.

For medium-resolution ($R \sim 10,000$) spectra, the RGB and AGB stars can be sampled with a line list comprising both neutral and ionised species, due to the low temperatures and gravities of these types of stars. The hotter stars on the subgiant (SG) branch and near the turn off of the MS do not have sufficiently strong ionised or neutral lines and require high resolution in order for heavy elemental abundances to be measured. On the lower MS neutral lines are sufficiently strong for abundances to be measured at medium-resolution, but the high gravities mean that the ionised features are too weak.

The possibility of simultaneous observation of multiple objects is a distinct benefit of medium-resolution instruments. The resulting sample of stars can be used to find basic patterns in chemical abundances and in stellar atmosphere structure. The SALT performance verification RSS data tested the conclusions drawn from the feasibility study. The resolution that was obtained was $R \sim 5,000$, well below the maximum possible resolution for RSS ($R \sim 10,000$). At this resolution only an upper limit of +0.5 dex could be placed on derived elemental abundances for Zr, Ba, Nd and La. The eleven stars observed using RSS were also used in a basic temperature calibration. The neutral features that vary with temperature, such as Zr I, show the effects that were predicted in the line strength feasibility study.

RSS and HRS on SALT are ideally configured to obtain medium- and high-resolution spectra of the faint MS stars in GCs, particularly 47 Tuc. The MS stars, for which heavy elemental abundances ($38 \leq Z \leq 63$) could theoretically be obtained at medium-resolution, are too faint for observation using AAOmega on the AAT. For the purposes of measuring heavy elemental abundances that instrument is better suited to obtaining spectra along the giant branch.

The survey of 97 giant stars in 47 Tuc using AAOmega on the AAT, observed stars from the tip of the AGB to below the HB on the RGB within a range of two magnitudes. This range allowed for comparison between the different giant branches.

Both CN and CH molecular bandheads were observed, as well as regions containing key light and heavy element lines. The resolution of these observations was $R \sim 6,500$. A sample of ten stars has been analysed in detail for the abundances of Fe and two *s*-process elements (Zr and Ba) using spectrum synthesis. The Fe and Zr abundances showed a homogeneous distribution between the 97 stars in 47 Tuc, while there was a large spread in the derived Ba abundances between the stars. However this latter effect is most likely due to imprecise microturbulence determination.

The CN and CH bands were investigated for all 97 stars and the well-known CN-CH anti-correlation was observed. The CN band was measured to determine the CN excess (δC) of each star, which was used as the measure of the strength of CN in the star. The survey stars show a bimodality in CN excess, as has previously been observed for this and other GCs (Norris & Freeman 1979; Cannon et al. 1998; Cannon et al. 2003; Briley et al. 2004). A radial gradient in CN strength also confirmed the work of Paltoglou & Freeman (1984), where the CN-weak stars were prevalent in the inner regions of the cluster, and CN-strong stars were prevalent in the outer regions. Light elements (Na, Si, Ca) were measured by spectrum synthesis and both Ca and Si were found to be homogenous between the 97 cluster stars. The abundance for Na had a very large scatter. It was determined that the Na abundance was correlated with the CN excess, also confirming a previously observed relationship (Cottrell & Da Costa, 1981), but with a larger sample and only for those stars with extreme CN excess ($\delta C \geq 0.13$).

This survey was the first attempt to carry out a large scale investigation of *s*-process elemental abundances in GC stars using a medium-resolution instrument. As was found for the preliminary study using the SALT PV RSS stars, upper limits could reasonably be placed on the heavy elemental abundances (Zr and Ba) derived, so far, for this dataset. The consistency of the light elemental abundances (Si and Ca) that were measured with the results from the high-resolution analysis of Lee 2525 shows how potentially successful this type of survey can be.

The main source of the uncertainties in the results from the medium-resolution spectra was the broad lines from which the abundances were derived. This was particularly an issue for the AAOmega spectra where exact abundances for Na, Si, Ca, Fe, Zr and Ba were determined using spectrum synthesis. The light elements had reasonably distinct features and the derived abundances were in good agreement with the results from the high-resolution analysis of Lee 2525. The same light element features in the high-resolution spectrum of Lee 2525 were synthesised to determine their abundances in order to make a direct comparison between techniques. In the high resolution analysis in Chapter 5, the light elements underwent equivalent width analysis to determine their abundances.

The main discrepancy between the medium- and high-resolution results for Lee 2525 was the Zr abundance. There was evidence of only a small enhancement of Zr in both the observed medium-resolution spectrum and the convolved medium-resolution spectrum, compared with the significant enhancements found in the high-resolution analysis. As the light elements were in such good agreement between the resolutions this discrepancy is most likely due to the Zr I feature that was analysed in the medium-resolution spectra being too blended to provide a reliable result.

8.2 The high resolution studies of 47 Tuc stars

In the analysis of the ANO 2.3 m telescope échelle spectrograph observation of Lee 2525, the light elemental abundances ($Z \leq 30$) and Fe abundances were determined using an equivalent width curve-of-growth analysis. This technique was used in order to make a comparison with the previous results for this star reported in Brown & Wallerstein (1992). The heavy elemental abundances (Sr, Zr, Y, Ba, La, Nd and Eu) for all the high-resolution datasets were determined using spectrum synthesis.

The analysis of Lee 2525 confirmed the Na-CN correlation reported in Brown & Wallerstein (1992), and the Na-O anti-correlation that has been reported for other stars in 47 Tuc (Carretta et al., 2004). The heavy elemental abundances generally agreed with the Brown & Wallerstein (1992) analysis except for the Zr abundance, which was found to be enhanced in this analysis compared with the depleted result in Brown & Wallerstein (1992). The enhanced Zr and the abundances of the other heavy elements in this star were comparable with the heavy element abundances determined for seven 47 Tuc giant stars analysed in Wylie et al. (2006). This result resolved the Zr abundance discrepancy between Brown & Wallerstein (1992) and Wylie et al. (2006).

The heavy elemental abundances determined for Lee 2525 were combined with the results from the analysis of the five 47 Tuc AGB stars observed using UVES on the VLT. The mean abundances for Fe and the heavy elements that were derived for the 47 Tuc stars, including Lee 2525, and for the stars in NGC 6388 and NGC 362 are listed in Table 8.1. The mean abundance and standard deviation for each GC sample relative to Arcturus are also included.

The results for the heavy elemental abundances of the five additional 47 Tuc AGB stars were in good agreement with the abundances determined for Lee 2525 and with the results reported in Wylie et al. (2006). However, while Wylie et al. (2006) found a star-to-star scatter in the *s*-process elemental abundances, no such scatter was found in these stars, indicating a homogeneous distribution of these elements in 47 Tuc stars.

As for the high-resolution analysis of Lee 2525, this sample did not agree with the *s*-process element results from James et al. (2004) and Alves-Brito et al. (2005). The main disagreement is in the magnitude of the light *s*-process elemental abundances (Sr, Y and

Table 8.1: Mean and standard deviation for the derived metallicity and heavy elemental abundances for NGC 6388, 47 Tuc and NGC 362 determined from the high-resolution spectra.

	NGC 6388		47 Tuc		NGC 362		NGC 6388		47 Tuc		NGC 362	
X	$\langle$[X/H]$\rangle$	σ	$\langle$[X/H]$\rangle$	σ	$\langle$[X/H]$\rangle$	σ	$\langle$[X/H]$_{Arc}\rangle$	σ	$\langle$[X/H]$_{Arc}\rangle$	σ	$\langle$[X/H]$_{Arc}\rangle$	σ
Fe I	-0.65	0.05	-0.90	0.09	-1.22	0.09	0.01	0.01	-0.29	0.10	-0.61	0.09
Fe II	-0.55	0.01	-0.88	0.37	-1.20	0.09	-0.02	0.06	-0.32	0.08	-0.64	0.09
X	$\langle$[X/Fe]$\rangle$	σ	$\langle$[X/Fe]$\rangle$	σ	$\langle$[X/Fe]$\rangle$	σ	$\langle$[X/Fe]$_{Arc}\rangle$	σ	$\langle$[X/Fe]$_{Arc}\rangle$	σ	$\langle$[X/Fe]$_{Arc}\rangle$	σ
Y I	0.55	0.25	0.55	0.08	0.35	0.10	0.61	0.25	0.48	0.08	0.41	0.10
Y II	0.65	0.09	0.50	0.10	0.30	0.17	0.59	0.09	0.38	0.10	0.23	0.17
Zr I	0.57	-	0.49	0.07	0.29	0.08	0.45	-	0.48	0.07	0.17	0.08
Zr II	0.47	0.10	0.65	-	0.34	0.12	0.46	0.10	0.53	-	0.33	0.12
Ba II	0.96	0.21	0.34	0.33	0.56	0.30	1.16	0.21	0.53	0.33	0.75	0.30
La II	0.39	0.02	0.32	0.07	0.36	0.12	0.35	0.02	0.28	0.07	0.32	0.12
Nd II	0.40	0.16	0.48	0.06	0.56	0.07	0.30	0.16	0.38	0.06	0.46	0.07
Eu II	0.57	0.09	0.46	0.08	0.78	0.05	0.21	0.09	0.10	0.08	0.42	0.05
X/Y	$\langle$[X/Y]$\rangle$	σ	$\langle$[X/Y]$\rangle$	σ	$\langle$[X/Y]$\rangle$	σ	$\langle$[X/Y]$_{Arc}\rangle$	σ	$\langle$[X/Y]$_{Arc}\rangle$	σ	$\langle$[X/Y]$_{Arc}\rangle$	σ
ls/Fe	0.58	0.13	0.53	0.02	0.32	0.10	0.56	0.15	0.46	0.03	0.29	0.09
hs/Fe	0.39	0.07	0.40	0.06	0.46	0.09	0.33	0.07	0.33	0.06	0.39	0.09
hs/*ls*	-0.18	0.06	-0.13	0.05	0.14	0.03	-0.23	0.08	-0.13	0.04	0.10	0.04

Zr) for which James et al. (2004) and Alves-Brito et al. (2005) find a range in values from −0.17 dex to +0.36 dex. The stars analysed were determined to have reasonably similar enhancements between elements of the same *s*-process peak, as was the case in Wylie et al. (2006). The *r*-process element Eu was enhanced in all the stars analysed for this thesis, which is consistent with previous studies.

8.3 The high resolution studies of NGC 362 and NGC 6388 stars

The spectra of thirteen stars in NGC 362 and two stars in NGC 6388 were analysed for their heavy elemental abundances.

The sample of stars in NGC 362 covered a range of stellar temperatures from 4250 K to 3900 K which provided a comprehensive analysis for this cluster. The NGC 362 stars all showed similar enhancements in the heavy elemental abundances. The light ($\widehat{\text{ls}}$) *s*-process elements were enhanced to a similar degree as the heavy *hs* *s*-process elements.

The two NGC 6388 stars also showed enhancements in their heavy elemental abundances, although the *ls* elements were more enhanced than the *hs* elements. This pattern of *s*-process element abundance enhancement was similar to the pattern observed in the 47 Tuc stars. These two clusters (47 Tuc and NGC 6388) have comparable metallicities and the similarity in heavy element abundances between the clusters is evidence that the relative enhancements of *ls* and *hs* elemental abundances is metallicity dependant. Clusters with the same metallicity are therefore expected to have the same *ls* and *hs* abundances. When compared with NGC 362 the three clusters analysed in this thesis produce a trend of decreasing *ls* element abundances with decreasing metallicity. This has ramifications for the [*hs/ls*] ratio which will be discussed in the below section.

The Eu abundance is enhanced in all three clusters. The abundances for 47 Tuc and NGC 6388 are in good agreement. However, Eu is considerably more enhanced in NGC 362.

The homogeneity of the heavy elemental abundances between the stars in each of these clusters is conclusive evidence that *s*-process elements are not being created within these stars and the *s*-process element abundance distribution in these clusters is the signature of some primordial or pollution event that took place earlier in the cluster's history.

There were several issues that arose in the analysis of the high-resolution spectra. The key issues were: determining a consistent placement of the continuum for spectra contaminated by strong molecular bands; departures from local thermodynamic equilibrium (LTE) affecting the line strengths of neutral species spectral features; and the veiling of spectral features due to circumstellar dust.

The continuum placement issues were dealt with by the careful selection of continuum

regions about each Fe I that was going to be measured. This was done in comparison to the Arcturus high-resolution atlas spectrum. A local normalisation was then carried out about each Fe line used in the curve-of-growth analysis. In the spectrum synthesis analysis the molecules and atoms included in the line list were calibrated with Arcturus. This provided a reasonable placement of the continuum in the synthesised spectrum for the determination of the heavy elemental abundances for each star.

Departures from LTE were recognised in Fe I lines during the derivation of the stellar parameters, and in Zr I lines during abundance analysis. The low excitation potential lines consistently resulted in the derived abundances being overabundant compared to those determined from the high excitation potential lines. Varying the stellar parameters could reduce the discrepancy, but any attempts to find consistency for both the Fe I and Zr I lines in an LTE analysis proved futile. Previous studies that dealt with this effect discarded the low excitation potential lines and derived stellar parameters based solely on the high excitation potential lines (Ruland et al. 1980; Asplund 2005). A similar analysis was pursued here for the high-resolution AGB stars in 47 Tuc, NGC 6388 and NGC 362.

A consequence of reducing the Fe line list to include only high excitation potential lines was that the range in χ is too small to reliably determine the T_{eff} in the curve-of-growth analysis. This study investigated stellar temperatures for the 47 Tuc stellar sample derived from a range of photometric values and compared them to the temperatures that were derived in McDonald & van Loon (2007). Upper and lower limits on the temperatures were established based on the McDonald & van Loon (2007) values and temperatures derived from 2MASS $(J - K)$ photometry. The corresponding values for the NGC 362 and NGC 6388 stars were also used to determine temperatures limits.

The NGC 362 stellar sample clearly showed the increase in the effects of departures from LTE on Fe I lines as the stellar temperatures and gravities decreased. For the hotter, higher gravity stars the non-LTE effect was small and there was good agreement between the abundances derived from all Fe lines. For the cooler, lower gravity stars the two Fe I line groups produced very different abundances the combination of which would have had detrimental effects on the derived stellar parameters if the departures from LTE had not been taken in to account.

The stars observed on the VLT were part of a programme studying mass loss rates in AGB stars (McDonald & van Loon, 2007). Many of the stars in the sample had an IR excess that indicates the presence of circumstellar dust. The derived metallicities for the 47 Tuc stars, once departures from LTE were taken into account, were much lower than is expected for that cluster. The effect of veiling has been observed in other types of dust-enshrouded stars which dilutes the spectral features and artificially reduces the derived metallicity of the star. An anti-correlation was found between IR excess and derived metallicity in the 47 Tuc stars. The two NGC 6388 stars had no IR excess but their derived metallicities agreed well with the accepted metallicity for that cluster. The sample of stars in NGC 362 included

stars with IR excess and there was some evidence of the same anti-correlation, but it was not conclusive.

Based on this we argue that the veiling was occurring to the same degree for all the weak to medium strength lines that were analysed. While the metallicity was lowered, the abundances measured relative to that metallicity represent the true abundances of the stars.

The differential analysis of the results relative to Arcturus also act to reduce the errors introduced in the analysis process and due to departures from LTE. This detailed treatment of the effects evident in these stars provided consistent and reliable abundance results.

8.4 Ramifications of the elemental abundance results

The abundance results for all three clusters showed homogeneity in the heavy elements between the stars in each cluster. The analysis of light elements in the AAOmega 47 Tuc star survey showed homogeneity in Si and Ca abundance, but a correlation of Na abundance to the CN bimodality in the cluster.

The heavy elemental abundances were considered in three distinct groupings: the light *s*-process elements (*ls* ≡ Sr, Y and Zr); the heavy *s*-process elements (*hs* ≡ Ba, La and Nd); and the *r*-process element Eu. For each of *ls* and *hs* the elements in the group were found to be similarly enhanced, except for Ba which often showed a range in values. The two Ba features upon which the Ba abundance was derived are very strong features which are very sensitive to microturbulence. This introduced a substantial uncertainty into the Ba abundance and so for the high-resolution analysis it was not included in the definition of *hs*. For the AAOmega survey Ba was the only *hs* element that could be measured. However, its abundance has been treated with caution.

When comparing the three clusters there is a distinct trend of decreasing *ls* abundance with decreasing metallicity. There is a slight trend of increasing *hs* abundances with decreasing abundance. This is reflected in the [*hs/ls*] ratio for the three clusters. The ratio is very similar for NGC 6388 and 47 Tuc ($\langle[hs/ls]\rangle = -0.18 \pm 0.06$ dex and $\langle[hs/ls]\rangle = -0.13 \pm 0.05$ dex, respectively) but for NGC 362 the ratio is much higher ($\langle[hs/ls]\rangle = +0.14 \pm 0.03$ dex). This is reflective of the lower metallicity of that cluster and is linked to theoretical models that predict this effect.

Europium is enhanced in all three clusters. The Eu abundances for 47 Tuc and NGC 6388 have a comparable enhancement, but the Eu abundance for NGC 362 is significantly more enhanced.

How have these abundance patterns been produced?

The homogeneity of the heavy elemental abundances throughout the individual clusters is evidence that the source of the elements was an event that happened prior to the formation of the stars that are currently being observed. There is no evidence that *s*-process elements are

currently being created within the stars that have been analysed in this thesis. These AGB stars have masses that are too low for them to be undergoing third dredge-up. Therefore the *s*-process element enhancements are extrinsic to these stars.

Two potential sources for these heavy elemental abundances are intermediate mass AGB stars and massive rotating stars. These two stellar environments produce different combinations of the *s*-process elements. Intermediate mass AGB stars produce 'main' *s*-process elements, which include both the *ls* and *hs* peaks. Hence they could be responsible for the enhancements observed in these clusters. Massive rotating stars produce 'weak' *s*-process elements, which include elements from the *ls* peak but not any elements that are heavier. The observed enhancements in both peaks that have been measured in this thesis therefore favours intermediate AGB stars as the source of the elemental abundance enhancements.

The *s*-process elemental abundances have been compared throughout this thesis with theoretical predictions for the creation of these elements in thermally pulsing AGB stars (Busso et al., 2001). However the chemical signature that is being compared to the theoretical predictions is actually that of stars which no longer exist. The stars that created the observed *s*-process element enhancements, the intrinsic stars, existed at an earlier time in the history of the cluster. They produced *s*-process elements during the thermally-pulsing stage of their evolution and polluted the gas cloud with *s*-process enriched material. It is from this material that the stars analysed here were formed. The chemical signature of the intrinsic stars is what is being compared to the theoretical predictions.

The results of this comparison showed that the same C^{13} pocket parameter (ST/1.5) provided the best fit to the [*hs/ls*] ratios for both 47 Tuc and NGC 6388 at their respective cluster metallicities. For NGC 362 the ST/3 C^{13} pocket parameter provided the best fit. These two predictions both modelled AGB stars with an initial mass of 1.5 $M_{\odot}$. A higher mass model may be a more appropriate choice for the NGC 362 stars. However, the time frames involved in the evolution of globular clusters permit only a very short window of opportunity for the pollution of the stellar forming material by thermally pulsing AGB stars. Very low initial mass thermally pulsing AGB stars (1.5 $M_{\odot}$) would need approximately $\sim$ 4 billion years to evolve to that stage. However, before that time supernovæwould have cleared the cluster of gas. An AGB star with an initial mass of 3.0 $M_{\odot}$ would need only $\sim$ 4 billion years and therefore could have polluted the intra-cluster medium within the GC formation timescale. Although at the lower end of the mass range, this is in agreement with the observed s-process element abundance pattern of intermediate mass thermally pulsing AGB stars that has been found in this thesis.

The light element abundance distribution that was determined for 47 Tuc from Lee 2525 and the AAOmega medium-resolution survey provides further information regarding the observed abundances.

The observed bimodality in CN strength is postulated to represent two distinct stellar populations in 47 Tuc, where one population has either polluted the gas cloud from which

the second population has formed or has directly polluted, via stellar winds, the low mass stars early in their life (Cannon et al., 1998). The CN-strong stars are enriched in N, and also in Na based on the results in this thesis. The more massive intermediate mass AGB stars ($M \geq 4\ M_{\odot}$) are likely sources of these enhancements as they undergo hot-bottom burning which can produce these variations in abundances, particulary for Na. However, massive stars are equally likely to produce these elements as their interiors reach temperatures that activate the necessary reactions to produce the key elements, which are then mixed up into the atmosphere and ejected from the stars in slow stellar winds. Massive rotating stars are thought to more successfully ejecta H-burning products via the slow stellar winds as the high rotation mixes more of the H-burning products up into the atmosphere. Both intermediate mass AGB stars and massive (rotating) stars are reasonable pollution candidates, but neither fully explains the observed abundances distribution.

The combination of the observed light and heavy element abundance patterns in 47 Tuc stars favours intermediate mass AGB stars as the source of the abundance enhancements. If the CN-weak population represents the original population then enhancements in elements expelled from CN-weak AGB stars should be seen in the CN-strong stars. This is the case for N and Na but not for the *s*-process abundances. There was no evidence of a correlation of *s*-process element enhancements with CN strength in the AAOmega survey results. However, due to the issues that need to be resolved regarding those abundances, the heavy elemental abundances derived from the AAOmega survey are not conclusive. The only high-resolution 47 Tuc star with a CN index that was analysed in this thesis was Lee 2525. Ironically, its CN index is on the cusp of being CN-weak or CN-strong which does not lend itself to any sort of conjecture. High-resolution analysis of CN-weak, CN-strong pairs would provide the evidence necessary for determining whether the CN-weak population was the source of the abundances patterns observed in 47 Tuc.

With respect to the Eu abundances found for the stars in each cluster, the homogeneity of this *r*-process element implies that the gas cloud underwent pollution by Type II supernova and the enhancements in *r*-process elements was then well-mixed through the cloud prior to star formation. Eu was found to be homogeneously enhanced in all the clusters and the abundances that were determined agreed well with previous studies lending support to the occurrence of this pollution event.

Further analysis of the chemical signatures of the stars in this thesis will provide a more comprehensive view of the pollution events that these clusters have under gone. While the Na and heavy element abundance enhancements are indicative of pollution by intermediate mass AGB stars, pollution by massive rotating stars is not discounted. The actual formation and evolution of GC stars is likely to include several different pollution events over the course of the cluster's history. This intricate history will eventually be revealed as greater detail in the chemical abundances of GCs is pursued.

8.5 Future Work

The research undertaken in this thesis has raised several issues regarding both the derivation of the elemental abundances and the application of the results to current theory.

The line strength analysis was a useful tool for determining the best lines to observe at medium-resolution for certain 47 Tuc stars. Similar feasibility studies can be made over a range of metallicities to see the resulting effects on line strength. The analysis of the medium- and high-resolution spectra has provided more criteria with which to refine the list in order to ensure that the abundances that are being determined are consistent between the different resolutions.

The AAOmega medium-resolution survey of 47 Tuc stars is currently being analysed for light and heavy elemental abundances. Further work is necessary to determine the exact source of the offset between the previous CN indices and those derived in this analysis. This will ensure that all the stars in the survey are classified correctly. The preliminary results presented here for both the CN indices and the synthesised abundances show this to be a very promising dataset. However, the *s*-process elemental abundances that have been measured in the preliminary subset did not provide results consistent with the high-resolution analyses. The red wavelength region will be investigated for any other *s*-process features that it might be possible to analyse by spectrum synthesis. The continued analysis of the AAOmega 47 Tuc survey stars will add to the preliminary results presented here and extend possible trends that have been seen in this dataset. Future observations of other GCs using AAOmega are also planned.

The high-resolution datasets have raised key issues in the derivation of stellar parameters. Further work is necessary in order to reliably place the continuum in the spectra of the remaining cool, low gravity giants that were observed for McDonald & van Loon (2007). Alternative methods to reliably locate the continuum in these stars need to be developed in order to accurately measure the equivalent widths of the spectral lines.

Further investigation of the issue with interpolating the low gravity MARCS models is also required before exact stellar parameters for the lowest temperature, lowest gravity stars in the available sample be determined. A detailed comparison between other grids of model atmospheres and their interpolation programmes could also prove useful.

The departures from LTE observed in the high-resolution stars have highlighted how important it is to take account of this effect when deriving stellar parameters, particularly for cool, low gravity stars. A line-by-line analysis comparing derived abundances from stars of different temperatures would establish the limits of this effect. In particular, given the similarity between the 47 Tuc and NGC 6388 stars, a detailed comparison of the Fe I lines used in the stellar parameter derivations may help to pinpoint the exact cause of the low metallicities found for the 47 Tuc stars. The study of low temperature, low gravity stars in NGC 6388 carried out in Wallerstein et al. (2007) also found very low spectroscopic

metallicities. The published equivalent widths from these stars will be analysed to see if there is the same variation in abundance derived from the high and low excitation potential Fe I lines that was observed in the high-resolution stars of this study.

The elemental abundances reported for NGC 6388 stars in Carretta et al. (2007) and Wallerstein et al. (2007) were determined by the measurement of equivalent widths, rather than spectrum synthesis. A secondary analysis of the NGC 6388 stars in this thesis using equivalent widths can be compared with these results and can also quantify the differences between the two techniques.

The Ba abundance derived for all of the stars in this thesis used strong lines of Ba II that are present in the spectra. However, this abundance was mostly unreliable because the Ba II lines upon which the abundance was derived are very sensitive to microturbulence. The issues with this abundance need to be resolved so that Ba can be analysed along side the other *s*-process elements.

The light and heavy elemental abundances derived in this thesis provide evidence as to the source of abundance patterns within a GC. The only high-resolution spectrum analysed for its light element abundances thus far was Lee 2525. The light elemental abundances of the remaining high-resolution GC stars need to be determined to fully define their chemical signature. The *s*-process elemental abundances alone are not sufficient to definitively confirm any particular pollution scenario. However, the *hs* and *ls* ratios in the three clusters all showed enhancements in their respective elements which is indicative of an intermediate mass AGB star being the source of the observed *s*-process enhancements.

Based on the interplay between the medium- and high-resolution spectra analysed here, the next stage is to obtain high resolution, high SNR spectra of key stars, such as Lee 2525, and carry out detailed chemical abundance analyses that can then be used as benchmarks for the larger medium-resolution samples. The techniques developed in this thesis provide a consistent and robust framework in which to analyse both medium- and high-resolution spectra.

Appendix A

Stars in AAOmega 47 Tuc medium-resolution survey

Table A.1: Star designation, CN excess, photometry and photometric parameters for the stars in the AAOmega 47 Tuc medium-resolution survey. The CN excesses (δC) included are the previous values from Norris & Freeman (1979) (N79) and Paltoglou & Freeman (1984), the raw values from this thesis (2009) and the values adjusted to match the previous value (2009_{adj}). The stars with no current values of δC had truncated wavelength regions that the automatic normalisation routine did not deal with. These stars will be dealt with individually.

Star Name	Mask ID	δC N79/P84	δC 2009	δC 2009_{adj}	V	$(V-K)$	T_{eff} $(V-K)$	$log\ g$ $(V-K)$	$(B-V)$	T_{eff} $(B-V)$	$log\ g$ $(B-V)$	J	$(J-K)$	T_{eff} $(J-K)$	$log\ g$ $(J-K)$
Pal502	1.08	0.02	-0.05	0.00	12.64	3.28	4158	1.27	1.36	4096	1.24	10.27	0.91	3935	1.19
W66	1.30		0.10	0.14	12.55	3.24	4181	1.25	1.34	4127	1.22	10.21	0.90	3951	1.15
Lee3622	1.17	0.03	0.02	0.07	12.60	3.24	4183	1.27	1.31	4175	1.26	10.25	0.89	3978	1.18
Lee5703	1.59	0.00			12.53	3.17	4221	1.26	1.28	4224	1.27	10.21	0.85	4063	1.18
W139	1.23				12.70	3.17	4223	1.33	1.12	4505	1.51	10.33	0.80	4188	1.31
Lee2525	1.15	0.10	0.07	0.12	12.43	3.16	4232	1.23	1.29	4207	1.22	10.14	0.87	4033	1.13
Pal661	1.14	0.22	0.21	0.25	12.54	3.15	4233	1.28	1.26	4257	1.29	10.25	0.86	4041	1.17
Pal262	1.01	0.25	0.17	0.21	12.72	3.14	4240	1.35	1.29	4207	1.33	10.42	0.84	4092	1.27
Lee4628	1.49	0.05	0.05	0.09	12.53	3.14	4241	1.28	1.31	4175	1.24	10.24	0.85	4057	1.18
Lee1513	1.20	0.21	0.13	0.18	12.41	3.14	4242	1.23	1.32	4159	1.18	10.12	0.85	4059	1.13
Lee1201	1.09	0.15	0.06	0.10	12.88	3.10	4266	1.43	1.26	4257	1.43	10.65	0.87	4022	1.30
Lee4737	1.53	0.05	0.00	0.05	12.96	3.10	4267	1.46	1.25	4274	1.47	10.73	0.87	4031	1.34
S364	1.26	0.25	0.27	0.32	12.45	3.07	4284	1.27	1.26	4257	1.25	10.23	0.85	4072	1.15
Lee2608	1.35		0.03	0.08	12.87	3.07	4285	1.44	1.22	4325	1.47	10.63	0.83	4101	1.33
Lee2306	1.03	0.05	-0.02	0.02	12.59	3.07	4288	1.33	1.29	4207	1.28	10.35	0.83	4115	1.23
Lee5601	1.61	0.03	0.00	0.05	12.88	3.06	4292	1.45	1.25	4274	1.44	10.67	0.85	4074	1.32
Pal1151	1.25	0.07	0.02	0.06	13.00	3.06	4295	1.50	1.25	4274	1.48	10.76	0.81	4154	1.41
W164	1.22		0.20	0.25	12.62	3.05	4300	1.35	1.12	4505	1.48	10.41	0.84	4086	1.22
Lee3305	1.05	0.04	0.03	0.08	13.03	3.02	4319	1.53	1.23	4308	1.52	10.85	0.84	4083	1.39
Lee4509	1.41	0.00			12.99	3.01	4326	1.51	1.21	4342	1.52	10.82	0.84	4088	1.37
Lee4602	1.52	0.18	0.16	0.21	13.07	2.99	4338	1.55	1.19	4377	1.58	10.90	0.82	4124	1.42
Lee1628	1.51	0.05	-0.02	0.02	12.94	2.99	4339	1.50	1.22	4325	1.49	10.75	0.79	4195	1.41
Lee3207	1.02	0.04	-0.02	0.02	13.11	2.97	4352	1.58	1.22	4325	1.56	10.94	0.80	4176	1.47

continued on next page

Star Name	Mask ID	N79/P84	δC 2009	2009_{adj}	V	$(V-K)$	T_{eff} $(V-K)$	$log\ g$ $(V-K)$	$(B-V)$	T_{eff} $(B-V)$	$log\ g$ $(B-V)$	J	$(J-K)$	T_{eff} $(J-K)$	$log\ g$ $(J-K)$
Lee2428	1.32	0.05	-0.02	0.03	13.23	2.96	4360	1.63	1.16	4431	1.68	11.05	0.78	4227	1.55
Lee5717	1.63		0.22	0.27	13.16	2.94	4372	1.61	1.16	4431	1.65	11.02	0.80	4183	1.49
Pal452	1.04	0.20	0.12	0.16	12.94	2.93	4378	1.53	1.24	4290	1.47	10.79	0.78	4229	1.43
Lee1301	1.10	0.28	0.13	0.18	12.64	2.91	4391	1.42	1.22	4325	1.37	10.51	0.78	4227	1.31
Lee2742	1.44	0.05	0.07	0.12	13.04	2.89	4406	1.59	1.08	4581	1.70	10.89	0.75	4318	1.53
Lee1316	1.21	0.01	-0.01	0.03	13.17	2.89	4411	1.64	1.17	4413	1.64	11.08	0.80	4192	1.50
Pal487	1.06	0.09	0.12	0.16	13.17	2.87	4422	1.65	1.15	4449	1.67	11.07	0.77	4259	1.54
Lee4626	1.47	0.24	0.18	0.22	13.27	2.87	4422	1.69	1.17	4413	1.68	11.16	0.76	4269	1.59
Lee1506	1.19	0.12	-0.02	0.02	13.27	2.87	4423	1.69	1.15	4449	1.71	11.19	0.79	4209	1.55
Lee2616	1.36	0.02	0.03	0.08	13.21	2.84	4448	1.68	1.14	4468	1.69	11.16	0.79	4207	1.53
Lee4506	2.53	0.04	0.00	0.05	13.54	2.83	4454	1.82	1.11	4524	1.86	11.45	0.73	4347	1.75
Lee2739	1.43	0.14	0.13	0.18	13.22	2.80	4472	1.70	1.18	4395	1.65	11.22	0.80	4180	1.52
Pal578	1.11	0.20	0.13	0.17	13.38	2.78	4488	1.77	1.14	4468	1.76	11.36	0.77	4264	1.63
Lee4636	1.55	0.29	0.22	0.27	13.30	2.78	4493	1.75	1.17	4413	1.69	11.30	0.77	4246	1.59
Lee1735	1.50		0.11	0.15	13.35	2.76	4505	1.77	1.09	4562	1.81	11.27	0.69	4482	1.76
Lee5705	2.67		0.05	0.09	13.86	2.76	4505	1.98	1.11	4524	1.99	11.80	0.70	4445	1.94
Lee1320	2.36	0.07	-0.01	0.03	13.52	2.76	4509	1.84	1.13	4486	1.83	11.55	0.78	4224	1.66
Lee1522	2.62	0.05	0.00	0.05	13.56	2.74	4519	1.87	1.08	4581	1.90	11.59	0.77	4254	1.70
Lee2528	2.32	0.41	0.30	0.35	13.54	2.73	4532	1.87	1.12	4505	1.85	11.53	0.72	4392	1.78
Lee2737	2.57	0.01	0.02	0.07	13.51	2.70	4553	1.87	1.13	4486	1.83	11.54	0.73	4352	1.74
Lee1408	1.13	0.21	0.16	0.20	13.49	2.69	4566	1.87	1.09	4562	1.86	11.52	0.72	4395	1.76
Lee1105	2.49		0.04	0.09	13.69	2.65	4598	1.97	1.10	4543	1.93	11.75	0.70	4431	1.86
Pal1158	1.27	0.03	0.02	0.07	13.20	2.63	4617	1.78	1.13	4486	1.70	11.22	0.65	4589	1.76
Pal571	2.31	0.23	0.12	0.16	13.75	2.62	4619	2.00	1.08	4581	1.98	11.84	0.71	4403	1.87
Lee1309	1.34	0.19	0.14	0.19	13.20	2.61	4635	1.79	1.04	4660	1.81	11.28	0.68	4494	1.71
Lee2601	2.51	0.13	0.11	0.16	13.83	2.60	4638	2.04	1.06	4620	2.03	11.94	0.71	4409	1.90
Lee1516	2.56		0.06	0.10	13.94	2.58	4660	2.10	1.04	4660	2.10	12.03	0.67	4514	2.01
Lee5514	2.71		0.20	0.24	14.15	2.54	4705	2.21	1.00	4742	2.23	12.29	0.68	4488	2.08
Lee3312	2.20	-0.01	-0.02	0.02	13.78	2.54	4714	2.07	1.08	4581	1.99	11.97	0.72	4379	1.86
Lee2302	2.14	0.22	0.20	0.24	14.07	2.53	4720	2.19	1.07	4601	2.12	12.26	0.72	4387	1.99
Lee2604	1.16	0.19	0.13	0.18	13.07	2.52	4731	1.79	1.04	4660	1.75	11.22	0.67	4517	1.67

continued on next page

Star Name	Mask ID	N79/P84	δC 2009	2009_{adj}	V	$(V-K)$	T_{eff} $(V-K)$	$log\ g$ $(V-K)$	$(B-V)$	T_{eff} $(B-V)$	$log\ g$ $(B-V)$	J	$(J-K)$	T_{eff} $(J-K)$	$log\ g$ $(J-K)$
Lee3519	2.52		0.12	0.17	14.40	2.50	4755	2.34	1.02	4701	2.31	12.57	0.67	4526	2.21
Lee1423	2.40		0.01	0.06	13.75	2.50	4761	2.08	1.03	4680	2.04	11.95	0.69	4468	1.91
Lee4514	2.42		0.06	0.11	14.35	2.48	4778	2.33	0.98	4784	2.33	12.51	0.64	4613	2.24
Lee3510	2.29		0.20	0.24	13.63	2.48	4780	2.04	1.09	4562	1.92	11.87	0.72	4390	1.81
Lee1304	2.28	0.21	0.14	0.18	14.51	2.47	4794	2.40	0.96	4827	2.42	12.70	0.66	4561	2.27
Lee1419	2.59		0.20	0.24	14.19	2.47	4795	2.27	0.97	4806	2.28	12.37	0.65	4595	2.16
Lee2310	2.17	0.05	0.00	0.05	14.50	2.43	4838	2.42	0.94	4871	2.44	12.71	0.64	4617	2.30
Lee4515	2.43		0.22	0.27	14.49	2.42	4848	2.42	0.98	4784	2.39	12.70	0.63	4642	2.31
Lee2418	2.25	0.18	0.13	0.17	14.48	2.42	4852	2.42	0.96	4827	2.41	12.67	0.61	4725	2.35
Lee1313	2.54		0.03	0.08	14.44	2.42	4855	2.40	1.00	4742	2.35	12.69	0.67	4532	2.23
Lee1312	2.34	0.01	-0.03	0.01	14.48	2.36	4927	2.46	1.05	4640	2.31	12.81	0.69	4468	2.20
Lee3306	2.18		0.01	0.06	0.00	0.00	4961	2.49	0.00	4960	2.49	0.00	0.00	4677	2.35
Lee8508	2.70		0.09	0.14	13.80	2.30	5006	2.22	0.87	5030	2.23	12.09	0.59	4793	2.12
Lee8528	2.69		0.10	0.14	13.72	2.28	5031	2.20	0.92	4915	2.15	12.03	0.59	4782	2.08
Lee1319	1.46		0.13	0.18	13.08	2.28	5037	1.95	0.93	4893	1.88	11.41	0.60	4735	1.80
Lee1529	2.64		0.08	0.12	13.90	2.22	5118	2.31	0.86	5054	2.28	12.25	0.56	4880	2.20
Lee2511	2.50		0.13	0.18	13.84	2.15	5202	2.33	0.84	5102	2.28	12.27	0.59	4789	2.13
Lee3201	2.47	0.02	0.02	0.07	13.78	2.15	5212	2.31	0.88	5007	2.21	12.19	0.55	4909	2.17
Lee1206	2.33	0.03	0.01	0.05	14.13	2.12	5252	2.46	0.84	5102	2.40	12.56	0.55	4931	2.32
Lee1207	2.30	0.10	0.07	0.11	14.07	2.11	5262	2.44	0.84	5102	2.37	12.52	0.56	4887	2.27
Pal306	2.03	0.04	0.03	0.08	14.02	2.10	5276	2.43	0.85	5077	2.34	12.49	0.57	4866	2.24
Lee1324	2.41		0.12	0.17	14.04	2.09	5287	2.44	0.85	5077	2.35	12.49	0.54	4957	2.30
Lee1104	2.19	0.02	0.01	0.05	14.04	2.09	5288	2.44	0.90	4960	2.30	12.51	0.55	4905	2.27
Lee1315	2.35	0.10	0.03	0.07	14.10	2.08	5297	2.47	0.81	5243	2.45	12.56	0.54	4946	2.31
Lee1519	2.55		0.15	0.19	13.89	2.08	5299	2.39	0.88	5007	2.26	12.31	0.50	5103	2.30
Lee3206	2.13	0.16	0.12	0.17	14.06	2.07	5303	2.46	0.84	5102	2.37	12.49	0.50	5095	2.37
Lee3415	2.21	0.06	0.06	0.11	14.11	2.07	5303	2.48	0.88	5007	2.35	12.55	0.52	5044	2.36
Lee3205	2.06	0.13	0.08	0.13	14.07	2.07	5307	2.46	0.83	5148	2.40	12.54	0.55	4938	2.30
Lee3310	2.23	0.03	0.08	0.12	14.03	2.07	5310	2.45	0.86	5054	2.34	12.51	0.55	4912	2.27
Lee2419	2.24	0.10	0.11	0.16	14.07	2.06	5316	2.47	0.85	5077	2.36	12.58	0.57	4852	2.26
Pal256	2.01	0.07	-0.01	0.04	14.00	2.06	5325	2.44	0.85	5077	2.34	12.47	0.53	4994	2.30

continued on next page

Star Name	Mask ID	N79/P84	δC 2009	2009_{adj}	V	$(V-K)$	T_{eff} $(V-K)$	$log\ g$ $(V-K)$	$(B-V)$	T_{eff} $(B-V)$	$log\ g$ $(B-V)$	J	$(J-K)$	T_{eff} $(J-K)$	$log\ g$ $(J-K)$
Lee8301	2.44		0.11	0.15	13.96	2.05	5334	2.43	0.85	5077	2.32	12.43	0.51	5060	2.31
Lee8302	2.45		0.05	0.10	14.06	2.05	5334	2.47	0.85	5077	2.36	12.57	0.56	4898	2.27
Pal1036	2.37	0.13	0.12	0.17	13.95	2.04	5341	2.43	0.86	5054	2.30	12.39	0.48	5185	2.36
Lee8202	2.46		0.10	0.14	14.08	2.04	5341	2.48	0.86	5054	2.36	12.55	0.52	5048	2.35
Lee2108	2.05	0.13	0.10	0.14	14.01	2.04	5347	2.45	0.84	5102	2.35	12.47	0.50	5115	2.36
Lee2201	2.09	0.13	0.10	0.15	13.97	2.03	5351	2.44	0.83	5148	2.36	12.44	0.51	5087	2.33
Lee3403	2.16	0.15	0.08	0.12	14.03	2.01	5383	2.48	0.84	5102	2.36	12.53	0.50	5099	2.36
Lee3307	2.48		0.05	0.10	14.23	1.95	5448	2.58	0.96	4827	2.31	12.76	0.48	5177	2.47
Lee2311	2.27	0.04	-0.02	0.03	13.98	1.75	5708	2.58	0.77	5435	2.48	12.66	0.44	5390	2.46
Lee4502	1.38	0.16	0.00	0.05	13.28	-0.51			0.96	4827	1.93	14.34	0.56	4902	1.96
Lee1704	1.42		-0.05	-0.01	13.00	-0.89			1.25	4274	1.48	14.35	0.46	5296	2.03
Lee4472	1.66		-0.10	-0.05	12.40	0.34			1.41	4020	1.11	12.54	0.48	5193	1.75

Appendix B

Spectra of CN bands in AAOmega 47 Tuc medium-resolution survey

The following figures show the section of wavelength from 4100 Å to 4350 Å for each of the stars in the 47 Tuc survey. The location of the CN and CH bandheads are indicated and the density of the bandheads in this region can be seen. The values of CN excess (δC) are included with the stars name, T_{eff} and *log g*.

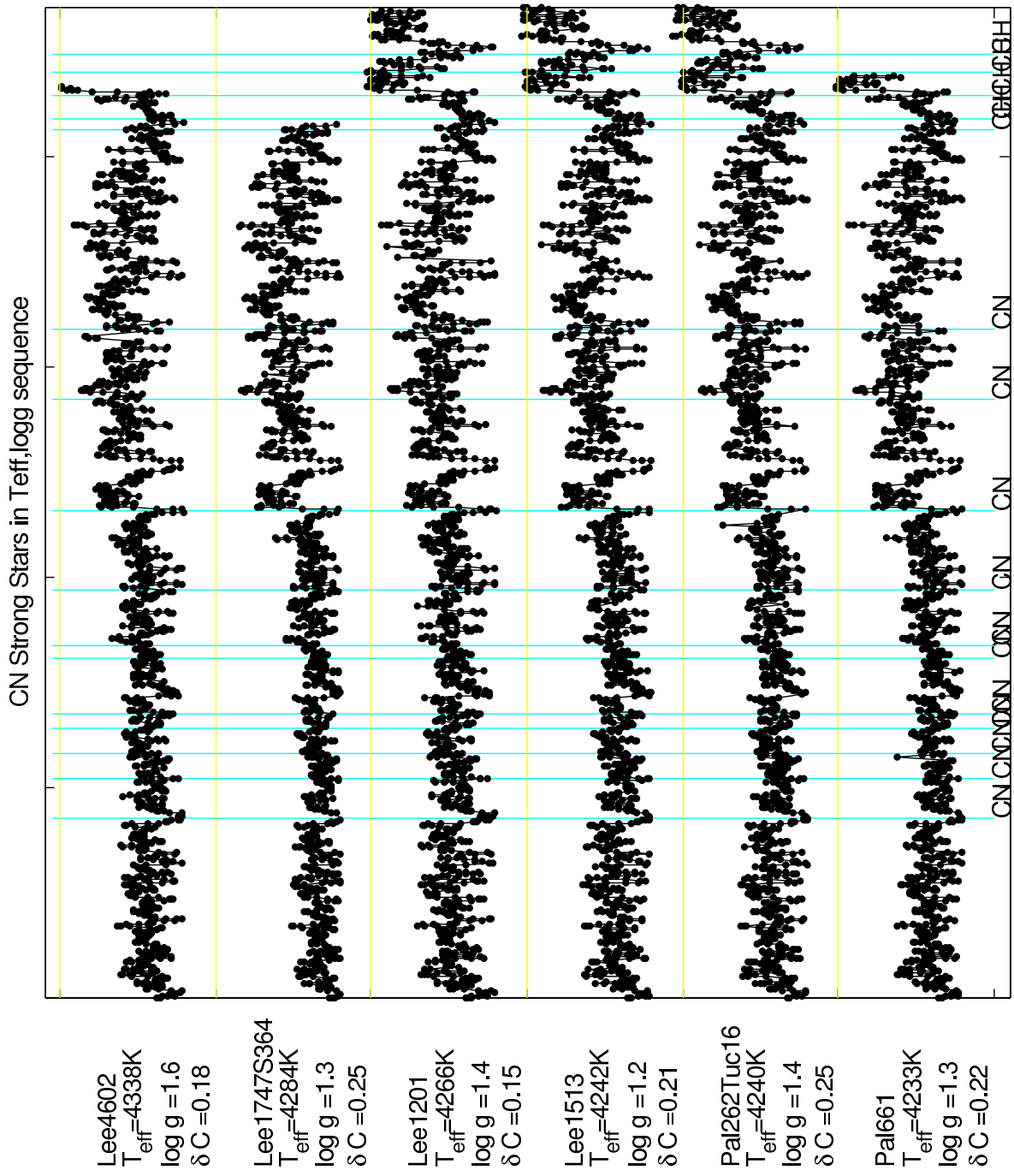
CN Strong Stars in Teff,logg sequence
Lee4602
T_eff=4338K
log g =1.6
δ C =0.18
Lee1747S364
T_eff=4284K
log g =1.3
δ C =0.25
Lee1201
T_eff=4266K
log g =1.4
δ C =0.15
Lee1513
T_eff=4242K
log g =1.2
δ C =0.21
Pal262Tuc16
T_eff=4240K
log g =1.4
δ C =0.25
Pal661
T_eff=4233K
log g =1.3
δ C =0.22
4100
4150
4200
4250
4300
CN

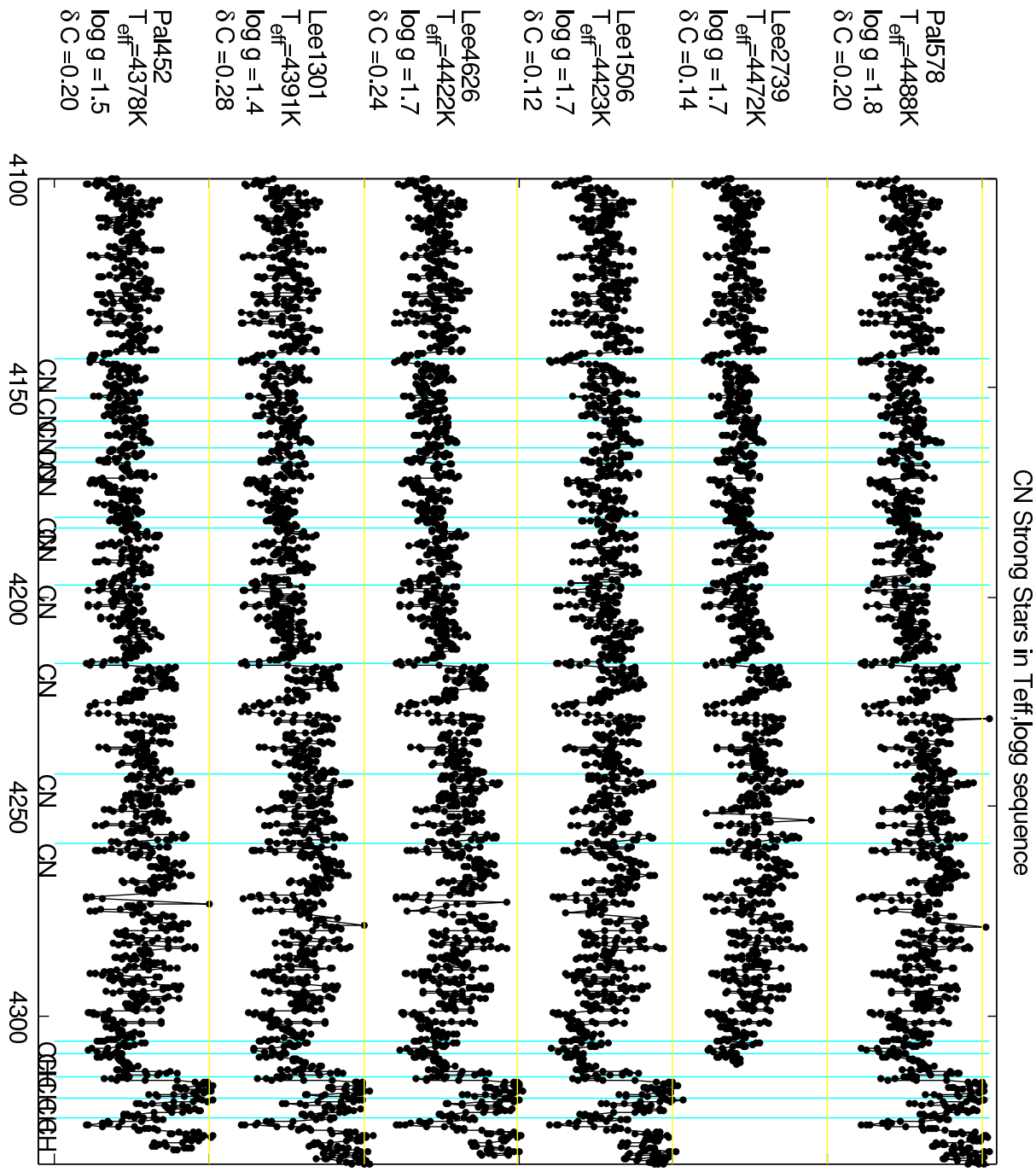
CN Strong Stars in Teff,logg sequence
Pal578
T_eff=4488K
log g =1.8
δ C =0.20
Lee2739
T_eff=4472K
log g =1.7
δ C =0.14
Lee1506
T_eff=4423K
log g =1.7
δ C =0.12
Lee4626
T_eff=4422K
log g =1.7
δ C =0.24
Lee1301
T_eff=4391K
log g =1.4
δ C =0.28
Pal452
T_eff=4378K
log g =1.5
δ C =0.20
4100
4150
4200
4250
4300
CN
CH

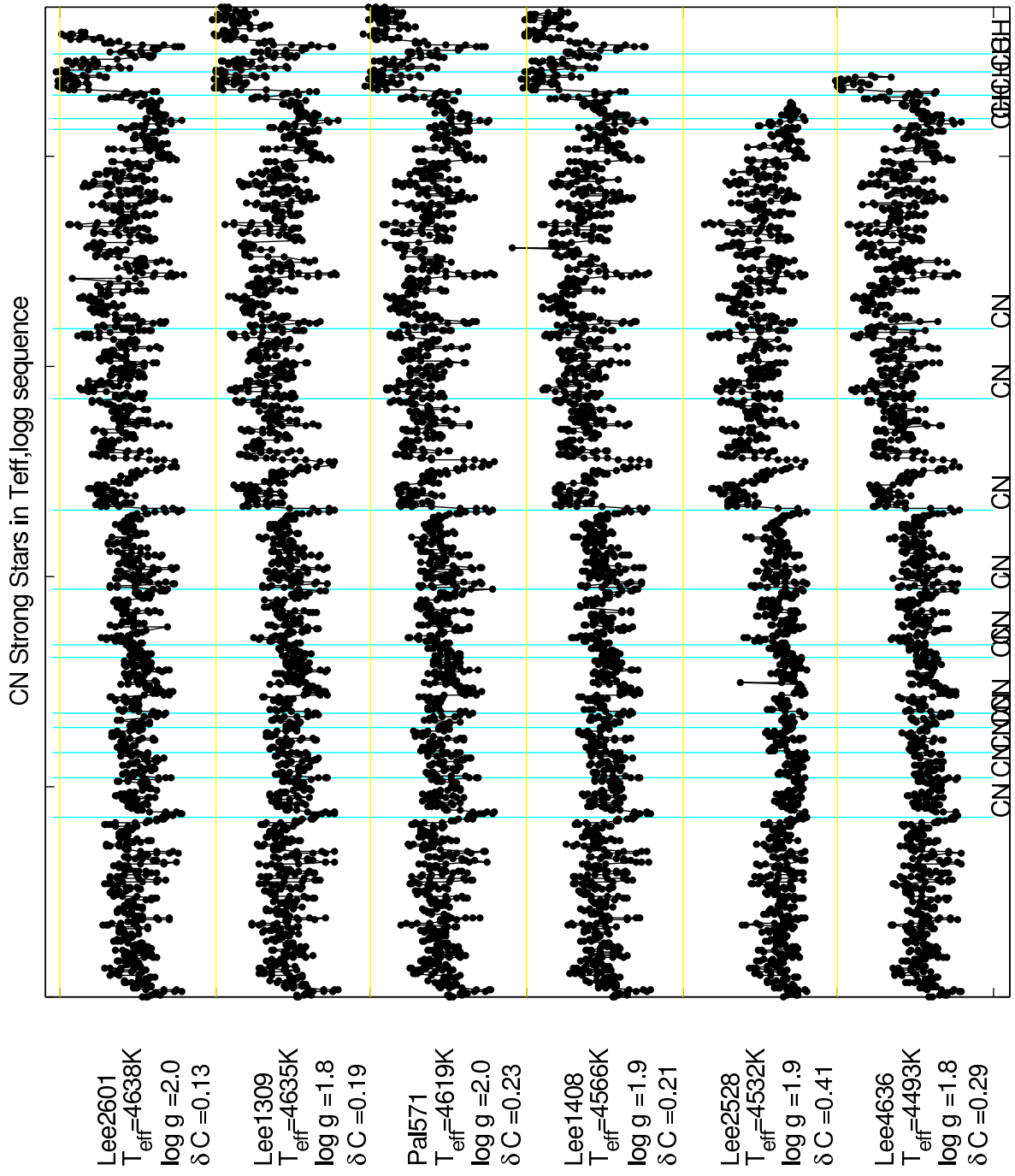
CN Strong Stars in Teff,logg sequence
Lee2601
T_eff=4638K
log g =2.0
δ C =0.13
Lee1309
T_eff=4635K
log g =1.8
δ C =0.19
Pal571
T_eff=4619K
log g =2.0
δ C =0.23
Lee1408
T_eff=4566K
log g =1.9
δ C =0.21
Lee2528
T_eff=4532K
log g =1.9
δ C =0.41
Lee4636
T_eff=4493K
log g =1.8
δ C =0.29
4100
4150
4200
4250
4300

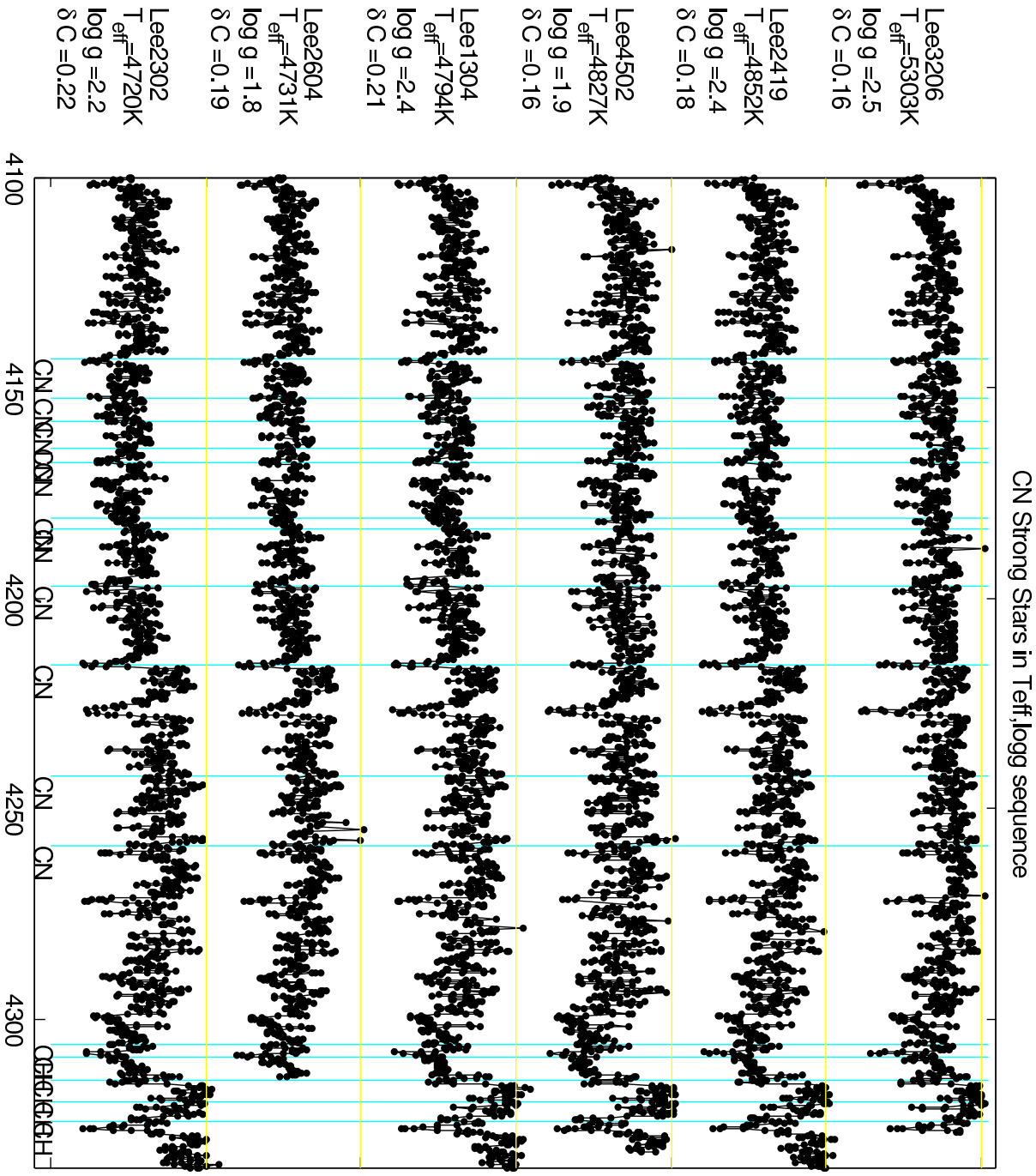
CN Strong Stars in Teff,logg sequence
Lee3206
T_eff=5303K
log g =2.5
δ C =0.16
Lee2419
T_eff=4852K
log g =2.4
δ C =0.18
Lee4502
T_eff=4827K
log g =1.9
δ C =0.16
Lee1304
T_eff=4794K
log g =2.4
δ C =0.21
Lee2604
T_eff=4731K
log g =1.8
δ C =0.19
Lee2302
T_eff=4720K
log g =2.2
δ C =0.22
4100
4150
4200
4250
4300
CN

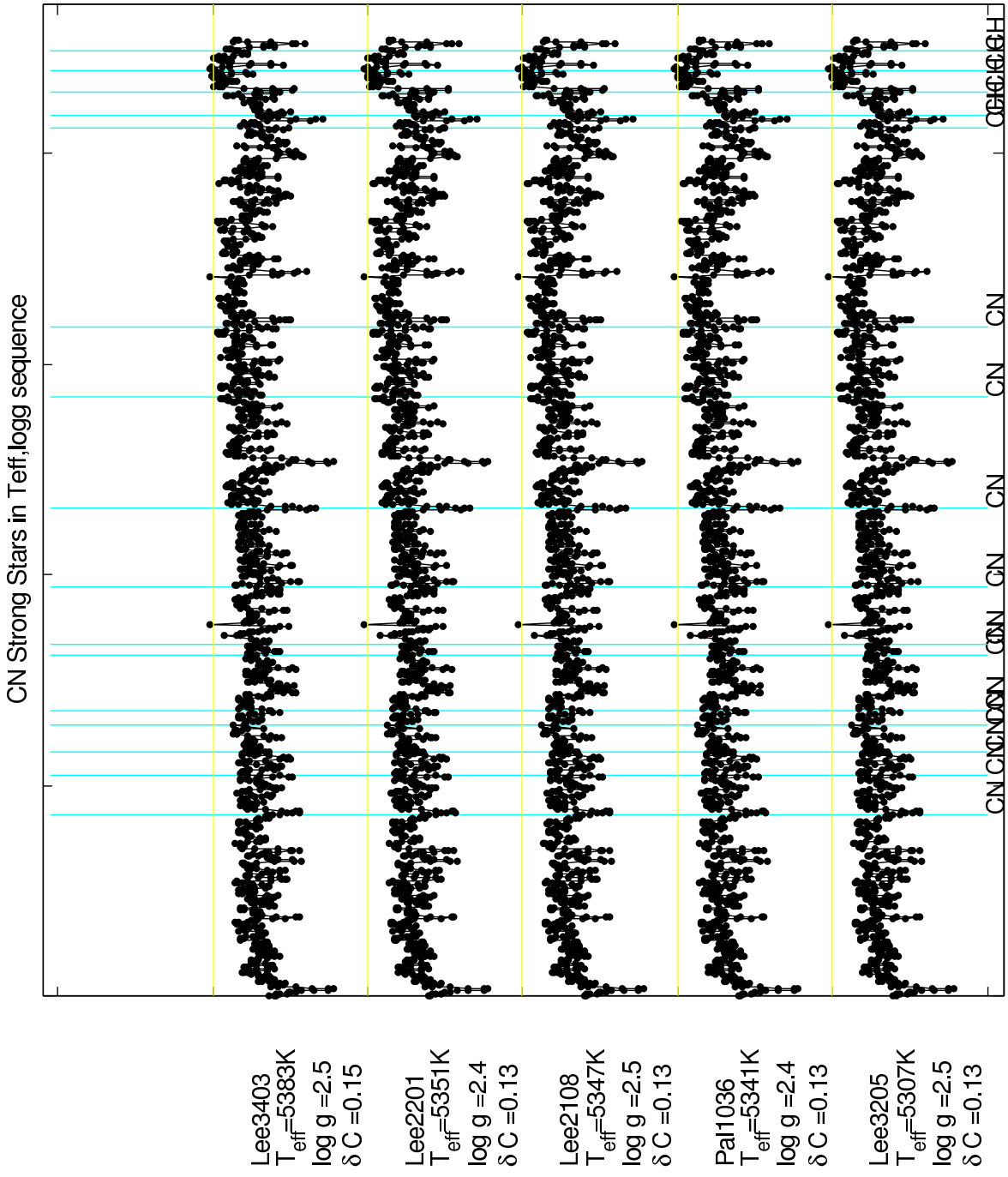
CN Strong Stars in Teff,logg sequence
Lee3403
T_eff=5383K
log g =2.5
δ C =0.15
Lee2201
T_eff=5351K
log g =2.4
δ C =0.13
Lee2108
T_eff=5347K
log g =2.5
δ C =0.13
Pal1036
T_eff=5341K
log g =2.4
δ C =0.13
Lee3205
T_eff=5307K
log g =2.5
δ C =0.13
4100
4150
4200
4250
4300
CN

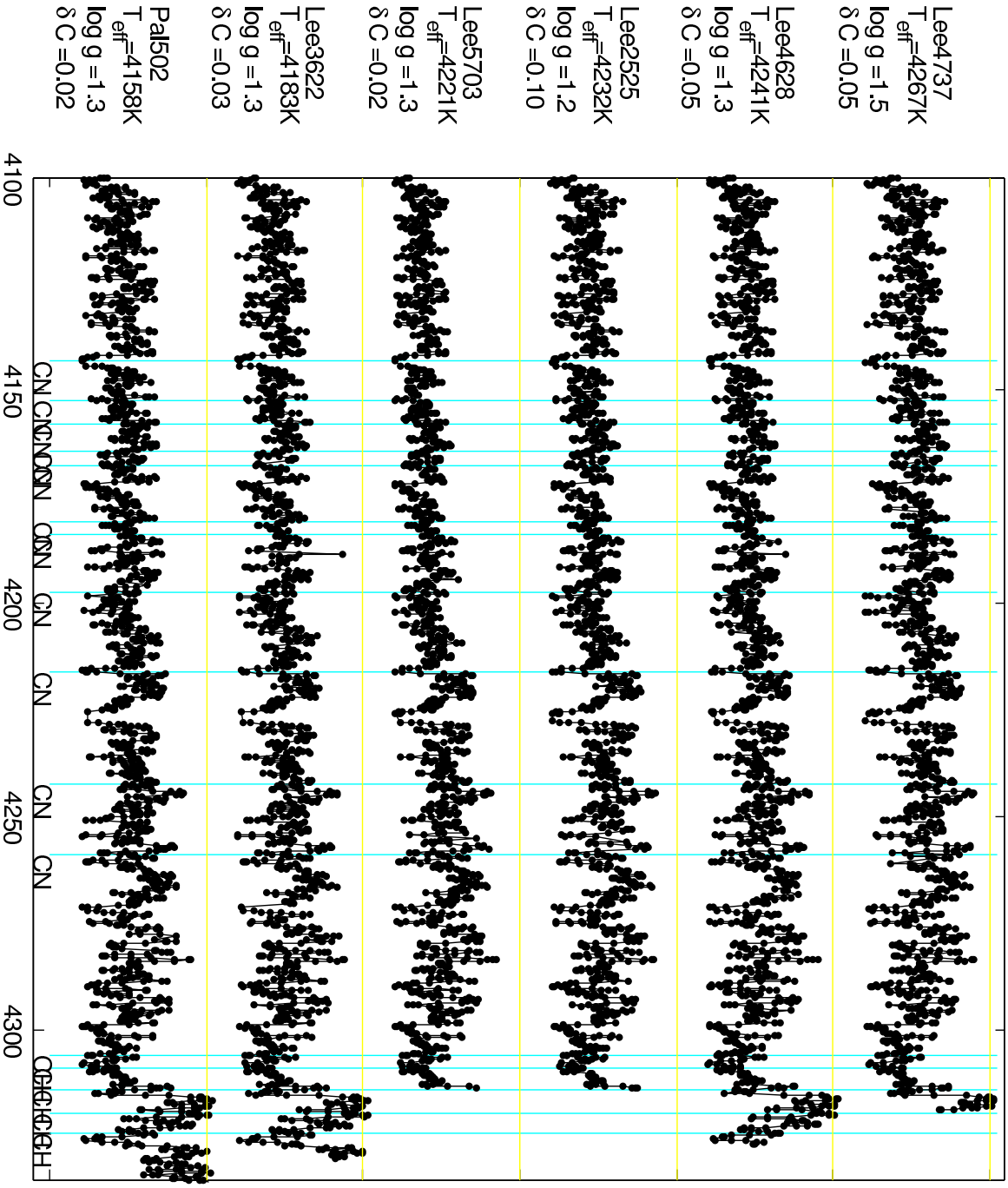
CN Weak Stars in Teff,logg sequence
Lee4737
T_eff=4267K
log g =1.5
δ C =0.05
Lee4628
T_eff=4241K
log g =1.3
δ C =0.05
Lee2525
T_eff=4232K
log g =1.2
δ C =0.10
Lee5703
T_eff=4221K
log g =1.3
δ C =0.02
Lee3622
T_eff=4183K
log g =1.3
δ C =0.03
Pal502
T_eff=4158K
log g =1.3
δ C =0.02
4100
4150
4200
4250
4300
CN
CH

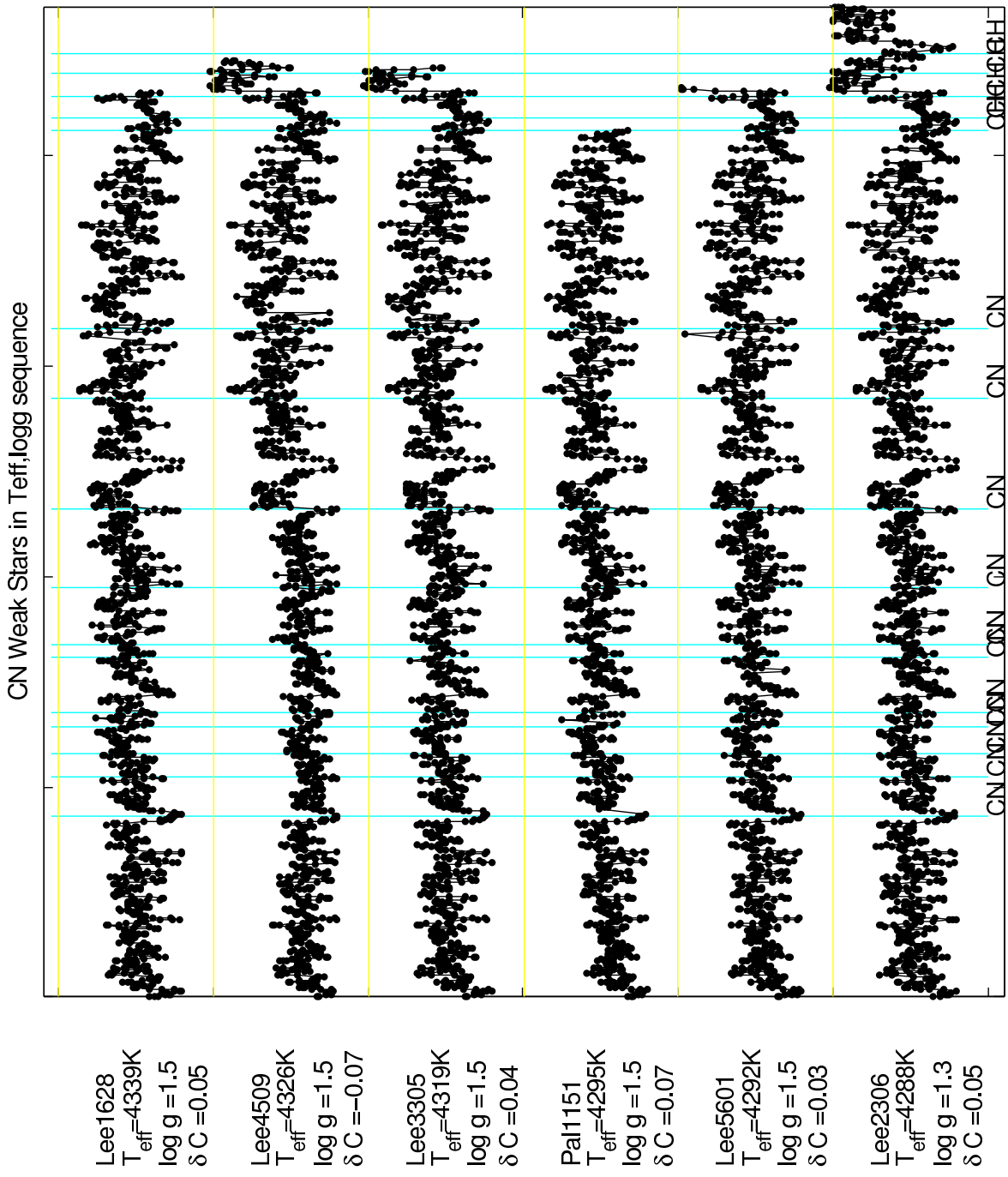
CN Weak Stars in Teff,logg sequence
Lee1628
T_eff=4339K
log g =1.5
δ C =0.05
Lee4509
T_eff=4326K
log g =1.5
δ C =−0.07
Lee3305
T_eff=4319K
log g =1.5
δ C =0.04
Pal1151
T_eff=4295K
log g =1.5
δ C =0.07
Lee5601
T_eff=4292K
log g =1.5
δ C =0.03
Lee2306
T_eff=4288K
log g =1.3
δ C =0.05
4100
4150
4200
4250
4300
CN

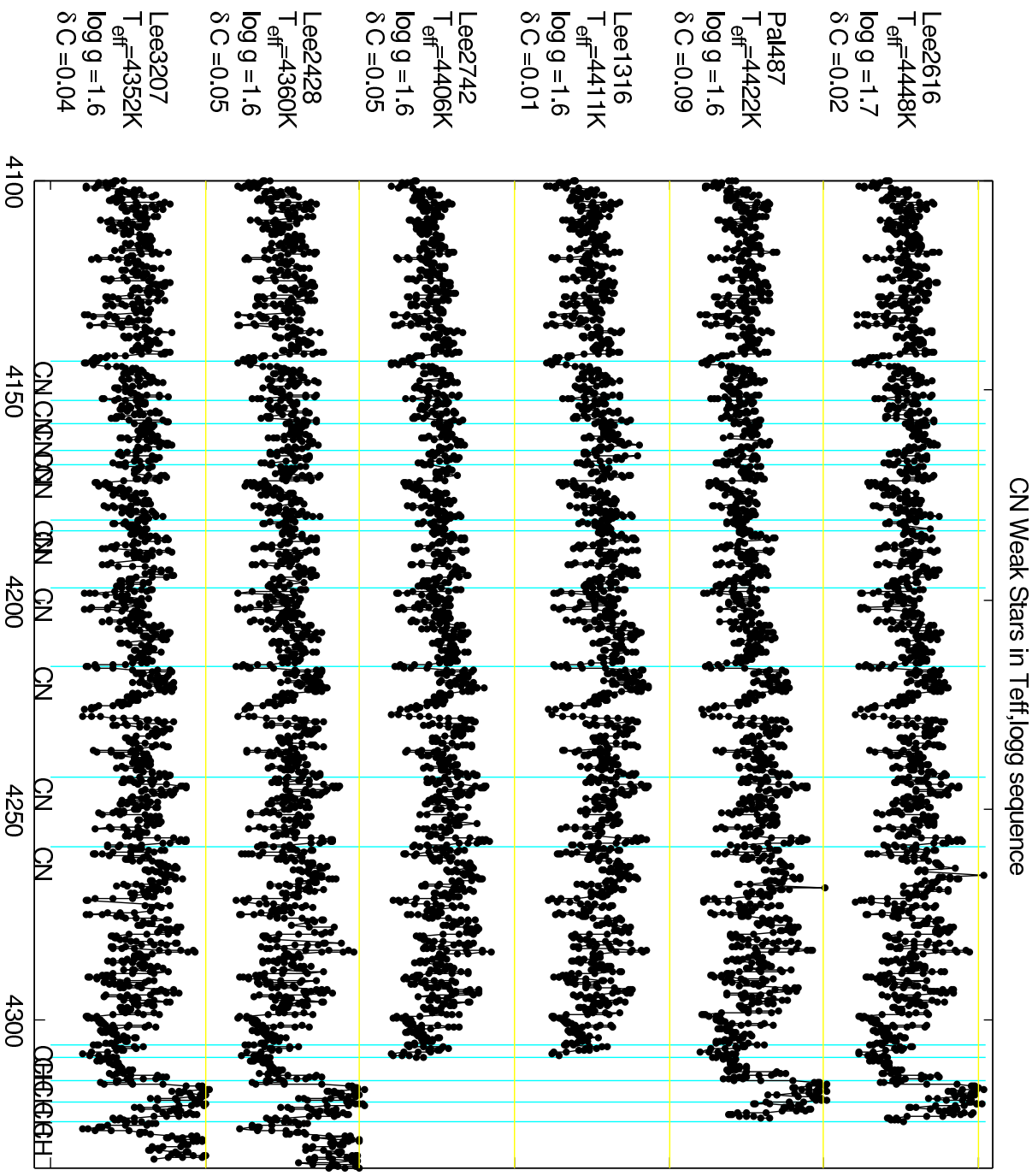
CN Weak Stars in Teff,logg sequence
Lee2616
T_eff=4448K
log g =1.7
δ C =0.02
Pal487
T_eff=4422K
log g =1.6
δ C =0.09
Lee1316
T_eff=4411K
log g =1.6
δ C =0.01
Lee2742
T_eff=4406K
log g =1.6
δ C =0.05
Lee2428
T_eff=4360K
log g =1.6
δ C =0.05
Lee3207
T_eff=4352K
log g =1.6
δ C =0.04
4100
4150
4200
4250
4300
CN
CH

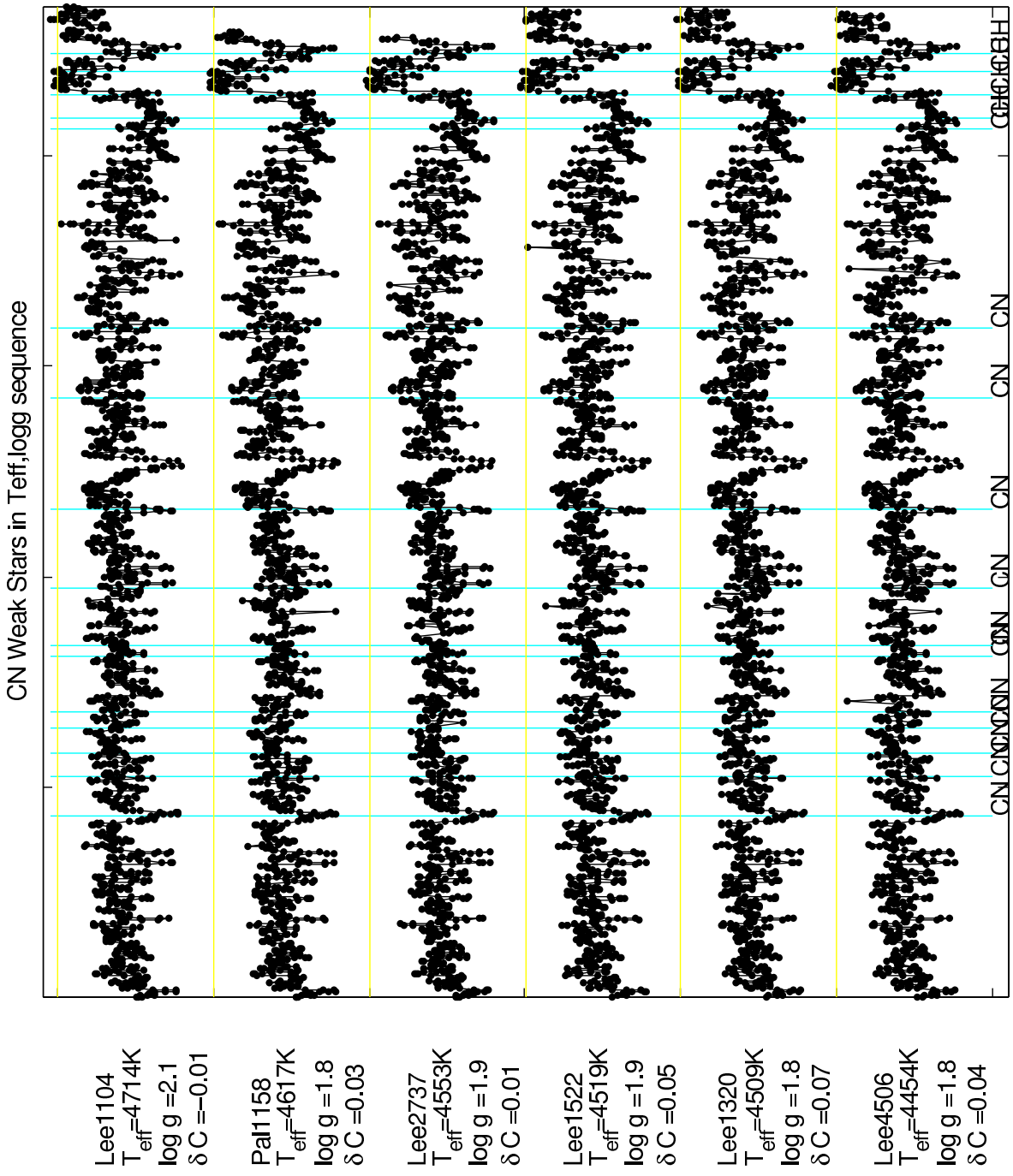
CN Weak Stars in Teff,logg sequence
Lee1104
T_eff=4714K
log g =2.1
δ C =−0.01
Pal1158
T_eff=4617K
log g =1.8
δ C =0.03
Lee2737
T_eff=4553K
log g =1.9
δ C =0.01
Lee1522
T_eff=4519K
log g =1.9
δ C =0.05
Lee1320
T_eff=4509K
log g =1.8
δ C =0.07
Lee4506
T_eff=4454K
log g =1.8
δ C =0.04
4100
4150
4200
4250
4300
CN
CH

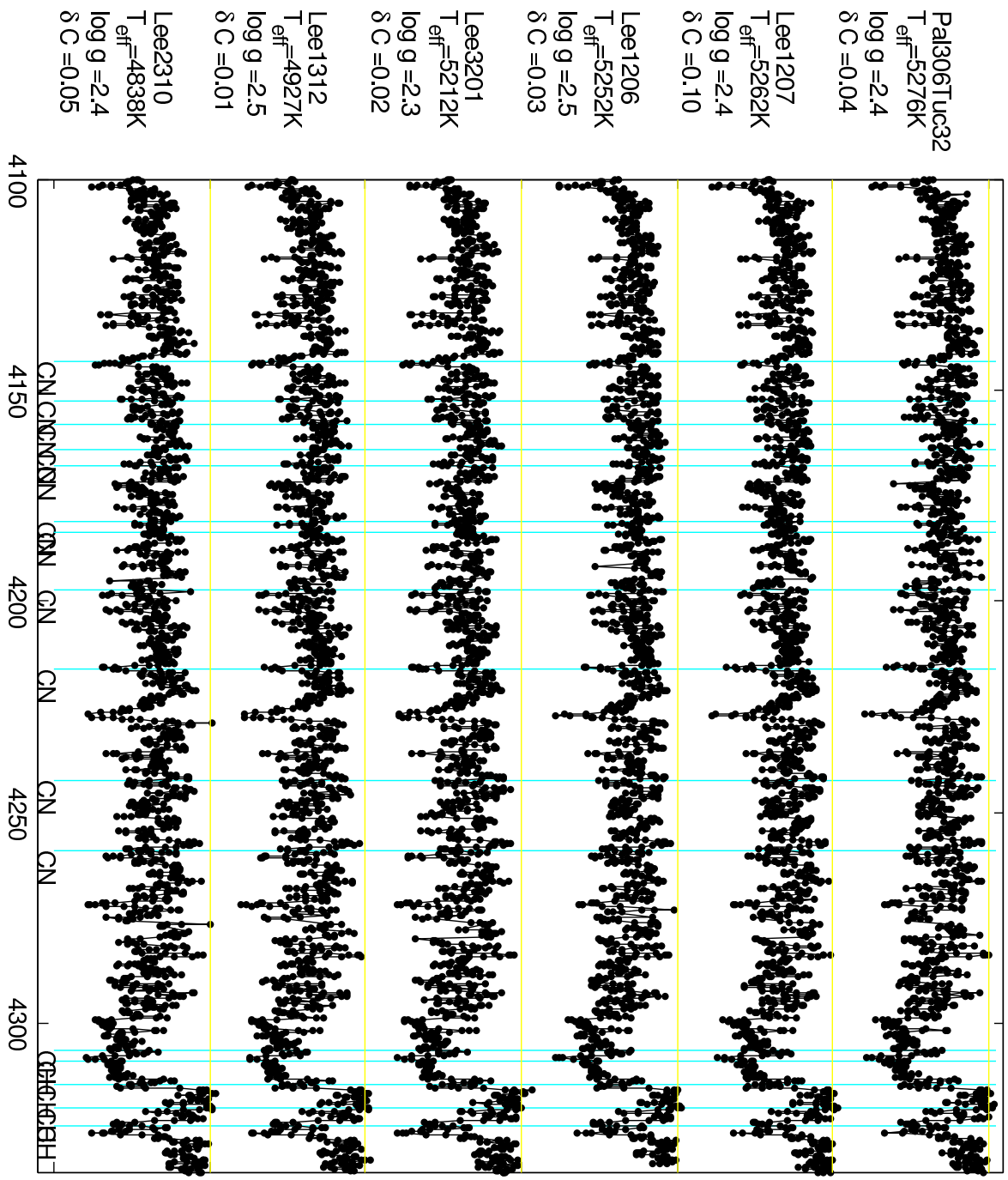
CN Weak Stars in Teff,logg sequence
Pal306Tuc32
T_eff=5276K
log g =2.4
δ C =0.04
Lee1207
T_eff=5262K
log g =2.4
δ C =0.10
Lee1206
T_eff=5252K
log g =2.5
δ C =0.03
Lee3201
T_eff=5212K
log g =2.3
δ C =0.02
Lee1312
T_eff=4927K
log g =2.5
δ C =0.01
Lee2310
T_eff=4838K
log g =2.4
δ C =0.05
4100
4150
4200
4250
4300
CN
CH

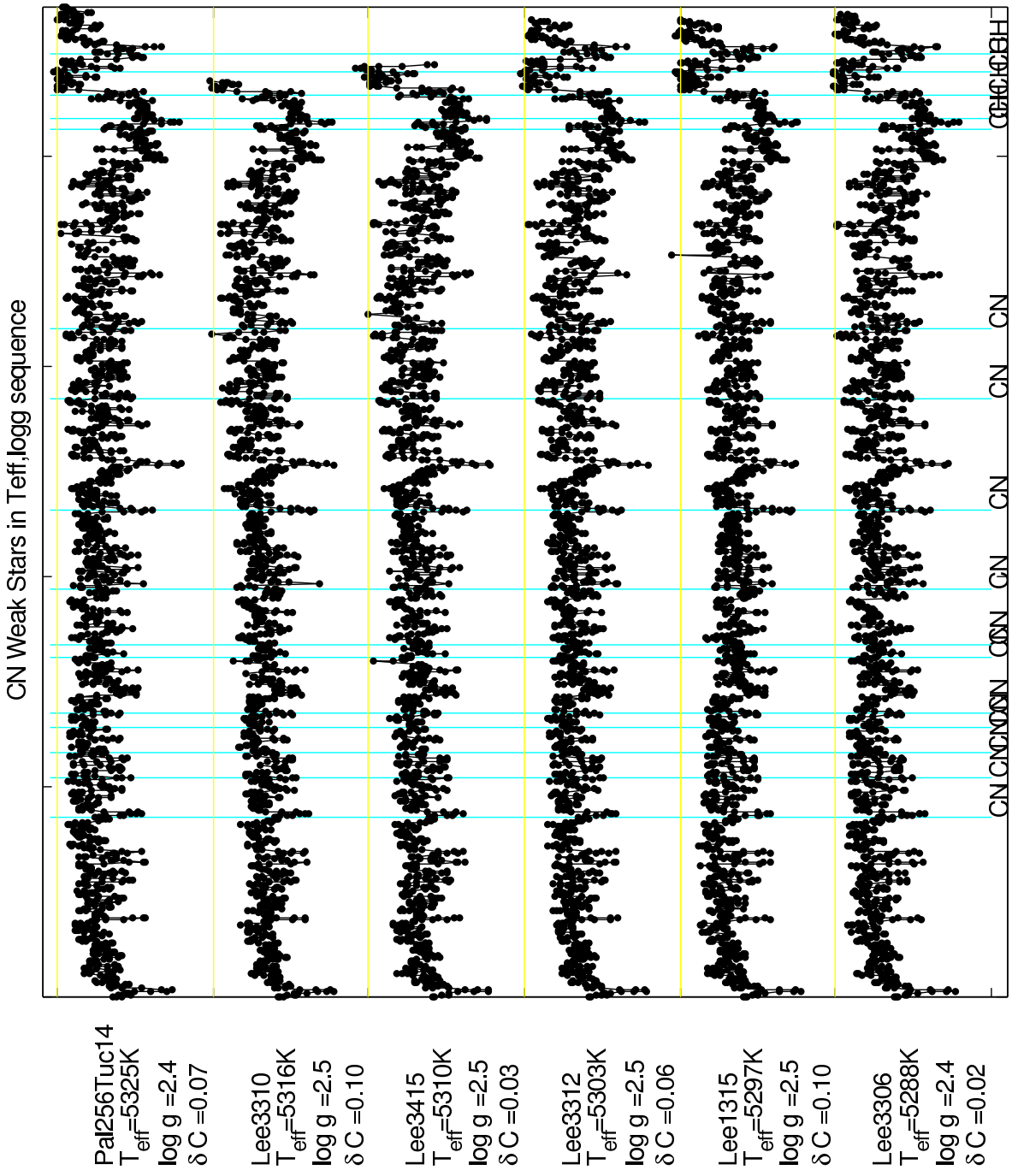
CN Weak Stars in Teff,logg sequence
Pal256Tuc14
T_eff=5325K
log g =2.4
δ C =0.07
Lee3310
T_eff=5316K
log g =2.5
δ C =0.10
Lee3415
T_eff=5310K
log g =2.5
δ C =0.03
Lee3312
T_eff=5303K
log g =2.5
δ C =0.06
Lee1315
T_eff=5297K
log g =2.5
δ C =0.10
Lee3306
T_eff=5288K
log g =2.4
δ C =0.02
4100
4150
4200
4250
4300

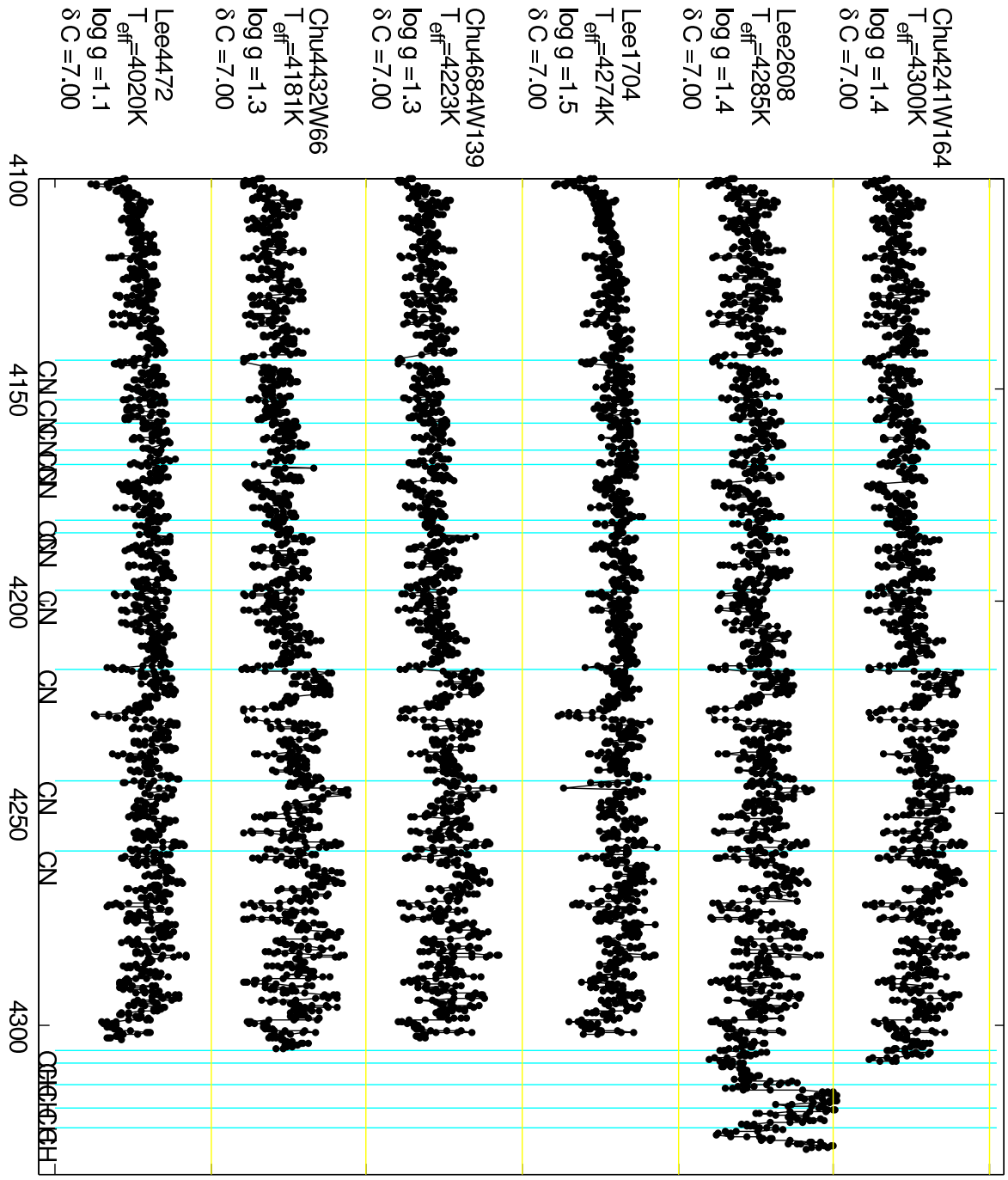
CN Unknown Stars in Teff,logg sequence
Chu4241W164
T_eff=4300K
log g =1.4
δ C =7.00
Lee2608
T_eff=4285K
log g =1.4
δ C =7.00
Lee1704
T_eff=4274K
log g =1.5
δ C =7.00
Chu4684W139
T_eff=4223K
log g =1.3
δ C =7.00
Chu4432W66
T_eff=4181K
log g =1.3
δ C =7.00
Lee4472
T_eff=4020K
log g =1.1
δ C =7.00
4100
4150
4200
4250
4300
CN

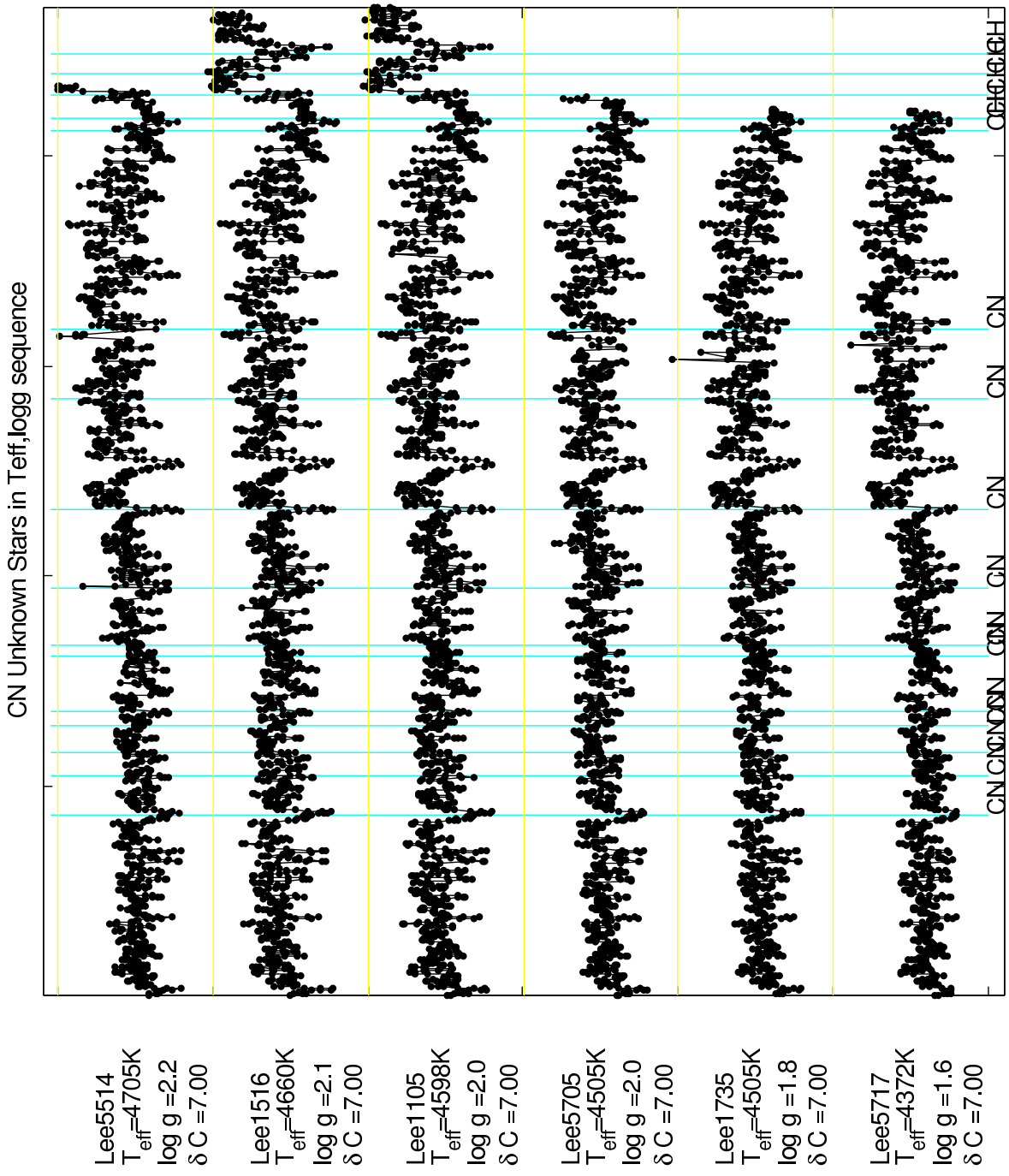
CN Unknown Stars in Teff,logg sequence
Lee5514
T_eff=4705K
log g =2.2
δ C =7.00
Lee1516
T_eff=4660K
log g =2.1
δ C =7.00
Lee1105
T_eff=4598K
log g =2.0
δ C =7.00
Lee5705
T_eff=4505K
log g =2.0
δ C =7.00
Lee1735
T_eff=4505K
log g =1.8
δ C =7.00
Lee5717
T_eff=4372K
log g =1.6
δ C =7.00
4100
4150
4200
4250
4300
CN

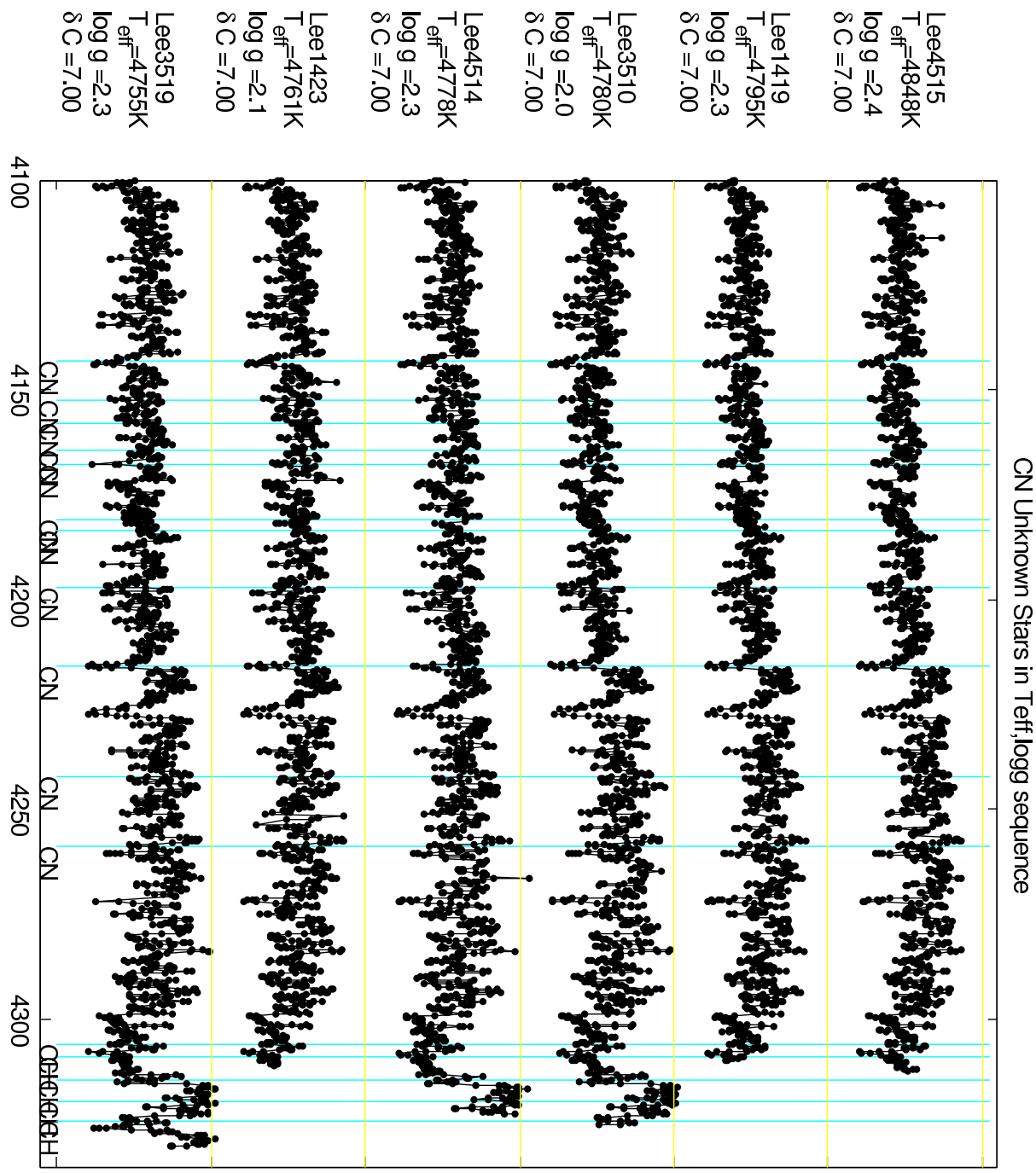
CN Unknown Stars in Teff,logg sequence
Lee4515
T_eff=4848K
log g =2.4
δ C =7.00
Lee1419
T_eff=4795K
log g =2.3
δ C =7.00
Lee3510
T_eff=4780K
log g =2.0
δ C =7.00
Lee4514
T_eff=4778K
log g =2.3
δ C =7.00
Lee1423
T_eff=4761K
log g =2.1
δ C =7.00
Lee3519
T_eff=4755K
log g =2.3
δ C =7.00
4100
4150
4200
4250
4300
CN
CH

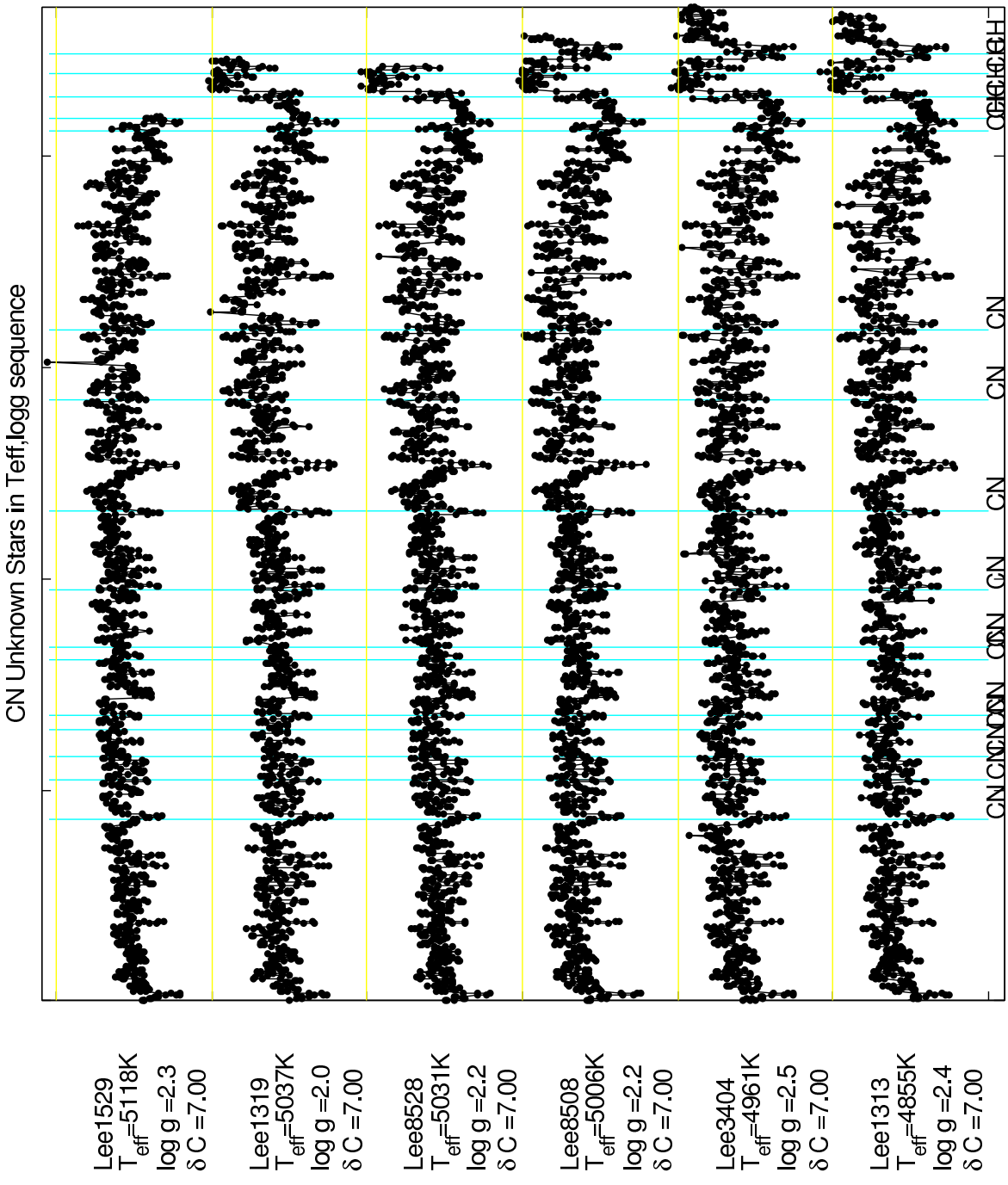
CN Unknown Stars in Teff,logg sequence
Lee1529
T_eff=5118K
log g =2.3
δ C =7.00
Lee1319
T_eff=5037K
log g =2.0
δ C =7.00
Lee8528
T_eff=5031K
log g =2.2
δ C =7.00
Lee8508
T_eff=5006K
log g =2.2
δ C =7.00
Lee3404
T_eff=4961K
log g =2.5
δ C =7.00
Lee1313
T_eff=4855K
log g =2.4
δ C =7.00
4100
4150
4200
4250
4300
CN

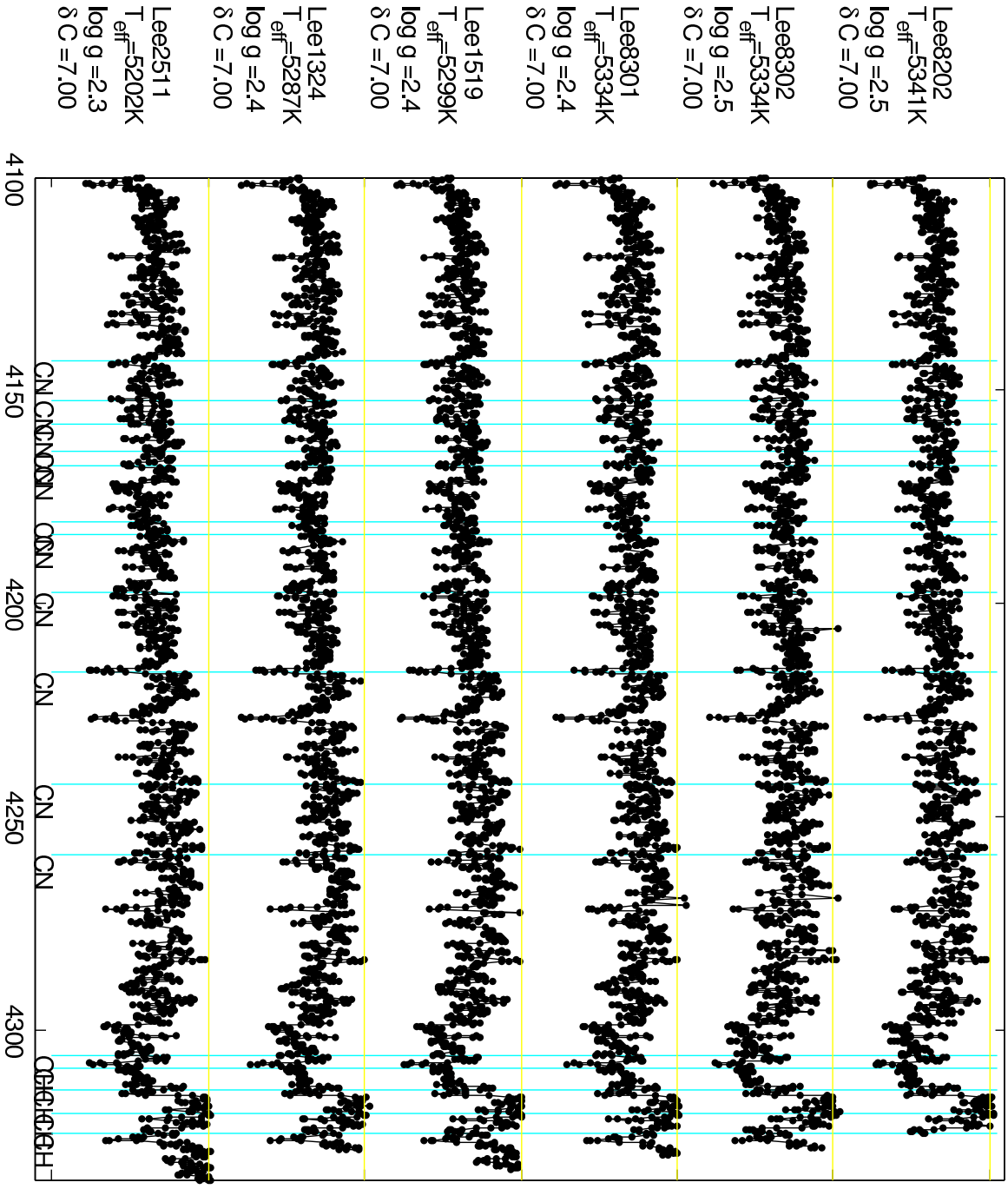
CN Unknown Stars in Teff,logg sequence
Lee8202
T_eff=5341K
log g =2.5
δ C =7.00
Lee8302
T_eff=5334K
log g =2.5
δ C =7.00
Lee8301
T_eff=5334K
log g =2.4
δ C =7.00
Lee1519
T_eff=5299K
log g =2.4
δ C =7.00
Lee1324
T_eff=5287K
log g =2.4
δ C =7.00
Lee2511
T_eff=5202K
log g =2.3
δ C =7.00
4100
4150
4200
4250
4300
CN
CH

Appendix C

Measured equivalent widths for high-resolution stars

Table C.1: Equivalent widths measured for Fe I and Fe II lines in the Arcturus and 47 Tuc high-resolution stellar spectra. The wavelength ((λ), species, excitation potential (χ) and *log gf* for each line is included.

					47 Tuc					
λ (Å)	Species	χ (eV)	*log gf*	Arcturus	Lee 2525	o02	o03	o04	o05	o09
6127.906	26.0	4.143	-1.399	73.1	98.8	80.3	68.2	71.2	48.9	62.1
6136.993	26.0	2.198	-2.950	139.1						
6151.617	26.0	2.176	-3.299	116.9	139.4					
6165.360	26.0	4.143	-1.474	67.4	78.0					
6173.334	26.0	2.223	-2.880	138.8	142.9					
6180.203	26.0	2.727	-2.586	111.0	124.5	112.9		119.6		104.0
6229.225	26.0	2.845	-2.805	86.8				100.7	129.9	92.5
6232.640	26.0	3.654	-1.223	117.9				107.9		107.0
6246.317	26.0	3.602	-0.733	139.1	152.3	136.6		125.8		
6270.222	26.0	2.858	-2.464	104.0		109.6	102.1	100.9		
6271.276	26.0	3.332	-2.703	57.9		72.6	82.8	58.3	78.8	55.3
6301.500	26.0	3.654	-0.718	141.7	156.6	144.3	138.7	140.6		129.6
6311.500	26.0	2.831	-3.141	75.6	95.1	82.0	93.2	99.1	54.8	80.0
6322.685	26.0	2.588	-2.426	141.6						
6336.823	26.0	3.686	-0.856	133.5		135.5	125.0	123.8		107.2
6344.148	26.0	2.433	-2.923	131.1						
6380.743	26.0	4.186	-1.376	75.1	84.9	72.7	73.5	68.4	64.3	63.2
6408.018	26.0	3.686	-1.018	124.4	133.9	131.3	138.0	135.4	96.6	112.5
6481.869	26.0	2.279	-2.984	135.6	139.0					
6518.365	26.0	2.831	-2.460	110.6	130.6	133.4	111.5	106.5		107.0
6574.227	26.0	0.990	-5.023	128.8	132.7					
6575.016	26.0	2.588	-2.710	132.7						
6581.207	26.0	1.485	-4.679	95.7	119.4					
6609.110	26.0	2.559	-2.692	130.3	148.0					
6699.141	26.0	4.593	-2.101	15.2						
6750.150	26.0	2.424	-2.621	142.6	137.3					
6810.257	26.0	4.607	-0.986	63.5	84.3	71.8	73.8	76.8		65.5
6837.006	26.0	4.593	-1.687	27.4	28.4				39.6	
6855.161	26.0	4.558	-0.742	88.0	72.5	70.2	78.4	73.8	41.8	61.4
4923.927	26.1	2.891	-1.504	148.8						
5234.625	26.1	3.221	-2.279	86.6						
5425.257	26.1	3.199	-3.390	43.9						
5991.376	26.1	3.153	-3.647	34.1						
6084.111	26.1	3.199	-3.881	24.3	24.4					
6149.258	26.1	3.889	-2.841	30.8						
6247.557	26.1	3.892	-2.435	41.9	42.0					
6369.462	26.1	2.891	-4.231	20.9						
6432.680	26.1	2.891	-3.687	42.9		44.0	44.1	42.5		39.4
6456.383	26.1	3.903	-2.185	51.0	50.9	47.9	50.4	47.6	39.2	43.6
6516.080	26.1	2.891	-3.432	56.1		56.2	45.1	51.1	26.6	54.9

Table C.2: Equivalent widths measured for Fe I and Fe II lines in the two NGC 6388 high-resolution stellar spectra and five of the NGC 362 high-resolution stellar spectra.

				NGC 6388		NGC 362				
λ (Å)	Species	χ (eV)	*log gf*	o09	o10	o10	o02	o04	xa2	o05
6127.906	26.0	4.143	-1.399	82.5	67.4	45.5	56.2	59.4	63.9	62.0
6136.993	26.0	2.198	-2.950							
6151.617	26.0	2.176	-3.299							
6165.360	26.0	4.143	-1.474	78.8		33.7	47.6	56.0	61.8	52.0
6173.334	26.0	2.223	-2.880							
6180.203	26.0	2.727	-2.586	132.5	113.5		104.3	107.6	104.6	76.7
6229.225	26.0	2.845	-2.805	107.9	114.6		69.8	74.3	90.2	
6232.640	26.0	3.654	-1.223	127.1	109.2	76.3	101.5	104.0	106.6	101.6
6246.317	26.0	3.602	-0.733	162.3			123.3	130.7	128.0	126.1
6270.222	26.0	2.858	-2.464	129.7	111.4		84.3	97.5	92.9	89.7
6271.276	26.0	3.332	-2.703		69.5	25.3	38.6		45.3	43.0
6301.500	26.0	3.654	-0.718	158.3	137.3	95.6	132.4	131.6	136.7	
6311.500	26.0	2.831	-3.141		82.1	41.0	61.7	64.9	76.9	71.5
6322.685	26.0	2.588	-2.426							
6336.823	26.0	3.686	-0.856	163.6	116.2	93.6	127.1	123.3	125.4	
6344.148	26.0	2.433	-2.923							
6380.743	26.0	4.186	-1.376	93.3	72.0	38.0	57.5	59.4	64.3	62.7
6408.018	26.0	3.686	-1.018	153.1	123.7	80.5	118.3	117.3	118.6	
6481.869	26.0	2.279	-2.984							
6518.365	26.0	2.831	-2.460	134.8	111.6	69.0	100.5	103.4	113.9	102.9
6574.227	26.0	0.990	-5.023							
6575.016	26.0	2.588	-2.710							
6581.207	26.0	1.485	-4.679							
6609.110	26.0	2.559	-2.692							
6699.141	26.0	4.593	-2.101							
6750.150	26.0	2.424	-2.621							
6810.257	26.0	4.607	-0.986	70.3		27.2	53.5	45.5	53.2	49.2
6837.006	26.0	4.593	-1.687		31.9	9.4	12.6		14.4	19.5
6855.161	26.0	4.558	-0.742	95.2	68.8	59.0	72.9	71.3	65.9	75.6
4923.927	26.1	2.891	-1.504							
5234.625	26.1	3.221	-2.279							
5425.257	26.1	3.199	-3.390							
5991.376	26.1	3.153	-3.647							
6084.111	26.1	3.199	-3.881							
6149.258	26.1	3.889	-2.841	29.6	31.5	18.0				27.1
6247.557	26.1	3.892	-2.435							
6369.462	26.1	2.891	-4.231	26.9	32.6	17.1	16.4			
6432.680	26.1	2.891	-3.687	51.4	46.6	30.5	38.0	42.3	32.0	
6456.383	26.1	3.903	-2.185	55.0	48.1	37.0	46.6	46.4	38.2	48.0
6516.080	26.1	2.891	-3.432	63.0	54.1	41.0	45.4	47.7	48.4	47.8

Table C.3: Equivalent widths measured for Fe I and Fe II lines in the six remaining NGC 362 high-resolution stellar spectra.

				NGC 362						
λ (Å)	Species	χ (eV)	*log gf*	x03	oa5	x01	ob2	o03	o08	x02
6127.906	26.0	4.143	-1.399	65.7	58.5	66.7	54.2	61.6	61.3	42.7
6136.993	26.0	2.198	-2.950							
6151.617	26.0	2.176	-3.299							
6165.360	26.0	4.143	-1.474	57.8	58.2	58.7	63	58.6	62.6	49.0
6173.334	26.0	2.223	-2.880							
6180.203	26.0	2.727	-2.586	114.0	118	118.6	107.5	120.9	117.1	85.7
6229.225	26.0	2.845	-2.805	96.9	89.3	87.0	84.9	86.4	87.7	63.6
6232.640	26.0	3.654	-1.223	104.5	110	114.4	99.7	105.1	104.3	97.4
6246.317	26.0	3.602	-0.733	129.9	142.3	141.2		132.8	127.6	121.0
6270.222	26.0	2.858	-2.464	97.7		106.7	98.7	98.8	110.2	84.9
6271.276	26.0	3.332	-2.703	46.4			56.4	50.8	52.6	32.8
6301.500	26.0	3.654	-0.718	134.2	149.6	148.7	130.6	136.9	136.2	123.2
6311.500	26.0	2.831	-3.141	77.5	76.3	76.2	75.2	77.7	71.5	52.3
6322.685	26.0	2.588	-2.426							
6336.823	26.0	3.686	-0.856	124.2	139.7	135.5	118.4	135.4	127.7	113.3
6344.148	26.0	2.433	-2.923							
6380.743	26.0	4.186	-1.376	59.8	65	64.4	55.9	62.4	59.1	55.2
6408.018	26.0	3.686	-1.018	114.7	129.4	127.0	114.5	125.7	116.1	107.6
6481.869	26.0	2.279	-2.984							
6518.365	26.0	2.831	-2.460	116.7	116.3	113.5	107.3	113.4	119.0	87.3
6574.227	26.0	0.990	-5.023							
6575.016	26.0	2.588	-2.710							
6581.207	26.0	1.485	-4.679							
6609.110	26.0	2.559	-2.692							
6699.141	26.0	4.593	-2.101							
6750.150	26.0	2.424	-2.621							
6810.257	26.0	4.607	-0.986	52.3	47.7	53.8	55.3	49.7	50.9	40.1
6837.006	26.0	4.593	-1.687	18.1					16.8	15.3
6855.161	26.0	4.558	-0.742	70.6	74.3	77.8	66.5	77.3	73.6	68.1
4923.927	26.1	2.891	-1.504							
5234.625	26.1	3.221	-2.279							
5425.257	26.1	3.199	-3.390							
5991.376	26.1	3.153	-3.647							
6084.111	26.1	3.199	-3.881							
6149.258	26.1	3.889	-2.841						22.0	29.8
6247.557	26.1	3.892	-2.435							
6369.462	26.1	2.891	-4.231	15.8	21.7	18.5	17.1	19.0		21.4
6432.680	26.1	2.891	-3.687	32.6	38.1	36.8	34.8	33.8	35.8	39.6
6456.383	26.1	3.903	-2.185	36.3	42.3	44.7	39.3	42.2	38.8	53.7
6516.080	26.1	2.891	-3.432	47.3	54.1	48.2	40.5	45.0	48.2	56.7

Table C.4: Equivalent widths measured for atomic lines in the Arcturus and Lee 2525 high-resolution stellar spectra. The wavelength ((λ), species, excitation potential (χ) and *log gf* for each line is included.

λ (Å)	Species	χ (eV)	*log gf*	Arcturus	Lee 2525	λ (Å)	Species	χ (eV)	*log gf*	Arcturus	Lee 2525
5577.34	8.0	1.967	-8.204	12.8		4840.874	22.0	0.900	-0.509	169.1	157.6
6300.30	8.0	0.000	-9.819	65.8	58.4	4915.229	22.0	1.887	-1.019	65.1	51.7
6363.78	8.0	0.020	-10.303	35.9		4926.148	22.0	0.818	-2.170	91.0	79.0
6154.23	11.0	2.102	-1.560	69.9	68.9	5453.643	22.0	1.443	-1.610	73.5	
6160.75	11.0	2.104	-1.260	93.5	85.5	5648.565	22.0	2.495	-0.260	64.2	
5711.09	12.0	4.346	-1.833	153.5		5739.469	22.0	2.249	-0.600	61.7	
6318.72	12.0	5.108	-1.730	73.5		5766.359	22.0	3.294	0.389	41.6	
6319.24	12.0	5.108	-1.950	57.3	45.3	5913.728	22.0	0.021	-4.198	43.9	
6799.00	12.0	5.753	-1.560	31.6		5918.535	22.0	1.067	-1.460	111.3	
6841.08	12.0	5.749	-1.610	51.6		5944.660	22.0	0.000	-4.059	60.4	109.9
6894.92	12.0	5.749	-1.640	40.5		6092.792	22.0	1.887	-1.379	53.5	33.0
6965.41	12.0	5.749	-1.510	53.9		6126.216	22.0	1.067	-1.425	132.3	62.8
7387.69	12.0	5.749	-1.020	80.2		6146.206	22.0	1.873	-1.151	45.4	
7875.43	12.0	5.932	-2.130	14.1		6186.140	22.0	2.175	-1.365	45.6	111.2
5557.06	13.0	3.143	-2.110	32.4		6273.388	22.0	0.021	-4.248	42.0	77.7
6696.02	13.0	3.143	-1.347	88.1	109.0	6303.756	22.0	1.443	-1.566	89.8	130.9
6698.67	13.0	3.143	-1.647	59.3	62.2	6312.236	22.0	1.460	-1.552	87.8	64.4
7835.31	13.0	4.022	-0.649	63.6		6336.099	22.0	1.443	-1.743	79.0	45.3
5517.53	14.0	5.082	-2.611	25.5		6497.684	22.0	1.443	-2.085	61.0	96.5
5690.43	14.0	4.930	-1.769	58.2		6508.120	22.0	1.430	-2.146	63.2	133.8
6142.48	14.0	5.619	-1.295	32.3	23.2	6554.223	22.0	1.443	-1.218	115.7	112.6
6145.02	14.0	5.616	-1.310	37.5	44.1	6556.062	22.0	1.460	-1.074	129.9	
6155.13	14.0	5.619	-0.754	72.6	58.2	6599.105	22.0	0.900	-2.085	114.2	25.2
6237.32	14.0	5.614	-0.975	54.5	37.8	6716.666	22.0	2.487	-1.409	24.6	
6243.82	14.0	5.616	-1.242	42.8		6743.122	22.0	0.900	-1.630	141.3	
6244.47	14.0	5.616	-1.093	42.7	9.0	7138.072	22.0	1.430	-2.375	15.4	
6414.98	14.0	5.871	-1.035	39.2	51.9	7271.506	22.0	1.443	-2.294	54.2	
6635.69	14.0	5.863	-1.664	12.7		7352.119	22.0	2.487	-0.967	27.7	

continued on next page

λ (Å)	Species	χ (eV)	*log gf*	Arcturus	Lee 2525	λ (Å)	Species	χ (eV)	*log gf*	Arcturus	Lee 2525
5512.98	20.0	2.933	-0.464	122.2		7391.513	22.0	1.501	-1.210	17.5	82.5
5590.11	20.0	2.521	-0.571	137.4		4865.611	22.1	1.116	-2.590	98.0	74.1
5867.56	20.0	2.933	-1.570	57.8		5492.862	22.1	1.581	-2.956	46.9	44.2
6156.02	20.0	2.521	-2.497	38.3	20.3	6491.561	22.1	2.061	-1.793	86.8	
6161.30	20.0	2.523	-1.266	117.3	114.4	6559.588	22.1	2.048	-2.480	61.9	
6162.17	20.0	1.899	-0.090	277.7	244.9	6606.949	22.1	2.061	-2.790	33.9	174.0
6166.44	20.0	2.521	-1.142	120.6	139.0	7214.716	22.1	2.590	-1.740	52.6	173.8
6169.04	20.0	2.523	-0.797	143.3		6216.354	23.0	0.275	-1.290	182.7	62.6
6169.56	20.0	2.526	-0.478	157.5		6251.827	23.0	0.287	-1.340	166.1	39.9
6455.60	20.0	2.523	-1.340	110.2	88.3	6504.164	23.0	1.180	-1.230	65.3	67.8
6471.66	20.0	2.526	-0.686	151.5	162.0	6454.990	27.0	3.632	-0.250	53.9	63.9
6493.78	20.0	2.521	-0.109	184.3	210.2	6632.433	27.0	2.280	-2.000	63.7	30.4
6499.65	20.0	2.523	-0.818	141.3	132.9	6175.360	28.0	4.089	-0.559	61.5	25.3
6508.00	20.0	2.526	-2.500	44.5	70.4	6186.709	28.0	4.105	-0.960	46.7	50.2
6572.78	20.0	0.000	-4.290	189.7	148.9	6204.600	28.0	4.088	-1.100	36.5	24.8
6245.64	21.1	1.507	-1.030	86.6	119.1	6223.981	28.0	4.105	-0.910	43.6	125.5
6604.60	21.1	1.357	-1.309	85.1	77.6	6635.118	28.0	4.419	-0.820	34.1	70.8
4758.12	22.0	2.249	0.425	105.9	154.7	4722.153	30.0	4.030	-0.338	77.5	
4820.41	22.0	1.503	-0.441	150.8	154.3	4810.528	30.0	4.078	-0.137	78.1	

Appendix D

A.S.A. 2006

Poster presentation at the 2006 Annual Scientific Meeting of the Astronomical Society of Australia in Canberra from the 2nd to the 6th of July, 2006.

Title: ***s*-process elemental abundances throughout the CMD of 47 Tuc**

s-process element abundances throughout the CMD of 47 Tuc

C.C. Worley, E.C. Wylie and P.L. Cottrell

Department of Physics and Astronomy, University of Canterbury, Christchurch, New Zealand

A recent study by Wylie et al (2006) has revealed that s-process element abundances are enhanced relative to iron in both red giant branch (RGB) and asymptotic giant branch (ABG) stars of 47 Tucanae. While it could be argued that the s-process element abundance results in the AGB stars were the result of internal nucleoprocessing and dredge-up of this processed material, it is thought that the luminosity at which this is observed is too low for currently accepted models of third dredge-up. Consequently, there is a need to undertake more detailed investigations of the abundances of s-process element abundances throughout the colour-magnitude diagram of 47 Tucanae to investigate the possibility that the s-process element abundance enhancements in the RGB and AGB stars are intrinsic to the cluster. This poster explores this by investigating the visibility of various s-process element lines in synthetic spectra of giant and dwarf stars throughout the CMD. The purpose of this study is to motivate a study of this cluster using the multi-object spectroscopy mode of the Robert Stobie Spectrograph (formerly known as the Prime Focus Imaging Spectrograph) on the Southern African Large Telescope.

Project Motivation and Spectrum Synthesis

Synthesised spectra were produced using MOOG (Sneden 1973) for a limited number of spectral regions containing Zr I (light s-process), La II, Nd II (heavy s-process) and Eu II (r-process) lines and at high (R ~ 60,000) and medium (R ~ 10,000) resolving powers.
The high resolving power provides comparison with current instrument at the AAT (see Wylie et al 2006) and future SALT instrumentation (SALT high resolution spectrograph, SALT HRS, Cottrell et al 2005), while the medium resolving power is the highest achievable with the Robert Stobie Spectrograph on SALT.

The parameters of the stellar models used in this synthesis are shown for each of the figures. The abundance of each of these key elements is varied relative to the model metallicity, [Fe/H]. The **red line** indicates a depletion of **-0.8 dex**; **black line** is for no variation, **0.0 dex**; **blue line** is **+0.5 dex**; **green line +1.0 dex**.
Linelists and stellar models were from the Kurucz website (http://???).

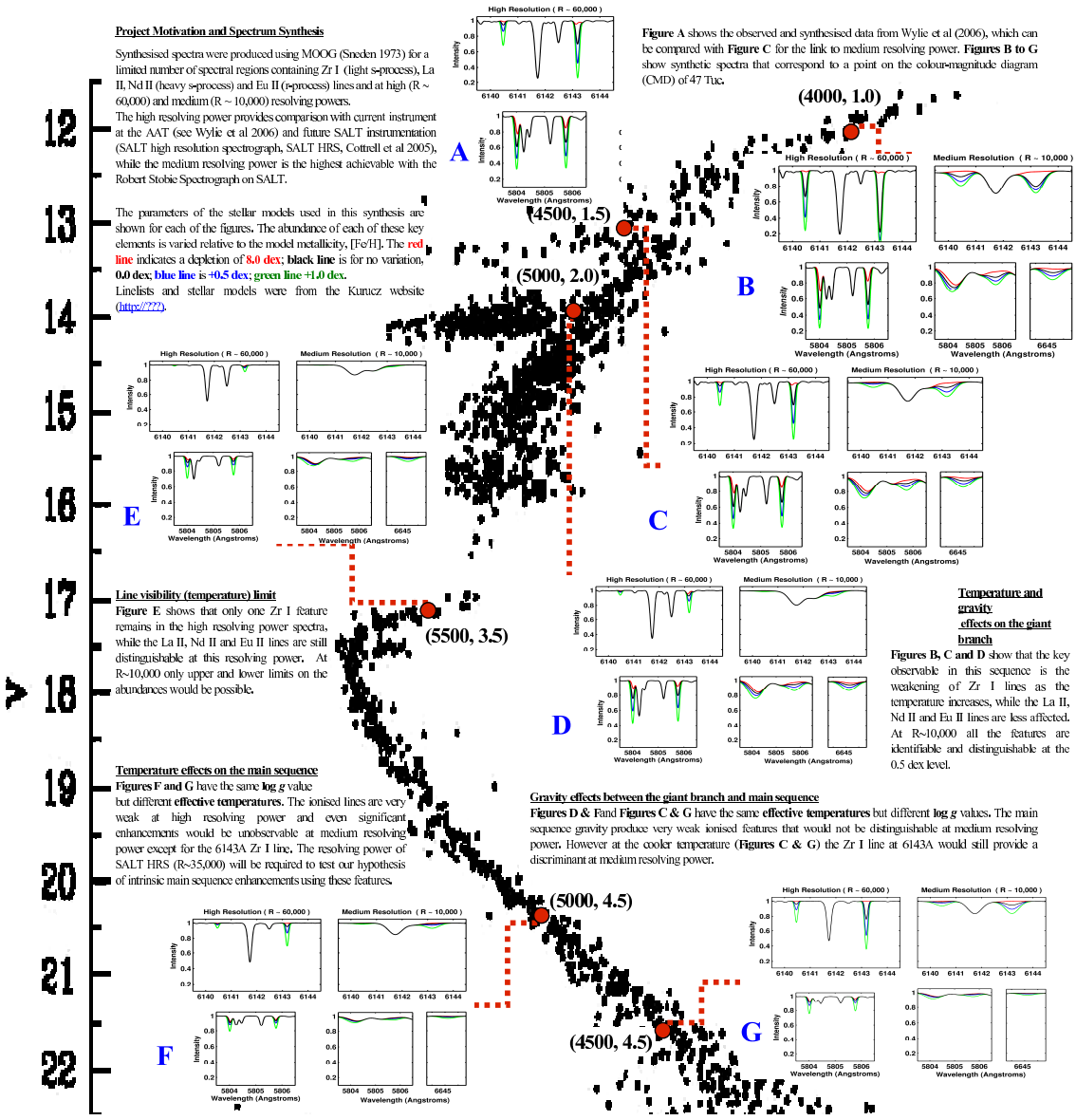

Figure A shows the observed and synthesised data from Wylie et al (2006), which can be compared with **Figure C** for the link to medium resolving power. **Figures B to G** show synthetic spectra that correspond to a point on the colour-magnitude diagram (CMD) of 47 Tuc.

Line visibility (temperature) limit

Figure E shows that only one Zr I feature remains in the high resolving power spectra, while the La II, Nd II and Eu II lines are still distinguishable at this resolving power. At R~10,000 only upper and lower limits on the abundances would be possible.

Temperature and gravity effects on the giant branch

Figures B, C and D show that the key observable in this sequence is the weakening of Zr I lines as the temperature increases, while the La II, Nd II and Eu II lines are less affected. At R~10,000 all the features are identifiable and distinguishable at the 0.5 dex level.

Temperature effects on the main sequence

Figures F and G have the same **log *g*** value but different **effective temperatures**. The ionised lines are very weak at high resolving power and even significant enhancements would be unobservable at medium resolving power except for the 6143A Zr I line. The resolving power of SALT HRS (R~35,000) will be required to test our hypothesis of intrinsic main sequence enhancements using these features.

Gravity effects between the giant branch and main sequence

Figures D & Fand **Figures C & G** have the same **effective temperatures** but different **log *g*** values. The main sequence gravity produce very weak ionised features that would not be distinguishable at medium resolving power. However at the cooler temperature (**Figures C & G**) the Zr I line at 6143A would still provide a discriminant at medium resolving power.

Conclusion

Synthetic spectra throughout the CMD of 47 Tuc show that medium resolving power (R~10,000) observations with the Robert Stobie Spectrograph on SALT will enable us to investigate light s- and heavy s-process element abundances on the giant branch to temperatures below the horizontal branch.
Some enhancements (for example of Zr I lines) would also be distinguishable on the main sequence below **effective temperatures** of 4500K.

REFERENCES

Cannon et al, 1998, MNRAS, 298, 601
Chun, M.S. & Freeman, K.C. 1978, AJ, 83, 376
Cottrell et al, 2005
Hesser et al, 1987, PASP, 99 739
Sneden, C.A. 1973, Ph.D. Thesis, University of Texas at Austin
Wylie et al, 2006, App. J,

Appendix E

N.Z.O.G. 2007

Poster presentation at 'A New Zeal for Old Galaxies' conference, hosted by Swinburne University (Melbourne, Australia), held in Rotorua, New Zealand, from the 25th to the 31st of March, 2007.

Title: ***s*-process elemental abundances throughout the CMD of 47 Tuc**

s-process element abundances throughout the CMD of 47 Tuc

C. Clare Worley*, Peter L. Cottrell and Elizabeth C. Wylie

Department of Physics and Astronomy, University of Canterbury, Christchurch, New Zealand

*Fellow of the New Zealand Federation of Graduate Women

A recent study by Wylie et al (2006) has revealed that s-process element abundances are enhanced relative to iron in both red giant branch (RGB) and asymptotic giant branch (AGB) stars of 47 Tuc. While it could be argued that the s-process element abundance results in the AGB stars were the result of internal nucleosynthesis and dredge-up of this processed material, it is thought that the luminosity at which this is observed is too low for currently accepted models of third dredge-up. Consequently, there is a need to undertake more detailed investigations throughout the colour-magnitude diagram (CMD) of 47 Tuc to investigate the possibility that the s-process element abundance enhancements in the RGB nd AGB stars are intrinsic to the cluster.

Observation Programme

The work presented here has been carried out as part of a campaign to observe large numbers of stars throughout the CMD of 47 Tuc. The Wylie et al (2006) data, shown in Figure 1, was obtained using UCLES, a high resolution instrument, on the AAT. Further observations of 47 Tuc RGB stars (see Table 1) were obtained during the performance verification (PV) commissioning phase of the Robert Stobie Spectrograph (RSS, formerly known as the Prime Focus Imaging Spectrograph) on the Southern African Large

Figure 1 shows the observed and synthesised data from Wylie et al (2006), which can be compared with Figure 2 for the link to medium resolving power.

A proposal has been submitted to observe ~250 stars in each of 3 different globular clusters using AAOmega on the AAT, which is a medium resolution instrument. A similar survey is planned later this year using the fully commissioned RSS. High resolution multiple object studies can be considered once the high resolution spectrograph (HRS) is installed on SALT in the near future.

47 Tuc CMD

The CMD of 47 Tuc provides the backdrop to this investigation.

The red lines at key apparent magnitude (V) levels show the extent of the CMD observed so far. The blue lines represent likely V limits to future observations. AAOmega will extend the RGB sample to below the horizontal branch (HB).

The different regions for RSS and HRS represent stars that will have s-process features observable by the respective instruments. Cooler faint main sequence (MS) stars are potentially observable with RSS, while HRS extends this to hotter and brighter MS stars.

AAT: UCLES

SALT RSS: Performance Verification

AAT: AAOmega

SALT HRS

SALT RSS

Spectrum Synthesis & Line Observability

Figures 2a and 3a show synthesised spectra produced using MOOG (Sneden 1973). Key elements were varied in abundance relative to the model abundance. The red line indicates a depletion of 8.0 dex; black line is for no variation, 0.0 dex; blue line is +0.5 dex; green line +1.0 dex.

high resolving power (R ~ 60,000) simulating UCLES (AAT) and the future SALT HRS (Cottrell et al 2005) and medium resolving powers (R ~ 10,000) simulating RSS (SALT) and AAOmega (AAT).

The spectral regions contain Zr I (light s-process), La II & Nd II (heavy s-process) and Eu II (r-process) lines. The spectra in Figure 2a were synthesised using a giant branch stellar model with $T_{eff} = 4500K$ and $\log g = 1.5$, while in Figure 3a a model with $T_{eff} = 5000K$ and $\log g = 2.0$ was used. Both models used a metallicity of $[Fe/H] = -0.5$, similar to the 47 Tuc metallicity of $[Fe/H] = -0.7$.

The s-process features are clearly visible in both the high and medium resolution syntheses in Figures 2a and 3a. The neutral lines are affected more by the increase in T_{eff} and $\log g$ than the ionised lines.

Table 1: SALT RSS PV 47 Tuc Stars

Star	V	B-V	Teff (K)	logg
Lee 3512	11.79	1.63	4100	0.7
Lee 1513	12.41	1.32	4800	1.3
Lee 2525	12.43	1.29	4800	1.4
Lee 0519	12.81	1.27	4800	1.5
Lee 0524	13.08	1.21	4800	1.7
Lee 1506	13.27	1.15	4700	1.8
Lee 3510	13.63	1.09	4800	2.0
Lee 2504	13.87	1.01	4800	1.9
Lee 4514	14.35	0.98	5000	2.4
Lee 4515	14.49	0.98	5000	2.5
Lee 4513	14.59	0.98	5000	2.5

SALT RSS PV Spectra

Figures 2b and 3b show the observed SALT RSS PV data. The resolution of the data is R~6000 and variations in the s-process features are evident. For both stars the abundance of Zr I is best fit by the model abundance. This also appears to be the case for the Nd II feature. The La II feature shows an enrichment of at least 0.5 dex.

s-process line visibility on the MS

The synthesised spectra in Figure 4 were generated using a stellar model with $T_{eff} = 5000K$ and $\log g = 4.5$. In Figure 5 $\log g$ is the same value but $T_{eff} = 4500K$ as it is further down the MS.

In Figure 4 the ionised lines are very weak at high resolving power and even significant enhancements would be unobservable at medium resolving power. The resolving power of SALT HRS (R~35,000) will be required to test our hypothesis of intrinsic main sequence enhancements using these features.

In Figure 5 the cooler MS model produces stronger neutral lines compared with Figure 4. At medium resolving powers the 6143A Zr I line is particularly distinct. Objects as faint as V=22 may be observable with RSS.

DISCUSSION

The synthetic spectra throughout the CMD of 47 Tuc show that medium resolving power (R~10,000) observations with the Robert Stobie Spectrograph on SALT will enable us to investigate light s- and heavy s-process element abundances on the giant branch to temperatures below the horizontal branch. The analysis of the SALT RSS PV stars has born out this conclusion. The initial analysis shows Zr I and Nd I to have solar ratio abundances, but La II appears to be enhanced. Analysis of these stars is ongoing.

The next stage is the large scale survey of 47 Tuc sampling approximately 250 stars on the giant branches to below the horizontal branch. AAOmega on the AAT and RSS on SALT are both suited to this type of project as they have the capability to observe multiple targets simultaneously.

REFERENCES

Cottrell et al. 2005, CDR Documentation for SALT HRS

Sneden, C.A., 1973, PhD. Thesis, University of Texas at Austin

Wylie et al. 2006, ApJ, 649, 248

Acknowledgements

We acknowledge the contribution of members of the SALT telescope and instrument teams towards this project, in particular Prof. Ken Nordsieck, the RSS principal investigator.

Appendix F

C.E.D.G.S.C. 2008

Poster presentation at the 'Chemical Evolution of Dwarf Galaxies and Stellar Clusters: The MPA/ESO/MPE/USM 2008 Joint Astronomy Conference' held in Garching, Germany, from the 21st to the 25th of July, 2008.

Title: **Chemical abundances of light and heavy *s*-process elements in 47 Tuc, NGC 362, NGC 6388 and M15 using SALT and VLT data.**

Chemical abundances of light and heavy s-process elements in 47 Tuc, NGC 362, NGC 6388 and M15 using SALT and VLT data

C.C.Worley[a], P.L.Cottrell[a], I.McDonald[b] & J. Th van Loon[b]

(a) Unversity of Canterbury, Christchurch, New Zealand; (b) University of Keele, Keele, U.K.

Corresponding author email address: clare.worley@pg.canterbury.ac.nz

The observed chemical abundances of light and heavy s-process elements in globular cluster stars are indicative of the type of enrichment that is occurring within a globular cluster (GC). Key high resolution studies to-date have reached varied conclusions, either indicating that s-process element abundances are homogenous within a cluster (James et al, A&A,v427,825,2005), or that abundance variations have been observed (Wylie et al, ApJ,649,2006). This research seeks to extend the number of stars analysed for s-process element abundances for the globular clusters: 47 Tuc, NGC 362, NGC 6388, and M15, using data obtained from the newly commissioned Southern African Large Telescope (SALT) and also data from the Very Large Telescope (VLT). The data obtained from SALT was of medium resolution (R~5000) using the Robert Stobie Spectrograph (RSS) to test the capability of that instrument to carry out a medium resolution survey of s-process element abundances in giant branch stars in 47 Tuc (Worley et al, PASA,v25,53,2008). The data obtained from the VLT is high resolution data from UVES for a programme to observe giant branch stars in five separate globular clusters for mass loss and chemical abundance analysis (McDonald & van Loon, A&A,v476,1261,2007).

Motivation

GC & Abundance Anomalies

If the gas cloud from which a GC forms was pristine at the time of formation then the only abundance anomalies that would be observed in the GC would be due to internal nucleoprocessing as the stars evolve, assuming only one generation of stars in the cluster (Busso et al,A&A,&A,37,239,1999).

TPs, AGBs & the s-process

On the ascent of the AGB a star may undergo Thermal Pulses (TPs) during which s-process elements are created.

The number of TPs the star has undergone affects the degree of enhancement of the s-process element abundances.

Theoretical limits indicate only intermediate mass AGB stars ($3M_{sol}$-$8M_{sol}$) undergo TPs.

AGB stars in GCs

AGB stars in GCs have masses ($<0.85M_{sol}$) which are too low for for TPs to occur.

So where does any scatter in s-process element abundances come from?

- Low mass AGB stars are undergoing TPs
- Random pollution of the initial gas cloud with s-process elements
- s-process element pollution of individual stellar atmospheres through some mechanism (e.g. stellar winds) during the course of the star's life

Solution: more data!

Large scale surveys of s-process element abundances in GCs will:

- Determine the exact nature of the abundance anomalies
- Compare AGB to RGB to main sequence stars to find the extent of the anomalies

Observations I: s- & r- process abundances in 47 Tuc

The 4 datasets discussed here are:

(A) AAT UCLES (R~40,000)

(B) SALT RSS Performance Verification (R~5,000)

(C) VLT UVES (R~110,000)

(D) AAO 2.3m Echelle (R~20,000)

Figures 1 & 2 show spectra from these datasets in the wavelength region which contains four Zr I lines and one Ba II line.

Figure 1 shows the medium resolution SALT dataset (B) and Figure 2 shows the three high resolution datasets (A), (C) & (D).

The single star (D) has been observed at both medium and high resolution. The high resolution spectrum is also overlaid on its medium resolution counterpart. This star is to connect observations from Wylie et al 2006, Brown & Wallerstein, AJ, v104, 1818,1992, and Worley et al, 2008.

The medium resolution dataset (B) was analysed in Worley et al 2008 to determine the capacity of medium resolution instruments (RSS, AAOmega) to carry out large scale s-process element abundance surveys of globular cluster stars. As shown in Figure 1 the s-process element features (Zr I and Ba II) are clearly resolved for the cooler stars, weakening as the temperature increases. At the higher operational resolution of RSS (R~10,000) variations of the s-process features corresponding to at least 0.3 dex will be possible (Worley et al 2008). Follow up work would be pursued via high resolution instruments corresponding to the datasets (A), (C) & (D), and also the high resolution spectrograph (HRS) to be installed on SALT (Barnes,S.I.,et al, 2008,Proc.SPIE 7014).

Figure 2 clearly shows the detail in the s-process features that can be obtained with high resolution data. The AAT dataset (A) was analysed in Wylie et al 2006 for s-process element abundances. The VLT dataset (C) was analysed for mass loss rates in McDonald & van Loon 2007. The abundance analysis of dataset (C) is the subject of this work. The star (D) is also part of the current research.

The mean abundances for key s- & r-process elements in the stars for each dataset (A)-(C) are presented in Table 1.

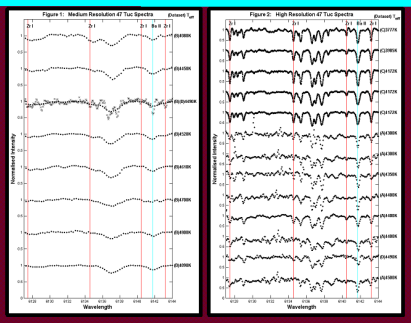

Table1: Mean abundances of 47 Tuc datasets

(A) Wylie et al 2006		(B) Worley et al 2008		(C) Current Research	
Instrument:	AAT UCLES	Instrument:	SALT PV RSS	Instrument:	VLT UVES
No. Stars	7	No. Stars	8	No. Stars	5
Y I	0.65 ± 0.20	Y I	- - -	Y I	0.63 ± 0.40
Zr I	0.69 ± 0.15	Zr I	0.3 ± 0.1	Zr I	1.28 ± 0.43
La II	0.31 ± 0.19	La II	0.1 ± 0.2	La II	0.13 ± 0.12
Nd II	0.42 ± 0.13	Nd II	0.2 ± 0.2	Nd II	- - -
Eu II	0.14 ± 0.12	Eu II	0.1 ± 0.2	Eu II	0.26 ± 0.10
[s/Fe]	0.65 ± 0.10	[s/Fe]	0.3 ± 0.1	[s/Fe]	0.96 ± 0.47
[hs/Fe]	0.37 ± 0.14	[hs/Fe]	0.1 ± 0.2	[hs/Fe]	0.27 ± 0.19
[hs/ls]	-0.28 ± 0.11	[hs/ls]	-0.1 ± 0.4	[hs/ls]	-0.70 ± 0.66

The seven stars in dataset (A) included both RGB and AGB stars. The spread of s-process element abundance values, as shown in Table 1A, indicates star-to-star variations in s-process element abundances for these 47 Tuc stars (Wylie et al 2006).

Dataset (C) is comprised of AGB stars (5 of 9 analysed here) and Table 1C also shows a large spread in abundance values between the stars in this 47 Tuc sample.

Overall the three datasets show an enhancement of both heavy and light s-process element abundances relative to Fe in giant branch stars of 47 Tuc. It is even evident at the lower resolution of the SALT RSS PV data in Table 1B. In each case the light s- (ls) elements, consisting of Y & Zr, are enhanced to a greater degree than the heavy s- (hs), consisting of La & Nd. The Zr abundances in dataset (C) are greatly enhanced compared to dataset (A).

For Eu (an r-process element and so not produced in TPs) dataset (C) returns higher abundances than datasets (A) and (D). This disagreement may be due to issues with the stellar parameter derivations for dataset (C). Further refinement of these parameters is ongoing. However a low spread of Eu abundance in each dataset confirms the abundance of that element is intrinsic to the cluster.

Observations II: GC s-process abundances

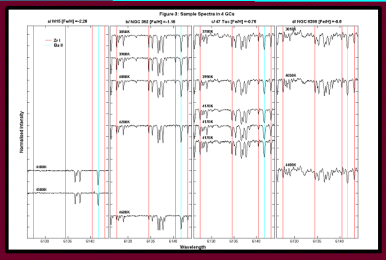

In this analysis a selection of giant stars from the GCs in the VLT dataset were analysed for their s-process element abundances. Figure 3 shows the Zr region for 15 stars in 4 of the GCs.

The stellar parameters for the stars were derived from measured equivalent widths using the spectrum synthesis programme MOOG. Models based on these parameters were then compared to the observed spectrum, also using MOOG, in order to determine the s-process element abundances.

Figure 4 shows two examples of the spectrum synthesis for the Zr region (left panels) and an Eu II & Y I region (right panels), for an AGB star in each of 47 Tuc (top panels) and NGC 362 (bottom panels). The abundance of each s-process element was altered until a fit to the spectrum was found. The abundance changes resulting in the best fit to the spectra are stated in the key for each panel. A synthesis at model abundance ([X/Fe]=0.0) and of element depletion are also shown.

Figure 3 shows not only the changing strength of the lines with metallicity but also the effect of temperature when comparing stars within a cluster. Cooler temperatures and higher metallicities mean molecules substantially affect the continuum placement of the spectrum and make the derivation of stellar parameters challenging. This is seen in Figure 3d which shows the spectrum of three stars in the most metal rich cluster (NGC 6388 [Fe/H]= -0.6).

Figure 3c displays the five 47 Tuc stars that have been analysed for s-process element abundances and continuum issues due to molecules are also evident at this metallicity. Figure 3b shows the NGC 362 spectra ([Fe/H]= -1.56) and while there is no contamination by molecules, the lines are weaker due to the low metallicity. For the most metal poor stars ([Fe/H]= -2.26 for M15), seen in Figure 3a, the only s-process feature that is still identifiable is the Ba II line.

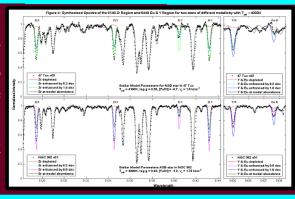

The s-process element abundance analysis of the 47 Tuc and NGC 362 stars are displayed in Table 2 with their derived effective temperature (T_{eff}), surface gravity (log g), microturbulence (v_t) and metallicity ([Fe/H]). Overall there is good agreement between the photometric and spectroscopic temperatures of the stars, and their metallicities correspond well to the cluster metallicity.

The spectra of the NGC 362 stars were not contaminated by molecules and so the stellar parameters were much easier to derive than for the 47 Tuc stars. The enhancements in NGC 362 (Table 2b) are not as great as those in 47 Tuc (Table 2a) which may not be unexpected as the lower metallicity means there are less seed nuclei from which the s-process elements can form. This is true for either the case of TPs occurring in these stars, or the case of some pollution mechanism which is occurs in the initial low metallicity gas cloud.

The key result is that the s-process element abundance enhancement observed in the 47 Tuc giant branch stars is also observed in the NGC 362 AGB stars.

There are uncertainties associated with the determination of the stellar parameters. This is due in part to continuum fitting and further refinement of these values is taking place. The stars x05 and x09 in 47 Tuc are proving challenging to find the best parameter fit and these two stars have returned the highest abundance enhancements. At these temperatures and metallicities the issue of LTE must also be considered.

However the spread in abundance enhancements is distinct within each cluster indicating that the star-to-star scatter is genuine.

Table 2: 47 Tuc & NGC 362 stellar parameters and abundances

Cluster	(a) 47 Tuc		[Fe/H] = -0.7			(b) NGC 362		[Fe/H] = -1.2		
Star	x05	x03	x04	x02	x09	o08	o03	x01	o02	o10
Phot T_{eff} (K)	3777	3985	4172	4172	4172	3850	3900	4000	4200	4600
Spec T_{eff} (K)	4100	4100	4170	4200	4250	3850	3900	4000	4200	4450
log g	0.10	0.30	0.60	1.00	1.00	0.30	0.25	0.40	1.00	2.00
v_t (kms^{-1})	1.00	1.00	1.00	1.50	1.00	1.75	1.75	1.75	1.50	1.25
[Fe I / H]	-0.68	-0.71	-0.76	-0.77	-0.71	-1.24	-1.23	-1.15	-1.21	-1.19
[Fe II / H]	-0.58	-0.72	-0.80	-0.87	-0.85	-1.15	-1.26	-1.23	-1.22	-1.20
[X/Fe]										
Y I	1.00 ± 0.20	0.20 ± 0.20	0.50 ± 0.20	0.35 ± 0.20	1.10 ± 0.20	0.00 ± 0.20	0.20 ± 0.20	0.15 ± 0.20	0.10 ± 0.20	0.35 ± 0.20
Zr I	1.60 ± 0.62	1.14 ± 0.20	1.10 ± 0.66	0.76 ± 0.24	1.00 ± 0.55	0.30 ± 0.12	0.70 ± 0.14	0.50 ± 0.06	0.45 ± 0.06	0.60 ± 0.03
Ba II	0.50 ± 0.20	0.20 ± 0.20	0.50 ± 0.20	0.30 ± 0.20	0.50 ± 0.20	0.20 ± 0.20	0.50 ± 0.20	0.20 ± 0.20	0.30 ± 0.20	0.50 ± 0.20
La II	0.15 ± 0.07	0.15 ± 0.07	0.00 ± 0.05	0.05 ± 0.07	0.30 ± 0.14	0.05 ± 0.07	0.31 ± 0.08	0.15 ± 0.20	0.15 ± 0.20	0.38 ± 0.11
Eu II	0.20 ± 0.14	0.15 ± 0.07	0.25 ± 0.20	0.30 ± 0.20	0.40 ± 0.14	0.60 ± 0.20	0.55 ± 0.07	0.55 ± 0.14	0.65 ± 0.14	0.70 ± 0.20

Conclusion & Future Work

The high resolution datasets for both 47 Tuc and NGC 362 show a real star-to-star scatter in s-process element abundances. To explain the scatter some pollution mechanism has occurred either internal or external to the stars.

The analysis of the VLT dataset is ongoing. The analysis of the NGC 6388 stars suffers the same continuum fitting issues encountered with 47 Tuc and abundances for these stars will be derived once these issues are resolved.

A medium resolution large scale survey of stars in 47 Tuc is planned for either SALT RSS or AAOmega on the AAT. While too faint for the AAT the main sequence stars in 47 Tuc can be observed using SALT. Comparison of any main sequence abundance anomalies to the observed giant branch anomalies will provide a definitive result as to the pollution mechanism at work in producing the s-process abundance variations.

Acknowledgements

CCW would like to thank Iain McDonald and Jacco van Loon for providing her with the VLT dataset with which to explore her analysis of s-process element abundances in GCs.

CCW & PLC would like to thank the New Zealand Marsden Fund for financial support for CCW to attend this conference.

Thank you also to the LOC for the opportunity to attend this conference and for their financial assistance.

Bibliography

Allen, D. M. & Barbuy, B. 2006, A&A, 454, 895

Alonso, A., Arribas, S., & Martínez-Roger, C. 1999, A&AS, 140, 261

Alves-Brito, A., Barbuy, B., Ortolani, S., Momany, Y., Hill, V., Zoccali, M., Renzini, A., Minniti, D., Pasquini, L., Bica, E., & Rich, R. M. 2005, A&A, 435, 657

Arlandini, C., Käppeler, F., Wisshak, K., Gallino, R., Lugaro, M., Busso, M., & Straniero, O. 1999, ApJ, 525, 886

Asplund, M. 2005, ARA&A, 43, 481

Basri, G. & Batalha, C. 1990, ApJ, 363, 654

Bell, R. A., Eriksson, K., Gustafsson, B., & Nordlund, A. 1976, A&AS, 23, 37

Bessell, M. S. 2004, Memorie della Societa Astronomica Italiana, 75, 306

Biemont, E., Grevesse, N., Hannaford, P., & Lowe, R. M. 1981, ApJ, 248, 867

Briley, M. M., Harbeck, D., Smith, G. H., & Grebel, E. K. 2004, AJ, 127, 1588

Brown, J. A. & Wallerstein, G. 1992, AJ, 104, 1818

Buckley, D. A. H., Burgh, E. B., Cottrell, P. L., Nordsieck, K. H., O'Donoghue, D., & Williams, T. B. 2006, in Proceedings of SPIE, Vol. 6269, Ground-based and Airborne Instrumentation for Astronomy., ed. I. S. McLean & I. Masanori, 62690A

Burbidge, E. M., Burbidge, G. R., Fowler, W. A., & Hoyle, F. 1957, RvMP, 29, 547

Busso, M., Gallino, R., Lambert, D. L., Travaglio, C., & Smith, V. V. 2001, ApJ, 557, 802

Caldwell, S. P. & Dickens, R. J. 1988, MNRAS, 234, 87

Cannon, R., da Costa, G., Norris, J., Stanford, L., & Croke, B. 2003, in Astronomical Society of the Pacific Conference Series, Vol. 296, New Horizons in Globular Cluster Astronomy, ed. G. Piotto, G. Meylan, S. G. Djorgovski, & M. Riello, 175

Cannon, R. D., Croke, B. F. W., Bell, R. A., Hesser, J. E., & Stathakis, R. A. 1998, MNRAS, 298, 601

Carretta, E., Bragaglia, A., Gratton, R. G., Momany, Y., Recio-Blanco, A., Cassisi, S., François, P., James, G., Lucatello, S., & Moehler, S. 2007, A&A, 464, 967

Carretta, E., Gratton, R. G., Bragaglia, A., Bonifacio, P., & Pasquini, L. 2004, A&A, 416, 925

Castelli, F. & Kurucz, R. L. 2003, in IAU Symposium, Vol. 210, Modelling of Stellar Atmospheres, ed. N. Piskunov, W. W. Weiss, & D. F. Gray, 20P–+

Cottrell, P., Albrow, M., Barnes, S., & Kershaw, G. 2005, Critical Design Review for the Southern African Large Telescope High-Resolution Spectrograph, Tech. rep.

Cottrell, P. L. & Da Costa, G. S. 1981, ApJ, 245, L79

Cottrell, P. L., Lawson, W. A., & Buchhorn, M. 1990, MNRAS, 244, 149

Decressin, T., Charbonnel, C., & Meynet, G. 2007a, A&A, 475, 859

Decressin, T., Meynet, G., Charbonnel, C., Prantzos, N., & Ekström, S. 2007b, A&A, 464, 1029

Den Hartog, E. A., Lawler, J. E., Sneden, C., & Cowan, J. J. 2003, ApJS, 148, 543

Dotter, A., Chaboyer, B., Jevremović, D., Baron, E., Ferguson, J. W., Sarajedini, A., & Anderson, J. 2007, AJ, 134, 376

Edvardsson, B., Andersen, J., Gustafsson, B., Lambert, D. L., Nissen, P. E., & Tomkin, J. 1993, A&A, 275, 101

Freeman, K. C. 1985, in IAU Symposium, Vol. 113, Dynamics of Star Clusters, ed. J. Goodman & P. Hut, 33

Fulbright, J. P., McWilliam, A., & Rich, R. M. 2006, ApJ, 636, 821

—. 2007, ApJ, 661, 1152

Gallino, R., Arlandini, C., Busso, M., Lugaro, M., Travaglio, C., Straniero, O., Chieffi, A., & Limongi, M. 1998, ApJ, 497, 388

Gilliland, R. L., Bono, G., Edmonds, P. D., Caputo, F., Cassisi, S., Petro, L. D., Saha, A., & Shara, M. M. 1998, ApJ, 507, 818

Gratton, R., Sneden, C., & Carretta, E. 2004, ARA&A, 42, 385

Gratton, R. C. 1987a, A&A, 177, 177

Gratton, R. G. 1987b, A&A, 179, 181

Gratton, R. G. & Sneden, C. 1994, A&A, 287, 927

Gray, D. F. 2005, The Observation and Analysis of Stellar Photospheres, 3rd edn. (Cambridge, UK: Cambridge University Press)

Griffin, R. & Griffin, R. F. c.1980, Arcturus equivalent widths provided to Professor Lambert's group at the University of Texas in Austin

Gustafsson, B., Edvardsson, B., Eriksson, K., Jørgensen, U. G., Nordlund, Å., & Plez, B. 2008, A&A, 486, 951

Hannaford, P., Lowe, R. M., Grevesse, N., Biemont, E., & Whaling, W. 1982, ApJ, 261, 736

Harris, W. E. 1996, AJ, 112, 1487

Hartwick, F. D. A. & Hesser, J. E. 1974, in BAAS, Vol. 6, BAAS, 216

Herwig, F. 2005, ARA&A, 43, 435

Hesser, J. E., Harris, W. E., Vandenberg, D. A., Allwright, J. W. B., Shott, P., & Stetson, P. B. 1987, PASP, 99, 739

Hinkle, K. & Wallace, L. 2005, in Astronomical Society of the Pacific Conference Series, Vol. 336, Cosmic Abundances as Records of Stellar Evolution and Nucleosynthesis, ed. T. G. Barnes, III & F. N. Bash, 321–+

Iliadis, C. 2007, Nuclear Physics of Stars (Wiley-VCH)

James, G., François, P., Bonifacio, P., Carretta, E., Gratton, R. G., & Spite, F. 2004, A&A, 427, 825

Karakas, A. I., Fenner, Y., Sills, A., Campbell, S. W., & Lattanzio, J. C. 2006, ApJ, 652, 1240

Kayser, A., Hilker, M., Grebel, E. K., & Willemsen, P. G. 2008, A&A, 486, 437

Koch, A. & McWilliam, A. 2008, AJ, 135, 1551

Kupka, F. G., Ryabchikova, T. A., Piskunov, N. E., Stempels, H. C., & Weiss, W. W. 2000, Baltic Astronomy, 9, 590

Kurucz, R. 1993, Diatomic Molecular Data for Opacity Calculations. Kurucz CD-ROM No. 15. Cambridge, Mass.: Smithsonian Astrophysical Observatory, 1993., 15

Kurucz, R. L. 1979, ApJS, 40, 1

Kurucz, R. L. & Peytremann, E. 1975, SAO Special Report, 362

Lattanzio, J. C. 2007, Stellar Interiors and Nucleosynthesis (SINs) Mug

Lattanzio, J. C. & Tout, C. A. 2006, in EAS Publications Series, Vol. 19, EAS Publications Series, ed. T. Montmerle & C. Kahane, 189

Lawler, J. E., Bonvallet, G., & Sneden, C. 2001a, ApJ, 556, 452

Lawler, J. E., Wickliffe, M. E., den Hartog, E. A., & Sneden, C. 2001b, ApJ, 563, 1075

Lee, S. W. 1977, A&AS, 27, 381

Marcolini, A., Gibson, B. K., Karakas, A. I., & Sánchez-Blázquez, P. 2009, MNRAS, 395, 719

Masseron, T. 2006, PhD thesis, Obs. de Paris

McDonald, I. & van Loon, J. T. 2007, A&A, 476, 1261

Myers, P. C., Fuller, G. A., Mathieu, R. D., Beichman, C. A., Benson, P. J., Schild, R. E., & Emerson, J. P. 1987, ApJ, 319, 340

Nordsieck, K. H., Burgh, E. B., Kobulnicky, H. A., Williams, T. B., O'Donoghue, D., Percival, J. W., & Smith, M. P. 2001, in BAAS, Vol. 33, BAAS, 1465

Norris, J. & Freeman, K. C. 1979, ApJ, 230, L179

Origlia, L., Ferraro, F. R., Fusi Pecci, F., & Rood, R. T. 2002, ApJ, 571, 458

Paltoglou, G. 1990, in BAAS, Vol. 22, BAAS, 1289

Paltoglou, G. 1991, in BAAS, Vol. 23, BAAS, 1328

Paltoglou, G. & Freeman, K. C. 1984, PhD thesis, Mt. Stromlo and Siding Spring Observatories, Institute of Advanced Studies, Australian National University

Peterson, R. C., Dalle Ore, C. M., & Kurucz, R. L. 1993, ApJ, 404, 333

Pignatari, M., Gallino, R., Meynet, G., Hirschi, R., Herwig, F., & Wiescher, M. 2008, ApJ, 687, L95

Pilachowski, C. A., Sneden, C., & Wallerstein, G. 1983, ApJS, 52, 241

Prantzos, N. & Charbonnel, C. 2006, A&A, 458, 135

Pumo, M. L., D'Antona, F., & Ventura, P. 2008, ApJ, 672, L25

Ramdani, A. & Jorissen, A. 2001, A&A, 372, 85

Rolfs, C. E. & Rodney, W. S. 1988, Cauldrons in the cosmos: Nuclear astrophysics (Chicago, IL: University of Chicago Press)

Ruland, F., Holweger, H., Griffin, R., & Biehl, D. 1980, A&A, 92, 70

Sbordone, L., Bonifacio, P., & Castelli, F. 2006, Proceedings of the International Astronomical Union, 2, 71

Sharp, R., Saunders, W., Smith, G., Churilov, V., Correll, D., Dawson, J., Farrel, T., Frost, G., Haynes, R., Heald, R., Lankshear, A., Mayfield, D., Waller, L., & Whittard, D. 2006, in Proceedings of the SPIE, Vol. 6269, Ground-based and Airborne Instrumentation for Astronomy, ed. I. S. McLean & I. Masanori, 62690G

Shetrone, M. D. & Keane, M. J. 2000, AJ, 119, 840

Skuljan, L. & Cottrell, P. L. 2002, MNRAS, 335, 1133

Smith, G. H. 1984, AJ, 89, 1545

Smith, V. V. & Lambert, D. L. 1990, ApJS, 72, 387

Sneden, C. 1973, PhD thesis, University of Texas at Austin

Sneden, C. & Cowan, J. J. 2003, Science, 299, 70

Sneden, C., Cowan, J. J., & Gallino, R. 2008, ARA&A, 46, 241

Sugar, J. & Corliss, C. 1985, J. Phys. Chem. Ref. Data 14, Supplement No. 2

Travaglio, C., Gallino, R., Arnone, E., Cowan, J., Jordan, F., & Sneden, C. 2004, ApJ, 601, 864

Trimble, V. 1975, RvMP, 47, 877

Villanova, S., Piotto, G., & Gratton, R. G. 2009, A&A, 499, 755

Wallerstein, G., Iben, I. J., Parker, P., Boesgaard, A. M., Hale, G. M., Champagne, A. E., Barnes, C. A., Käppeler, F., Smith, V. V., Hoffman, R. D., Timmes, F. X., Sneden, C., Boyd, R. N., Meyer, B. S., & Lambert, D. L. 1997, RvMP, 69, 995

Wallerstein, G., Kovtyukh, V. V., & Andrievsky, S. M. 2007, AJ, 133, 1373

Worley, C. C., Cottrell, P. L., Freeman, K. C., & Wylie-de Boer, E. C. 2009, MNRAS, 1471

Worley, C. C., Cottrell, P. L., & Wylie de Boer, E. C. 2008, Publications of the Astronomical Society of Australia, 25, 53

Wylie, E. C., Cottrell, P. L., Sneden, C. A., & Lattanzio, J. C. 2006, ApJ, 649, 248

Yong, D., Grundahl, F., Johnson, J. A., & Asplund, M. 2008, ApJ, 684, 1159